TECHNISCHE UNIVERSITÄT MÜNCHEN
Fakultät für Medizin
Lehrstuhl für Biologische Bildgebung

Methods for Spectral Analysis in Optoacoustic Physiological and Molecular Imaging

Stratis Tzoumas

Vollständiger Abdruck der von der Fakultät für Medizin der Technischen Universität München zur Erlangung des akademischen Grades eines

Doktors der Naturwissenschaften (Dr. rer. nat.)

genehmigten Dissertation.

Vorsitzender: Prof. Dr. Percy A. Knolle
Prüfer der Dissertation:
1. Prof. Vasilis Ntziachristos, Ph.D.
2. Prof. Dr. Fabian Theis
3. Priv.-Doz. Dr. Ronald Sroka

Die Dissertation wurde am 19.05.2016 bei der Technischen Universität München eingereicht und durch die Fakultät für Medizin am 15.02.2017 angenommen.

Acknowledgements

This work would not have been possible without the support of a number of people.

First, I have to thank sincerely my advisor and mentor Dr. Vasilis Ntziachristos for introducing me to the exciting field of biomedical imaging, for offering me the opportunity to work with freedom on novel ideas, and for teaching me how to follow unexplored research paths with confidence. Without his support, open-mindedness and the trust he showed towards me, most of this work would not have been accomplished. His genuine enthusiasm for novel ideas and discoveries always served as the best motivation for carrying out this work.

As far as mentoring is concerned, I also have to thank deeply Dr. Amir Rosenthal for all these exciting intellectual interactions during this period. I will never forget our four-hour discussion in the lobby of our hotel in San Francisco, which gave concrete shape to the idea of the eigenspectra and was one of the most rewarding moments of my Ph.D. I am deeply thankful for his advice and friendship. I would also like to thank Dr. Nicolas Breziere for being always supportive and available for questions and advice.

I would like to thank my colleges, officemates and friends Panos, Andrei, Pouyan, Christian, Jake, Moritz and Amy for creating an inviting work environment through their unique characters and their incredible sense of humour. Especially, I would like to thank Panos for being always there in critical and stressful times and for putting off a lot of fires.

I would like to thank my closest collaborators and co-authors Dr. Antonio Nunes and Dr. Melanie Kimm. Through our joint work, I learned a lot about cancer biology and our cross-disciplinary collaboration was a unique experience for me. Especially, I would like to thank Ivan Olefir for our fruitful collaboration. I am thankful that it was him working next to me in the most exciting parts of this work. I would like to equally thank all my close collaborators and co-authors Dr. Pouyan Mohajerani, Dr. Nikos Deliolanis, Stefan Morscher, Andrii Kravtsiv, Yuan Gao, Dr. Andreas Buehler, Dr. Stefan Stangl, Dr. Gabrielle Multhoff, Dr. Christine Bayer, Christian Lutzweiler, Dr. Daniel Razansky, Dr. Angelika Zaremba, Dr. Karin Schaefer and Yiyong Han for our exciting interactions.

I am obliged to Susanne, Zsuzsi, Silvia, Doris and Christoph for their constant help and support in administrative matters, and the technical assistants Sarah, Uwe and Florian for their great work and devotion. Without them, our research in IBMI would not have been possible.

Importantly, I would like to thank my family for their support, and especially my parents who taught me that the most important step in solving a problem is to describe it accurately and retrace to the definition of its fundamental parameters. I realize now that this strategy for approaching problems is evident in many parts of my thesis, and it is probably one of my most valuable skills, gained at the age of 15 when I was solving high school mathematical problems with them. I would also like to thank Eva for her patience and support during this period.

Finally, I have to thank sincerely the Alexander Onassis Foundation for offering me the financial support to complete this work. I would also like to thank personally Ioanna Kailani and Stella Tatsi for their help.

Abstract

Multispectral Optoacoustic Tomography (MSOT) offers the potential to perform potent molecular and physiological imaging in small animals and humans. Molecular imaging aims at resolving light-absorbing reporter molecules, such as fluorescent dyes, at depths and resolutions that were not previously available to optical methods; an ability with the potential to facilitate a wide spectrum of needs in biological research. MSOT physiological imaging aims at the accurate quantification of blood oxygen saturation (sO_2) in high resolution within the tissue by spectrally resolving oxygenated and deoxygenated hemoglobin. Due to the lack of established methods that can resolve tissue oxygenation non-invasively and in high resolution, MSOT blood sO_2 imaging has the potential to offer new insights in a number of pathophysiological interrogations.

The sensitivity and quantification accuracy of MSOT imaging rely highly on the spectral analysis method employed. MSOT presents a unique spectral analysis problem, whereby the light fluence attenuation with tissue depth introduces changes in the detected spectral responses of absorbing molecules, as compared to their spectral signatures; a phenomenon termed 'spectral coloring'. Due to spectral coloring and a multitude of noise sources, spectral analysis of MSOT images consists a particularly challenging problem. This work develops spectral analysis methods for enhancing the sensitivity and quantification accuracy of molecular and physiological MSOT imaging.

The problem of MSOT molecular imaging is formulated as a detection problem where the goal is to detect the distribution of a molecular target within the tissue with high sensitivity and specificity. This goal is realized through the development of a statistical sub-pixel detection framework which models the background tissue spectra in a statistical manner and suppresses them for spectrally resolving the target molecule. The novel detection framework is validated through simulations and experimental data, and it is found to increase the MSOT molecular imaging capacity, substantially. The MSOT sensitivity is further studied with respect to the number of the excitation wavelengths utilized, while first insights on the feasibility and sensitivity of fluorescent labeled immune cell imaging with MSOT are also provided.

Quantitative blood sO_2 MSOT imaging has been so far impeded by spectral coloring, due to the effects of space and wavelength dependent light fluence. A novel concept for modeling the spectrum of light fluence as an affine function of basis spectra, termed fluence *eigenspectra*, is introduced. This fluence model is used for formulating the blood sO_2 estimation problem as a non-linear spectral unmixing problem, which is in the following solved by introducing a constrained non-linear inversion scheme. The novel method developed, termed *eigenspectra* MSOT (eMSOT), is validated in a number of simulations, imaging phantoms and controlled *in vivo* experiments and is found to offer substantially increased sO_2 quantification accuracy as compared to previously used spectral optoacoustic methods. eMSOT is further applied in small animal imaging studies for the quantification of blood oxygenation gradients in the skeletal muscle and hypoxic tumors. The measurements are validated through *post mortem* histological analysis, indicating that eMSOT is capable of quantitatively resolving tumor hypoxia.

To achieve the high image quality needed for molecular and physiological imaging, this work further considers the problem of reducing electronic noise typically present in MSOT data. A spatiospectral transformation is identified for sparsely representing MSOT data and this transformation is used for denoising MSOT signals and images, thus overcoming the need for repetitive signal acquisitions and averaging which may compromise imaging speed.

Zusammenfassung

Die Multispektrale Optoakustische Tomographie (*Multispectral Optoacoustic Tomography*, MSOT) ist ein bildgebendes Verfahren zur molekularen und physiologischen Bildgebung bei Kleintieren und dem Menschen. Molekulare Bildgebung ermöglicht die Darstellung von Kontrastmitteln (absorbierender Reportermoleküle, wie z.B. Fluoreszenzfarbstoffe) in Tiefen und Auflösungen, wie es anderen optischen Methoden bisher nicht möglich war. Aufgrund der hohen Auflösung hat die Methode das Potenzial bei diversen biologischen Fragestellungen angewendet zu werden. Durch die MSOT physiologische Bildgebung können oxygeniertes und desoxygeniertes Hämoglobin quantifiziert werden. Dadurch ist es möglich, mittels MSOT quantitative Aussagen über die Sauerstoffsättigung des Blutes (sO_2) innerhalb eines Gewebes zu machen. Aufgrund des Mangels an alternativen Methoden, die Gewebe-Oxygenierung in hoher Auflösung und nicht-invasiv darzustellen, birgt die MSOT Bildgebung das Potential neue Erkenntnisse bezüglich einer Vielzahl pathophysiologischer Fragestellungen zu liefern.

Die Sensitivität und Quantifizierungsgenauigkeit der MSOT Bildgebung ist dabei in hohem Maße von den angewandten Spektralanalysenmethode abhängig. Die Spektralanalyse der MSOT Bildgebung bringt ein spezifisches Problem hervor, da die Lichtfluenzdämpfung innerhalb tiefem Gewebe die spektralen Messungen der absorbierenden Moleküle verändert. Dieses Phänomen wird als spektrale Verfärbung bezeichnet. Aufgrund der spektralen Verfärbung und einer Vielzahl an Geräuschquellen, birgt die Spektralanalyse der MSOT Bildgebung ein besonders schwieriges Problem. In vorliegender Arbeit werden Spektralanalysemethoden entwickelt, welche die Sensitivität und Quantifizierungsgenauigkeit der molekularen und physiologischen MSOT Bildgebung verbessern sollen.

Das Problem der molekularen Bildgebung mittels MSOT ist vor allem ein Detektionsproblem. Die Verteilung der molekularen Absorber mit hoher Sensitivität und Spezifität zu ermitteln stellt eine große Herausforderung dar. Dieses Ziel wurde im Rahmen dieser Arbeit durch die Entwicklung von statistischen Sub-Pixel Detektionsverfahren realisiert. Die Leistung dieser hier vorgestellten neuartigen Erkennungsverfahren wurde mittels Simulationen und experimentellen Daten evaluiert. Die hier vorgestellten Ergebnisse zeigen, dass die molekulare Bildgebungssensitivität von MSOT erheblich verbessert wurde. Weiterhin wurde die Sensitivität von MSOT hinsichtlich der Anzahl der verwendeten Anregungswellenlängen untersucht, wobei auch erste Erkenntnisse zur Durchführbarkeit und Sensitivität der MSOT Immunzellen-Bildgebung vorgestellt werden.

Die Quantitative Blut (sO_2) MSOT Bildgebung war bisher aufgrund der spektralen Verfärbung nur sehr eingeschränkt möglich. Diese entsteht aufgrund der raum- und wellenlängenabhängigen Lichtfluenz. In der vorliegenden Arbeit wird ein neues Konzept zur Modellierung des Spektrums der Lichtfluenz als affine Funktion von Basisspektren, genannt „Eigenspektren“, vorgestellt. Dieses neue Fluenzmodell wird bei der Umwandlung des Blut sO_2- Schätzproblems in ein nicht lineares spektrales Entmischungs-Problem genützt, welches im Folgenden durch die Einführung eines beschränkten nicht linearen Inversions-Algorithmus gelöst wird. Die neu entwickelte Methode namens „Eigenspektra MSOT“ (eMSOT) wird anhand einer Vielzahl von Simulationen, Blutphantomen und kontrollierten *in vivo* Experimenten validiert und es zeigte sich, dass die sO_2-Quantifizierungsgenauigkeit im Vergleich zu früher verwendeten spektralen optoakustischen Methoden erheblich verbessert wurde. Im Weiteren wird eMSOT bei Bildgebungsstudien an Kleintieren angewandt, um die Quantifizierung des Blut-Oxygenierungsgradienten im Skelettmuskel und hypoxischen Tumoren durchzuführen. Die Messungen wurden durch *post mortem* histologische Untersuchungen validiert. Die Ergebnisse zeigen, dass eMSOT in der Lage ist, Sauerstoffmangel in Tumoren quantitativ aufzulösen.

Schließlich befasst sich diese Arbeit mit der Verminderung des elektronischen Hintergrundgeräusches, welches typischerweise in MSOT Daten auftritt. Um unspezifisches Hintergrundrauschen von spezifischem Signal zu trennen, wurde eine räumlich-spektrale Transformation verwendet. Hier-

durch konnte auf multiple Signalerfassung und -mittelung verzichtet werden, was zu einer Beeinträchtigung der Bildgebungsgeschwindigkeit hätte führen können.

Publication record

The present work is a publication based dissertation that is based on six publications that are published in international journals († indicates equal author contribution):

1. **S. Tzoumas**, N.C. Deliolanis, S. Morscher, V. Ntziachristos, "Unmixing molecular agents from absorbing tissue in multispectral optoacoustic tomography," *Medical Imaging, IEEE Transactions on*, vol. 33, no. 1, pp. 48-60, 2014.

2. **S. Tzoumas**, A. Kravtsiv, Y. Gao, A. Buehler, V. Ntziachristos, "Statistical molecular target detection framework for multispectral optoacoustic tomography," *Medical Imaging, IEEE Transactions on*, vol. 35, no. 12, pp. 2534-2545, 2016.

3. **S. Tzoumas**, A. Nunes, N.C. Deliolanis, V. Ntziachristos, "Effects of multispectral excitation on the sensitivity of molecular optoacoustic imaging," *Journal of Biophotonics*, vol. 8, no. 8, pp. 629-637, 2015.

4. **S. Tzoumas**†, A. Zaremba†, U. Klemm, A. Nunes, K. Schaefer, V. Ntziachristos, "Immune cell imaging using multi-spectral optoacoustic tomography," *Optics Letters*, vol. 39, no. 12, pp. 3523-2526, 2014.

5. **S. Tzoumas**†, A. Nunes†, I. Olefir, S. Stangl, P. Symvoulidis, S. Glasl, C. Bayer, G. Multhoff, V. Ntziachristos, "Eigenspectra optoacoustic tomography achieves quantitative blood oxygenation imaging deep in tissues," *Nature Communications*, vol. 7, pp. 12121, 2016

6. **S. Tzoumas**, A. Rosenthal, C. Lutzweiler, D. Razansky, V. Ntziachristos, "Spatiospectral denoising framework for multispectral optoacoustic imaging based on sparse signal representation," *Medical Physics*, vol. 41, no. 11, pp. 113301, 2014.

Throughout the period of my Ph.D. work, I further contributed to the following additional publications which are relevant to this work but not included in this thesis as individual Chapters:

7. P. Mohajerani, **S. Tzoumas**, A. Rosenthal, V. Ntziachristos, "Optical and Optoacoustic Model-Based Tomography: Theory and current challenges for deep tissue imaging of optical contrast," *IEEE Signal Processing Magazine*, vol. 32, no. 1, pp. 88-100, 2015.

8. C. Lutzweiler, **S. Tzoumas**, A. Rosenthal, V. Ntziachristos, D. Razansky, "High-throughput sparsity-based inversion scheme for optoacoustic tomography," *Medical Imaging, IEEE Transactions on* , Published Online, DOI:10.1109/TMI.2015.2490799.

9. Y. Han, **S. Tzoumas**, A. Nunes, V. Ntziachristos, A. Rosenthal, "Sparsity-based acoustic inversion in cross-sectional multiscale optoacoustic imaging," *Medical Physics*, vol. 42, no. 9, pp. 5444-5452, 2015.

List of abbreviations

MSOT	Multi-spectral Optoacoustic Tomography
CT	Computed Tomography
MRI	Magnetic Resonance Imaging
PET	Positron Emission Tomography
SPECT	Single Photon Emission Tomography
BOLD	Blood Oxygenation Level Dependent
ICG	Indocyanine Green
iRFP	Infrared Fluorescent Protein
DOS	Diffuse Optical Spectroscopy
DOT	Diffuse Optical Tomography
RTE	Radiative Transfer Equation
DA	Diffusion Approximation
OPO	Optical Parameter Oscillator
LMM	Linear Mixture Model
ICA	Independent Component Analysis
BSS	Blind Source Separation
VCA	Vertex Component Analysis
GLRT	Generalized Likelihood Ratio Test
AMF	Adaptive Matched Filter
ACE	Adaptive Coherence Estimator
EC-GLRT	Elliptically Contoured – Generalized Likelihood Ratio Test
PCA	Principal Component Analysis
eMSOT	Eigenspectra Multi-spectral Optoacoustic Tomography

Contents

Chapter 1

Methods for spectral analysis in optoacoustic physiological and molecular imaging – An overview

1.1 Introduction

1.1.1 Motivation: Physiological and molecular imaging

Biomedical imaging is playing today a fundamental role in healthcare and life sciences. Radiological imaging modalities such as X-ray imaging and computed tomography (CT), ultrasound, Magnetic Resonance Imaging (MRI), Single Photon Emission Tomography (SPECT) and Positron Emission Tomography (PET) have been established as indispensable tools in the clinical routine for the successful diagnosis and treatment of disease. Additionally, the growing number of genetically modified animal models has further spurred the use of imaging in small animals for basic science, drug discovery and translational research. Most of the existing radiological imaging methods have been down-scaled for small animal imaging while new technologies have been developed specifically for this purpose [1]. *In vivo* imaging is emerging today as a basic tool for biomedical research, complementing or replacing *ex vivo* observations based on microscopy [2].

Aside to mapping tissue anatomy, recent efforts have been largely focused on physiological and molecular imaging. Physiological imaging provides spatially resolved information on tissue physiology parameters, such as blood flow, perfusion or blood and tissue oxygenation, which are important for diagnosing and monitoring a number of pathologies including cardiovascular diseases and cancer. Molecular imaging [3] typically seeks to map spatially the distribution of specific molecular probes for visualizing among others, receptors, gene expression or for cell imaging and tracking [4]. Physiological and molecular imaging aim at recognizing disease before this is expressed through anatomical alterations, identify and characterize non-anatomical phenotypes related to specific pathologies and unravel the underlying molecular mechanisms of the disease or the specific mechanisms of therapeutic approaches [4]. Therefore, the development of potent physiological and molecular imaging methods is of substantial importance for providing both novel diagnostic abilities in the clinical setting and valuable tools for therapy research in the preclinical arena.

Established radiological imaging modalities have been continuously improved for performing anatomical (CT, MRI, ultrasound), physiological (primarily MRI and ultrasound) and molecular imaging (primarily PET/SPECT) in humans and small animals. The fundamental physical principle that each method exploits largely defines its characteristic abilities and limitations. For instance, MRI can image physiology through the contrast of the paramagnetic deoxygenated hemoglobin (Hb), but the lack of magnetic contrast of oxygenated hemoglobin (HbO_2) limits its ability to directly quantify blood oxygenation [5]. PET offers potent molecular imaging capabilities [6], but its lack of anatomical contrast, low resolution, high cost and the use of ionizing radiation make it non-ideal for routine use in small animal imaging studies. In general, each imaging method is typically ideal for specific applications and novel applications often spur the development of innovative methods.

Limitations of established radiological imaging modalities in certain domains have motivated the exploration of novel methods primarily based on light for achieving molecular and physiological

imaging in small animals and humans. Optical imaging offers direct access to physiological information due to the optical contrast of the molecules of HbO_2 and Hb. Furthermore, it also allows for potent and versatile molecular imaging by using a large toolbox of functionalized fluorescence probes and reporter genes [7]. Although light poses limitations in terms of penetration depth, optical imaging is non-ionizing and it is typically associated with low cost which makes it particularly attractive for preclinical small animal imaging applications.

Optical microscopy has been for centuries one of the most valuable tools for biological discovery. However, even advanced microscopy techniques cannot deliver images beyond the first millimeter of scattering tissue [8]. Probing light deeper into opaque tissue for *in vivo* imaging is confronted with photon diffusion, i.e. the complex propagation of photons after multiple elastic scattering events due to their interaction with tissue molecules. The establishment of diffusion theory for photon propagation in tissues [9] and the development of light propagation models [10] enabled the design of rigorous tomographic inversion methods that allowed for mapping diffused photon distribution in deep tissue. This effort offered new abilities in deep-tissue molecular and physiological imaging in small animals and humans [11]. Diffuse optical tomography (DOT) enabled for the first time the visualization of fluorescence distribution through opaque living organisms [12] as well as hemodynamics imaging in humans through the intrinsic optical contrast of hemoglobin [13]. However, due to the high scattering of photons in tissue, diffuse optical imaging remains a low resolution method, often failing to visualize in detail the specific biodistribution of molecules. Moreover, due to the nature of diffuse light propagation, the imaging inverse problem (i.e. the image reconstruction problem) is particularly ill-posed, typically requiring a number of approximations and regularization methods, and may result in reduced spatial accuracy and specificity. Such complications may often restrict the successful application of pure optical imaging modalities.

The development of optoacoustic (also termed photoacoustic) imaging in the early 21st century brought a paradigm shift to the field of biomedical optics. By replacing the detection of scattered photons with the detection of ultrasound, produced as a result of the light-tissue interaction, optoacoustic imaging demonstrated the first deep-tissue ($>$ 1cm), high resolution images of optical contrast [14, 15]. Optoacoustic imaging is based on the generation of pressure waves as a result of the thermoelastic expansion due to transient light absorbed by molecules. Since the generated pressure waves (ultrasound) scatter 2-3 orders of magnitude less than photons in tissue, the optoacoustic method can deliver high resolution images of optical absorption contrast [16]. Importantly, the image formation problem is largely simplified, since it is not confronted anymore with light propagation in tissue, and it is typically solved through an analytical solution or a rather well-posed linear inverse problem. A numerical comparison between the image reconstruction inverse problems of diffuse optical versus optoacoustic tomography, clearly demonstrate the merits of the latter imaging method [17].

An essential aspect of biomedical optoacoustic imaging is the spectrum, i.e. the spectroscopic information obtained through the excitation of tissue with different wavelengths of visible and near-infrared light. While conventional optoacoustic imaging delivers high resolution anatomical images of optical absorption contrast, it is mainly the spectral information that allows extracting valuable physiological and molecular information. Multispectral Optoacoustic Tomography (MSOT) can detect the spectra of HbO_2 and Hb in tissue and, therefore, it offers the potential to estimate blood oxygen saturation in high resolution across entire organs and tissues [18–20]. This ability, not available through previously existing imaging methods, has the potential to offer new insights into tissue physiology as well as a number of pathologies such as cancer hypoxia. Moreover, MSOT offers the potential for high resolution molecular imaging by using the existing fluorescence toolbox or alternative contrast mechanisms such as absorbing nanoparticles [21]. MSOT allows for visualizing such molecules at depths and resolutions not available previously to optical methods, an ability that offers the potential to faciliate a wide spectrum of needs in biological research such as tumour targeting, clearance of injected pharmaceuticals [22], localization of protein expression in advanced biological models [23] and cell imaging. Developing methods for advancing the physiological and molecular imaging abilities of MSOT is of substantial importance for disseminating MSOT in biomedical research and for its clinical translation.

1.1.2 Objectives

Before the initiation of the herein described efforts, robust small animal MSOT imaging scanners had already been developed [24] along with dedicated image reconstruction algorithms for delivering high

image quality [25]. Moreover, early MSOT imaging studies had already showcased the potential for molecular imaging through the visualization of fluorescent dyes, fluorescent proteins and absorbing nanoparticles within small animals [21], as well as the potential of imaging tissue physiology through the spectral differentiation between HbO_2 and Hb in healthy tissue and tumors [18, 19]. However, the spectral optoacoustic imaging problem had not been thoroughly studied or conclusively solved.

MSOT presents a rather unique spectral analysis problem, whereby the light fluence attenuation with tissue depth introduces changes in the detected spectral responses of the absorbing molecules, as compared to their spectral signatures measured in the photospectrometer; a phenomenon commonly termed 'spectral coloring' or 'spectral corruption' [26]. Early *in vivo* studies using spectral optoacoustic methods did not consider the effects of light propagation and spectral coloring and used simple approximate spectral analysis algorithms. As a result, early multi-spectral optoacoustic methods offered reduced sensitivity in imaging molecular targets and reduced quantification accuracy in the estimation of blood oxygen saturation. Although it was early recognized that spectral coloring posed a significant limitation for accurate molecular and physiological imaging [27], there was a lack of dedicated spectral unmixing algorithms that could consider and overcome such effects for improving the molecular and physiological imaging capacity of MSOT.

From a biomedical application point of view, there is a strong need for methods that can operate robustly in experimental tissue data and offer (1) potent molecular imaging capacity through the visualization of molecular probes with high sensitivity and specificity, and (2) accurate physiological imaging through the quantification of blood oxygen saturation within tissue. Such methods need to be thoroughly validated through simulations and controlled animal experiments before applied for novel biological observations.

The objective of this work is to develop robust multispectral analysis methods for increasing the sensitivity and quantification accuracy of MSOT in molecular and physiological imaging applications, evaluate the performance of these methods through simulations and appropriately designed animal experiments and establish their abilities in key biomedical imaging applications. The three main objectives addressed by this work are the following:

The first objective relates to molecular imaging, i.e. the mapping of optical absorbing agents administered or expressed in tissue. The goal herein is the identification and development of spectral analysis algorithms that can be applied on MSOT images to resolve the distribution of molecular probes of interest from the absorbing tissue background. The methods should offer high sensitivity, i.e. resolve targets present in low concentrations within tissue, and high specificity, i.e. minimize the possibility of false positives. It is also an objective of this work to assess the influence of experimental parameters on the MSOT molecular imaging capacity for indicating optimal directions in conducting *in vivo* experiments. Finally, a further goal of this work is to apply MSOT combined with advanced spectral analysis algorithms for imaging labeled immune cells and establishing the sensitivity limits in this application.

The second objective relates to physiological imaging and specifically to the accurate quantification of blood oxygenation with MSOT. As previously established, spectral coloring leads to the alteration of the optoacoustically recorded spectra with depth and hinders the accurate computation of blood oxygenation within deep tissue. The goal herein is to develop a novel method that models the light fluence within tissue and account for spectral coloring; thus enabling the accurate estimation of blood oxygenation within deep tissue. The method should offer high estimation accuracy for tissue depths relevant to small animal imaging and be thoroughly validated through simulations and *in vivo* controlled experiments. Finally, a further goal of this work is to investigate the ability of MSOT coupled with appropriate spectral analysis algorithms to image and quantify cancer hypoxia.

The need for multiple excitation wavelengths for accurate molecular and physiological imaging in combination with the need for repetitive signal acquisition and averaging for ensuring low noise levels imposes a substantial overhead on the temporal resolution of MSOT. A third objective of this work is to introduce a signal denoising framework for removing electronic noise from MSOT signals and images. The denoising framework should overcome the need for repetitive signal acquisition and averaging, thus enhancing the MSOT temporal resolution.

1.1.3 Outline

This work is organized as a publication based dissertation with one introductory Chapter and six additional Chapters corresponding to six individual publications.

This first Chapter outlines the motivation of this work, provides background theory on important concepts and methodologies [1] and serves as an introduction to the developments presented in Chapters 2-7. Section 1.2 reviews the potential of MSOT in performing molecular and physiological imaging and compares the characteristics of this technology to the ones of established imaging modalities. Section 1.3 offers background theory on light propagation, optoacoustic imaging and image formation and describes the MSOT imaging systems used in the context of this work. Sec. 1.4 formulates the MSOT spectral unmixing problem and describes its main challenges. Subsections 1.4.1 and 1.4.2 introduce the more specific problems of spectral analysis for molecular imaging and physiological imaging, respectively, review relevant prior work and offer theoretical reasoning for the novel methods developed herein. Finally, Sec. 1.5 summarizes this work and provides an outlook for important future goals.

Chapters 2-5 relate to the problem of MSOT molecular imaging. Chapter 2 formulates the MSOT molecular imaging problem as a detection problem where the goal is to detect the distribution of an extrinsic molecular target with a distinct spectrum, with high sensitivity and specificity. By creating a simulation framework and compiling an experimental MSOT dataset with available ground truth, the performance of different spectral unmixing and sub-pixel detection methods, typically used in remote sensing hyperspectral imaging, is investigated within the context of MSOT. Statistical sub-pixel detection algorithms are found to outperform alternative approaches under the condition that the optical agent of interest is sparsely present within the tissue. Based on this finding, in Chapter 3 a novel statistical sub-pixel detection framework is introduced that is particularly suited to the characteristics of MSOT molecular imaging.

Aside to algorithmic aspects, experimental aspects of MSOT molecular imaging are further investigated in Chapters 4-5. In Chapter 4, the sensitivity of MSOT molecular imaging is studied with respect to the number of the excitation wavelengths used using simulations and *in vivo* animal experiments. In Chapter 5, MSOT coupled with a statistical detection algorithm is investigated for the application of immune cell imaging. The optoacoustic signal of fluorescent labeled T-cells and macrophages is quantified using imaging phantoms, and animal experiments are performed for providing first insights on the feasibility and sensitivity of MSOT immune cell imaging.

Chapter 6 relates to the problem of MSOT physiological imaging and introduces a spectral analysis algorithm for quantifying tissue blood oxygenation with MSOT. By introducing a novel model for describing the light fluence spectrum within the tissue (termed fluence *eigenspectra*), this problem is formulated as a non-linear spectral unmixing problem and solved through the introduction of a constrained non-linear inversion scheme. The method presented, termed *eigenspectra* MSOT, is applied for the quantification of blood oxygenation gradients in skeletal muscle and hypoxic tumors, and the results obtained are validated through histological analysis.

Finally, Chapter 7 presents a sparse representation of MSOT signals and images and an associated denoising algorithm and validates its performance in simulated and experimental data.

1.2 Molecular and physiological imaging with MSOT

Small animal MSOT imaging offers the potential to perform molecular and physiological imaging with complementary abilities to currently existing biomedical imaging modalities. This section describes the biomedical motivation behind this work, placing MSOT imaging in the general map of small animal imaging modalities.

1.2.1 Molecular imaging with MSOT

Molecular imaging refers to the observation of specific processes in the cellular and molecular level, typically achieved by administering reporter molecules that selectively bind to a receptor or by utilizing reporter genes in genetically engineered animal models [3]. Molecular imaging is playing an increasingly important role in basic biological and oncology research [34], with applications ranging from receptor imaging [4], cancer research (i.e. study of angiogenesis, hypoxia and apoptosis) [34], and early cancer detection [6] to immune cell and stem cell imaging and tracking [35].

[1] Basic theory on optoacoustic imaging and light propagation is provided in Sec. 1.3 of Chapter 1. Throughout Chapters 1-7 a number of signal processing methods and tools are used or discussed such as wavelets [28], Principal Component Analysis and Independent Component Analysis [29], detection theory and statistical signal processing [30, 31] and some concepts from linear and constrained non-linear optimization [32, 33]. Such concepts are not hereby introduced or explained and the interested reader is referred to published textbooks [28–33].

The majority of established biomedical imaging modalities have been investigated in molecular imaging applications: PET/SPECT provide a potent tool for molecular imaging with paramount sensitivity (picomolar concentration)[36], but the low spatial resolution (1mm) and mainly the complexity and high cost associated with the use of radio-tracers may restrict its widespread application in biology research labs. Although MRI is typically considered a low sensitivity imaging modality [36], it has achieved molecular and cell imaging in particular though iron-oxide nanoparticles [37]. Nevertheless, it is a costly imaging method and iron nanoparticles may be associated with high toxicity for certain applications. Ultrasound has recently demonstrated promising molecular imaging abilities through targeted [38] or genetically encoded microbubbles [39], but it has not become a widespread molecular imaging method yet. Conversely, optical imaging through bioluminescence and fluorescence imaging and tomography have emerged as popular molecular imaging methods in biological labs due to their high sensitivity (sub-nanomolar scale [36]), easiness of use and low cost [7]. Nevertheless, diffuse optical methods are associated with a low spatial resolution or surface-weighted imaging ability, a performance which often fails to provide accurate information on the exact molecule biodistribution.

MSOT imaging achieves a resolution that is higher than that of PET/SPECT and optical imaging and comparable to the one of high-field MRI in small animal imaging applications. It offers higher temporal resolution than other molecular imaging methods (with the exception of ultrasound), high throughput abilities, and it is associated with relatively low cost and easiness of use; therefore offering very favourable characteristics for its dissemination in the biology laboratory [21].

The optical absorption contrast of optoacoustic tomography renders all absorbing molecules as potential optoacoustic contrast agents. For instance, fluorescent dyes that absorb light in the near infrared, such as Indocyanine green (ICG), Alexa Fluor dyes or IRDye800CW and near-infrared fluorescent proteins (iRFP) have all been considered for optoacoustic contrast generation [40]. Fluorescent dyes present a particularly interesting contrast mechanism due to the availability of fluorescent probes with specific molecular function, which have been also used for molecular MSOT imaging [41, 42]. Since the optoacoustic contrast is proportional to the absorbed energy that is converted into thermal energy, fluorescent dyes with low quantum yield typically result in a higher optoacoustic signal.

Contrary to optical fluorescence imaging methods – where autofluorescence is rather negligible in the near-infrared - optoacoustic imaging is associated with a high background-tissue contrast (mainly stemming from tissue intrinsic hemoglobin in the visible/near-infrared) which limits its sensitivity in detecting such extrinsically administered molecules. Typically fluorescent dyes need to accumulate in very high amounts to achieve absorption contrast comparable to that of blood in tissue. For instance, the fluorochrome AlexaFluor750 which is associated with a molar extinction coefficient of 290,000 $cm^{-1}M^{-1}$ and a quantum yield of 0.12 would need to be present at a concentration of > 10 µM to achieve comparable absorption contrast to the one of blood in an artery (approx. 2.8 cm^{-1} at 750 nm [43]). This high concentration required for obtaining sufficient contrast results in an unfavourable sensitivity of optoacoustic imaging as compared to pure optical imaging modalities.

There are two primary directions, considered for enhancing the sensitivity of optoacoustic imaging in molecular imaging applications: (1) The development of novel contrast mechanism for optoacoustic imaging, i.e. highly absorbing small molecules and nanoparticles. (2) The development of multispectral imaging approaches and spectral analysis algorithms that resolve weak signal contributions of reporter molecules from the absorbing tissue background. The two approaches are complementary since multispectral methods can be combined with specifically designed absorbing molecules or nanoparticles for enhancing the sensitivity. As far as the first goal is concerned, recent studies have revealed a multitude of absorbing molecules that can serve as potential optoacoustic contrast agents. Aside to fluorescent dyes, absorbing molecules such as melanin produced due to Tyrosinase gene expression has been used as a genetically encoded molecular agent [44, 45]. Moreover absorbing nanoparticles such as carbon nanotubes [46] and gold nanoparticles [40] have been shown to offer two to four orders of magnitude higher absorption (per particle) as compared to fluorescent dyes [21].

Each molecule absorbs light with a distinct spectral pattern according to its molecular composition. Multispectral imaging and spectral unmixing capitalizes on this principle to resolve molecular targets of interest from the absorbing tissue background with high sensitivity and specificity. The molecular target detection problem for MSOT imaging is formulated in Sec. 1.4.1.

1.2.2 Imaging physiology with MSOT

Tissue oxygenation is, among others (e.g. perfusion, blood flow), a crucial physiological parameter which is also associated with a multitude of pathological conditions including cardiovascular diseases and cancer. For instance, the oxygenation level in cancer is a key measure to understand the outcome of certain therapies and the probability of metastasis [47] while low tissue oxygenation can potentially also serve as a marker for ischemia or stroke. Due to the importance of tissue oxygenation in physiological and pathological processes, a number of imaging and sensing methods have been developed towards this goal (Fig. 1.1). The metric of interest is typically the partial pressure of oxygen (pO_2) in blood and tissue (unit mmHg). An alternative metric is the oxygen saturation of hemoglobin in blood (sO_2), defined as the ratio of the amount of oxygen bound to hemoglobin to the total oxygen-carrying capacity of hemoglobin. sO_2 can be used to infer pO_2 in blood through the oxygen dissociation curve of hemoglobin [48]. Since oxygen is primarily delivered into cells through hemoglobin, sO_2 measurements can offer a good estimate of tissue oxygenation levels.

The gold standard for studying tissue oxygenation (pO_2) and hypoxia largely relies on invasive methods such as the local insertion of a polarography needle electrode or immunohistochemistry after the injection of exogenous hypoxia markers, such as pimonidazole [49]. One of the first imaging methods able to quantify tissue oxygenation is ^{15}O PET [50], although this method is not widely applicable mainly due to the short half-life of ^{15}O (2 min). Hypoxia imaging methods using PET have also been considered, for example through the administration of 2-nitroimidazole based tracers (e.g. [^{18}F]FMISO) [49]. Nevertheless, these radiolabel-based approaches only provide information on cell hypoxia and they do not allow for quantification of tissue oxygenation. PET imaging also suffers from low spatial resolution, high cost and short-time imaging windows.

MRI offers label-free oxygenation-related contrast through BOLD imaging [5], which provides contrast on paramagnetic deoxygenated hemoglobin. However, BOLD-MRI cannot sense oxyhemoglobin and the BOLD signal intensity also relates to the relative orientation of the vessels with respect to the magnetic field [5]. Substantial research has been conducted for quantifying blood oxygen saturation using BOLD-MRI methods, by developing biophysical models that exploit prior knowledge on tissue composition [51, 52]. Nevertheless, accurate blood sO_2 quantification using quantitative BOLD-MRI is considered still a very challenging problem. Electron paramagnetic resonance imaging has recently demonstrated the ability to measure quantitatively tissue oxygenation (pO_2) through the administration of exogenous spin probes [53]. Although the technology appears very promising in this direction, it offers reduced spatial and temporal resolution (1 mm and 1 min, respectively) while it is also associated with high cost. Furthermore, the results depend on the probe's biodistribution which may be insufficient in non-perfused parts of tissue such as hypoxia volumes in tumors.

Optical methods have been traditionally considered for sensing blood oxygenation due to the differences between the oxyhemoglobin and deoxyhemoglobin absorption spectra. Arterial sO_2 is clinically assessed by the pulse oximeter, an optical technology that can only be applied for measuring the oxygenation of the pulsating arterial blood. Optical microscopy methods like phosphorescence quenching microscopy [55], hemoglobin photospectroscopy methods [56] or optoacoustic (photoacoustic) microscopy [57] can visualize oxygenation in blood vessels and capillaries [58]. Such methods have provided rich novel insight into tissue physiology, blood oxygenation and oxygen exchange in the microcirculation [59]. Nevertheless, microscopy methods are either restricted to superficial ($<$1mm depth) measurements or require complicated, invasive procedures for reaching deep tissue areas. Diffuse optical methods received significant attention in the last two decades for sensing and imaging HbO_2 and Hb deeper in tissue [11, 60]. Diffuse optical spectroscopy (DOS) can deliver average values of tissue blood sO_2 that are not spatially resolved [61], while spectral diffuse optical tomography (DOT) resolves a low resolution map of tissue blood sO_2 using rigorous image reconstruction methods [62]. Due to the high heterogeneity of tissue and the large differences of blood sO_2 between arteries, veins and capillaries, such low resolution measures are often hard to interpret or validate, especially in the application of small animal imaging.

The multitude of imaging methods developed for imaging tissue and blood oxygenation underscores the importance of this metric in assessing physiology and pathological conditions. MSOT appears optimally suited for this task as it is able to detect the spectra of HbO_2 and Hb in high resolution deep within tissues. Its attributes that are not available in previously considered methods, namely high spatial ($<$0.2 mm) and temporal resolution (appr. 1 sec per multispectral image), non-invasive imaging capacity and easiness of use, suggest that this technology could provide a valuable

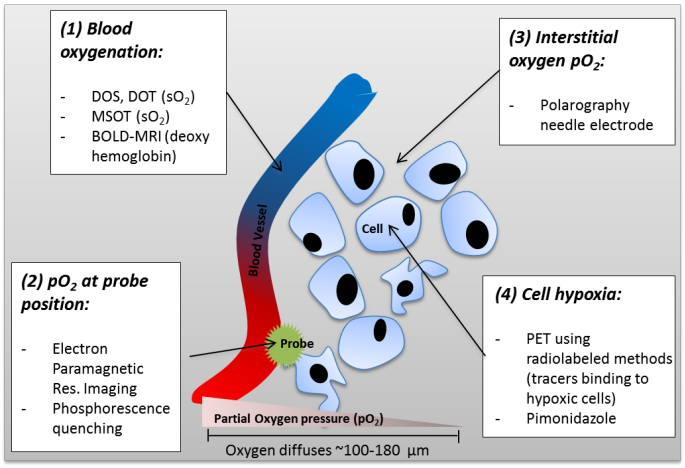

Figure 1.1: Schematic representation of different strategies for imaging tissue oxygenation: (1) Agent-free through blood oxygenation imaging (BOLD-MRI, DOT, DOS, MSOT). (2) Through pO_2 measurements at probe location (electron paramagnetic res. imaging and phosphorescence quenching microscopy). (3) Through invasive measurements of interstitial pO_2 (Polarography needle electrode). (4) Through the detection of tracers binding to hypoxic cells (PET, Pimonidazole staining). The schematic is re-drawn and adapted from [54]

tool for assessing tissue physiology in biological studies. Despite the principal MSOT suitability for non-invasive imaging of blood oxygenation, its accuracy has remained limited by the dependence of the light fluence on depth and light color. Unless explicitly accounted for, the wavelength dependent light fluence profile alters the detected spectral features and results in inaccurate estimates of blood sO_2 [27]. Despite a decade of research in quantitative optoacoustic imaging [26], the problem of light fluence correction has not been conclusively solved. The blood sO_2 quantification problem using MSOT measurements is described in Sec. 1.4.2 where prior work towards this goal is further reviewed.

1.3 Background methodology: Optoacoustic instrumentation, image formation and light propagation models

This Section briefly reviews basic background principles of photoacoustic imaging and image formation, fundamental aspects of light propagation models, as well as the optoacoustic imaging system that was used for all experiments described in Chapters 2-7. It is not the purpose of this Section to thoroughly describe the physics of optoacoustic imaging and light propagation which are analytically described in published textbooks [63–65], but rather to offer an introduction to principles and methods that served as a basis for the work described in following Chapters.

1.3.1 MSOT imaging system

In recent years, a number of different optoacoustic imaging systems have been developed. The imaging characteristics of such systems depend in major on the geometry of the ultrasound sensors surrounding the sample, the frequency bandwidth and focal characteristics of the ultrasound sensors and the illumination deployed. 3D imaging geometries utilizing planar [66], spherical/hemispherical [67–69] or more complex detection geometries [70] can offer visualization of larger volumes with nearly isotropic resolution, typically at the expense of limited view, temporal resolution or easiness of use. Conversely, 2D imaging systems use focused ultrasound arrays [14, 24, 71, 72] to produce an image at a transverse slice at the focal plane of the ultrasound elements. These geometries do not offer an isotropic resolution, but they typically require fewer detectors for ensuring high image quality, allow high temporal resolution and can achieve larger angle of coverage within the 2D plane, which enhances image quality. The bandwidth of the ultrasound sensors employed is selected according to the resolution and imaging depth aimed. Systems utilizing high-frequency ultrasound sensors achieve high resolution [73–75] at the expense of reduced imaging depth, due to

high-frequency ultrasound attenuation; thus, they are typically selected for imaging smaller samples. A recent review of the different small animal optoacoustic imaging systems is presented in [76]. All experimental data used in the context of this work were acquired using either one prototype or one commercially available 2D small animal imaging MSOT system. Both systems utilize a curved 2D ultrasound array focused on an x-y plane for obtaining images at a transverse slice of the animal body. The geometry and characteristics of these systems are briefly described in the following:

Prototype MSOT cart system

A prototype MSOT cart system designed for achieving 2D video-rate multispectral optoacoustic imaging of small animals is described analytically in [24, 71]. Imaging is performed in a water-filled chamber with the water temperature maintained at 34°C. The animals are placed in a custom-built animal holder, surrounded by a transparent foil and submerged into water, ventilated through a breathing mask (see Fig. 1.2(a)). Imaging is performed in the x-y plane corresponding to the focal area of the ultrasound array (white rectangle in Fig. 1.2(a)), and the acquired images correspond to 2D transverse slices of the animal's body (Fig. 1.2(b)). A linear stage (NRT150, Thorlabs GmbH, Karlsfeld, Germany) is used for translating the animal holder in the z-axis for imaging different parts of the body. The system employs a concave 64 element ultrasound array of radius 40 mm, covering an angle of 172° (Imasonic SaS, Voray, France). Each transducer element of the ultrasound array is shaped to create a cylindrical focus with a focal distance of 40 mm (confocal arrangement). The piezoelectric transducer elements have a central frequency of 5 MHz, a bandwidth (6 dB) of > 50 % and a sensitivity of 18 µV/Pa. The array is associated with a pitch of 1.88 mm. Sample illumination is performed using a wavelength tunable optical parameter oscillator (OPO) pulsed laser (PhocusTM, Opotek Inc., USA) with a pulse duration of <10 ns. The laser repetition rate is 10 Hz, and the peak pulse energy is 90 mJ at 750 nm. The laser beam is coupled into 630 fibers which split into ten arms appropriately deployed over an arc of 270 around the sample. The arms are positioned 3 cm from the animal and create a ring-shaped illumination pattern of approx. 7 mm width at the surface of the animal. The laser pulse fluence on the surface of the objects is < 20 mJ/cm^2. A custom made data acquisition (DAQ) system is used for acquiring the pressure signals recorded by the ultrasound transducers, which are digitized at 40 MSamples/s. The system is associated with a theoretical resolution of 150 µm in the x-y plane and 800 µm in the z plane.

MSOT in Vision system

An evolution of the original MSOT cart system, named MSOT in Vision 256-TF, was developed and commercialized by iThera-Medical GmbH, Munich, Germany. The system shares most of the design characteristics of the original MSOT cart system but utilizes a different ultrasound array and illumination (Fig. 1.2(c)). MSOT in Vision employs a curved ultrasound array of a radius of 40 mm that spans an angle of 270°. It employs 256 elements, with a pitch of 0.735 mm focused at 37 mm radius, thus achieving toroidal focusing. The area of the individual ultrasound elements is 36% of the original cart system. Illumination is performed through a tunable laser based on an optical parametric oscillator with a tuning range in the near-infrared (680–980 nm) (InnoLas Laser GmbH, Krailing) and repetition rate 10 Hz. Illumination is deployed again at an angle of 270° around the sample but using five fiber bundle arms instead of ten. The system achieves higher and more uniform resolution in the x-y plane and reduces limited-view reconstruction artifacts due to the larger angle of coverage, therefore substantially enhancing the image quality (Fig. 1.2(d)). A systematic comparison of the two systems is reported in [77].

Experimental procedure

A number of animal experiments were performed in the context of this work. All procedures involving animal experiments were approved by the Government of Upper Bavaria. Two different mouse breeds were used, namely athymic Nude-Foxn1 mice (Harlan, Germany) and CD1 mice (Charles River). All imaging procedures were performed under anesthesia using 1.8% Isoflurane. During imaging, animals were typically breathing 100% O_2 or medical air (20% O_2). In certain cases, mice were sacrificed during MSOT imaging with an overdose of CO_2. In most cases mice were sacrificed after MSOT acquisition by a Ketamine/Xylazine overdose and were in the following stored at -80°C for further analysis.

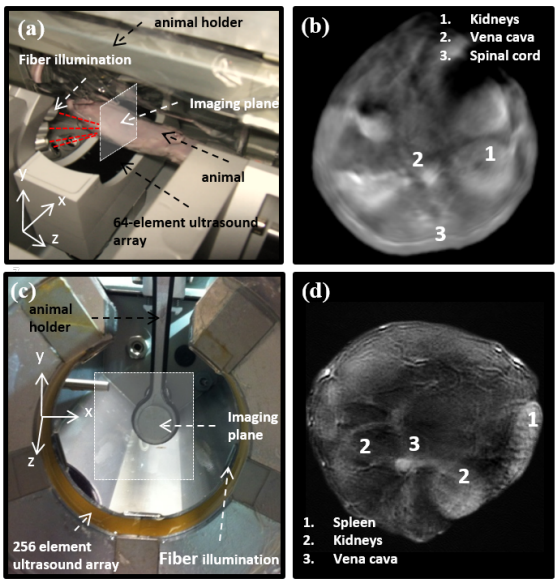

Figure 1.2: (a) Annotated color photograph of the MSOT cart system obtained during an *in vivo* imaging experiment. The animal holder, the fiber illumination, the imaging plane, the animal and the ultrasound transducer are annotated with dashed arrows. The image is reprinted and adapted from [78]. (b) Reconstructed optoacoustic image at a transverse plane corresponding to the abdominal area of a mouse, obtained using the MSOT cart system. Highly absorbing organs and vascular structures are annotated. (c) Annotated color photograph of the imaging chamber of the MSOT in Vision system. The animal holder, the imaging plane, the ultrasound transducer and the fiber illumination are annotated. (d) Reconstructed optoacoustic image at a transverse plane corresponding to the abdominal area of a mouse, obtained using the MSOT in Vision system. Organs containing a high concentration of blood like the spleen and the kidneys are evident due to the high absorption contrast.

1.3.2 Optoacoustic imaging and image formation

Upon photon absorption by molecules, part of the absorbed energy density is converted into heat by thermalization. The small rise in local temperature leads to local rise in pressure $p_0(\mathbf{r})$. Assuming that most of the absorbed energy is thermalized rather than re-emitted as radiation and under the assumption that the optical excitation pulse is short enough to justify thermal and stress confinement [63], the initial pressure distribution $p_0(\mathbf{r})$ can be directly linked to the absorbed energy density $H(\mathbf{r})$ through the following equation:

$$p_0(\mathbf{r}) = \Gamma(\mathbf{r})H(\mathbf{r}) = \Gamma(\mathbf{r})\Phi(\mathbf{r})\mu_a(\mathbf{r}) \tag{1.1}$$

In Eq. 1.1 $\Gamma(\mathbf{r})$ is the material dependent Grüneisen parameter. The absorbed energy density $H(\mathbf{r})$ can be written as a product of the local light fluence $\Phi(\mathbf{r})$ and the local optical absorption coefficient $\mu_a(\mathbf{r})$, i.e. the probability of photon absorption per unit path length (unit cm^{-1}). $\mu_a(\mathbf{r})$ is the main quantity of interest in optoacoustic imaging.

The tomographic image reconstruction problem of optoacoustic imaging aims at retrieving the initial ultrasound pressure distribution, $p_0(\mathbf{r}) = p(\mathbf{r}, t = 0)$ from the time-resolved pressure signals $p(\mathbf{r}_d, t)$, measured at the ultrasound detectors, placed at positions $\mathbf{r}_d$. Under the common assumption of an acoustically homogeneous and acoustically non-absorbing medium, the optoacoustic pressure wave propagation is described by the following partial differential equation (PDE), where c is the speed of sound [79]:

$$\frac{\partial^2}{\partial t^2}p(\mathbf{r}, t) - c^2\nabla^2 p(\mathbf{r}, t) = \Gamma(\mathbf{r})\frac{\partial}{\partial t}H(\mathbf{r}, t) \tag{1.2}$$

Under the previously discussed assumptions, the optoacoustic image reconstruction problem reduces to solving the wave propagation PDE (Eq. 1.2) with boundary conditions defined by the measured pressure signals $p(\mathbf{r}_d, t)$. The mathematical problem can be equivalently defined for two ($\mathbf{r} \in R^2$) or three dimensions ($\mathbf{r} \in R^3$), in practice corresponding to systems that utilize an ultrasound array that is focused on a 2-D plane or for un-focused 3-D systems, respectively.

Under the approximation $H(\mathbf{r},t) = H(\mathbf{r})\delta(t)$, where $\delta(t)$ is the Dirac delta function, a Green's function of the PDE in Eq. 1.2 can be derived [79], defining an alternative and simpler formulation of the problem that is given by a Poisson-type integral:

$$p(\mathbf{r}_d,t) = \frac{1}{4\pi c}\frac{\partial}{\partial t}\int dA \frac{p_0(\mathbf{r})}{|\mathbf{r}-\mathbf{r}_d|}\bigg|_{ct=|\mathbf{r}-\mathbf{r}_d|} \tag{1.3}$$

This integral also referred to as the spherical Radon transform, relates the measured pressure waves to the initial pressure distribution through an integration over a sphere in the 3D space, or a circle in the 2D formulation. This formulation is usually the basis for deriving practical inversion schemes for image reconstruction in optoacoustic tomography.

There are two main categories of tomographic reconstruction algorithms in optoacoustic imaging. Back-projection analytical formulas [80] offer a closed form solution for $p_0(\mathbf{r})$, derived by solving Eq. 1.2 analytically. Conversely, model-based inversion approaches [25] perform a numerical, instead of analytical, inversion of Eq. 1.3. Typical model-based implementations operate either in time [25, 81, 82] or in the frequency domain [83]. The linear operator of Eq. 1.3 is discretized in the form of a forward model matrix $\mathbf{M}$ - which relates the discretized measured pressure signals to the discretized initial pressure distribution:

$$\mathbf{p_d} = \mathbf{M}\mathbf{p_0}. \tag{1.4}$$

In Eq. 1.4, $\mathbf{p_d}$ is a column vector representing the discretized measured acoustic field at the detectors' position and $\mathbf{p_0}$ is a column vector representing the initial pressure distribution on the grid discretizing the domain. The initial pressure distribution can be estimated from the numerical inversion of Eq. 1.4, i.e. by solving the least-squares problem $\mathbf{p_{rec}} = argmin_{\mathbf{p_0}} \parallel \mathbf{p_d} - \mathbf{M}\mathbf{p_0} \parallel_2^2$. This can be performed either by computing the pseudoinverse of the model matrix, $\mathbf{M}^\dagger$ or by minimizing the residual norm through an iterative method such as gradient descent or conjugate gradient methods [25].

Model-based reconstruction approaches have been shown to offer an enhanced image quality for the particular detection geometry of the MSOT systems used [25], [84]. For this reason, the model-based approach was used for image reconstruction in this work. The image reconstruction framework described in [25] and [81] was employed. To increase the numerical stability, a quadratic Tikhonov regularization was added for the inversion of Eq. 1.4. Particularly for the case of sO_2 estimation (Chapter 6) inversion was performed using both Tikhonov regularization and a non-negativity constrained iterative inversion algorithm to ensure physical interpretation [85].

In practice, optoacoustic image reconstruction methods recover an approximate and often distorted estimate of the initial pressure distribution due to a number of practical limitations and additional physical effects that are typically not accounted for during signal acquisition and image reconstruction. First, the finite bandwidth of piezoelectric ultrasound sensors operates as a band-pass filter to the otherwise broadband optoacoustic pressure signals. This band-pass operator propagates distortions to the reconstructed image by introducing negative pixel values and inconsistent relative intensities of larger versus smaller structures [86]. Second the 3D finite aperture of ultrasound transducers creates an inhomogeneous sensitivity field that is spatially dependent and also depends on the frequencies of the emitted pressure waves [82, 87]. Integration of the pressure waves on the surface of the ultrasound elements distorts the shape of reconstructed structures and affects the reconstructed intensities. This effect is particularly prominent when utilizing 2D focused ultrasound sensors, as is the case with the systems used in this work [88]. Third, the limited density of sensor positions induces spatial under-sampling which superimposes streak artifacts in the image domain [79], while the limited angle of coverage may result in a substantially degraded estimation of $p_0(\mathbf{r})$ in parts of the object that are not fully covered by the ultrasound sensors [89] (limited view reconstruction artifacts). Fourth, another image distortion effect stems from ultrasound attenuation [90, 91], and acoustic heterogeneities [92]. These effects are typically considered less prominent for low frequency tomographic optoacoustic systems and are thus not considered in the simplified wave propagation model of Eq. 1.2. Fifth, sources of electronic noise and parasitic signals typically contaminate the measurements and subsequently the reconstructed images [78]. Substantial prior work has been dedicated to independently addressing the issues mentioned above [82, 86–90, 92]. Nevertheless, it is not possible to account for all such factors simultaneously and such methodologies typically complicate image reconstruction often rendering the problem ill-posed and highly computationally demanding, or require additional measurements.

The majority of studies based on reconstructed optoacoustic images for further processing (i.e. spectral unmixing or quantification) implicitly assume that the images offer an accurate representation of the absorbed energy density $H(\mathbf{r})$ [26]. As discussed in the previous paragraph, this assumption is often not justified in experimental practice due to a number of effects that are not easily accounted for by tomographic reconstruction. The assumption followed herein is that the reconstructed optoacoustic images are related to the absorbed energy density through the following relation:

$$P(\mathbf{r}) = C(\mathbf{r})H(\mathbf{r}) + n(\mathbf{r}) \tag{1.5}$$

In Eq. 1.5 $P(\mathbf{r})$ indicates the reconstructed optoacoustic image. $C(\mathbf{r})$ corresponds to a spatially varying, unknown scaling factor that includes the effects of the Grüneisen parameter and system calibration effects. Without loss of generality for the methods developed in Chapters 2-6, the scaling factor $C(\mathbf{r})$ can be also assumed sample dependent, i.e. dependent on the relative structures (or the spatial frequency content) of the sample imaged, thus possibly including some of the scaling effects (but not the image distortions) inflicted due to the systems' electrical and spatial impulse response. The additive term $n(\mathbf{r}) = a(\mathbf{r}) + w(\mathbf{r})$ corresponds to various sources of superimposed noise such as reconstruction artifacts $a(\mathbf{r})$, that are dependent on $C(\mathbf{r})H(\mathbf{r})$, and electronic noise $w(\mathbf{r})$, which is assumed Gaussian and independent of $C(\mathbf{r})H(\mathbf{r})$.

1.3.3 Light propagation models

Light propagation in absorbing and scattering media is typically modeled analytically by the Radiative Transfer Equation (RTE), which is a particle-based method and neglects wave effects. The RTE relates the light radiance $L(\mathbf{r}, \hat{\mathbf{s}}, t)$, at position $\mathbf{r}$, at time t, and propagating along the direction of the unit vector $\hat{\mathbf{s}}$, to the absorption and scattering coefficients in the medium (μ_a and μ_s , respectively) and the light source term $Q(\mathbf{r}, \hat{\mathbf{s}}, t)$. The absorption (scattering) coefficient is defined as the probability of photon absorption (scattering, respectively) per unit path length (unit cm^{-1}). The radiative transfer equation can be derived from the energy conservation principle [63] and Maxwell's equations [65]. In optoacoustic imaging based on pulsed laser excitation only the temporally integrated absorbed energy density is of interest and thus only the time-independent version of the radiative transfer equation is of relevance:

$$(\hat{\mathbf{s}} \cdot \nabla + \mu_t)L(\mathbf{r}, \hat{\mathbf{s}}) - \mu_s \int \Theta(\hat{\mathbf{s}}, \hat{\mathbf{s}}')L(\mathbf{r}, \hat{\mathbf{s}}')d\hat{\mathbf{s}}' = Q(\mathbf{r}, \hat{\mathbf{s}}) \tag{1.6}$$

In Eq. 1.6, the function $\Theta(\hat{\mathbf{s}}, \hat{\mathbf{s}}')$ is the probability that a photon travelling in direction $\hat{\mathbf{s}}'$ will travel in direction $\hat{\mathbf{s}}$ due to an elastic scattering event and $\mu_t = \mu_a + \mu_s$. The fluence $\Phi(\mathbf{r})$ is the integral of the radiance $L(\mathbf{r}, \hat{\mathbf{s}})$ over all angles $\hat{\mathbf{s}}$.

$$\Phi(\mathbf{r}) = \int L(\mathbf{r}, \hat{\mathbf{s}}')d\hat{\mathbf{s}}' \tag{1.7}$$

Eq. 1.6 is hard to solve computationally but numerical Monte Carlo methods of light propagation are considered equivalent to the RTE [63]. Monte Carlo light propagation methods obtain macroscopic physical values such as the fluence by probabilistically modeling the trajectory of multiple photons in absorbing and scattering media. A large number of photons need to be tracked for deriving macroscopic physical quantities, which makes Monte Carlo a computationally expensive approach.

In biomedical optics, the diffusion approximation (DA) of the RTE is typically used to reduce the complexity of Eq. 1.6. The DA can be solved numerically for arbitrary tissues while analytical solutions can also be derived in ideal scenarios. To derive the DA from the RTE, the radiance L is expanded as a series of spherical harmonics and truncated after the first term (P1 approximation) and the source Q is further assumed isotropic. The time-independent DA relates the fluence Φ to the optical absorption and scattering in the medium and the isotropic source term Q_0 as in [63]:

$$\mu_a \Phi(\mathbf{r}) - \nabla \cdot (D\nabla)\Phi(\mathbf{r}) = Q_0(\mathbf{r}) \tag{1.8}$$

In Eq. 1.8, $D = [3(\mu_a + \mu_s')]^{-1}$ is the optical diffusion coefficient and μ_s' is the reduced scattering coefficient defined as $\mu_s' = (1 - g)\mu_s$, where g is the scattering anisotropy factor, expressing the forward component of scattering. Two conditions are typically considered sufficient for ensuring the

validity of Eq. 1.8. First $\mu_s' >> \mu_a$, which is valid for turbid media such as biological tissue, and second that the observation is sufficiently far from the source. The reduced scattering coefficient μ_s' is indicative of the average distance a photon travels in tissue before its initial direction is randomized. Thus, the DA is considered valid for depths $> 1/\mu_s'$, which corresponds to approx. 1 mm for biological tissue in the near-infrared range [93].

An analytical solution of Eq. 1.8 can be derived in ideal cases, as the case of an infinite homogeneous medium. The simplest form of such solutions is defined in the 1D case, where the fluence Φ at a depth z is derived as a function of the incident fluence on the medium's surface Φ_0 and the effective attenuation coefficient $\mu_{eff} = \sqrt{3\mu_a(\mu_a + \mu_s')}$:

$$\Phi(z) = \Phi_0 \exp(-\mu_{eff} z) \tag{1.9}$$

In the general case of arbitrary tissues with spatially varying absorption and scattering coefficients and an arbitrary boundary, the fluence can be obtained through a finite element solution of the DA [10].

This work adopts the DA as the gold standard for simulating light fluence in tissue as it is concerned with whole body small animal imaging (tissue depth of up to 1 cm is considered) and it does not focus particularly on the tissue surface (<1 mm) where the DA offers reduced accuracy. A 2D finite element solution of the DA is used in Chapters 2-4 for simulating the fluence field in tissue and thus simulating the effects of spectral coloring on the spectral signatures of molecular targets. The 1-D analytical solution of the DA (Eq. 1.9) is used in Chapter 6 for deriving the fluence *eigenspectra*. A 2D and a 3D finite element solutions of the DA are used in Chapter 6 for simulating tissues with arbitrarily varying optical properties, which serve as a validation of the accuracy of the *eigenspectra* method in estimating blood oxygenation. Moreover, a Monte Carlo numerical simulation of the photon fluence in multi-layered tissue [94] is used in Chapter 6 for validating the accuracy of the *eigenspectra* in the ballistic and semi-ballistic regime.

1.4 The multispectral optoacoustic imaging problem

The excitation wavelength (λ) dependent and position ($\mathbf{r}$) dependent multispectral optoacoustic images $P(\mathbf{r}, \lambda)$ can be related to the concentrations of the absorbing molecules through the following relation:

$$P(\mathbf{r}, \lambda) = C(\mathbf{r})\Phi(\mathbf{r}, \lambda) \sum_i c_i(\mathbf{r})\epsilon_i(\lambda) + n(\mathbf{r}, \lambda) \tag{1.10}$$

$\Phi(\mathbf{r}, \lambda)$ denotes the space and wavelength dependent light fluence, $c_i(\mathbf{r})$ corresponds to the concentration of the i^{th} absorber at position $\mathbf{r}$ and $\epsilon_i(\lambda)$ corresponds to the molar absorption coefficient (absorption spectrum) of the i^{th} absorber at excitation wavelength λ. $n(\mathbf{r}, \lambda) = a(\mathbf{r}, \lambda) + w(\mathbf{r}, \lambda)$ is a superimposed noise term corresponding to both image reconstruction artifacts $a(\mathbf{r}, \lambda)$ and independent electronic noise $w(\mathbf{r}, \lambda)$. $C(\mathbf{r})$ is an unknown space-varying scaling factor that corresponds to the Grüneisen parameter map and system calibration effects. As discussed in subsection (1.3.2) $C(\mathbf{r})$ may also absorb further scaling effects due to ultrasound attenuation and the spatial and frequency dependent sensitivity field of the imaging system. Since $C(\mathbf{r})$ is assumed wavelength independent, the implicit assumption of this statement is that the relative frequency content of optoacoustic signals does not change substantially across the different excitation wavelengths, so that the scaling effect due to the electrical and spatial impulse response of the system (which are space and acoustic frequency dependent) are assumed independent of the excitation wavelength. This assumption is reasonable since the tissue structures are typically similar across different excitation wavelengths.

Eq. 1.10 states that aside to the chromophores' absorption spectra and the noise the light fluence is a strongly wavelength dependent quantity. As light propagates from shallow to deep tissue, it is absorbed by the tissue molecules. Light absorption depends on the excitation wavelength, therefore different wavelengths of optical excitation attenuate differently with tissue depth. This phenomenon introduces a space and wavelength dependent light fluence which alters the spectral measurements introducing the "spectral coloring" effect [26, 27].

The ultimate goal of MSOT is to estimate the concentrations of all tissue absorbers $c_i(\mathbf{r})$ from the reconstructed images $P(\mathbf{r}, \lambda)$. The absorption spectra of tissue intrinsic molecules $\epsilon_i(\lambda)$ are typically considered know, and dictionaries containing such spectra are available in the literature (Fig. 1.3). Nevertheless, due to the large number of unknown parameters in Eq. 1.10, i.e. $C(\mathbf{r})$,

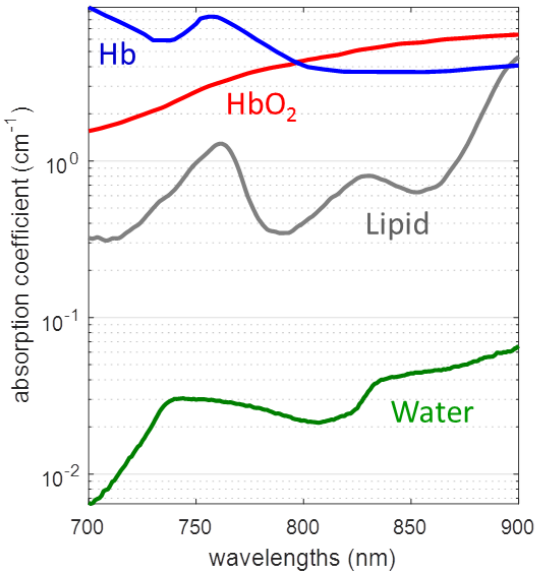

Figure 1.3: Distinct absorption spectra of prominent tissue absorbers: Oxygenated hemoglobin (red) and deoxygenated hemoglobin (blue), lipids (grey) and water (green). Tabulated values obtained from [43] and [95]

.

$\Phi(\mathbf{r},\lambda)$ and $n(\mathbf{r},\lambda)$, $c_i(\mathbf{r})$ quantification is a challenging goal which, despite the substantial efforts, is still considered an unmet problem [26]. The most challenging task is the estimation of the fluence $\Phi(\mathbf{r},\lambda)$ which depends on the unknown $\mu_a(r)$ and $\mu_s'(\mathbf{r})$ (Eq. 1.8) and therefore introduces a non-linearity to Eq. (1.10). Given an estimation of $\Phi(\mathbf{r},\lambda)$, the concentrations of the absorbers $c_i(\mathbf{r})$ can be estimated up to a common scaling factor per pixel. This valuable information allows for computing blood oxygenation which is a ratio-metric quantity. Nevertheless, even if $\Phi(\mathbf{r},\lambda)$ is estimated the unknown scaling factor $C(\mathbf{r})$ further complicates the accurate estimation of the absolute concentrations of tissue absorbers.

Substantial prior work has been dedicated for modeling and retrieving light fluence maps $\Phi(\mathbf{r},\lambda)$ computationally from multispectral optoacoustic images. These efforts are thoroughly discussed in Sec. (1.4.2). Computational $c_i(\mathbf{r})$ quantification methods have been investigated in the case of simulations and simple phantom configurations. Nevertheless, quantitative extraction of the absorbers' concentrations $c_i(\mathbf{r})$ has not been achieved for experimental *in vivo* data. In experimental practice most studies operating on tissue images for molecular and physiological imaging adopt approximate spectral analysis methods that do not model or fully account for $\Phi(\mathbf{r},\lambda)$. Such methods are further discussed in Sec. (1.4.1) and Sec. (1.4.2).

The current work does not aim at solving the general quantification problem defined in Eq. 1.10. Instead it exploits the spectral information for extracting valuable bio-medically relevant information by formulating two more specific but also more feasible sub-problems. Having the two distinct goals of molecular imaging (extracting molecular targets high sensitivity/specificity) and physiological imaging (quantifying blood oxygen saturation) in mind, the general problem defined in 1.10 is reformulated and simplified. For molecular imaging, the goal is to develop a detection scheme for discriminating extrinsically administered dyes from the absorbing tissue background with high sensitivity and specificity, a topic that is introduced in Sec. 1.4.1. As described in the following section, this goal does not require modeling the light fluence $\Phi(\mathbf{r},\lambda)$, but rather the spectral variability of the target molecule and the tissue background. For physiological imaging, the goal is to develop an algorithmic framework for estimating the relative concentrations of HbO_2 and Hb in each pixel, in order to compute blood sO_2. This topic is introduced in Sec. 1.4.2. This problem does not require calculation of the absolute value of $\Phi(\mathbf{r},\lambda)$ at each position $\mathbf{r}$, but only requires modeling and accounting for the normalized spectrum of the light fluence at each position. The two sub-problems are analytically described in the following subsections along with concepts and theory that serve as a basis for the methodologies introduced in Chapters 2-6. Prior work for addressing these problems is also discussed in the following two subsections and classified into Sec.

1.4.1 or Sec. 1.4.2, according to its relevance to the particular problem.

1.4.1 Detecting molecular agents with MSOT

Problem statement

When the goal of imaging is to accurately extract the biodistribution of a specific molecule within the tissue, the spectral unmixing problem formulates as a detection problem. By reformulating Eq. 1.10 to separate the contribution of the tissue background and the target molecule we obtain the following relation:

$$\begin{aligned} P(\mathbf{r},\lambda) &= B(\mathbf{r},\lambda) + c_t(\mathbf{r})T(\mathbf{r},\lambda), \\ B(\mathbf{r},\lambda) &= C(\mathbf{r})\Phi(\mathbf{r},\lambda)\sum_i c_b^i(\mathbf{r})\epsilon_b^i(\lambda) + n(\mathbf{r},\lambda), \\ T(\mathbf{r},\lambda) &= C(\mathbf{r})\Phi(\mathbf{r},\lambda)\epsilon_t(\lambda) \end{aligned} \tag{1.11}$$

In Eq. 1.11 $c_b^i(\mathbf{r})$ and $\epsilon_b^i(\lambda)$ correspond to the concentrations and absorption spectra of tissue-intrinsic molecules, while $c_t(\mathbf{r})$ and $\epsilon_t(\lambda)$ are the concentration and absorption spectrum of the extrinsically administered molecular target. Molecular target detection seeks to decide between two competing hypotheses for each pixel in the image, namely $c_t(\mathbf{r}) = 0$ (non-existing target), or $c_t(\mathbf{r}) > 0$ (existing target). For detecting the distribution of molecular targets, models that capture the background spectral variability $B(\mathbf{r},\lambda)$ and the target spectral variability $T(\mathbf{r},\lambda)$ are required. The background spectral variability is notably more difficult to be accurately modelled than $T(\mathbf{r},\lambda)$, due to the uncertainties related to background tissue absorbers, the severe spectral coloring effects due to the light fluence $\Phi(\mathbf{r},\lambda)$ and a multitude of noise sources $n(\mathbf{r},\lambda)$ that can affect the spectral measurements.

Prior art

Early spectral optoacoustic methods considered for resolving an extrinsically administered agent utilized only two excitation wavelengths [15, 46, 96]. Two images at distinct wavelengths (one corresponding to high and one to low absorption of the target molecule) are subtracted and the contrast resolved is attributed to the agent under the assumption that the background tissue absorption $B(\mathbf{r},\lambda)$ is approximately constant for the two wavelengths selected. With the introduction of OPO tunable lasers in multispectral optoacoustic imaging, the fast acquisition of multiple wavelengths was made possible; thus enabling the introduction of more elaborate spectral unmixing methods in the context of MSOT.

Initial spectral unmixing methods typically assumed a constant light fluence across space and spectrum ($\Phi(\mathbf{r},\lambda) = \Phi_0$) [18, 19, 97], an assumption that reduces Eq. 1.10 into a linear mixture model (LMM) [98], i.e. the optacoustic spectra are modeled as a linear combination of distinct absorption spectra of the underlying molecules. In the following, an image proportional to the concentrations of the target molecule is obtained by solving the system of linear equations using linear least squares methods. In this linear unmixing approach, the spectra of HbO_2 and Hb are typically used for modelling the background tissue absorption $B(\mathbf{r},\lambda)$ [18]. Under this approximation, the spectrally unmixed components can be retrieved for each pixel in the image through the following least-squares minimization solution:

$$\mathbf{c} = (\mathbf{E}^T\mathbf{E})^{-1}\mathbf{E}^T\mathbf{x} \tag{1.12}$$

In Eq. 1.12 $\mathbf{x}$ is the $L \times 1$ vector corresponding to the measured MSOT spectrum of a pixel at L distinct excitation wavelengths, $\mathbf{E}$ is a $L \times K$ matrix containing K columns corresponding to the target and the background molecules' absorption spectra at the selected wavelengths ($\epsilon^i(\lambda)$), and $\mathbf{c}$ is the unmixed $K \times 1$ component vector containing to the relative concentration of each molecule at the corresponding pixel. Wavelength optimization strategies under the LMM assumption have also been investigated [99]. Due to its simplicity and efficiency in many scenarios, this straightforward approach is most commonly used in molecular imaging applications for retrieving the biodistribution of fluorescent dyes [18, 97], fluorescent proteins [100, 101] and absorbing nanoparticles [102]. Nevertheless, the approximate nature of the LMM renders the linear unmixing approach prone to severe false positive detection artifacts when the molecular targets are present in low concentration.

Blind source separation (BSS) algorithms were also considered for addressing the MSOT related spectral unmixing problem. Specifically, the Independent Component Analysis (ICA) [103] and the Vertex Component Analysis (VCA) [104] were applied in experimental MSOT data containing a molecular target [105, 106]. ICA separates the original MSOT image into K additive sub-components by iteratively maximizing the higher statistical moments (kurtosis) of the sub-component images. VCA recovers the unknown spectra of the major components under the assumption that some of the pixels exhibit pure spectra while all other pixels follow a linear mixture of these spectra. In the following it adopts the LMM using the recovered spectra and a least square solution as in Eq. 1.12. ICA was found to outperform linear unmixing significantly in certain MOST molecular imaging studies [105], but the particular reasons and the conditions required for this performance enhancement were not thoroughly explored. Another complication of using blind source separation algorithms for molecular imaging application is their non-automatic, user-dependent performance. Typically BSS methods decompose an MSOT image into K components associated with K different spectra, and the user is called to identify the component of interest based on the retrieved spectrum and the spatial intensity map. Due to this user-dependent performance, BSS is unable to offer an automatic solution of high specificity, and thus, it is in general not optimally suited for molecular imaging applications.

The necessity for high sensitivity and specificity in molecular imaging studies drives the need for the identification and design of novel spectral detection methods that can offer better performance than linear unmixing in terms of sensitivity while also operating globally and in an automatic fashion. Irrespective of the approach followed, the performance evaluation of the detection schemes needs to be performed in a statistical manner, i.e. by considering large validation datasets that exhibit properties realistic to experimental molecular imaging applications. The main challenge in the design of appropriate multispectral detectors is to accurately model the background spectral variability $B(\mathbf{r}, \lambda)$ which is affected by a number of factors and is thus difficult to model using exact spectra. This observation motivated the consideration and development of statistical spectral detection algorithms that model the background as a multivariate statistical distribution.

Statistical sub-pixel detection

When considering statistical methods in the context of MSOT molecular imaging, there are two important factors that need to be taken into account. First, the spectrum of the molecular target will be typically present in a sub-pixel level, i.e. it is unlikely that the target is the only contributor within a given pixel (since the molecule will be commonly mixed with hemoglobin). Instead it will be presented superimposed upon the spectrum of the background. This fact demands the adoption of an additive statistical model and prevents the successful application of full-pixel detection or common binary classification methods for this goal [107]. This analysis adopts a simple linear model, namely $\mathbf{x} = \mathbf{b} + \kappa\boldsymbol{\epsilon}$, where $\mathbf{x}$ is the measured spectrum, $\boldsymbol{\epsilon}$ is the spectrum of the molecular target which is assumed known, κ is a scalar ≥ 0 and $\mathbf{b}$ is the background modelled using a multivariate statistical distribution. The implicit assumption of this model is that that the light fluence $\Phi(\mathbf{r}, \lambda)$ does not substantially distort the target spectrum $\boldsymbol{\epsilon}$, i.e. $T(\mathbf{r}, \lambda) \approx \epsilon_t(\lambda)$. The second consideration for deriving a statistical detection algorithm relates to the statistical metric that needs to be optimized. Detection methods that minimize the probability of error or the misclassification rate [30] are not well suited to this problem as the spatial extend of the molecular target may be much smaller than the one of the background (common in molecular imaging applications). In this case the probability of error will be minimized by classifying each pixel as background [107]. Similarly to other hyperspectral detection applications [107] the Neyman-Pearson criterion [30] is adopted instead. In this context, the probability of detection is maximized while retaining the probability of false alarm (i.e. probability of misclassifying a pixel as target) under a constant threshold.

The Neyman-Pearson criterion leads to a well-defined family of statistical detection algorithms that are derived through the likelihood ratio (LR) criterion:

$$\Lambda(\mathbf{x}) = \frac{p(\mathbf{x} \mid H_1)}{p(\mathbf{x} \mid H_0)} > \gamma \tag{1.13}$$

In Eq. 1.13 $p(\mathbf{x} \mid H_1)$ is the conditional probability density function (pdf) of the observation $\mathbf{x}$ under the hypothesis H_1 of signal presence, $p(\mathbf{x} \mid H_0)$ is the conditional pdf of the observation $\mathbf{x}$ under the hypothesis H_0 of signal absence and γ is a selected threshold. The assumptions of

the additive signal model and further assumptions on the probability distributions of the signal and the background (e.g. multivariate Gaussian) lead to Neyman-Pearson optimal algorithms such as the matched filter [30]. Despite their theoretical optimality, LR detectors are typically not available due to the unknown parameters of the signal and background distributions. Alternatively, the generalized likelihood ratio test (GLRT) maximizes the likelihood in both the nominator and denominator in Eq. 1.13 to derive practical detectors [108–111]. GLRT combined with the additive signal model and the assumption that the background $\mathbf{b}$ follows a multivariate Gaussian distribution leads to the Adaptive Matched Filter (AMF) [109]. AMF and its variations have found wide practical applications in a multitude of fields, such as Radar detection [109], ultrasound beamforming [112] and hyperspectral remote sensing for military target [107] and gaseous plume detection [113]. AMF is introduced in the context of MSOT molecular imaging in Chapter 2 and it is found to outperform previously considered approaches in cases where the target is present in "low probability" within the data, i.e. cases where the molecule of interest is sparsely present within tissue.

In the design of statistical detection algorithms there are two aspects that largely define the performance of the detector, namely the selection of a multivariate statistical distribution to model the background $\mathbf{b}$, and the estimation of the statistics of this distribution, typically the mean $\boldsymbol{\mu}$ and the covariance matrix $\mathbf{G}$ [114]. GLRT detectors have been derived under the assumption of multivariate Gaussian distribution [108, 109] (e.g. AMF) or t-distribution [111] [named elliptically contoured-GLRT (EC-GLRT)]. A statistical characterization of background data can help to select a detector that operates best under the conditions of the problem. A more challenging task is the accurate estimation of the background statistics themselves. Typically statistical sub-pixel detection algorithms applied on hyperspectral images use all available image pixels to compute the μ and $\mathbf{G}$ of the background statistical distribution. This implies that the target needs to be present in low probability within the data so that it does not significantly influence the computation of these statistics. However, this approach may lead to considerable performance degradation when the target is distributed over large areas within the image [113, 115]. For developing an accurate detector with global applicability, independently of the target size or intensity, novel approaches are required for robustly estimating the background statistics.

Chapters 2-3 study statistical sub-pixel detection in the context of MSOT molecular imaging. Chapter 2 introduces statistical sub-pixel detection algorithms, previously employed in hyperspectral remote sensing imaging, in the context of MSOT molecular imaging. Statistical sub-pixel detection is found to substantially outperform previously considered methods in the case of localized molecular targets. Nevertheless, it is also recognized that statistical sub-pixel detection algorithms operate optimally only in cases when the molecular target is sparsely present within the data. Thus, their performance may degrade in cases of extensive molecular agent distribution. Following this observation, Chapter 3 introduces a statistical sub-pixel detection scheme developed according to the characteristics of MSOT molecular imaging. Both the aspects of background statistical modelling and the estimation of the parameters of the background statistical distribution are considered. A novel approach is developed for estimating the covariance matrix of the background distribution, which allows for global applicability independently of the extent of the molecular target distribution.

1.4.2 Quantification of blood sO_2 with MSOT

Problem statement

The most prominent optical absorbers of tissue in the near-infrared window are oxygenated and deoxygenated hemoglobin (Fig. 1.3). While water and lipids also exhibit considerable absorption for higher wavelengths, their contributions are typically considered insignificant for excitation wavelengths below 900 nm. Therefore, the tissue absorption coefficient $\mu_a(\mathbf{r}, \lambda)$ at position $\mathbf{r}$ and excitation wavelength λ can be approximated as a linear combination of the concentrations of the two absorbers $c_{Hb}(\mathbf{r})$, $c_{HbO_2}(\mathbf{r})$, multiplied by their absorption spectra ($\epsilon_{Hb}(\lambda)$, $\epsilon_{HbO_2}(\lambda)$, respectively):

$$\mu_a(\mathbf{r}, \lambda) \approx \epsilon_{HbO_2}(\lambda) c_{HbO_2}(\mathbf{r}) + \epsilon_{Hb}(\lambda) c_{Hb}(\mathbf{r}) \tag{1.14}$$

Given the absolute values of $\mu_a(\mathbf{r}, \lambda)$, and the known spectra of hemoglobin, the concentrations of HbO_2 and Hb can be straightforwardly estimated by solving the system of linear equations of Eq. 1.14. Blood sO_2 can be in the following computed as the ratio between the oxygenated and the total hemoglobin concentration:

$$sO_2(\mathbf{r}) = \frac{c_{HbO_2}(\mathbf{r})}{c_{HbO_2}(\mathbf{r}) + c_{Hb}(\mathbf{r})} \tag{1.15}$$

Optoacoustic imaging does not offer direct information on tissue optical absorption since the intensity of the reconstructed images is also influenced by the space and wavelength dependent light fluence $\Phi(\mathbf{r}, \lambda)$ and further space varying scale factors (see Eq. 1.10). As already discussed, wavelength independent scaling factors do not impede the computation of blood oxygen saturation. However, the space and wavelength dependent light fluence needs to be accounted for, for retrieving the relative concentrations of HbO_2 and Hb and computing blood sO_2. The separation of the unknown light fluence $\Phi(\mathbf{r}, \lambda)$ from $\mu_a(\mathbf{r}, \lambda)$ consists the main challenge for performing quantitatively accurate physiological imaging with spectral optoacoustic methods.

Prior art

Optoacoustic quantification approaches typically seek to retrieve $\mu_a(\mathbf{r}, \lambda)$ from the reconstructed optoacoustic images. Due to the significance of this goal, a multitude of approaches have been proposed in the literature that either seek to measure or calibrate for the light fluence $\Phi(\mathbf{r}, \lambda)$ in tissue directly or model it using light propagation or heuristic models and retrieve it computationally from multispectral optoacoustic images [26]. Despite intensive efforts, no method has demonstrated to this point reliable and validated application in experimental optoacoustic images of tissue for the purpose of blood sO_2 estimation [26]. In this Section, we briefly review previous approaches for the problem of fluence correction and sO_2 estimation from optoacoustic images. It is not the scope of this section to thoroughly discuss all such methods, which are also presented in recent review papers [26, 116]. It is rather a goal to classify the different approaches and focus the discussion on the most general and widely studied approach, the optical property quantification method.

Calibration methods: One approach for quantifying $\mu_a(\mathbf{r}, \lambda)$ is through calibration, i.e. by independently measuring, calibrating or canceling the effects of $\Phi(\mathbf{r}, \lambda)$ at certain positions within tissue. Fluence measurements have been demonstrated *in vivo* through the invasive localized insertion of an absorber with known optical properties within tissue [27]. The spectrum of light fluence at the absorber location is measured and used for fluence correction in the vicinity of the absorber. Nevertheless, the highly invasive nature of this method has limited its practical use.

Similar approaches seek to measure the light fluence by introducing non-invasively, i.e. through systemic injection, an absorber (e.g. gold nanorods) that demonstrates a non-linear dependence on fluence [117] or a reversibly switchable fluorescent protein [118], the transition time of which depends on the photon density. Another agent-free approach suggests measuring the light fluence at a certain position within the tissue by locally tagging light using the acousto-optics principle [119]. The aforementioned concepts have been demonstrated in simulations or proof of principle phantom experiments but due to their experimental complexity, their practical application *in vivo* has not been demonstrated.

Another approach presented in [120] exploits fluence cancellation through the division of optoacoustic images obtained at two different oxygenation states of tissue. This fluence cancellation method allows for quantifying the absolute sO_2 values at a tissue position under the assumption that the sO_2 at this position changes between two different states and this change is highly localized. While the method is interesting, its applicability is restricted to very specific cases.

Case specific methods: Aside to calibration methods, most approaches that seek to quantify $\mu_a(\mathbf{r}, \lambda)$ in optoacoustic imaging rely on computational methods that separate $\mu_a(\mathbf{r}, \lambda)$ from $\Phi(\mathbf{r}, \lambda)$ using optoacoustic images and a model for light fluence. The vast majority of such algorithms model the light fluence $\Phi(\mathbf{r}, \lambda; \mu_a(\mathbf{r}, \lambda), \mu_s'(\mathbf{r}, \lambda))$ as a function of the spatial distribution of the optical absorption $\mu_a(\mathbf{r}, \lambda)$ and scattering $\mu_s'(\mathbf{r}, \lambda)$ coefficients in tissue, using a light propagation model such as the DA. A number of studies have focused on providing a solution for simplified scenarios, e.g. assuming a cylindrical absorber in a purely scattering medium [121], a small absorption perturbation upon a known absorption/scattering background [122, 123] or assuming known tissue scattering [124–126]. Since in practice such knowledge on tissue optical properties is not available in arbitrary tissue images, these approaches, although theoretically interesting and possibly useful in specific scenarios, are not generally applicable in complex tissue images for the purpose of fluence correction and sO_2 estimation.

Optical property quantification approach: In the general case, methods that use a light propagation model to model light fluence $[\Phi(\mathbf{r}, \lambda) = \Phi(\mathbf{r}, \lambda; \mu_a(\mathbf{r}, \lambda), \mu_s'(\mathbf{r}, \lambda))]$ need to recover both

the absorption $\mu_a(\mathbf{r},\lambda)$ and the scattering coefficient $\mu_s'(\mathbf{r},\lambda)$. It has been shown that the absorption and scattering coefficients cannot be recovered simultaneously from a monochromatic optoacoustic image $P(\mathbf{r})$, due to non-uniqueness [93]; thus additional information such as (1) multiple illumination patterns [127, 128] or (2) multispectral excitation and knowledge of the spectra of the underlying absorbers is required for obtaining a solution [93, 129]. The first concept has only been studied theoretically, and it includes the challenge of dividing two optoacoustic images, a process that may dramatically increase noise in experimental data. The second concept has been studied both theoretically and experimentally, and it is perhaps the method that has come closest to providing a general quantification framework, offering promise for experimental data application [26].

Under this problem formulation, estimates on $\mu_a(\mathbf{r},\lambda)$ and $\mu_s'(\mathbf{r},\lambda)$ can be obtained by comparing the observed absorbed energy density $H^{obs}(\mathbf{r},\lambda)$ to the modelled one $H(\mathbf{r},\lambda) = \mu_a(\mathbf{r},\lambda)\Phi(\mathbf{r},\lambda;\mu_a(\mathbf{r},\lambda),\mu_s'(\mathbf{r},\lambda))$. Specifically, let $\boldsymbol{\mu_a}$ and $\boldsymbol{\mu_s'}$ denote two column vectors containing the $\mu_a(\mathbf{r},\lambda)$ and $\mu_s'(\mathbf{r},\lambda)$ values of the discretized domain, and let $\mathbf{H^{obs}}$ be a column vector containing the measured discretized absorbed energy density, the optical property quantification approach seeks to obtain $\boldsymbol{\mu_a}$ and $\boldsymbol{\mu_s'}$ by minimizign the following residual norm:

$$Argmin\varepsilon_{\boldsymbol{\mu_a},\boldsymbol{\mu_s'}} = \frac{1}{2} \parallel \mathbf{H}(\boldsymbol{\mu_a},\boldsymbol{\mu_s'}) - \mathbf{H^{obs}} \parallel^2 + R(\boldsymbol{\mu_a},\boldsymbol{\mu_s'}) \tag{1.16}$$

In Eq. 1.16, R denotes a regularization term. A change of variables from (μ_a, μ_s') to (μ_a , D, D being the diffusion coefficient) or to (c_i μ_s', c_i being the concentration of the i^{th} absorber) results in alternative but equivalent problem formulations [93]. In each case, the unknown parameters are iteratively updated until the modelled absorbed energy density $\mathbf{H}(\boldsymbol{\mu_a},\boldsymbol{\mu_s'})$ converges to the measured one $\mathbf{H^{obs}}$. Using a Gauss-Newton method where the Jacobian and the Hessian matrix are computed efficiently from the DA equation, Cox et. al. showed that this approach can converge to the unknown parameters in a numerical simulation if the wavelength dependence of the unknown absorbers (absorption spectra) and the wavelength dependence of scattering are incorporated as constraints [93]. Evolving from that seminal work, the optical property quantification scheme, either considering multispectral measurements or multiple illumination patterns, has been theoretically investigated in numerical simulations using alternative minimization methods [130], Bayesian inversion approaches [131], or different light propagation models such as the RTE [132] or Monte Carlo [133]. Experimentally, an adapted version of the method presented in [93] has been investigated by Laufer et. al. [134] for quantifying the concentrations of chromophores in a simple phantom geometry. In this case, the steps of image reconstruction and minimization of Eq. 1.16 are combined in one single inversion scheme. Quantification of the absolute concentration values of the phantom absorbers was found possible. Nevertheless, the high complexity of the method even in the case of the simple phantom configurations considered further indicates the difficulty of extending this approach to the case of arbitrary complex tissue data.

Despite its advantage as the most general method proposed so far for quantitative optoacoustic imaging, the optical property quantification approach is associated with a number of complications that limit its straightforward application in experimental optoacoustic images of tissue. *First* the large scale inverse problem defined is highly computationally demanding since it includes a vast number of optimization variables (namely $\mu_a(\mathbf{r},\lambda)$ and $\mu_s'(\mathbf{r},\lambda)$ for each pixel, reaching thousands of unknowns for moderate resolutions). Notably, the inversion procedure required several hours even in a simplified case of partially uniform optical properties involving only 12 unknowns [134]. This indicates that in the general case of a high resolution optoacoustic image this approach would be rather computationally intractable using current methods. The high computational complexity of the method may further impede its statistical evaluation over extensive data-sets for assessing the converging or diverging behaviour of the non-linear optimization scheme under different conditions. *Second* the utilization of a light propagation model demands accurate knowledge of the tissue boundary and the incident light distribution which may be challenging to measure accurately in certain systems. *Third*, a significant complication of the optical property quantification approach is the requirement of full knowledge of the absorbed energy density $H(\mathbf{r},\lambda)$ in the whole illuminated 3D volume, since the usage of a light propagation model does not allow to focus the analysis only on a well-reconstructed part of the image. This restriction complicates the application of this approach in the case of 2D imaging systems and compromises its application in cases where $H(\mathbf{r},\lambda)$ is corrupted by substantial artifacts in some parts of the reconstructed image (i.e. limited view geometries). *Fourth*, the minimization problem of (Eq. 1.16) assumes knowledge of the absolute values of the absorbed energy density $H(\mathbf{r},\lambda)$. As previously discussed, the estimation of the absolute values

of $H(\mathbf{r},\lambda)$ may be challenging due to a number of scaling effects (scaling factor $C(\mathbf{r})$) and is only possible through a perfectly calibrated system, error-free reconstruction process, and knowledge of the Grüneisen parameter $\Gamma(\mathbf{r})$.

Heuristic approach. Another approach worth mentioning models the light fluence heuristically, not through a light propagation model but through its distinct spatial characteristics. The logarithmic transform of the optoacoustic image is sparsely represented into a library composed of two distinct bases with different spatial characteristics [135]. A Fourier base was selected for capturing the smoothly varying function of $\Phi(\mathbf{r})$ and a Haar wavelet base for representing $\mu_a(\mathbf{r})$, in a sparse manner. Orthogonal matching pursuit was used for decomposition by maximizing the sparsity of the combined representation, and thus separating the smoothly varying $\Phi(\mathbf{r})$ from $\mu_a(\mathbf{r})$. The performance of the method was demonstrated on phantom images. Limitations of the method include its requirement of highly accurate image reconstruction and its high sensitivity to reconstruction artifacts and near-zero values. Additionally, the method cannot distinguish between the light fluence and the optical absorption when the latter is varying smoothly within the image.

sO_2 estimation in *in vivo* data: Perhaps the most common approximation that is often used for estimating blood sO_2 in experimental multispectral optoacoustic images of tissue is the linear unmixing approximation, where the light fluence $\Phi(\mathbf{r},\lambda)$ is considered constant across space and wavelength, and the blood sO_2 estimation problem reduces to the solution of Eq. 1.14 and 1.15 [18, 19]. Although this method is popular due to its simplicity, a number of studies (including the work presented in Chapter 6) demonstrate that this common approximation may substantially misestimate blood sO_2 in deep tissue regions.

Eigenspectra MSOT

The characteristics of the blood sO_2 estimation problem in MSOT imaging along with the particular challenges associated with the optical property quantification approach, served as a motivation for introducing a novel problem formulation and developing a method, termed *eigenspectra* MSOT, to approach this problem. eMSOT is analytically described in Chapter 6. This subsection provides the reasoning behind the creation of this novel approach and the theoretical and practical advantages offered by this concept.

The *eigenspectra* MSOT method for blood sO_2 estimation was developed with three particular criteria in mind: (1) The need for a computational fluence correction method that relies only on normalized optoacoustic spectra and not on absolute values of the absorbed energy density $H(\mathbf{r},\lambda)$ which may not be available due to the unknown scaling factor $C(\mathbf{r})$. (2) The need for a method that can be applied on a well-reconstructed part of the image without requiring full knowledge of $H(\mathbf{r},\lambda)$ in the whole illuminated volume, which may be highly corrupted at parts due to reconstruction artifacts (e.g. from limited view) or unavailable in 2D imaging systems. (3) The need for a small scale inverse problem that can be solved efficiently. Given the characteristics of MSOT images described before, these three criteria were considered crucial for enabling a direct application of a method in experimental data. Such criteria cannot be satisfied if a light propagation model is used to model the light fluence as a function of the spatially varying absorption and scattering coefficient. Nevertheless a specific fluence model is required for separating $\Phi(\mathbf{r},\lambda)$ from $\mu_a(\mathbf{r},\lambda)$.

By combining Eq. 1.10 with Eq. 1.14 and omitting the noise factor, the following reformulation can be achieved:

$$P(\mathbf{r},\lambda) = C(\mathbf{r}) \parallel \mathbf{\Phi}(\mathbf{r}) \parallel_2 \frac{\Phi(\mathbf{r},\lambda)}{\parallel \mathbf{\Phi}(\mathbf{r}) \parallel_2}(c_{Hb}(\mathbf{r})\epsilon_{Hb}(\lambda) + c_{HbO_2}(\mathbf{r})\epsilon_{HbO_2}(\lambda)) \tag{1.17}$$

In Eq. 1.17, $\mathbf{\Phi}(\mathbf{r})$ is a vector corresponding to the light fluence spectrum at position $\mathbf{r}$, and $||\mathbf{\Phi}(\mathbf{r})||_2$ is its norm across all excitation wavelengths. $\Phi(\mathbf{r},\lambda)/ \parallel \mathbf{\Phi}(\mathbf{r}) \parallel_2$ is the normalized wavelength dependence of light fluence at a specific position (normalized spectrum), abbreviated as $\Phi'(\mathbf{r},\lambda)$. The space-only dependent factors $C(\mathbf{r})$ and $\parallel \mathbf{\Phi}(\mathbf{r}) \parallel_2$ do not affect the estimation of sO_2 which is calculated as a ratio once the relative concentrations of HbO_2 and Hb are known. By defining $C'(\mathbf{r}) = C(\mathbf{r}) \parallel \mathbf{\Phi}(\mathbf{r}) \parallel_2$, $c'_{HbO2}(\mathbf{r}) = C'(\mathbf{r})c_{HbO_2}(\mathbf{r})$ and $c'_{Hb}(\mathbf{r}) = C'(\mathbf{r})c_{Hb}(\mathbf{r})$, Eq. 1.17 reformulates into the following equation:

$$P(\mathbf{r},\lambda) = \Phi'(\mathbf{r},\lambda)(c'_{Hb}(\mathbf{r})\epsilon_{Hb}(\lambda) + c'_{HbO_2}(\mathbf{r})\epsilon_{HbO_2}(\lambda)) \tag{1.18}$$

If the relative concentrations $c'_{HbO2}(\mathbf{r})$ and $c'_{Hb}(\mathbf{r})$ are recovered, the blood oxygen saturation can be computed for each pixel through Eq. 1.19:

$$sO_2(\mathbf{r}) = \frac{c'_{HbO_2}(\mathbf{r})}{c'_{HbO_2}(\mathbf{r}) + c'_{Hb}(\mathbf{r})} \tag{1.19}$$

An estimate of the wavelength dependence of the light fluence $\Phi'(\mathbf{r}, \lambda)$, i.e. the spectral pattern of the light fluence, is required for accurately extracting the relative values of $c'_{HbO_2}(\mathbf{r})$ and $c'_{Hb}(\mathbf{r})$. In Chapter 6 a novel model is introduced that describes the spectrum of the light fluence $\Phi'(\mathbf{r}, \lambda)$ as an affine function of a number of base spectra termed fluence *eigenspectra*, independently of the specific spatial distribution of the optical properties of tissue. The hypothesis that a few basis spectra can accurately model Φ' is based on the observation that the spectrum of light fluence is not an arbitrary function of wavelength, but it can only lie within a limited subspace of spectral patterns, which are related to the spectra of the main tissue absorbers, i.e. the ones of HbO_2 and Hb.

This spectral fluence model introduced in Chapter 6 and the problem reformulation of Eq. 1.18 satisfy all three previously defined criteria: (1) The formulation of Eq. 1.18 does not rely on the accurate computation of $H(\mathbf{r}, \lambda)$ in an absolute sense as only the relative concentrations of hemoglobin are of relevance in this problem formulation. (2) The spectral fluence model introduced decorrelates the spatial dependence introduced by light propagation models and allows for focusing the analysis in a well-reconstructed part of an image without demanding full knowledge of $H(\mathbf{r}, \lambda)$ in the whole illuminated volume. This particular property is very beneficial since it allows for bypassing the challenge of considerable reconstruction artifacts which are mainly presented in some parts of the image and particularly in areas not fully covered by the detectors in limited view imaging systems. (3) The novel problem formulation allows for a per-pixel inversion and thus it defines a small scale inverse problem that can be solved with high computational efficiency.

Chapter 6 describes the concept behind the creation of the novel *eigenspectra* model analytically and validates its accuracy using light propagation simulation with tissue physiological optical properties. It further introduces a constrained inversion algorithm for solving Eq. 1.18 termed *eigenspectra* MSOT. The constrained inversion algorithm incorporates further heuristic constraints on the spatial characteristics of the light fluence which are crucial for ensuring inversion stability and accurate sO_2 estimation. The accuracy of the *eigenspectra* MSOT is validated statistically through an extensive set of simulations as well as blood phantoms and controlled *in vivo* experiments. Because eMSOT satisfies the three criteria previously defined, it allows for direct application in experimental *in vivo* data without further algorithmic adjustments. The *eigenspectra* MSOT is used for assessing oxygenation in healthy tissue and hypoxic tumors and the results obtained are found to correspond well to the expected physiological states, literature-derived values and histological gold standards that are performed for validation. The performance of the method is compared to established methods previously used for analysing *in vivo* MSOT data.

1.5 Summary and future outlook

The present work studies the problem of MSOT spectral analysis for the purpose of molecular and physiological imaging. Both application fields are of key significance for revealing the unique features of the technology and disseminating it as a potent imaging tool, capable of addressing a wide range of needs in biological research. Due to the different properties required for successful molecular and physiological imaging, the two problems are addressed separately. Spectral analysis methods are developed with the goals of optimizing the sensitivity/specificity in the case of molecular imaging and the quantification accuracy of blood sO_2 estimation in the case of physiological imaging.

Molecular MSOT imaging is formulated as a multispectral detection problem, and a validation platform based on experimental animal data is introduced for formally studying this problem under realistic conditions. Statistical sub-pixel detection algorithms are considered for this goal due to their ability to accurately model, in a statistical manner, the spectral variability of tissue background, which is otherwise difficult to be modelled using exact spectra. Since conventional statistical sub-pixel detection algorithms, originally developed for remote sensing hyperspectral imaging, are not optimally suited to the characteristics of MSOT imaging, a novel statistical detection framework is developed which offers both high sensitivity and robust detection performance independently of the type of molecular imaging application. The method developed is found to substantially outperform previously considered approaches, such as linear unmixing, offering up to five times enhanced molecular imaging sensitivity and global, automatic and user-independent performance.

It is expected that this method will serve as a valuable tool for future MSOT molecular imaging applications. While this work thoroughly studied the aspect of modelling the background spectral variability, the corruption of the target spectrum due to spectral coloring was not thoroughly studied and presents one possible direction for future investigation.

Besides algorithmic aspects, experimental parameters affecting the MSOT sensitivity, such as the number of excitation wavelengths, are further studied for optimizing imaging protocols. It is demonstrated that multispectral excitation and statistical detection algorithms can enhance the sensitivity 14-40 times as compared to monochromatic optoacoustic imaging, underlining the importance of multispectral methods in molecular imaging studies. More excitation wavelengths are found to offer a rather consistent but asymptotical performance enhancement.

Following these observations, MSOT utilizing multiple excitation wavelengths and coupled with a statistical sub-pixel detection algorithm is investigated for the application of immune cell imaging. The feasibility of imaging fluorescent labeled T-cells in tissue is demonstrated and first insights on the sensitivity of MSOT in this application are derived through phantoms and animal experiments. MSOT is found capable of detecting down to 2,500 fluorescent labeled macrophages injected within a small volume in tissue, an ability that bears promise for *in vivo* cell imaging applications. Nevertheless, despite the substantial sensitivity enhancement achieved through multispectral methods, the molecular sensitivity of MSOT in the case of fluorescent dyes still compares unfavourably to the one of pure optical methods. Specifically in the case of immune cell imaging, the MSOT sensitivity achieved is still substantially lower than the one offered by bioluminescence [136]. Therefore, aside to multispectral methods, more potent contrast mechanisms with higher absorption coefficients are required for achieving potent molecular imaging with MSOT.

Accurate imaging of blood oxygen saturation within deep tissue has been a long standing challenge in the field of optoacoustic imaging. The challenge lies both in the particular nature of this non-linear inverse problem but also in the difficulty of validating the quantification accuracy of algorithms in experimental data. Since there exists no established and reliable method that can offer blood oxygenation measurements non-invasively and in high resolution, obtaining ground truth on blood sO_2 values *in vivo* is particularly challenging. *Eigenspectra* MSOT was developed for providing a novel solution to this problem that could be successfully applied to complex experimental images of tissue. Through numerous simulations, blood phantoms and specifically designed *in vivo* and *post mortem* controlled experiments the ability of *eigenspectra* MSOT to offer substantially enhanced quantification accuracy over previously utilized approximate methods was demonstrated. Aside to controlled experiments, the method was also applied for quantifying blood oxygenation in the muscle and hypoxic tumors in mice. The resulting sO_2 maps appeared in agreement with the expected physiological values and *post mortem* histological validation of tumor perfusion and hypoxia – a result that bears promise for the direct application of the method in pathophysiology imaging studies.

As far as *eigenspectra* MSOT is concerned, numerous directions for future work can be identified that relate both to methodology development and to its biomedical application. From a theoretical standpoint, a more detailed study of the characteristics of the inverse problem defined would be of interest. While eMSOT convergence and accuracy are established through a statistical validation employing an extensive and versatile set of simulations, the non-linear optimization problem defined by eMSOT is non-convex, i.e. accurate convergence cannot be theoretically guaranteed. The investigation of approaches for a convex relaxation of the inverse problem would offer the advantage of a theoretical stability proof, and it is an important goal of future research. Furthermore, a basic assumption of the method is that the primary tissue absorbers are oxygenated and deoxygenated hemoglobin and the effects of less prominent tissue absorbers are disregarded. Although the application of eMSOT in the case of experimental tissue images indicated a good performance, a more detailed study on the possible influence of other less prominent near-infrared tissue absorbers such as water and lipids would be beneficial. Moreover, wavelength optimization for minimizing such influence would potentially further increase the quantification accuracy of eMSOT.

From a biological imaging standpoint, a direct next goal would be the comparative study of eMSOT with other imaging methods capable of sensing oxygenation related values, such as BOLD-MRI. Moreover, an interesting application of the novel method would be the study and quantification of tumor hypoxia effect on various cancer therapies using a large pool of animal models. Finally, perhaps the most important future goal would be the adaptation of the method for quantifying blood oxygenation in arteries, veins and the capillary bed of humans, using a clinical hand-held MSOT imaging technology.

Chapter 2

Unmixing molecular agents from absorbing tissue in multispectral optoacoustic tomography

2.1 Summary

The paper "Unmixing molecular agents from absorbing tissue in multispectral optoacoustic tomography" is authored by Stratis Tzoumas, Nikolaos Deliolanis, Stefan Morscher and Vasilis Ntziachristos. The version herein (Appendix A) is published in the Journal "IEEE Transactions on Medical Imaging" [137].

While a number of molecular imaging studies have used multispectral optoacoustic methods for resolving molecular agents such as fluorochromes and absorbing nanoparticles, no work has quantitatively assessed the relative performance of different spectral analysis methods in such applications. The contribution of this manuscript is threefold. *First*, the MSOT molecular imaging problem is formulated as a detection problem where the goal of spectral analysis methods is to detect a molecular target with high sensitivity, i.e. accurate detection at low target concentrations, and high specificity, i.e. minimization of false positive detection artifacts. The particular characteristics and challenges of the problem are discussed, and numerical simulations are performed to estimate the magnitude of background and target spectral variability. *Second*, the work reviews and implements state-of-the-art optical target detection algorithms, originally developed for remote sensing hyperspectral imaging. Candidate algorithms from all three major categories are considered, namely structured, statistical and blind unmixing approaches. Aside to methods that were previously considered in MSOT imaging such as linear unmixing and blind source separation via ICA, statistical sub-pixel detection algorithms such as the AMF and ACE are introduced for the first time in the context of MSOT. For quantitatively assessing the performance of ICA, which demands a manual step of component selection, the algorithm semi-blind ICA is implemented. *Third*, for quantitatively assessing the detection performance of different algorithms in terms of sensitivity a synthetic target implantation simulation framework is introduced, where molecular targets with different spectral characteristics are artificially implanted onto experimentally derived MSOT images of *in vivo* tissue. This framework is developed for enabling a quantitative performance evaluation under realistic conditions. Since the spectral background stems from experimental MSOT images, all physical and experimental challenges of the problem are included, while the position of the implanted molecular targets is known precisely and their intensity can be manipulated artificially. Moreover, two purely experimental MSOT imaging datasets of *in vivo* and *post mortem* animals containing fluorescent targets are collected for supporting the quantitative results obtained from simulations.

This study led to a number of interesting conclusions. Both simulated and experimental data indicate that statistical sub-pixel detection algorithms like AMF can offer a substantially enhanced performance as compared to structured methods (linear unmixing) and a comparable or better performance as compared to blind unmixing (semi-blind ICA) when small targets are considered. AMF is found more robust than ACE in cases of high noise and when considering only a few excitation wavelengths. The results derived from the synthetic target implantation data appear in good agreement with the purely experimental dataset, indicating the validity of the proposed

quantitative evaluation framework. Finally, it is demonstrated that in the case of statistical sub-pixel detection algorithms a global threshold could be defined for enabling molecular imaging of high specificity.

I drafted the article, which was continuously advanced through discussions with all co-authors. I performed the numerical simulations of MSOT images and reviewed the field of hyperspectral remote sensing imaging for identifying appropriate approaches. I implemented the spectral unmixing methods and the artificial target implantation framework. The experimental *in vivo* and *post mortem* data were acquired by Nikolaos Deliolanis and Stefan Morscher.

2.2 Publication

S. Tzoumas, N.C. Deliolanis, S. Morscher, V. Ntziachristos, "Unmixing molecular agents from absorbing tissue in multispectral optoacoustic tomography," *Medical Imaging, IEEE Transactions on* , vol. 33, no. 1, pp. 48-60, 2014.

Chapter 3

Statistical molecular target detection framework for multispectral optoacoustic tomography

3.1 Summary

The paper "Statistical molecular target detection framework for multispectral optoacoustic tomography" is authored by Stratis Tzoumas, Andrii Kravtsiv, Yuan Gao, Andreas Bühler and Vasilis Ntziachristos. The version herein (Appendix B), has been submitted to the Journal "IEEE Transactions on Medical Imaging."

Chapter 2 identified statistical sub-pixel detection algorithms, like the AMF, as a very promising approach for MSOT molecular imaging. By modeling the MSOT tissue background spectra in a statistical manner, AMF offers enhanced ability in suppressing the background and revealing molecular targets of interest. Nevertheless, limitations were also identified. The AMF assumes that the spatially-varying MSOT tissue spectra follow a multivariate Gaussian distribution, that the spectrum of the target molecule is precisely known and that the molecular target lies in "low probability" within the data. This latter assumption, in particular, restricts the application of AMF to molecular imaging cases where the target molecule is sparsely present within the tissue and does not allow for universal applicability. When the molecular agent is present in high amounts within the tissue, the presence of the target signal within the data compromises the accurate computation of the background statistics, i.e. the covariance matrix, which is typically computed from all available pixels of the image under test, with maximum likelihood. This effect, commonly referred to as *covariance contamination* in the literature, may cause considerable performance degradation.

The objective of this work is to develop a robust statistical detection framework that is specifically suited to the characteristics of MSOT molecular imaging. For achieving this, the aspects of background statistical modeling and covariance estimation are studied. Using a large experimental MSOT imaging dataset, we perform a statistical characterization of MSOT background tissue images and conclude to a detector that is based on the t-distribution, named EC-GLRT detector. More importantly, we introduce a novel method for estimating the covariance matrix of the background tissue statistical distribution by merging information from the image under test and an archive of agent-free (and therefore uncontaminated) MSOT tissue images that serve as training data. The performance of the novel statistical detection framework is assessed through target implantation simulations and specifically designed *in vivo* controlled experiments, and it is compared to previously considered methods.

The quantitative evaluations of the detection performance indicate that the EC-GLRT detector can offer an enhanced detection performance as compared to AMF. Moreover, the proposed covariance estimation approach is found to offer robust detection performance independently of the molecular target size or intensity. Simulated and experimental data indicate that the performance of the developed statistical detection framework outperforms AMF in the case of large molecular targets and offers equivalent performance in the case of weakly absorbing targets. Importantly, the proposed method offers an automatic and universal performance independently of the target size or intensity.

I drafted the article, which was continuously advanced through discussions with all co-authors. Yuan Gao and I performed the statistical characterization of MSOT data and implemented the data-specific EC-GLRT detector. Andrii Kravtsiv and I implemented the simulation framework for quantitatively assessing the detection performance. I designed the proposed covariance estimation scheme and integrated it to the EC-GLRT detection approach. I collected the experimental data for validating the detector's performance.

3.2 Publication

S. Tzoumas, A. Kravtsiv, Y. Gao, A. Buehler, V. Ntziachristos, "Statistical molecular target detection framework for multispectral optoacoustic tomography," *Medical Imaging, IEEE Transactions on*, vol. 35, no. 12, pp. 2534-2545, 2016.

Chapter 4

Effects of multispectral excitation on the sensitivity of molecular optoacoustic imaging

4.1 Summary

The study "Effects of multispectral excitation on the sensitivity of molecular optoacoustic imaging" is authored by Stratis Tzoumas, Antonio Nunes, Nikolaos Deliolanis and Vasilis Ntziachristos. The version herein (Appendix C) is published in the "Journal of Biophotonics" [138].

Aside to spectral analysis methods, further experimental considerations, such as the number of excitation wavelengths used, can play an important role in the molecular imaging sensitivity of MSOT. While Chapter 2 and 3 study algorithmic aspects of the MSOT molecular imaging sensitivity, the effect of excitation wavelengths has not been thoroughly investigated. This is the topic of this follow-up work.

A complication of studying the effect of wavelengths on the detection sensitivity of MSOT is the strong relation of sensitivity with the spectral analysis method assumed. An additional complication relates to the selection of excitation wavelengths and the spectral signature of the molecular target of interest. Therefore, to understand the effect of wavelengths in the context of optoacoustic molecular imaging studies, we consider five different molecular optoacoustic methods, i.e. monochromatic optoacoustic imaging, two dual-wavelength subtraction methods employing different strategies for wavelength selection, linear unmixing methods employing a wavelength selection approach, and statistical sub-pixel detection, via the AMF considering a varying number of excitation wavelengths spanning from 4 to 20 equidistant excitation wavelengths. The detection performance of the different methods is quantitatively assessed through the target implantation simulations introduced in Chapter 2. Controlled *in vivo* experiments are further performed for confirming the observations on synthetic data under realistic *in vivo* experimental conditions.

The quantitative analysis performed on both simulated (synthetic) and experimental data suggests that MSOT can effectively enhance the molecular imaging sensitivity over monochromatic optoacoustic imaging in the order of 14 - 40 times, a result that was previously undocumented. Compared to dual-wavelength subtraction methods, MSOT studies at >10 wavelengths can also reach up to an order of magnitude sensitivity enhancement. When using 20 wavelength, the sensitivity can be enhanced up to more than 4 times as compared to 3 optimally selected wavelengths and linear unmixing, indicating that due to the complex nature of the spectral unmixing problem the common assumption that three wavelengths are adequate for spectrally unmixing a single molecule from the tissue hemoglobin spectra can be an oversimplification. The quantitative evaluations indicate a rather consistent statistical trend of sensitivity enhancement with wavelengths when using statistical sub-pixel detection. Nevertheless, it was also observed that in certain cases, fewer wavelengths can result in equivalent or better performance than more – indicating that a possible wavelength rejection strategy may result in better class separability between the target agent and the absorbing background.

Vasilis Ntziachristos and I designed the experiments performed for this study and interpreted the results. I drafted the article in close communication with Vasilis Ntziachristos and Nikolaos

Deliolanis. Antonio Nunes, Nikolaos Deliolanis and I acquired the experimental data.

4.2 Publication

S. Tzoumas, A. Nunes, N.C. Deliolanis, V. Ntziachristos, "Effects of multispectral excitation on the sensitivity of molecular optoacoustic imaging," *Journal of Biophotonics*, vol. 8, no. 8, pp. 629-637, 2015.

Chapter 5

Immune cell imaging using multi-spectral optoacoustic tomography

5.1 Summary

The letter "Immune cell imaging using multi-spectral optoacoustic tomography" is authored by Stratis Tzoumas, Angelika Zaremba, Uwe Klemm, Antonio Nunes, Karin Schaefer and Vasilis Ntziachristos. The version herein (Appendix D) is published in the journal "Optics Letters" [139]. In this paper, I share the first authorship with Angelika Zaremba.

With recent cell-based therapy studies, such as cell-based cancer immunotherapy, showing the potential to develop into a novel therapeutic platform, imaging methods capable of resolving cell migration and homing have gained substantial significance. Bioluminescence and fluorescence imaging which are often considered for this goal offer reduced spatial resolution and surface weighted imaging performance and therefore are not ideally suited for resolving the exact cell biodistribution. MSOT has the potential to resolve contrast stemming from fluorescent dyes in high resolution, deep within tissue. In this work the abilities of MSOT imaging coupled with statistical sub-pixel detection are investigated in the context of immune cell imaging. While previous studied showed the ability of optoacoustic imaging to resolve labeled cells, no systematic study has been performed to assess the MSOT sensitivity in cell imaging.

The objective of this work is to investigate the MSOT detection ability and sensitivity for immune cells, labeled with fluorescent dyes. Although fluorescence labels are sub-optimal in terms of optoacoustic signal intensity, they are well-establish and allow to be also visualized with optical methods, for validating the MSOT readings.

In this study Jurkat Lymphocytes and J774A.1 mouse macrophages are labeled with a lipophilic, near-infrared fluorescent cyanine dye (DiR). DiR is incorporated into the cell membrane and provides absorption contrast with a distinct absorption spectrum, which can be resolved by MSOT. Experiments are performed for optimizing cell labeling and quantifying labeling efficiency and cell viability. In the following, imaging phantoms are prepared, which contain cells at known concentrations. Analysis of the MSOT phantom images allows for quantifying and comparing the level of absorbance of the labeled cells. To confirm the ability of MSOT to detect labeled cells in tissues and provide first insights on the number of cells required for successful detection, animal experiments are performed. Different amounts of labeled macrophages are injected into the brain of euthanized mice, and the mice are imaged using MSOT and subsequently with cryoslicing fluorescence imaging, for validating the position of the cells. Spectral analysis of the MSOT images using AMF is performed to resolve the spectrum of DiR.

The analysis of the phantom images indicates a linear relationship between the number of labeled cells and the MSOT signal. The absorbance of labeled cells is quantified, and it is further established that macrophages exhibit an increased signal as compared to the T cells, a result that is explained due to the larger surface of macrophages which allows for more efficient DiR labeling. The analysis of the animal MSOT images indicates that MSOT coupled with AMF is capable of detecting down to 2,500 labeled macrophages injected in a small volume within the tissue. This result suggests that

MSOT combined with AMF can serve as a promising cell imaging method.

Angelika Zaremba, Vasilis Ntziachristos and I designed the experiments performed for this study. Angelika Zaremba, Vasilis Ntziachristos and I drafted the paper which was advanced through feedback from all other co-authors. Angelika Zaremba, Karin Schaefer, and Uwe Klemm performed and optimized the cell labeling. Uwe Klemm Angelika Zaremba and I performed the phantom and animal experiments. I analyzed the phantom and the animal data.

5.2 Publication

S. Tzoumas[†], A. Zaremba[†], U. Klemm, A. Nunes, K. Schaefer, V. Ntziachristos, "Immune cell imaging using multi-spectral optoacoustic tomography," *Optics Letters*, vol. 39, no. 12, pp. 3523-2526, 2014.

Chapter 6

Eigenspectra optoacoustic tomography achieves quantitative blood oxygenation imaging deep in tissues

6.1 Summary

The work "Eigenspectra optoacoustic tomography achieves quantitative blood oxygenation imaging deep in tissues" is authored by Stratis Tzoumas, Antonio Nunes, Ivan Olefir, Stefan Stangl, Panagiotis Symvoulidis, Sarah Glasl, Christine Bayer, Gabriele Multhoff and Vasilis Ntziachristos. The version herein (Appendix E) is currently under review in the journal "Nature Communications". In this paper, I share the first authorship with Antonio Nunes.

Measurement of tissue and blood oxygenation is crucial for understanding tissue physiology and is also related to a number of pathological conditions such as cardiovascular disease and cancer hypoxia. A multitude of imaging and sensing methods have been considered for imaging tissue oxygenation. Nevertheless, there exists today no established, gold standard method that can quantitatively image oxygenation with high accuracy, high spatial and temporal resolution and across entire tissues. MSOT detects the spectra of oxygenated and deoxygenated hemoglobin in high resolution, deep within tissue; therefore appearing very promising for this goal. However, the accuracy of MSOT in blood sO_2 estimation within deep tissue remains to date limited.

Light propagating in tissue attains a spectrum that varies with location due to wavelength-dependent fluence attenuation by tissue optical properties. Unless explicitly accounted for, the wavelength dependent light fluence attenuation alters the detected optoacoustic spectra; an effect commonly termed *spectral corruption*. Despite substantial prior work, the problem of light fluence correction in optoacoustic imaging has not been conclusively solved. Therefore, spectral corruption has limited the quantification accuracy of optoacoustic spectroscopic methods and impeded the goal of accurate blood sO_2 estimation deep in tissues.

In this work a new concept is introduced, which models the wavelength dependence (i.e. the spectrum) of light fluence as an affine function of a few reference base spectra, independently of the specific distribution of tissue optical properties. This model, termed fluence *eigenspectra*, is derived by applying Principal Component Analysis (PCA) on a training set of light fluence spectral patterns, which are computed by simulating light propagation in tissues at different oxygenation states of hemoglobin and different tissue depths. The *eigenspectra* model for light fluence allows for formulating the MSOT blood sO_2 estimation problem as a non-linear spectral unmixing problem. For solving this problem, a constrained non-linear inversion scheme is developed, termed *eigenspectra* MSOT (eMSOT). The non-linear inversion scheme incorporates constraints on the spatial characteristics of light fluence for achieving accurate convergence and good inversion stability.

The accuracy of the *eigenspectra* model and eMSOT is validated statistically through an extensive dataset comprised of numerical simulations of light propagation in arbitrary tissues. Furthermore imaging phantoms containing blood at different oxygenation levels and controlled *in vivo*

experiments are performed for validating the eMSOT quantification accuracy in experimental data. Finally, eMSOT is applied for quantifying blood oxygenation gradients in the skeletal muscle of animals and in tumors during tumor growth or O_2 challenge, and the *in vivo* MSOT readings are compared to correlative histological analysis.

Numerical simulations suggest that the *eigenspectra* model offers high accuracy in modelling the spectrum of optical fluence in arbitrary tissues. Furthermore, the validation of eMSOT through numerical simulations indicates that the eMSOT blood sO_2 estimation accuracy is substantially enhanced as compared to linear unmixing which as previously used for sO_2 is experimental *in vivo* data. This conclusion is also supported by the blood phantom and the controlled *in vivo* experiments analysis. In the case of skeletal muscle imaging, the blood oxygenation gradients resolved appeared in agreement with the expected physiological state and previous studies based on invasive microscopy methods. In the case of tumor imaging, the hypoxic areas resolved *in vivo* with eMSOT were in agreement with the perfusion and hypoxia maps obtained through *post mortem* histological analysis.

I conceived the concept of the *eigenspectra*. I implemented and optimized eMSOT and performed the simulations and the numerical validations together with Ivan Olefir. The concept was continuously advanced through discussions with Ivan Olefir and Vasilis Ntziachristos. I performed the blood phantom experiments together with Panagiotis Symvoulidis. Antonio Nunes, Stefan Stangl, Gabrielle Multhof, Vasilis Ntziachristos and I designed the experimental animal study. Antonio Nunes performed all *in vivo* imaging experiments with the help of Sarah Glasl. Antonio Nunes, Sarah Glasl, Stefan Stangl and Christine Bayer performed the histological analysis. I analyzed all experimental MSOT data. All authors contributed in interpreting the data and writing the paper. Vasilis Ntziachristos supervised the project.

6.2 Publication

S. Tzoumas[†], A. Nunes[†], I. Olefir, S. Stangl, P. Symvoulidis, S. Glasl, C. Bayer, G. Multhoff, V. Ntziachristos, "Eigenspectra optoacoustic tomography achieves quantitative blood oxygenation imaging deep in tissues," *Nature Communications*, vol. 7, pp. 12121, 2016

Chapter 7

Spatiospectral denoising framework for multispectral optoacoustic imaging based on sparse signal representation

7.1 Summary

The work "Spatiospectral denoising framework for multispectral optoacoustic imaging based on sparse signal representation" is authored by Stratis Tzoumas, Amir Rosenthal, Christian Lutzweiler, Daniel Razansky and Vasilis Ntziachristos. The version herein (Appendix F) is published in the journal "Medical Physics" [78].

Accurate molecular and physiological MSOT imaging demands the acquisition of optoacoustic signals at multiple excitation wavelengths as well as repetitive signal acquisition and averaging for minimizing the influence of electronic noise. Due to the limited repetition rate of pulsed lasers, this demand may compromise the temporal resolution of MSOT imaging. The development of denoising methods which prevent the need for signal averaging in time could potentially advance the dynamic capabilities of the technology.

In this work, a denoising method is developed for MSOT imaging by exploiting the inherent sparsity of multispectral optoacoustic signals both in space as well as across the spectral dimension. By reviewing fundamental characteristics of multispectral optoacoustic signals in space and across excitation wavelengths, a combined spatiospectral transformation is proposed for offering an appropriate sparse representation of such signals. The localized and broadband nature of optoacoustic signals in time is captured through a wavelet transform while the inherent compressibility of the signals in the spectral domain is captured through a Karhunen-Loève transformation. Noise suppression is achieved in the following by applying thresholding on this combined wavelet - Karhunen-Loève representation of the signals or images. For validating the accuracy of the method simulations are formed where white Gaussian noise or parasitic noise is superimposed onto experimental MSOT signals of *in vivo* tissue. Purely experimental data containing parasitic noise are further collected for evaluating the direct applicability of the method.

The combined representation proposed allows for representing MSOT data in a particularly sparse manner, as evaluated through a Lorenz curve analysis. Moreover, the denoising method proposed allows for efficient noise suppression with minimal signal loss and considerably outperforms previously proposed denoising strategies, based on wavelet thresholding, that do not consider multispectral information. Importantly, the sparse representation proposed offers promise for further applications such as the enhancement of image reconstruction speed, which is implemented in a follow-up study [140].

I conceived and designed the spatiospectral denoising algorithm with the help of Amir Rosenthal. I implemented the denoising method, collected the experimental data and implemented the simulations for the quantitative validation of the method. I drafted the article which was continuously improved through discussions with all other co-authors.

7.2 Publication

S. Tzoumas, A. Rosenthal, C. Lutzweiler, D. Razansky, V. Ntziachristos, "Spatiospectral denoising framework for multispectral optoacoustic imaging based on sparse signal representation," *Medical Physics*, vol. 41, no. 11, pp. 113301, 2014.

Bibliography

[1] F. Kiessling, J. Pichler, and P. Hauff, *Small animal imaging*. Springer, 2011.

[2] M. Baker, "Whole-animal imaging: The whole picture," *Nature*, vol. 463, no. 7283, pp. 977–980, 2010.

[3] R. Weissleder and U. Mahmood, "Molecular Imaging 1," *Radiology*, vol. 219, no. 2, pp. 316–333, 2001.

[4] R. Weissleder and M. Nahrendorf, "Advancing biomedical imaging," *Proceedings of the National Academy of Sciences*, vol. 112, no. 47, pp. 14424–14428, 2015.

[5] S. Ogawa, T.-M. Lee, A. R. Kay, and D. W. Tank, "Brain magnetic resonance imaging with contrast dependent on blood oxygenation," *Proceedings of the National Academy of Sciences*, vol. 87, no. 24, pp. 9868–9872, 1990.

[6] S. S. Gambhir, "Molecular imaging of cancer with positron emission tomography," *Nature Reviews Cancer*, vol. 2, no. 9, pp. 683–693, 2002.

[7] R. Weissleder and V. Ntziachristos, "Shedding light onto live molecular targets," *Nature Medicine*, vol. 9, no. 1, pp. 123–128, 2003.

[8] V. Ntziachristos, "Going deeper than microscopy: the optical imaging frontier in biology," *Nature Methods*, vol. 7, no. 8, pp. 603–614, 2010.

[9] A. Yodh and B. Chance, "Spectroscopy and imaging with diffusing light," *Physics Today*, vol. 48, no. 3, pp. 34–41, 1995.

[10] S. Arridge, M. Schweiger, M. Hiraoka, and D. Delpy, "A finite element approach for modeling photon transport in tissue," *Medical Physics*, vol. 20, p. 299, 1993.

[11] A. Gibson and H. Dehghani, "Diffuse optical imaging," *Philosophical Transactions of the Royal Society of London A: Mathematical, Physical and Engineering Sciences*, vol. 367, no. 1900, pp. 3055–3072, 2009.

[12] V. Ntziachristos, C.-H. Tung, C. Bremer, and R. Weissleder, "Fluorescence molecular tomography resolves protease activity in vivo," *Nature Medicine*, vol. 8, no. 7, pp. 757–761, 2002.

[13] A. T. Eggebrecht, S. L. Ferradal, A. Robichaux-Viehoever, M. S. Hassanpour, H. Dehghani, A. Z. Snyder, T. Hershey, and J. P. Culver, "Mapping distributed brain function and networks with diffuse optical tomography," *Nature Photonics*, vol. 8, no. 6, pp. 448–454, 2014.

[14] X. Wang, Y. Pang, G. Ku, X. Xie, G. Stoica, and L. V. Wang, "Noninvasive laser-induced photoacoustic tomography for structural and functional in vivo imaging of the brain," *Nature Biotechnology*, vol. 21, no. 7, pp. 803–806, 2003.

[15] R. A. Kruger, W. L. Kiser, D. R. Reinecke, G. A. Kruger, and K. D. Miller, "Thermoacoustic molecular imaging of small animals," *Molecular Imaging*, vol. 2, no. 2, p. 113, 2003.

[16] L. V. Wang and S. Hu, "Photoacoustic tomography: in vivo imaging from organelles to organs," *Science*, vol. 335, no. 6075, pp. 1458–1462, 2012.

[17] P. Mohajerani, S. Tzoumas, A. Rosenthal, and V. Ntziachristos, "Optical and optoacoustic model-based tomography: Theory and current challenges for deep tissue imaging of optical contrast," *Signal Processing Magazine, IEEE*, vol. 32, no. 1, pp. 88–100, 2015.

[18] M. Li, J. Oh, X. Xie, G. Ku, W. Wang, C. Li, G. Lungu, G. Stoica, and L. V. Wang, "Simultaneous molecular and hypoxia imaging of brain tumors in vivo using spectroscopic photoacoustic tomography," *PROCEEDINGS-IEEE*, vol. 96, no. 3, p. 481, 2008.

[19] E. Herzog, A. Taruttis, N. Beziere, A. A. Lutich, D. Razansky, and V. Ntziachristos, "Optical imaging of cancer heterogeneity with multispectral optoacoustic tomography," *Radiology*, vol. 263, no. 2, pp. 461–468, 2012.

[20] N. C. Burton, M. Patel, S. Morscher, W. H. Driessen, J. Claussen, N. Beziere, T. Jetzfellner, A. Taruttis, D. Razansky, B. Bednar, *et al.*, "Multispectral opto-acoustic tomography (MSOT) of the brain and glioblastoma characterization," *Neuroimage*, vol. 65, pp. 522–528, 2013.

[21] V. Ntziachristos and D. Razansky, "Molecular imaging by means of multispectral optoacoustic tomography (MSOT)," *Chemical Reviews*, vol. 110, no. 5, pp. 2783–2794, 2010.

[22] A. Taruttis, S. Morscher, N. C. Burton, D. Razansky, and V. Ntziachristos, "Fast multispectral optoacoustic tomography (MSOT) for dynamic imaging of pharmacokinetics and biodistribution in multiple organs," *PLoS One*, vol. 7, no. 1, p. e30491, 2012.

[23] N. C. Deliolanis, A. Ale, S. Morscher, N. C. Burton, K. Schaefer, K. Radrich, D. Razansky, and V. Ntziachristos, "Deep-tissue reporter-gene imaging with fluorescence and optoacoustic tomography: a performance overview," *Molecular Imaging and Biology*, vol. 16, no. 5, pp. 652–660, 2014.

[24] D. Razansky, A. Buehler, and V. Ntziachristos, "Volumetric real-time multispectral optoacoustic tomography of biomarkers," *Nature Protocols*, vol. 6, no. 8, pp. 1121–1129, 2011.

[25] A. Rosenthal, D. Razansky, and V. Ntziachristos, "Fast semi-analytical model-based acoustic inversion for quantitative optoacoustic tomography," *Medical Imaging, IEEE Transactions on*, vol. 29, no. 6, pp. 1275–85, 2010.

[26] B. Cox, J. Laufer, S. Arridge, and P. Beard, "Quantitative spectroscopic photoacoustic imaging: a review," *Journal of Biomedical Optics*, vol. 17, no. 6, p. 61202, 2012.

[27] K. Maslov, H. Zhang, and L. Wang, "Effects of wavelength-dependent fluence attenuation on the noninvasive photoacoustic imaging of hemoglobin oxygen saturation in subcutaneous vasculature in vivo," *Inverse Problems*, vol. 23, no. 6, p. S113, 2007.

[28] S. Mallat, *A wavelet tour of signal processing*. Academic press, 1999.

[29] R. O. Duda, P. E. Hart, and D. G. Stork, *Pattern classification*. John Wiley & Sons, 2012.

[30] S. M. Kay, *Fundamentals of statistical signal processing, Vol. II: Detection Theory*. Prentice Hall, 1998.

[31] D. G. Manolakis, V. K. Ingle, and S. M. Kogon, *Statistical and adaptive signal processing: spectral estimation, signal modeling, adaptive filtering, and array processing*. Artech House, 2005.

[32] P. C. Hansen, *Rank-deficient and discrete ill-posed problems: numerical aspects of linear inversion*. SIAM, 1998.

[33] D. P. Bertsekas, *Nonlinear programming*. Athena Scientific, 1999.

[34] R. Weissleder and M. J. Pittet, "Imaging in the era of molecular oncology," *Nature*, vol. 452, no. 7187, pp. 580–589, 2008.

[35] M. F. Kircher, S. S. Gambhir, and J. Grimm, "Noninvasive cell-tracking methods," *Nature Reviews Clinical Oncology*, vol. 8, no. 11, pp. 677–688, 2011.

[36] C. S. Levin, "Primer on molecular imaging technology," *European Journal of Nuclear Medicine and Molecular Imaging*, vol. 32, no. 2, pp. S325–S345, 2005.

[37] D. E. Sosnovik and R. Weissleder, "Emerging concepts in molecular MRI," *Current Opinion in Biotechnology*, vol. 18, no. 1, pp. 4–10, 2007.

[38] J. U. Voigt, "Ultrasound molecular imaging," *Methods*, vol. 48, no. 2, pp. 92–97, 2009.

[39] M. G. Shapiro, P. W. Goodwill, A. Neogy, M. Yin, F. S. Foster, D. V. Schaffer, and S. M. Conolly, "Biogenic gas nanostructures as ultrasonic molecular reporters," *Nature Nanotechnology*, vol. 9, no. 4, pp. 311–316, 2014.

[40] G. P. Luke, D. Yeager, and S. Y. Emelianov, "Biomedical applications of photoacoustic imaging with exogenous contrast agents," *Annals of Biomedical Engineering*, vol. 40, no. 2, pp. 422–437, 2012.

[41] D. Razansky, N. J. Harlaar, J. L. Hillebrands, A. Taruttis, E. Herzog, C. J. Zeebregts, G. M. van Dam, and V. Ntziachristos, "Multispectral optoacoustic tomography of matrix metalloproteinase activity in vulnerable human carotid plaques," *Molecular Imaging and Biology*, vol. 14, no. 3, pp. 277–85, 2012.

[42] A. Taruttis, M. Wildgruber, K. Kosanke, N. Beziere, K. Licha, R. Haag, M. Aichler, A. Walch, E. Rummeny, and V. Ntziachristos, "Multispectral optoacoustic tomography of myocardial infarction," *Photoacoustics*, vol. 1, no. 1, pp. 3–8, 2013.

[43] "Optical absorption of hemoglobin." http://omlc.org/spectra/hemoglobin.

[44] J. Stritzker, L. Kirscher, M. Scadeng, N. C. Deliolanis, S. Morscher, P. Symvoulidis, K. Schaefer, Q. Zhang, L. Buckel, and M. Hess, "Vaccinia virus-mediated melanin production allows MR and optoacoustic deep tissue imaging and laser-induced thermotherapy of cancer," *Proceedings of the National Academy of Sciences*, vol. 110, no. 9, pp. 3316–3320, 2013.

[45] A. P. Jathoul, J. Laufer, O. Ogunlade, B. Treeby, B. Cox, E. Zhang, P. Johnson, A. R. Pizzey, B. Philip, T. Marafioti, *et al.*, "Deep in vivo photoacoustic imaging of mammalian tissues using a tyrosinase-based genetic reporter," *Nature Photonics*, vol. 9, no. 4, pp. 239–246, 2015.

[46] A. De La Zerda, C. Zavaleta, S. Keren, S. Vaithilingam, S. Bodapati, Z. Liu, J. Levi, B. R. Smith, T.-J. Ma, and O. Oralkan, "Carbon nanotubes as photoacoustic molecular imaging agents in living mice," *Nature Nanotechnology*, vol. 3, no. 9, pp. 557–562, 2008.

[47] P. Vaupel and L. Harrison, "Tumor hypoxia: causative factors, compensatory mechanisms, and cellular response," *The Oncologist*, vol. 9, no. Supplement 5, pp. 4–9, 2004.

[48] K. Schmidt-Nielsen, *Animal physiology: adaptation and environment*. Cambridge University Press, 1997.

[49] I. Serganova, J. Humm, C. Ling, and R. Blasberg, "Tumor hypoxia imaging," *Clinical Cancer Research*, vol. 12, no. 18, pp. 5260–5264, 2006.

[50] R. S. Frackowiak, G.-L. Lenzi, T. Jones, and J. D. Heather, "Quantitative measurement of regional cerebral blood flow and oxygen metabolism in man using 15O and positron emission tomography: theory, procedure, and normal values," *Journal of Computer Assisted Tomography*, vol. 4, no. 6, pp. 727–736, 1980.

[51] X. He and D. A. Yablonskiy, "Quantitative BOLD: mapping of human cerebral deoxygenated blood volume and oxygen extraction fraction: default state," *Magnetic Resonance in Medicine*, vol. 57, no. 1, pp. 115–126, 2007.

[52] T. Christen, P. Bouzat, N. Pannetier, N. Coquery, A. Moisan, B. Lemasson, S. Thomas, E. Grillon, O. Detante, C. Rémy, *et al.*, "Tissue oxygen saturation mapping with magnetic resonance imaging," *Journal of Cerebral Blood Flow & Metabolism*, vol. 34, no. 9, pp. 1550–1557, 2014.

[53] M. Elas, B. B. Williams, A. Parasca, C. Mailer, C. A. Pelizzari, M. A. Lewis, J. N. River, G. S. Karczmar, E. D. Barth, and H. J. Halpern, "Quantitative tumor oxymetric images from 4D electron paramagnetic resonance imaging (EPRI): Methodology and comparison with blood oxygen level-dependent (BOLD) MRI," *Magnetic Resonance in Medicine*, vol. 49, no. 4, pp. 682–691, 2003.

[54] J. Price, S. Robinson, and D. Koh, "Imaging hypoxia in tumours with advanced MRI.," *The quarterly journal of nuclear medicine and molecular imaging*, vol. 57, no. 3, p. 257, 2013.

[55] W. L. Rumsey, J. M. Vanderkooi, and D. F. Wilson, "Imaging of phosphorescence: a novel method for measuring oxygen distribution in perfused tissue," *Science*, vol. 241, no. 4873, pp. 1649–1651, 1988.

[56] R. N. Pittman and B. R. Duling, "Measurement of percent oxyhemoglobin in the microvasculature," *Journal of Applied Physiology*, vol. 38, no. 2, pp. 321–327, 1975.

[57] H. F. Zhang, K. Maslov, G. Stoica, and L. V. Wang, "Functional photoacoustic microscopy for high-resolution and noninvasive in vivo imaging," *Nature Biotechnology*, vol. 24, no. 7, pp. 848–851, 2006.

[58] A. Devor, S. Sakadžić, V. J. Srinivasan, M. A. Yaseen, K. Nizar, P. A. Saisan, P. Tian, A. M. Dale, S. A. Vinogradov, M. A. Franceschini, *et al.*, "Frontiers in optical imaging of cerebral blood flow and metabolism," *Journal of Cerebral Blood Flow & Metabolism*, vol. 32, no. 7, pp. 1259–1276, 2012.

[59] A. G. Tsai, P. C. Johnson, and M. Intaglietta, "Oxygen gradients in the microcirculation," *Physiological Reviews*, vol. 83, no. 3, pp. 933–963, 2003.

[60] S. R. Arridge, "Methods in diffuse optical imaging," *Philosophical Transactions of the Royal Society of London A: Mathematical, Physical and Engineering Sciences*, vol. 369, no. 1955, pp. 4558–4576, 2011.

[61] E. Sevick, B. Chance, J. Leigh, S. Nioka, and M. Maris, "Quantitation of time-and frequency-resolved optical spectra for the determination of tissue oxygenation," *Analytical Biochemistry*, vol. 195, no. 2, pp. 330–351, 1991.

[62] A. Corlu, R. Choe, T. Durduran, K. Lee, M. Schweiger, S. R. Arridge, E. Hillman, and A. G. Yodh, "Diffuse optical tomography with spectral constraints and wavelength optimization," *Applied Optics*, vol. 44, no. 11, pp. 2082–2093, 2005.

[63] L. V. Wang and H. Wu, *Biomedical optics: principles and imaging*. John Wiley & Sons, 2012.

[64] L. V. Wang, *Photoacoustic imaging and spectroscopy*. CRC press, 2009.

[65] J. Ripoll, *Principles of Diffuse Light Propagation*. World Scientific, 2012.

[66] E. Zhang, J. Laufer, and P. Beard, "Backward-mode multiwavelength photoacoustic scanner using a planar Fabry-Perot polymer film ultrasound sensor for high-resolution three-dimensional imaging of biological tissues," *Applied Optics*, vol. 47, no. 4, pp. 561–577, 2008.

[67] R. Kruger, R. Lam, D. Reinecke, S. Del Rio, and R. Doyle, "Photoacoustic angiography of the breast," *Medical Physics*, vol. 37, no. 11, p. 6096, 2010.

[68] H.-P. Brecht, R. Su, M. Fronheiser, S. A. Ermilov, A. Conjusteau, and A. A. Oraevsky, "Whole-body three-dimensional optoacoustic tomography system for small animals," *Journal of Biomedical Optics*, vol. 14, no. 6, pp. 064007–064007–8, 2009.

[69] X. L. Deán-Ben and D. Razansky, "Adding fifth dimension to optoacoustic imaging: volumetric time-resolved spectrally enriched tomography," *Light: Science & Applications*, vol. 3, no. 1, p. e137, 2014.

[70] J. Gateau, M. A. A. Caballero, A. Dima, and V. Ntziachristos, "Three-dimensional optoacoustic tomography using a conventional ultrasound linear detector array: whole-body tomographic system for small animals," *Medical Physics*, vol. 40, no. 1, p. 013302, 2013.

[71] A. Buehler, E. Herzog, D. Razansky, and V. Ntziachristos, "Video rate optoacoustic tomography of mouse kidney perfusion," *Optics Letters*, vol. 35, no. 14, pp. 2475–2477, 2010.

[72] J. Xia, M. R. Chatni, K. Maslov, Z. Guo, K. Wang, M. Anastasio, and L. V. Wang, "Whole-body ring-shaped confocal photoacoustic computed tomography of small animals in vivo," *Journal of Biomedical Optics*, vol. 17, no. 5, pp. 0505061–0505063, 2012.

[73] E. Zhang, J. Laufer, R. Pedley, and P. Beard, "In vivo high-resolution 3D photoacoustic imaging of superficial vascular anatomy," *Physics in Medicine and Biology*, vol. 54, no. 4, p. 1035, 2009.

[74] J. Gateau, A. Chekkoury, and V. Ntziachristos, "High-resolution optoacoustic mesoscopy with a 24 MHz multidetector translate-rotate scanner," *Journal of Biomedical Optics*, vol. 18, no. 10, pp. 106005–106005, 2013.

[75] M. Omar, J. Gateau, and V. Ntziachristos, "Raster-scan optoacoustic mesoscopy in the 25-125 MHz range," *Optics Letters*, vol. 38, no. 14, pp. 2472–2474, 2013.

[76] J. Xia and L. V. Wang, "Small-animal whole-body photoacoustic tomography: a review," *Biomedical Engineering, IEEE Transactions on*, vol. 61, no. 5, pp. 1380–1389, 2014.

[77] A. Dima, N. C. Burton, and V. Ntziachristos, "Multispectral optoacoustic tomography at 64, 128, and 256 channels," *Journal of Biomedical Optics*, vol. 19, no. 3, pp. 036021–036021, 2014.

[78] S. Tzoumas, A. Rosenthal, C. Lutzweiler, D. Razansky, and V. Ntziachristos, "Spatiospectral denoising framework for multispectral optoacoustic imaging based on sparse signal representation," *Medical Physics*, vol. 41, no. 11, p. 113301, 2014.

[79] A. Rosenthal, V. Ntziachristos, and D. Razansky, "Acoustic inversion in optoacoustic tomography: A review," *Current Medical Imaging Reviews*, vol. 9, no. 4, p. 318, 2013.

[80] M. Xu and L. V. Wang, "Universal back-projection algorithm for photoacoustic computed tomography," *Physical Review E*, vol. 71, no. 1, p. 016706, 2005.

[81] X. L. Deán-Ben, V. Ntziachristos, and D. Razansky, "Acceleration of optoacoustic model-based reconstruction using angular image discretization," *Medical Imaging, IEEE Transactions on*, vol. 31, no. 5, pp. 1154–1162, 2012.

[82] K. Wang, S. A. Ermilov, R. Su, H.-P. Brecht, A. A. Oraevsky, and M. A. Anastasio, "An imaging model incorporating ultrasonic transducer properties for three-dimensional optoacoustic tomography," *Medical Imaging, IEEE Transactions on*, vol. 30, no. 2, pp. 203–214, 2011.

[83] Z. Yuan and H. Jiang, "Three-dimensional finite-element-based photoacoustic tomography: Reconstruction algorithm and simulations," *Medical Physics*, vol. 34, p. 538, 2007.

[84] T. Jetzfellner, D. Razansky, A. Rosenthal, R. Schulz, K.-H. Englmeier, and V. Ntziachristos, "Performance of iterative optoacoustic tomography with experimental data," *Applied Physics Letters*, vol. 95, no. 1, pp. 013703–013703–3, 2009.

[85] L. Ding, X. L. Deán-Ben, C. Lutzweiler, D. Razansky, and V. Ntziachristos, "Efficient non-negative constrained model-based inversion in optoacoustic tomography," *Physics in Medicine and Biology*, vol. 60, no. 17, p. 6733, 2015.

[86] A. Rosenthal, V. Ntziachristos, and D. Razansky, "Optoacoustic methods for frequency calibration of ultrasonic sensors," *Ultrasonics, Ferroelectrics and Frequency Control, IEEE Transactions on*, vol. 58, no. 2, pp. 316–326, 2011.

[87] A. Rosenthal, V. Ntziachristos, and D. Razansky, "Model-based optoacoustic inversion with arbitrary-shape detectors," *Medical Physics*, vol. 38, p. 4285, 2011.

[88] D. Queirós, X. L. Deán-Ben, A. Buehler, D. Razansky, A. Rosenthal, and V. Ntziachristos, "Modeling the shape of cylindrically focused transducers in three-dimensional optoacoustic tomography," *Journal of Biomedical Optics*, vol. 18, no. 7, pp. 076014–076014, 2013.

[89] A. Buehler, A. Rosenthal, T. Jetzfellner, A. Dima, D. Razansky, and V. Ntziachristos, "Model-based optoacoustic inversions with incomplete projection data," *Medical Physics*, vol. 38, p. 1694, 2011.

[90] B. E. Treeby, E. Z. Zhang, and B. Cox, "Photoacoustic tomography in absorbing acoustic media using time reversal," *Inverse Problems*, vol. 26, no. 11, p. 115003, 2010.

[91] X. L. Deán-Ben, D. Razansky, and V. Ntziachristos, "The effects of acoustic attenuation in optoacoustic signals," *Physics in Medicine and Biology*, vol. 56, no. 18, p. 6129, 2011.

[92] X. L. Dean-Ben, R. Ma, D. Razansky, and V. Ntziachristos, "Statistical approach for optoacoustic image reconstruction in the presence of strong acoustic heterogeneities," *Medical Imaging, IEEE Transactions on*, vol. 30, no. 2, pp. 401–408, 2011.

[93] B. Cox, S. Arridge, and P. Beard, "Estimating chromophore distributions from multiwavelength photoacoustic images," *Journal of the Optical Society of America. A, Optics, image science, and vision*, vol. 26, no. 2, pp. 443–455, 2009.

[94] L. Wang, S. L. Jacques, and L. Zheng, "MCML-Monte Carlo modeling of light transport in multi-layered tissues," *Computer Methods and Programs in Biomedicine*, vol. 47, no. 2, pp. 131–146, 1995.

[95] "Tissue spectra." http://www.ucl.ac.uk/medphys/research/borl/intro/spectra.

[96] L. Li, H. F. Zhang, R. J. Zemp, K. Maslov, and L. V. Wang, "Simultaneous imaging of a lacZ-marked tumor and microvasculature morphology in vivo by dual-wavelength photoacoustic microscopy," *Journal of Innovative Optical Health Sciences*, vol. 1, no. 02, pp. 207–215, 2008.

[97] D. Razansky, C. Vinegoni, and V. Ntziachristos, "Multispectral photoacoustic imaging of fluorochromes in small animals," *Optics Letters*, vol. 32, no. 19, pp. 2891–2893, 2007.

[98] N. Keshava and J. F. Mustard, "Spectral unmixing," *Signal Processing Magazine, IEEE*, vol. 19, no. 1, pp. 44–57, 2002.

[99] G. P. Luke and S. Y. Emelianov, "Optimization of in vivo spectroscopic photoacoustic imaging by smart optical wavelength selection," *Optics Letters*, vol. 39, no. 7, pp. 2214–2217, 2014.

[100] D. Razansky, M. Distel, C. Vinegoni, R. Ma, N. Perrimon, R. W. Köster, and V. Ntziachristos, "Multispectral opto-acoustic tomography of deep-seated fluorescent proteins in vivo," *Nature Photonics*, vol. 3, no. 7, pp. 412–417, 2009.

[101] G. S. Filonov, A. Krumholz, J. Xia, J. Yao, L. V. Wang, and V. V. Verkhusha, "Deep-Tissue Photoacoustic Tomography of a Genetically Encoded Near-Infrared Fluorescent Probe," *Angewandte Chemie International Edition*, vol. 51, no. 6, pp. 1448–1451, 2012.

[102] S. Mallidi, T. Larson, J. Tam, P. P. Joshi, A. Karpiouk, K. Sokolov, and S. Emelianov, "Multiwavelength photoacoustic imaging and plasmon resonance coupling of gold nanoparticles for selective detection of cancer," *Nano Letters*, vol. 9, no. 8, pp. 2825–2831, 2009.

[103] A. Hyvarinen, "Fast and robust fixed-point algorithms for independent component analysis," *Neural Networks, IEEE Transactions on*, vol. 10, no. 3, pp. 626–634, 1999.

[104] J. M. P. Nascimento and J. M. B. Dias, "Vertex component analysis: a fast algorithm to unmix hyperspectral data," *Geoscience and Remote Sensing, IEEE Transactions on*, vol. 43, no. 4, pp. 898–910, 2005.

[105] J. Glatz, N. C. Deliolanis, A. Buehler, D. Razansky, and V. Ntziachristos, "Blind source unmixing in multi-spectral optoacoustic tomography," *Optics Express*, vol. 19, no. 4, pp. 3175–3184, 2011.

[106] X. L. Deán-Ben, N. C. Deliolanis, V. Ntziachristos, and D. Razansky, "Fast unmixing of multispectral optoacoustic data with vertex component analysis," *Optics and Lasers in Engineering*, vol. 58, pp. 119–125, 2014.

[107] D. Manolakis and G. Shaw, "Detection algorithms for hyperspectral imaging applications," *Signal Processing Magazine, IEEE*, vol. 19, no. 1, pp. 29–43, 2002.

[108] E. J. Kelly, "An adaptive detection algorithm," *Aerospace and Electronic Systems, IEEE Transactions on*, vol. 22, no. 2, pp. 115–127, 1986.

[109] F. C. Robey, D. R. Fuhrmann, E. J. Kelly, and R. Nitzberg, "A CFAR adaptive matched filter detector," *Aerospace and Electronic Systems, IEEE Transactions on*, vol. 28, no. 1, pp. 208–216, 1992.

[110] S. Kraut, L. Scharf, and R. Butler, "The adaptive coherence estimator: a uniformly most-powerful-invariant adaptive detection statistic," *Signal Processing, IEEE Transactions on*, vol. 53, no. 2, pp. 427–438, 2005.

[111] J. Theiler and B. R. Foy, "EC-GLRT: Detecting weak plumes in non-Gaussian hyperspectral clutter using an elliptically-contoured generalized likelihood ratio test," in *Geoscience and Remote Sensing Symposium, 2008. IGARSS 2008. IEEE International*, vol. 1, pp. I–221–I–224, IEEE.

[112] J.-F. Synnevag, A. Austeng, and S. Holm, "Adaptive beamforming applied to medical ultrasound imaging," *Ultrasonics, Ferroelectrics, and Frequency Control, IEEE Transactions on*, vol. 54, no. 8, pp. 1606–1613, 2007.

[113] S. Niu, S. E. Golowich, V. K. Ingle, and D. G. Manolakis, "Implications and mitigation of model mismatch and covariance contamination for hyperspectral chemical agent detection," *Optical Engineering*, vol. 52, no. 2, pp. 026202–026202, 2013.

[114] S. Matteoli, M. Diani, and J. Theiler, "An overview of background modeling for detection of targets and anomalies in hyperspectral remotely sensed imagery," *Selected Topics in Applied Earth Observations and Remote Sensing, IEEE Journal of*, vol. 7, no. 6, pp. 2317–2336, 2014.

[115] J. Theiler and B. R. Foy, "Effect of signal contamination in matched-filter detection of the signal on a cluttered background," *Geoscience and Remote Sensing Letters, IEEE*, vol. 3, no. 1, pp. 98–102, 2006.

[116] C. Lutzweiler and D. Razansky, "Optoacoustic imaging and tomography: reconstruction approaches and outstanding challenges in image performance and quantification," *Sensors*, vol. 13, no. 6, pp. 7345–7384, 2013.

[117] B. Cox, J. Laufer, and P. Beard, "Quantitative photoacoustic image reconstruction using fluence dependent chromophores," *Biomedical Optics Express*, vol. 1, no. 1, pp. 201–208, 2010.

[118] X. L. Deán-Ben, A. C. Stiel, Y. Jiang, V. Ntziachristos, G. G. Westmeyer, and D. Razansky, "Light fluence normalization in turbid tissues via temporally unmixed multispectral optoacoustic tomography," *Optics Letters*, vol. 40, no. 20, pp. 4691–4694, 2015.

[119] K. Daoudi, A. Hussain, E. Hondebrink, and W. Steenbergen, "Correcting photoacoustic signals for fluence variations using acousto-optic modulation," *Optics Express*, vol. 20, no. 13, pp. 14117–14129, 2012.

[120] J. Xia, A. Danielli, Y. Liu, L. Wang, K. Maslov, and L. V. Wang, "Calibration-free quantification of absolute oxygen saturation based on the dynamics of photoacoustic signals," *Optics Letters*, vol. 38, no. 15, pp. 2800–2803, 2013.

[121] M. Sivaramakrishnan, K. Maslov, H. F. Zhang, G. Stoica, and L. V. Wang, "Limitations of quantitative photoacoustic measurements of blood oxygenation in small vessels," *Physics in Medicine and Biology*, vol. 52, no. 5, p. 1349, 2007.

[122] J. Ripoll and V. Ntziachristos, "Quantitative point source photoacoustic inversion formulas for scattering and absorbing media," *Physical Review E*, vol. 71, no. 3, p. 031912, 2005.

[123] R. J. Zemp, "Quantitative photoacoustic tomography with multiple optical sources," *Applied Optics*, vol. 49, no. 18, pp. 3566–3572, 2010.

[124] B. Cox, S. Arridge, K. Kostli, and P. Beard, "Quantitative photoacoustic imaging: fitting a model of light transport to the initial pressure distribution," in *Biomedical Optics 2005*, pp. 49–55, International Society for Optics and Photonics.

[125] Z. Yuan, Q. Wang, and H. Jiang, "Reconstruction of optical absorption coefficient maps of heterogeneous media by photoacoustic tomography coupled with diffusion equation based regularized Newton method," *Optics Express*, vol. 15, no. 26, pp. 18076–18081, 2007.

[126] Z. Yuan and H. Jiang, "Quantitative photoacoustic tomography," *Philosophical Transactions of the Royal Society A: Mathematical, Physical and Engineering Sciences*, vol. 367, no. 1900, pp. 3043–3054, 2009.

[127] G. Bal and G. Uhlmann, "Inverse diffusion theory of photoacoustics," *Inverse Problems*, vol. 26, no. 8, p. 085010, 2010.

[128] G. Bal and K. Ren, "Multi-source quantitative photoacoustic tomography in a diffusive regime," *Inverse Problems*, vol. 27, no. 7, p. 075003, 2011.

[129] G. Bal and K. Ren, "On multi-spectral quantitative photoacoustic tomography in diffusive regime," *Inverse Problems*, vol. 28, no. 2, p. 025010, 2012.

[130] H. Gao, H. Zhao, and S. Osher, "Bregman methods in quantitative photoacoustic tomography," *CAM report*, vol. 10, p. 42, 2010.

[131] A. Pulkkinen, B. Cox, S. Arridge, J. Kaipio, and T. Tarvainen, "A bayesian approach to spectral quantitative photoacoustic tomography," *Inverse Problems*, vol. 30, no. 6, p. 065012, 2014.

[132] T. Saratoon, T. Tarvainen, B. Cox, and S. Arridge, "A gradient-based method for quantitative photoacoustic tomography using the radiative transfer equation," *Inverse Problems*, vol. 29, no. 7, p. 075006, 2013.

[133] R. Hochuli, S. Powell, S. Arridge, and B. Cox, "Forward and adjoint radiance Monte Carlo models for quantitative photoacoustic imaging," in *SPIE BiOS*, pp. 93231P–93231P, International Society for Optics and Photonics, 2015.

[134] J. Laufer, B. Cox, E. Zhang, and P. Beard, "Quantitative determination of chromophore concentrations from 2D photoacoustic images using a nonlinear model-based inversion scheme," *Applied Optics*, vol. 49, no. 8, pp. 1219–1233, 2010.

[135] A. Rosenthal, D. Razansky, and V. Ntziachristos, "Quantitative optoacoustic signal extraction using sparse signal representation," *Medical Imaging, IEEE Transactions on*, vol. 28, no. 12, pp. 1997–2006, 2009. Rosenthal, Amir Razansky, Daniel Ntziachristos, Vasilis IEEE Trans Med Imaging. 2009 Dec;28(12):1997-2006. Epub 2009 Jul 21.

[136] B. A. Rabinovich, Y. Ye, T. Etto, J. Q. Chen, H. I. Levitsky, W. W. Overwijk, L. J. Cooper, J. Gelovani, and P. Hwu, "Visualizing fewer than 10 mouse T cells with an enhanced firefly luciferase in immunocompetent mouse models of cancer," *Proceedings of the National Academy of Sciences*, vol. 105, no. 38, pp. 14342–14346, 2008.

[137] S. Tzoumas, N. Deliolanis, S. Morscher, and V. Ntziachristos, "Unmixing molecular agents from absorbing tissue in multispectral optoacoustic tomography," *Medical Imaging, IEEE Transactions on*, vol. 33, no. 1, pp. 48–60, 2014.

[138] S. Tzoumas, A. Nunes, N. C. Deliolanis, and V. Ntziachristos, "Effects of multispectral excitation on the sensitivity of molecular optoacoustic imaging," *Journal of Biophotonics*, vol. 8, no. 8, pp. 629–637, 2015.

[139] S. Tzoumas, A. Zaremba, U. Klemm, A. Nunes, K. Schaefer, and V. Ntziachristos, "Immune cell imaging using multi-spectral optoacoustic tomography," *Optics Letters*, vol. 39, no. 12, pp. 3523–3526, 2014.

[140] C. Lutzweiler, S. Tzoumas, A. Rosenthal, V. Ntziachristos, and D. Razansky, "High-throughput sparsity-based inversion scheme for optoacoustic tomography," *Medical Imaging, IEEE Transactions on*, 2015.

[141] S. Tzoumas, A. Kravtsiv, Y. Gao, A. Buehler, and V. Ntziachristos, "Statistical molecular target detection framework for multispectral optoacoustic tomography," *IEEE Transactions on Medical Imaging*, vol. 35, no. 12, pp. 2534–2545, 2016.

[142] S. Tzoumas, A. Nunes, I. Olefir, S. Stangl, P. Symvoulidis, S. Glasl, C. Bayer, G. Multhoff, and V. Ntziachristos, "Eigenspectra optoacoustic tomography achieves quantitative blood oxygenation imaging deep in tissues," *Nature communications*, vol. 7, 2016.

Appendix A

Publication: Unmixing molecular agents from absorbing tissue in multispectral optoacoustic tomography

The version herein has been published in the journal "IEEE Transactions on Medical Imaging" [137].

Unmixing Molecular Agents From Absorbing Tissue in Multispectral Optoacoustic Tomography

Stratis Tzoumas*, Nikolaos C. Deliolanis, Stefan Morscher, and Vasilis Ntziachristos*

***Abstract*—Detection of intrinsic or extrinsically administered chromophores and photo-absorbing nanoparticles has been achieved by multi-spectral optoacoustic tomography (MSOT). The detection sensitivity of MSOT depends not only on the signal to noise ratio considerations, as in conventional optoacoustic (photoacoustic) tomography implementations, but also on the ability to resolve the molecular targets of interest from the absorbing tissue background by means of spectral unmixing or sub-pixel detection methods. However, it is not known which unmixing methods are optimally suited for the characteristics of multispectral optoacoustic images. In this work we investigated the performance of different sub-pixel detection methods, typically used in remote sensing hyperspectral imaging, within the context of MSOT. A quantitative comparison of the different algorithmic approaches was carried out in an effort to identify methods that operate optimally under the particulars of molecular imaging applications. We find that statistical sub-pixel detection methods can demonstrate a unique detection performance with up to five times enhanced sensitivity as compared to linear unmixing approximations, under the condition that the optical agent of interest is sparsely present within the tissue volume, as common when using targeted agents and reporter genes.**

***Index Terms*—Molecular imaging, multispectral imaging, optoacoustic/photoacoustic tomography, spectral unmixing, sub-pixel target detection.**

I. Introduction

OPTOACOUSTIC tomography, also termed photoacoustic tomography, is a highly promising biological and medical imaging method capable of producing high resolution optical images of tissues. The ability to image oxygenated and deoxygenated hemoglobin and a variety of fluorochromes or photo-absorbing dyes and nanoparticles has been now well documented [1]–[8]. Optoacoustic imaging is performed by illuminating the object of interest with transient light intensity, which causes a thermo-elastic expansion of the absorbing moieties within the object and generates broad-band ultrasonic waves. These ultrasound waves can then be reconstructed into a 2-D or 3-D image using filtered back-projection algorithms [9] or model-based approaches [10], [11], the latter typically providing better quantification.

Of particular importance to biomedical research is the use of multispectral methods, capable of resolving different chromophores of biological importance [12]. Multispectral optoacoustic tomography [13] has been shown capable to visualize inflammation [14] and cancer targeting agents [15]–[17], genetically expressed proteins [12], [18]–[20] or photo-absorbing nanoparticles [21]–[24] at depths and resolutions that were not available previously to optical methods. MSOT involves the illumination of tissues with light at different wavelengths in the visible and near-infrared region of the spectrum, typically generating datasets, at three geometrical dimensions and along the spectral and time dimension, the latter demonstrated studying for example the dynamic fluorochrome bio-distribution *in vivo* [25].

Related to the work herein is the sensitivity and specificity achieved by different spectral processing methods to resolve intrinsic (expressed) and extrinsic (injected) chromophores and photo-absorbing nanoparticles from the absorbing tissue background. In particular, while it can be easily predicted that, given a number of wavelength observations, different spectral processing (spectral unmixing) methods will have different abilities to extract the bio-distribution of such chromophores, the particular performance of different approaches in the context of MSOT has not been yet studied. The term sensitivity refers here to the minimum amount of the absorbing agent necessary in order to be detectable using multispectral methods, while specificity refers to the minimization of false positives in this extraction procedure.

MSOT presents a rather unique spectral problem, whereby depth can alter perceived spectral features and complicate the unmixing problem. Optical fluence attenuation with depth introduces changes in the detected spectral responses of the absorbing chromophores in tissue, as compared to their spectral signatures measured in the photospectrometer. Moreover, since the optical agents of interest appear usually in a mixture with intrinsic tissue chromophores (e.g., blood), their spectral response will typically appear in a linear combination with background tissue spectral responses.

Manuscript received July 24, 2013; accepted August 19, 2013. Date of publication August 29, 2013; date of current version December 27, 2013. The work of S. Tzoumas was supported by the DFG GRK 1371 grant. The work of V. Ntziachristos was supported by the European Research Council through the Advanced Investigator Award and the European Union project FAMOS (FP7 ICT, Contract 317744). *Asterisk indicates corresponding author.*

*S. Tzoumas is with the Institute for Biological and Medical Imaging (IBMI), and Chair for Biological Imaging, Technische Universität München and Helmholtz Zentrum München, 85764 Neuherberg, Germany (e-mail: stratis.tzoumas@helmholtz-muenchen.de).

N. C. Deliolanis was with the Institute for Biological and Medical Imaging (IBMI), Technische Universität München and Helmholtz Zentrum München, 85764 Neuherberg, Germany. He is now with the Fraunhofer Project Group for Automation in Medicine and Biotechnology, 1-2 Theodor-Kutzer-Ufer, 68167, Mannheim, Germany (e-mail: ndeliolanis@yahoo.com).

S. Morscher is with iThera Medical GmbH, Ingolstädter Landstrasse 1, 85764, Neuherberg, Germany, and also with the Institute for Biological and Medical Imaging (IBMI), Technische Universität München and Helmholtz Zentrum München, 85764 Neuherberg, Germany (e-mail: stefan.morscher@ithera-medical.com).

*V. Ntziachristos is with the Institute for Biological and Medical Imaging (IBMI), and Chair for Biological Imaging, Technische Universität München and Helmholtz Zentrum München, 85764 Neuherberg, Germany (e-mail: v.ntziachristos@tum.de).

Digital Object Identifier 10.1109/TMI.2013.2279994

The problem of separating all intrinsic and extrinsic tissue chromophores in the context of quantitative optoacoustic spectroscopy has been previously formulated as a complex nonlinear inversion (or nonlinear image reconstruction) problem [26]–[28]. Nonlinear inversion approaches based on light propagation models have been considered for quantitatively separating all distinct chromophores within tissue [26], [29]–[31]. However, due to the high dimensionality, complexity, and ill-posed nature of the inversion problem, such methods are being so far mainly restricted to simple phantoms, or tissue cases with very simple structure. In the case of experimental tissue imaging, a variety of spectral processing methods spanning, from simple image subtraction at two different wavelengths [2], intraclass correlation [3], and linear least squares fitting using dictionary based spectra of tissue absorption [12], [15], [17], [19], to more sophisticated, blind-source separation algorithms such as independent component analysis (ICA) [32] have been reported. ICA has been found to perform better than linear least squares fitting [33] for the extraction of extrinsic optical absorbers. Limitations have been also identified however. Blind approaches produce a number of components that need to be visually inspected by an expert to select the most relevant one based on experience and prior knowledge, an approach that may introduce uncertainty. An additional complication is that such methods cannot possibly provide confidence limits on the result produced for detection with high specificity.

The aim of this paper was to investigate different algorithmic approaches for the detection of molecular agents in the context of MSOT, provide an accurate framework for the evaluation of their performance under different conditions, and identify optimal directions for tissue imaging. In Section II, the problem is theoretically described and formulated and the key concepts and major challenges of the MSOT-related spectral unmixing are introduced (Section II-A). Additionally, a short review of the state-of-the-art optical target detection algorithms developed and used in remote sensing hyperspectral imaging is presented (Section II-B), considering structured, statistical and blind unmixing approaches. In the methodology (Section III), simulations are initially performed to estimate the magnitude of the MSOT-related spectral uncertainty expected in tissue measurements (Section III-B). To tackle the challenge of a quantitative evaluation, an extensive synthetic dataset is compiled (Section III-C1) that is based on experimental MSOT measurements, and the study is further supported using two experimentally collected datasets (Section III-C2) with known ground-truth. A comparison of the different detection approaches is presented for both datasets in terms of sensitivity (Sections IV-B, IV-C, IV-D) as well as specificity (Section IV-E), while the concluding remarks on algorithmic performance, optimal choices and future research directions are presented in Section V.

II. Background

The following section initially provides theoretical background and discusses practical considerations regarding the MSOT related unmixing problem (Section II-A). Moreover, it introduces the main categories of optical target detection algorithms developed and applied in remote sensing hyperspectral imaging (Section II-B), discussing their properties and their potential application in the case of MSOT.

A. Formulation of the Unmixing Problem in MSOT

1) Mixed Pixel and Spectral Unmixing: The contrast of MSOT imaging is due to photo-absorbing moieties that can be intrinsic to tissue, for example hemoglobin or expressed molecules (e.g., fluorescent proteins) or extrinsically administered such as fluorescent agents or nanoparticles. Despite the generally high resolution of MSOT imaging, this is typically not high enough to resolve substances in a molecular level. For this reason, each MSOT pixel (voxel), corresponds usually to more than one photo-absorber and has a spectral response that is a linear combination of the spectral responses of all these absorbers. Due to this per pixel spectral mix, we will refer to the MSOT pixel as a "mixed pixel," and the molecular targets of interest as "sub-pixel" targets. Since the targets typically lie in a sub-pixel level, only spectral unmixing related methods can produce robust solutions for this problem.

Spectral unmixing is then a process of estimating the discrete material components with distinctive spectral signatures from multispectral measurements [34]. The most popular mixing model is the linear mixture model (LMM), which assumes that the measured spectrum is a linear combination of a number of distinctive spectral signatures

$$\mathbf{x} = \mathbf{SA} + \mathbf{n} \tag{1}$$

whereby $\mathbf{x}$ is a $M \times N$ matrix, with M being the number of wavelengths and N the image dimensionality (number of pixels), representing the multispectral measurements. $\mathbf{S}$ is a $M \times K$ matrix, with K representing the number of distinct components, containing the distinct spectral responses of the different materials, also called end-members. $\mathbf{A}$ is the $K \times N$ unknown matrix containing the amount of each distinct material in the mixed pixel, also called the abundances. Finally, $\mathbf{n}$ is the noise associated with the measurements or the model error.

2) Uncertainty in the Spectral Responses of the Absorbers: The most prominent tissue optical absorbers are oxygenated and deoxygenated hemoglobin, nevertheless water, lipids, melanin and various other metabolites and structural elements can also have an influence on the measurements. The unique spectral signatures of such elements are generally known. However, MSOT can achieve high-resolution deep tissue imaging and, in this case, the individual spectral responses of various photo-absorbers measured by MSOT are expected to change due to the wavelength-dependent light propagation in tissue, a phenomenon that is also referred to as "spectral coloring" [28]. As light propagates from shallow to deep tissue it is absorbed by the tissue intrinsic chromophores. This absorption is dependent on the wavelength, which means that different wavelengths of optical excitation attenuate differently with depth. In other terms, if the optical fluence incident on tissue surface has a flat (uniform) spectral distribution, the spectral profile of photons reaching different positions at different depths would be nonuniform with the nonuniformity increasing generally with depth. Since each absorber in deep tissue is

illuminated by an unknown, nonuniform spectral profile of optical fluence incident, its corresponding spectral response will deviate also from its original spectral signature. This phenomenon of "spectral coloring" has been observed in multispectral optoacoustic measurements and discussed in literature [28], [35]. For a mathematical formulation of this phenomenon, let us assume a position $\mathbf{r}$ within tissue. Then, the absorption spectrum, $M_{(\mathbf{r})}(w)$ measured by MSOT, would be proportional to a nonlinear mixture model of the local absorbers, as described in

$$M_{(\mathbf{r})}(w) \sim U_{(\mathbf{r})}(w) \sum_i a_i(\mathbf{r}) S_i(w). \tag{2}$$

In (2), w denotes the wavelength and $U_{(\mathbf{r})}(w)$ is the spatially varying function of optical fluence with respect to wavelength. $\mathbf{S}_i$ is the spectral signature (also termed end-member) of the absorbing component i ($S_i(w) = \varepsilon_{\mathrm{i}}(w)/\|\varepsilon_{\mathrm{i}}\|_\infty$, where $\varepsilon_{\mathrm{i}}(w)$ is the wavelength dependent molar extinction coefficient of the material). Finally, $\alpha_{\mathrm{i}}(\mathbf{r})$ indicates the amount (also termed abundance) of the absorbing component i present at a position $\mathbf{r}$ ($\alpha_{\mathrm{i}}(\mathbf{r}) \sim \|\boldsymbol{\varepsilon}_{\mathrm{i}}\|_\infty \, \mathrm{c}_{\mathrm{i}}(\mathbf{r})$, where $\mathrm{c}_{\mathrm{i}}(\mathbf{r})$ is the molar concentration of the component i at position $\mathbf{r}$). Several heuristic methods have been proposed in order to estimate $U_{(\mathbf{r})}$directly from optoacoustic images [36], [37], whereas other methods attempt to estimate simultaneously $U_{(\mathbf{r})}(W)$ and $\alpha_{\mathrm{i}}(\mathbf{r})$ using a light propagation model and solving the nonlinear inversion problem [29], [30], [38]. Due to nonuniqueness and the ill-posed nature of the optical fluence problem, as well as uncertainties associated with estimating the optical properties of tissue, such heuristic and model based approaches may not be sufficiently robust in tissue measurements with high heterogeneity and structural complexity.

In addition to the "spectral coloring" phenomenon that is introduced due to optical fluence attenuation, inexact solutions of the acoustic inversion problem, exemplified in limited-view setups, and optoacoustic signal distortions, may superimpose negative values in parts of the image [39], and thus negative spectra. Such negative values are common in optoacoustic reconstructions, and, although lacking physical meaning, they may still contain valuable structural and spectral information regarding the presence of a molecular target. Moreover, the possible influence of additional, unaccounted for, tissue absorbers, the electronic noise and laser power fluctuations, typically present in experimental measurements, further complicate the spectral unmixing problem. All these challenges typically encountered in biological tissue images lead in the following to the consideration of statistical methods for addressing the unmixing problem.

3) Intensity Modulations With Depth: An additional complication induced due to optical fluence attenuation, besides spectral coloring, is the attenuation of the MSOT signal intensity in different pixels across the image, as a function of depth and optical properties. In ideal reconstructions, the intensity of optoacoustic images is expected to drop rapidly with tissue depth. However in practice the image intensity also depends on a number of additional parameters, like the instrumentation and the frequencies utilized by the imaging system, the focal area and sensitivity field of the ultrasound sensors, the frequency dependent ultrasound attenuation, as well as the reconstruction algorithm used for image formation. This observation also directed herein the consideration of unmixing algorithms that operate in a scale invariant manner, so as to avoid algorithmic bias towards high intensity image areas.

B. Optical Target Detection Algorithms

In contrast to the typical linear and nonlinear spectral unmixing methods, which attempt to resolve all the spectrally distinct components present in the image, sub-pixel detection algorithms [40], [41] focus only on the detection of a distinct spectral target. In this manner they ignore and suppress other absorption contributions considered as background clutter, offering more flexibility in modeling the background also as a multivariate statistical distribution. Sub-pixel detection algorithms are usually classified into three different categories according the *a priori* knowledge they assume regarding the target and background end-members. Representative algorithms of each category are presented here.

1) Known End-Members: Under this category lie algorithms that require full prior knowledge of the spectra of the target as well as the background. A popular algorithm in this category is the orthogonal subspace projection (OSP) [42], that is given by the following equation:

$$\boldsymbol{\alpha} = \frac{\mathbf{S}^T \mathbf{P}_B^{\perp} \mathbf{x}}{\mathbf{S}^T \mathbf{P}_B^{\perp} \mathbf{S}} \tag{3}$$

whereby $\boldsymbol{\alpha}$ is the $1 \times N$ estimated abundance of the target of interest in each image pixel; $\mathbf{S}$ is a $M \times 1$ vector containing the target spectrum; $\mathbf{P}_{\mathbf{B}}^{\perp} = \mathbf{I} - \mathbf{B}\mathbf{B}^{\#}$, where $\mathbf{I}$ is the $M \times M$ identity matrix, $\mathbf{B}$ is the $M \times K$ matrix containing the spectra forming the background, and $\mathbf{B}^{\#} = (\mathbf{B}^{\mathrm{T}}\mathbf{B})^{-1}\mathbf{B}^{\mathrm{T}}$ is the $K \times M$ pseudo-inverse of the matrix $\mathbf{B}$. The purpose of $\mathbf{P}_{\mathbf{B}}^{\perp}$ operator is to remove from the measurements $\mathbf{x}$ the part that belongs to the background. In the application of the OSP to MSOT images, the matrix $\mathbf{S}$ contains the spectral response of the optical absorber of interest, retrieved from literature or from individual measurements, and the background end-member matrix $\mathbf{B}$ includes the spectra that are assumed to form the tissue background. We note that the detection performance of the orthogonal subspace projection is equivalent to the one of linear least squares fitting.

2) Uncertainty in Background End-Members: In applications where the background end-members come with uncertainty, it is preferred that the background is not modeled using distinct spectra, but as a statistical distribution. Multivariate normal distributions are usually employed for such modeling. Although the assumption that the spectral background follows a normal distribution is not always accurate, Gaussian modeling usually exhibits good performance in many implementations. Methods in this category initiated from the detector of Kelly [43] that is derived using the generalized likelihood ratio (GLR) approach. The most famous adaptations of this detector are the adaptive matched filter (AMF) [44] and the scale invariant adaptive cosine estimator (ACE) [45], that have both found great application for optical target detection problems in remote sensing hyper-spectral imaging [40].

The AMF is defined by

$$\mathrm{D}(\mathbf{x}'_{\mathbf{r}}) = \frac{(\mathbf{S}^T\mathbf{G}^{-1}\mathbf{x}'_{\mathbf{r}})^2}{N(\mathbf{S}^T\mathbf{G}^{-1}\mathbf{S})} \tag{4}$$

whereby $\mathbf{x}'_{\mathbf{r}}$ is the $M \times 1$ vector corresponding to a specific pixel (at position $\mathbf{r}$) of the original multispectral data $(\mathbf{x})$ after subtracting the mean from each spectral dimension $(\mathbf{x}')$, $\mathbf{G}^{-1}$ is the inverse $M \times M$ covariance matrix of the demeaned background, $\mathbf{S}$ is the $M \times 1$ spectrum of the target agent and N is the number of background pixels used for the estimation of the covariance matrix $\mathbf{G}$. If the value of the scalar test statistic $\mathrm{D}(\mathbf{x}'_{\mathbf{r}})$ is larger than a defined threshold, the specific pixel at position $\mathbf{r}$ is recognized as a positive target.

Under the assumption that the targets appear with low probability in the image, all available demeaned multispectral data $\mathbf{x}'$ (N pixels) can be used to estimate the covariance of the background $(\mathbf{G})$ with maximum likelihood. From an MSOT application perspective, the assumption of low target probability restricts the use of the AMF to cases where the target agent is confined (e.g., tumor targeting with probes or reporter genes) but it would fail to give accurate results in cases where the optical agent is distributed throughout tissue, as for example in the case of agents that remain for long in the blood circulation or in the background tissue. In such cases, a multispectral measurement of the background can be retrieved before injection, in order to compute the background covariance matrix $(\mathbf{G})$ and use it in the formula of AMF for successful performance.

A rather intuitive, alternative to the GLR [43], [44], interpretation of the function of the AMF is through the sphering transformation that it performs. The sphering or whitening transformation is performed by subtracting the mean from the multispectral data $\mathbf{x}$, and multiplying them with the operator $\mathbf{G}^{-1/2}$. The effect of the sphering transformation is crucial since it suppresses the dominant spectral background contributions, enhancing the spectral outliers. After the sphering transformation, the image is projected in the direction of the transformed target spectrum $(\mathbf{S}^{\mathrm{T}}\mathbf{G}^{-1/2})$.

The AMF makes the assumption that the local background in each tested area of the image has the same covariance $\mathbf{G}$ with the one that has been calculated from all image pixels. This assumption is not always very accurate, especially in images that demonstrate significant intensity variations like the multispectral optoacoustic images. The adaptive cosine estimator [45] is the scale invariant alternative to AMF, and is given by (5). As it has been discussed in (Section II-A), scale invariance is a key property for the MSOT case

$$\mathrm{D}(\mathbf{x}'_{\mathbf{r}}) = \frac{(\mathbf{S}^T\mathbf{G}^{-1}\mathbf{x}'_{\mathbf{r}})^2}{(\mathbf{S}^T\mathbf{G}^{-1}\mathbf{S})\mathbf{x}'^T_{\mathbf{r}}\mathbf{G}^{-1}\mathbf{x}'_{\mathbf{r}}}. \tag{5}$$

Both AMF and ACE share a constant false alarm rate (CFAR) property [44]. The CFAR property allows the detection value to be invariant of the background scaling, thus a globalized detection threshold can be defined and applied independently of the detection scenario. This would enable the definition of confidence limits for such algorithms in the detection procedure, making them more appropriate for biomedical imaging studies.

3) Unknown End-Members—Anomaly Detection: Anomaly detection [46] is typically employed when there is no prior knowledge either on the spectrum of interest or on the background spectra. In this case, the background is modeled in a statistical sense and the possible targets ("anomalies") are recognized as the spectral outliers, namely pixels that exhibit significantly different spectrum from their local background. The detection of such outliers is usually performed by measuring the Mahalanobis distance [46] of each pixel from the center of the background distribution, or by maximizing or minimizing higher order statistics by means of projection pursuit [47] or by using the ICA [48].

Such blind approaches incorporate uncertainty in their performance and may not offer optimal characteristics for biomedical applications. However, since the ICA algorithm has showcased good performance in the extraction of molecular agents [32], [33], we included a version of the ICA algorithm in the evaluation presented in the next sections. ICA also employs a sphering transformation as a preprocessing stage, including all the associated advantages (background suppression and enhancement of spectral outliers) and limitations (assumption of low probability targets). Instead of a direct projection on a known spectrum though, it iteratively maximizes non-Gaussianity using higher order statistics, such as kurtosis, for the extraction of independent components and their corresponding spectral responses. In MSOT applications, one of these independent components corresponds usually to the optical agent of interest and is identified as the component with a spectral response that is visually "similar" to the one of the photo-absorber of interest.

III. Methods

A. Algorithm Implementation and Application in the Context of MSOT

The OSP, AMF, and ACE algorithms are implemented in MATLAB according to the equations of paragraph (Section II-B). The background spectra $(\mathbf{B})$, in the case of OSP, and the spectrum of interest $(\mathbf{S})$ are taken from literature and interpolated to the wavelengths used in the specific imaging case. Assuming that hemoglobin is the major tissue absorber, the spectra of Hb and HbO_2 are used in OSP to model the background, ignoring any spectral coloring phenomena discussed in (Section II-A2). A flat spectrum is additionally included for background modeling, as it has been experimentally found to increase the unmixing performance in MSOT measurements [17]. Finally, in the case of AMF and ACE all available pixels of the multispectral images are used for the calculation of the background covariance matrix $\mathbf{G}$.

Since ICA demands a step of manual component selection it cannot be included as such in an automated evaluation process. In an effort to make ICA more robust and automatic, we search for a single independent component, while constraining the resulting spectrum to lie "close" to the theoretically expected one. This constrain can be employed in the context of semi-blind ICA framework proposed and explained in [49] which was implemented using the FastICA [50] algorithm. The optimization procedure of ICA is adapted so that the resulting spectrum resembles the *a priori* known target spectrum, with respect to a correlation tolerance. Such a correlation tolerance can vary from 0 to 1, with 0 promoting purely statistical independence and 1

indicating complete spectrum constrain. In this way the application of ICA may become automatic and the step of component selection is eliminated. We note that when the correlation tolerance is 1, semi-blind ICA is theoretically equivalent to the adaptive matched filter without though the CFAR property. In the following we experiment with varying values for the correlation tolerance, to explore possible advantages of statistical independence against pure spectral priors.

B. Simulation of Photon Propagation and "Spectral Coloring" in Deep Tissue

To gain estimates on the spectral coloring phenomenon (Section II-A2) expected in tissues, we employed numerical simulations of light propagation in a tissue-mimicking model. The simulations were based on a 2-D finite element solution of the diffusion equation [51], which is typically used to model light propagation in turbid media [52]. We assumed a uniform hemoglobin distribution at a constant oxygen saturation level for background tissue modeling, and a geometry of a circular tissue slice with a radius of 1 cm. In such ideal conditions, the wavelength-dependent photon fluence $U_{(\mathrm{d})}(w)$ can be calculated as a function of depth, d. An estimation of the deep-tissue "colored" versions $(S_{\mathrm{col}}(w))$ of the original end-members $(S(w))$ of various chromophores, was calculated through a multiplication with the estimated photon fluence $(S_{\mathrm{col}}(w) = U_{(\mathrm{d})}(w)S(w))$. The background tissue spectral curves were normalized so that the absorption coefficient at the isosbestic point of 800 nm was kept constant at $\mu_\alpha = 0.3$ cm^{-1}, whereas the reduced scattering coefficient was also considered constant at $\mu_{\mathrm{s}}' = 15\ \mathrm{cm}^{-1}$. These values were selected as representatives to realistic optical properties of tissue in the near infrared [51]. The results of the simulation are presented in (Section IV-A), while the light propagation model itself is used in (Section III-C1) for the production of a close-to-reality synthetic MSOT dataset.

C. Synthetic and Experimentally Collected MSOT Datasets

To overcome the challenge of accurate and quantitative evaluation of the different algorithmic approaches, we have compiled close-to-reality synthetic datasets (Section III-C1), based on experimental MSOT images of animals. Moreover, *ex vivo* and *in vivo* (Section III-C2) datasets have been collected, where ground-truth on the approximate position of the molecular target of interest was available.

All optoacoustic images used in this study were acquired using an experimental multispectral optoacoustic system [13], [53]. The system utilizes an ultrasound array of 64 elements covering a limited angle view of 172°. The ultrasound array is focused in a 2-D plane, resulting in an in-plane resolution of 150 μm and an elevational resolution of approximately 800 μm. The ultrasound sensors have a central frequency of $\sim$5 MHz with -6 dB bandwidth of $>50\%$ and an approximate sensitivity of $\sim$18 μV/Pa. For laser excitation, a tunable optical parametric oscillator laser is employed delivering pulses ($<$10 ns) at 10 Hz repetition rate. Tissue illumination is achieved through a number of fiber bundles deployed appropriately to create a uniform illumination ring of $\sim$7 mm width on the surface of the animal, which is exposed to a maximal fluence of $\sim$20 mJ$\cdot$cm^{-2} at 750 nm. Since the laser power varies between wavelengths and individual pulses, the per-pulse energy of the laser is measured using a laser diode in order to appropriately scale the signals before image reconstruction.

1) Synthetic Datasets, Based on Experimental MSOT Images: In order to create a close-to-reality validation dataset with exact knowledge of the position, boundaries and relative absorption of a molecular target of interest, the concept of target implantation [54] was employed and adapted to the MSOT case. Four synthetic datasets corresponding to two different tissue backgrounds and two different molecular targets were formed in this manner as explained analytically below.

Two different multispectral images were acquired from the regions of the brain and the kidneys of a nude mouse [Fig. 1(a)], at 20 uniformly sampled wavelengths from 700 nm to 890 nm with a step of 10 nm. Before image reconstruction, signals are subject to denoising, performed by a 100-times repetitive signal acquisition and averaging, and band-pass filtering within the bandwidth of the ultrasound sensors. The resulting signals corresponded to a measured peak SNR of $\sim$35 dB. Image reconstruction was performed using a model-based inversion approach [10], [11] and Tikhonov regularization during the inversion procedure for reducing reconstruction artifacts due to limited angle view. The two resulting multispectral optoacoustic images, serve as the tissue background $\mathrm{B}_{(\mathrm{x,y})}(W)$ on which molecular targets are artificially implanted.

After image reconstruction, the tissue area is manually segmented and a finite element solution of the diffusion approximation is computed, based on this geometry, to simulate the optical fluence for different wavelengths. Uniform optical properties of $\mu_\alpha = 0.3\ \mathrm{cm}^{-1}$ and $\mu_{\mathrm{s}}' = 15\ \mathrm{cm}^{-1}$ at 800 nm were assumed, and a uniform background oxygenation of 70% [Fig. 1(b)].

On each of the multispectral backgrounds $\mathrm{B}_{(\mathrm{x,y})}(W)$ corresponding to brain and kidneys, molecular targets with the spectral specifications of Indocyanine Green (ICG) and IntegriSense750 were locally added creating thus four distinct datasets, each corresponding to a specific background-agent scenario (namely Brain with ICG, Brain with IntegriSense750, Kidneys with ICG, and Kidneys with IntegriSense750). Each one of these datasets consists of six image instances where the target agent has been implanted at different randomly selected regions of interest (ROI) within the tissue area. Such regions (ROIs) were set to be small disks of 4-pixel radius [Fig. 1(c)] simulating small orthotopic tumors within tissue. According to the position of the implanted molecular target $(\mathrm{x_c}, \mathrm{y_c})$, and the wavelength-dependent optical fluence simulations $U_{(\mathbf{r})}(w)$, the colored spectrum of the agent $\mathrm{S}_{\mathrm{col}}$ was calculated according to (6) [Fig. 1(d)]

$$S_{\mathrm{col}}(w) = \frac{U_{(x_c,y_c)}(w)}{\left\|\mathbf{U}_{(x_c,y_c)}\right\|_2} \frac{S(w)}{\|\mathbf{S}\|_\infty}. \tag{6}$$

The resulting colored spectrum $\mathbf{S}_{\mathrm{col}}$ is in the following appropriately scaled according to the relative position of the molecular agent in tissue and the optical fluence model assumed. This is achieved by multiplying the spectrum with the norm of optical fluence across the wavelengths for the specific position, $\|\mathbf{U}_{(\mathrm{x_c,y_c})}\|_2$. An additional scaling factor $(\mathrm{C_{cal}})$ aims to match the spectrum with the background scaling, accounting

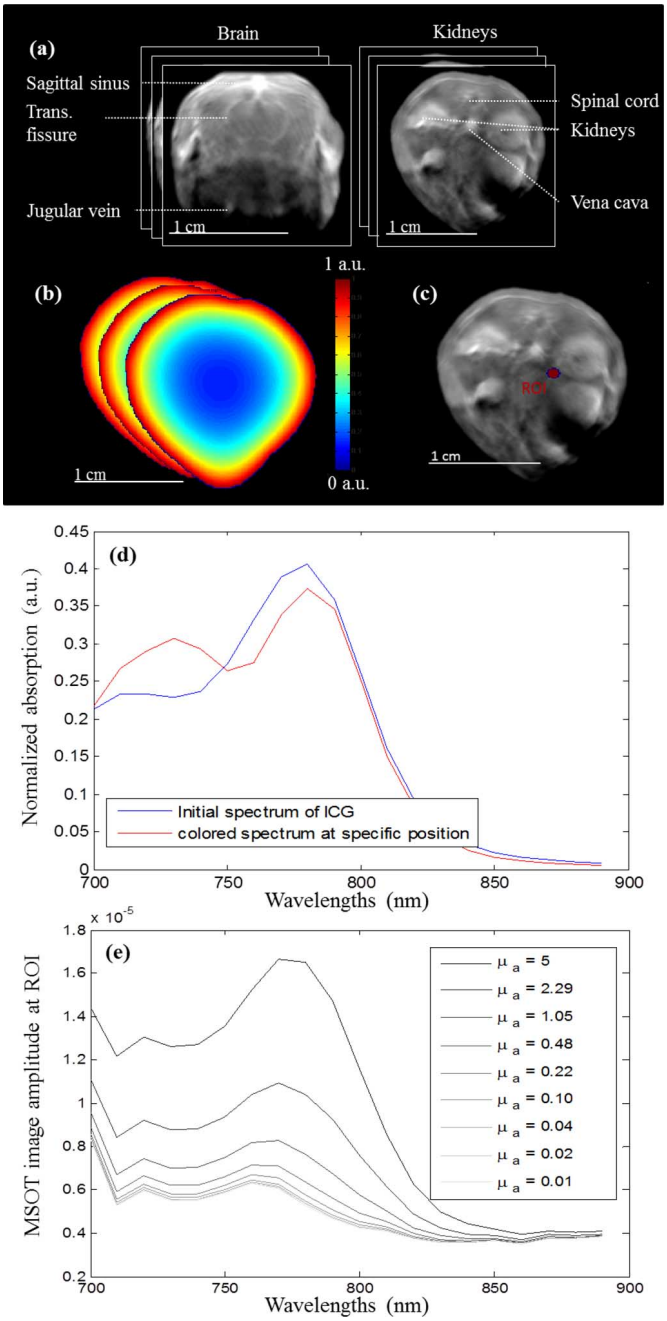

Fig. 1. Creation of a synthetic MSOT dataset. (a) Acquisition of multispectral backgrounds from real measurements. (b) Segmentation of tissue area and application of a diffusion approximation light propagation model. (c) Selection of a ROI for the implantation of a molecular target. (d) Calculation of target spectral coloring according to its position in tissue. (e) Impact of the agent on the spectral background for different simulated agent concentrations corresponding to a peak absorption coefficient from 5 cm^{-1} to 0.01 cm^{-1}.

for a number of system absolute values such as the system scaling, the transducer sensitivity, the absolute illumination and the Grüneisen parameter that is hereby assumed constant. The calibration factor $\mathrm{C_{cal}}$ is computed after comparing the optoacoustic image of a phantom with known optical properties with its theoretically expected absorption as predicted by its optical properties and the optical fluence model assumed. More specifically the phantom consists of a cylindrical (2 cm diameter) scattering medium (1% solution of intralipid), with a cylindrical india ink insertion in the middle (3 mm diameter) with an absorption coefficient of $\mu_\alpha = 0.23$ cm^{-1} at 700 nm, as measured using a photospectrometer.

In a final step, for each image instance, different levels of absorption are simulated for the target agent by superimposing the appropriately scaled spectrum $(\mathrm{C_{cal}}\|\mathbf{U}_{(\mathrm{x_c,y_c})}\|_2\mathbf{S}_{\mathrm{col}})$ in the region of interest, multiplied with 25 logarithmically decreasing simulated absorption coefficients $\mu_\alpha^{\mathrm{sim}}$ [as in (7)] spanning from 5 to 0.01 cm^{-1} [Fig. 1(e)]. The simulated absorption coefficient values $\mu_\alpha^{\mathrm{sim}}$ correspond to the peak absorption of the target agent. In this manner close-to-reality synthetic MSOT images $(\mathrm{I}_{(\mathrm{x,y})}(w))$ are formed that contain a component of an extrinsic optical agent at a known region, and with gradually decreasing simulated levels of absorption. A pipeline describing the creation of such a dataset is visualized in Fig. 1

$$I_{(x,y)}(w) = \begin{cases} B_{(x,y)}(w), & (x,y) \notin \mathrm{ROI} \\ B_{(x,y)}(w) + C_{\mathrm{cal}} \left\|\mathbf{U}_{(x_c,y_c)}\right\|_2 \mu_\alpha^{\mathrm{sim}} S_{\mathrm{col}}(w), & (x,y) \in \mathrm{ROI} \end{cases}. \tag{7}$$

The main advantage of the technique described above is that it creates multispectral images where the exact knowledge of the position and area covered by the target component is available, while including all challenges encountered in experimental *in vivo* measurements. Moreover it enables the compilation of an unlimited dataset of different agent and background scenarios, with gradually decreasing agent "concentrations." We hereby note that the simulated absolute values of absorption $(\mu_\alpha^{\mathrm{sim}})$ of the target agent are subject to a number of assumptions (tissue optical properties, constant Grüneisen parameter) and additional system effects (i.e., spatial and acoustoelectric impulse response) not considered here. However, it is only the relevant values that are of interest in the context of this study for the comparative evaluation of the algorithmic performance, that is demonstrated in (Section IV-B).

The detection performance of the different algorithmic approaches may depend on a number of experimental and system parameters that affect the ability of unmixing algorithms to successfully model the target and background spectral variability. Such parameters include the levels of electronic noise (that relate to the detectors' sensitivity and optical fluence), the spectral band of illumination (wavelength sampling) and the laser power fluctuations with wavelength.

For investigating the algorithmic performance under different noise levels, random Gaussian noise, independent and of the same standard deviation across all projections and wavelengths, was artificially superimposed to the initial signals of the Brain and Kidneys background before image reconstruction. In this manner, five additional datasets were formed, corresponding to peak SNR levels in the signal domain, from 20 to 34 dB. For testing the algorithmic performance with respect to the number of excitation wavelengths utilized, the initial multispectral dataset, corresponding to 20 wavelengths, is subsampled in order to create six additional datasets corresponding to a varying number of uniformly sampled wavelengths, from 16 to 5. Finally, for investigating the effect of laser power fluctuation on the algorithmic performance, the multispectral images are

multiplied with a random vector of mean 1 and a standard deviation varying from 0.01 to 0.1. The effect of such system parameters in the algorithmic performance is demonstrated in (Section IV-C).

2) Ex Vivo and In Vivo Experimental Data: An *ex vivo* dataset collected for evaluation purposes consists of MSOT measurements obtained from euthanized nude mice ($n = 3$). In two of these mice the esophagus was filled with Cy7 fluorochrome with peak absorption coefficient of 4.6 cm^{-1} and 2.3 cm^{-1}. In the third mouse, a capillary tube has been inserted through the esophagus and filled with Cy7 at varying levels of peak absorption, namely 14.7 cm^{-1}, 7.4 cm^{-1}, and 3.7 cm^{-1}. Imaging was performed in the lower neck region at 30 wavelengths from 690 nm to 835 nm with a step size of 5 nm. Signal denoising was performed by averaging a hundred signal repetitions and the images were reconstructed using model-based inversion.

In vivo measurements were obtained from nude mice ($n = 4$) with orthotopically implanted brain tumors, genetically expressing a fluorescent protein (FP). The tumors were implanted at different depths in the brain and their positions were located with *post mortem* cryoslicing fluorescent imaging [55]. MSOT, performed *in vivo*, obtained 21 sequential slices per mouse at a step of 1 mm across the entire mouse brain, covering the entire mouse brain. The wavelengths used for this application are from 690 nm to 720 nm with a step of 5 nm plus 730 nm, 750 nm, 770 nm, 800 nm, and 830 nm. Signal denoising was performed by averaging 20 signal repetitions, and the images were reconstructed using model-based inversion.

D. Evaluation Consideration

1) Evaluation in Terms of Sensitivity: In order to compare the different detection approaches in terms of sensitivity, a metric defining whether a target is visible or not needs to be applied. We assumed that a target was visible if it could be distinguished from the background, and no considerable false positives were involved. False positives were defined as the background pixels with detection values that were larger than the mean detection value of pixels corresponding to the actual signal. In this respect, we can define a target as visible if it satisfies the following inequality:

$$\sum_{(x,y)\in D_t} D_{(x,y)} > \sum_{(x,y)\in D_b \wedge D(x,y)>\bar{T}} D_{(x,y)} \qquad (8)$$

where D is the image returned by the detection algorithm, D_t is the image region that corresponds to the component of interest, D_b the region corresponding to the background and $\overline{T}$ is the mean detection value of the target pixels. This detection metric enables a quantitative comparison of the sensitivity limits of different algorithmic approaches (Section IV-B) on the synthetic dataset (Section III-C1). Since each imaging instance of the synthetic dataset includes a target implanted in gradually decreasing simulated levels of (peak) absorption coefficient from $\mu_\alpha^{\text{sim}} = 5$ cm^{-1} to $\mu_\alpha^{\text{sim}} = 0.01$ cm^{-1}, the sensitivity limit for an unmixing algorithm on the specific imaging instance can be defined as the lowest agent absorption level where the implanted target is successfully detected according to metric (8).

In the cases of *ex vivo* and *in vivo* datasets, since the exact position and area of the component of interest cannot be possibly extracted with accuracy, no quantitative evaluation is ventured. The detected components overlaid on the original optoacoustic images are presented instead, for a qualitative visual comparison (Section IV-C).

2) Evaluation in Terms of Specificity: A detector can be considered to operate with high specificity if it has a negligible false alarm rate. When a detector has a constant false alarm rate (CFAR) property (Section II-B2), the detection value is relatively immune to background structure and scaling, thus a globalized detection threshold associated with some specific false alarm rate can be defined and applied independent of the imaging scenario. This possibility bears a major significance from an application perspective, since it would enable utilizing MSOT imaging in biological studies with high specificity, and without any need of prior knowledge on the expected result or validation using other imaging modalities.

By applying the adaptive matched filter and the adaptive cosine estimator to the artificial dataset (Section III-C1), we are able to define a threshold for high confidence detection, that allows a minimum amount of 0.03% false positives on it (less than 12 pixels for a 200×200 image). This threshold is not applied in the evaluation for reasons of consistency with the OSP and the semi-blind ICA, but its application is presented in (Section IV-E).

IV. Results

A. Spectral Coloring in Deep Tissue Calculated From Optical Fluence Simulations

Herein the results of the light-propagation simulations of (Section III-B) that estimate the optical flux related "spectral coloring" are presented. Fig. 2(a) and (b) presents the depth-profile of optical fluence for a number of different wavelengths, for the case of a background oxygenation of 30% and 90%, respectively. Fluence ratios for different wavelengths are provided for 1 cm depth under the figures, indicating great discrepancies among different wavelengths. Fig. 2(c)–(f) demonstrates the effect of the wavelength dependent optical fluence in the measured spectra. The figure presents the normalized colored versions of the spectral signatures of intrinsic tissue absorbers (HbO_2, Hb) and molecular agents (Cy7) under varying background tissue conditions. The green curves correspond to the initial spectral signatures of the absorbers, the red curves to the expected coloring in 1 cm depth, and the black areas to intermediate cases. All curves are normalized to disregard any scaling involved and highlight the changes in the shape of the spectra. The spectral coloring is computed after multiplying the original spectral signature with the optical flux $U_{(\mathbf{r})}(w)$, calculated from the simulations in (Section III-B). Since hemoglobin can be found in varying oxygenation levels in different regions of biological tissue, a wide spectrum of uniform background oxygenations is being considered by the simulations. Fig. 2 presents spectral coloring examples

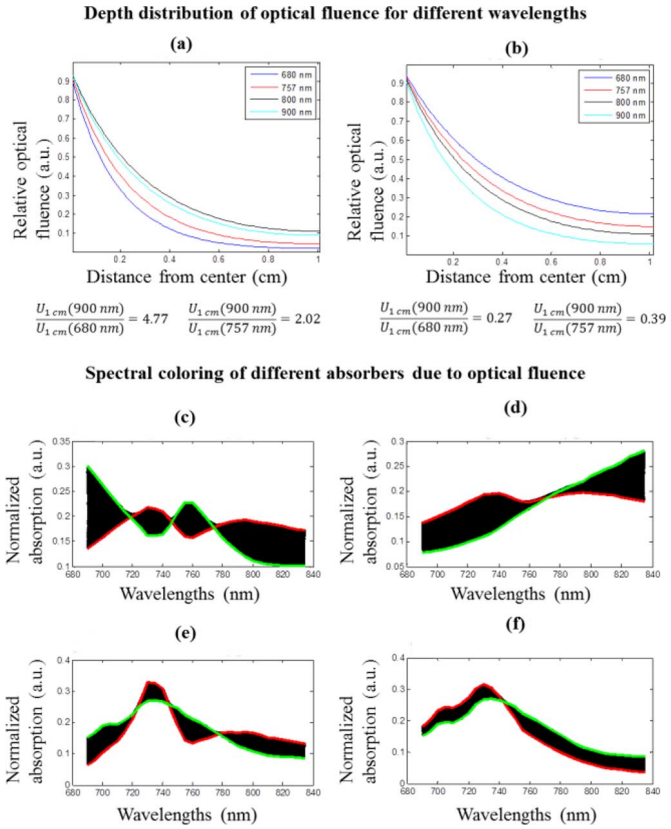

Fig. 2. Spectral coloring of optical absorbers in deep tissue. (a), (b) Profile of optical fluence with depth for a number of important wavelengths, for two different background oxygenation levels (30% and 90%, respectively). (c)–(f) Estimated spectral coloring due to the wavelength dependent optical attenuation for HbO2, Hb, and Cy7, respectively, for background oxygenations of 30% [(c), (e)] and 90% [(d), (f)]. The green curve corresponds to the original spectrum while the red one to the spectrum expected in 1-cm-deep tissue. Black areas correspond to intermediate cases.

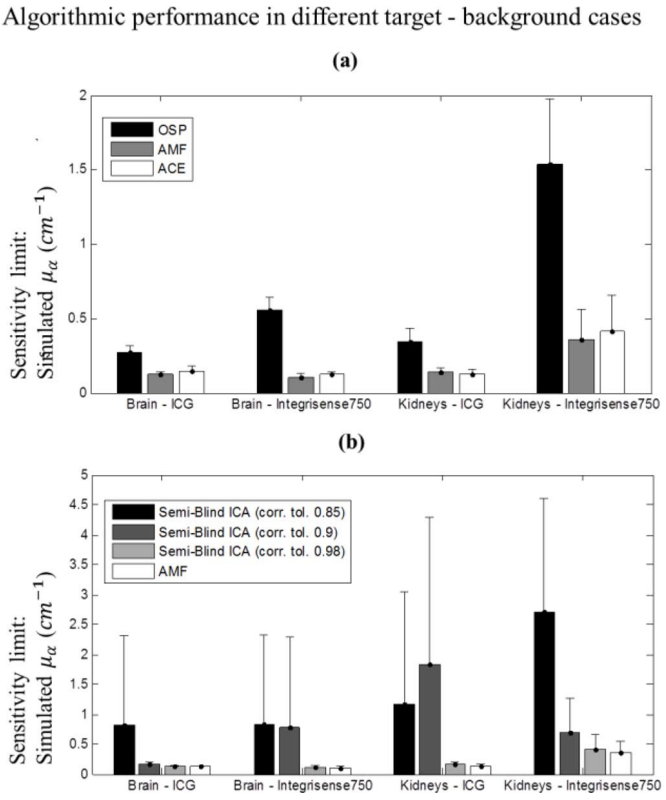

Fig. 3. Sensitivity limits of the different algorithmic approaches for the four discrete synthetic datasets. (a) Comparison between structured and statistical approaches. (b) Comparison between blind and deterministic statistical approaches. The sensitivity limit (y axis) is defined as the minimum simulated peak absorption coefficient ($\mu_a^{\rm sim}$) of the agent that is required for successful detection, according to (8).

under the assumption of 30% [Fig. 2(c) and (e)] and 90% [Fig. 2(d) and (f)] uniform background tissue oxygenation.

Fig. 2 highlights the inherent physical complexity of the MSOT-related unmixing problem, introduced due to optical fluence. Since each absorbing molecule can have a different spectral response depending on its position, exact modeling of the targets as well as the background is not feasible using a finite number of distinct spectra in a linear mixture model. The diffusion approximation model that has been used here is a well-established method for modeling light propagation in tissue [38], [52]. While there is in general significant uncertainty in estimating the exact optical properties of tissue, the representative values used here can offer good insight to the extent of the spectral coloring phenomenon expected in measurements on animals. Corresponding effects of this phenomenon can be observed in tissue-mimicking phantoms as well as multispectral optoacoustic measurements of tissue [35].

B. Detection Performance on the Synthetic Datasets

In this section, we summarize the results of the performance comparison of the considered sub-pixel detection algorithms on the synthetic datasets described in (Section III-C1). In each image instance of the synthetic datasets, the target absorber has been added in gradually decreasing amounts corresponding to a simulated peak absorption coefficient from $\mu_\alpha^{\rm sim} = 5$ cm^{-1} to $\mu_\alpha^{\rm sim} = 0.01$ cm^{-1}. Each detection algorithm is applied consequently to all multispectral images from higher to lower target amount until the target is not detectable. The lowest successfully detected $\mu_\alpha^{\rm sim}$, [according to (8)] is stored for each case and its value corresponds to the sensitivity limit of the detection algorithm on the specific image instance. A sensitivity matrix is computed for each distinct dataset (e.g., brain—ICG) after applying each unmixing algorithm to all six image instances (where the agent has been implanted in a different position), storing the calculated sensitivity (in cm^{-1}) for each case.

In Fig. 3 statistics of these matrices in terms of mean and standard deviation are presented for each distinct dataset and all algorithms considered. The bar height indicates the average sensitivity limit of a specific algorithm on all six image instances of a distinct dataset. The error-bar corresponds to the standard deviation of the sensitivity limits in that set. A lower sensitivity limit demonstrates better detection performance since the algorithm is able to extract the agent of interest in lower concentrations. Fig. 3(a) shows a direct comparison between structured (OSP) and statistical (AMF, ACE) unmixing algorithms, while Fig. 3(b) evaluates the performance of semi-blind-ICA under varying spectral constrains. Semi-blind-ICA is applied with varying correlation tolerances from 0.85 to 0.98. Fig. 4 presents two detection examples

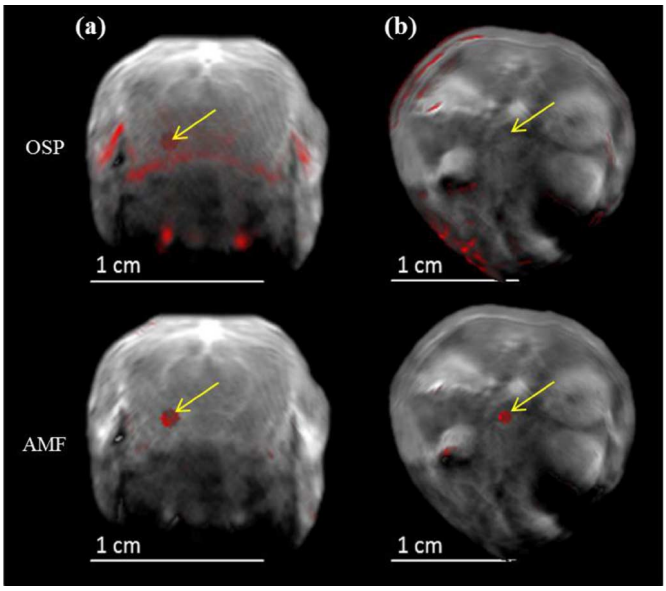

Fig. 4. Detection example from the synthetic dataset. The detection results of OSP and AMF are overlaid to the anatomical optoacoustic image with red color. (a) Brain background with an implanted target of ICG at a simulated absorption coefficient of 0.13 cm^{-1}. (b) Kidneys background with an implanted target of Integrisense750 at a simulated absorption coefficient of 0.8 cm^{-1}. In both cases the target is successfully detected with the AMF but not with OSP.

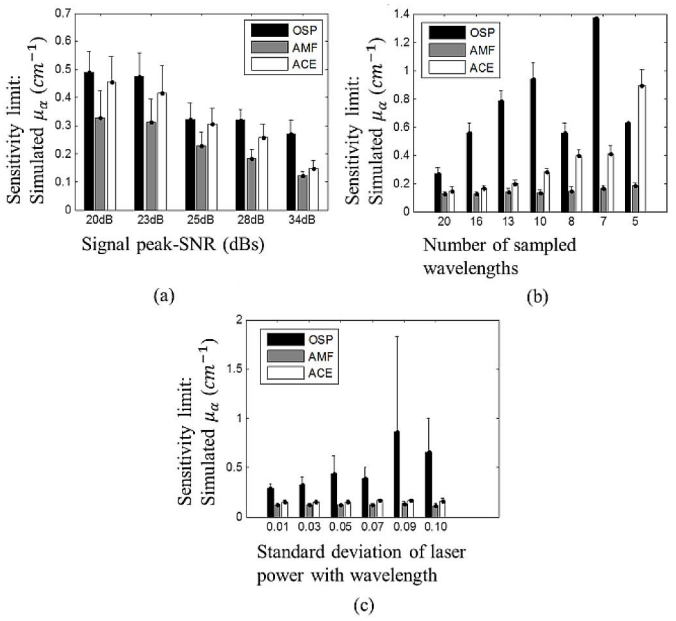

Fig. 5. Algorithmic performance with respect to system parameters for the Kidneys—ICG case. Effect of: (a) noise levels, (b) wavelength sampling, and (c) laser power fluctuation in the detection sensitivity of the different algorithmic approaches.

where the implanted agent could be detected using AMF but was below the false positive levels when using OSP.

The evaluation suggests that statistical algorithms such as AMF and ACE can consistently outperform OSP that assumes known background spectra, increasing the sensitivity of detection from two [Fig. 3(a)–"Brain-ICG"] to five times [Fig. 3(a)–"Kidneys-Integrisense750"]. While a significant variability in the sensitivity limits under different conditions (background, target agent, location of the implanted target) is observed, the comparative algorithmic performance appears to be consistent in all cases.

The performance of semi-blind ICA depends significantly on the correlation tolerance chosen [Fig. 3(b)]. As the spectral constrain increases, the performance of semi-blind ICA increases also, approaching the performance of AMF. While semi-blind ICA might converge to the correct "colored" target spectrum at times, achieving better performance than AMF, it can also diverge significantly, converging to an irrelevant solution. This introduces an uncertainty in the detection performance, which is also statistically worse than the one of AMF according to the evaluation. Furthermore, semi-blind ICA starts its convergence process from a random guess, which makes its detection performance nonreproducible and thus unsuitable for biological studies. Finally, the performance of AMF and ACE is comparable.

C. Experimental Conditions Affecting the Detection Performance

In the following the algorithmic performance is investigated with respect to varying imaging conditions and system parameters, such as the noise levels, the number of wavelengths utilized as well as intensity errors related to laser power fluctuation.

Fig. 5(a) presents the effect of noise in the detection performance of the three algorithmic approaches. Both the AMF and the ACE demonstrate a gradual performance degradation with additive random noise which affects their statistical modeling capabilities. The performance of OSP is also influenced by random noise, in a lower degree however, since the false positive artifacts that limit its performance mainly stem from image structures rather than random noise.

Fig. 5(b) compares the algorithmic performance with respect to the number of wavelengths utilized. All three algorithmic approaches appear to perform better given a larger number of wavelengths. The detection performance of ACE appears to be the fastest one to degrade as the wavelength sampling becomes sparser, whereas the performance of AMF appears more robust. OSP demonstrated rather unpredictable performance fluctuations with different wavelength sampling, however the globally best results are achieved when the full wavelength bandwidth is used.

Finally, Fig. 5(c) presents the effect of intensity fluctuations with wavelength to the algorithmic performance, showing that statistical detection algorithms appear to be relatively immune to this effect, However, the performance of OSP that relies on dictionary based spectra for background modeling is highly affected by such kind of noise.

All three graphs [Fig. 5(a), (b), and (c)] correspond to the Kidneys—ICG dataset, however a similar behavior is observed in all four agent-background cases.

D. Detection Performance on the Ex Vivo and In Vivo Datasets

Following, a visual qualitative comparison of the detection results from the different algorithmic approaches is presented for the cases of *in vivo* and *ex vivo* datasets. The detection result

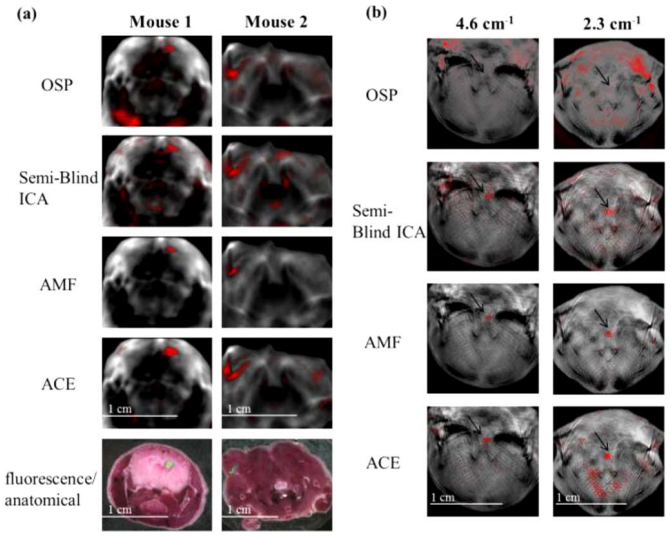

Fig. 6. (a) Visualization of the detection result of the different algorithms in the case of two mice of the *in vivo* scenario (Section III-C2). The detection results of the different algorithms can be visually compared with the overlay of the fluorescence (green) on the anatomical images of cryoslicing fluorescence imaging. (b) Visualization of the detection result of the different algorithms in the case of the *ex vivo* scenario (Section III-C2) of euthanized mice with fluorochrome in the esophagus. The position of the fluorochrome should be exactly in the middle of the reconstructed images (see arrow).

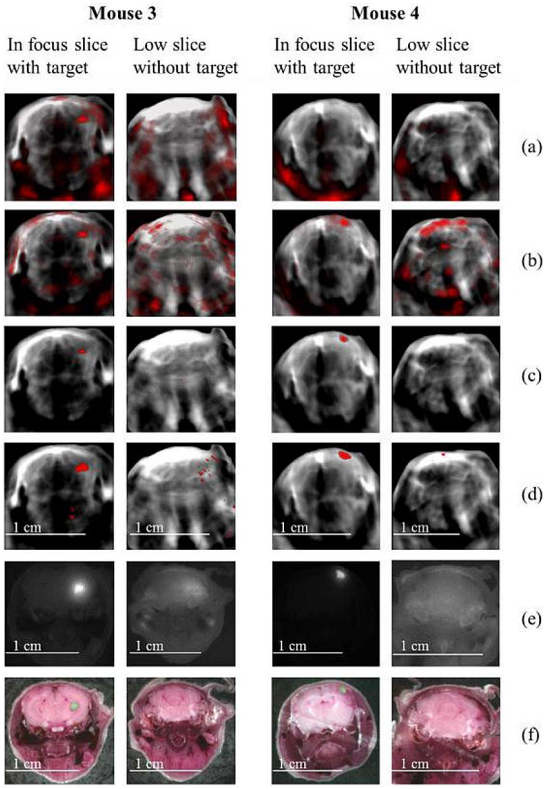

Fig. 7. Detection results of (a) OSP, (b) semi-blind ICA (corr. tolerance 0.96), (c) AMF, and (d) ACE in cases of agent present (left) and absent (right) for two different mice of the *in vivo* dataset (Section III-C2). In the cases of AMF and ACE a global threshold (Section III-D2) has been applied. (e)–(f) Validation by means of cryoslicing fluorescence imaging.

is overlaid onto the optoacoustic image at a single wavelength for an anatomical reference of the detected component.

The detection images from the *in vivo* dataset (Section III-C2), where the target is a fluorescent protein expressed in tumors in the brain of four mice, are presented in Fig. 6(a) and Fig. 7. The images correspond to a slice of the brain containing the tumor. Corresponding cryoslicing fluorescence images overlaid with the plain color images are also presented for comparison.

Similarly, the algorithmic performance on two examples of the *ex vivo* dataset (Section III-C2) is presented in Fig. 6(b). In this case the agent component should be exactly in the middle of the anatomical slice, at the mouse's esophagus. A black arrow is pointing the position of the expected component.

The detection performance of the different algorithmic approaches on the experimental datasets appears consistent with the evaluation performed on the synthetic one. In the *in vivo* case, the adaptive matched filter accurately detects the position of the tumor in all four cases with an insignificant false positive rate, whereas the OSP fails to detect it completely in one case (Fig. 7: Mouse 4) and yields significant false positives, exceeding the detection value of the actual target, in two other cases (Fig. 6(a): Mouse 1, Fig. 7: Mouse 3). In the *ex vivo* case, statistical detection methods have been found able to successfully detect the agent component down to an absorption coefficient of 2.3 cm^{-1}, whereas clear detection using the orthogonal subspace projection was not possible in any case, as the algorithm was constantly producing false positives at much higher intensities. Being scale invariant, ACE appeared more capable in capturing the size and the boundaries of the tumors (Mouse 1, Mouse 3), although this is something hard to quantify. Moreover, its performance relies more on the noise levels and the quality of the reconstructed image as scale normalization may significantly enhance noise. Finally, semi-blind ICA needs to be significantly constrained in order to converge to a relevant solution (a correlation tolerance of 0.96 had to be used in order to achieve correct convergence). When the spectral constrain is relaxed and smaller correlation tolerances are used, the algorithm converges to an irrelevant solution in most of the cases, indicating that statistical independence is not a robust standalone criterion.

E. Comparison in Terms of Specificity

In addition to the comparison in terms of sensitivity presented before, the specificity of the detection performance was also investigated. Fig. 7 demonstrates the significance of applying a global threshold to the detection result in a real application scenario from the *in vivo* study (Section III-C2). The two column groups correspond to mice 3 and 4 of the *in vivo* dataset (Section III-C2). The left columns correspond to axial slices in the brain where there is a tumor and a specific signal of the fluorescent protein, while in the right ones are slices where there is no tumor and thus no relevant signal is present. For the cases of AMF and ACE global detection thresholds were utilized as described in (Section III-D2). A non-CFAR algorithm cannot be associated with a globalized threshold, returning thus a false bio-distribution component even in the absence of an agent, as well as irrelevant false positive artifacts when an actual component is present. Such

detection performance could possibly lead to a wrong diagnosis if the result is not validated by another imaging modality.

V. Discussion

The extraction of the bio-distribution of extrinsic optical agents injected or expressed in tissue is an important application of MSOT imaging with a potential to facilitate a wide spectrum of needs in biological research, such as tumor targeting, clearance of injected pharmaceuticals or localization of protein expression in advanced biological models. The impact of unmixing algorithms on the resulting diagnosis has been hereby made obvious, especially by the demonstrated results of the *in vivo* datasets (Figs. 6 and 7). In general, success of molecular imaging studies for any biomedical application depends to a large extent on the performance of both the system and the algorithms utilized. Specifically for the case of MSOT, the solution of the nonlinear optical problem [27], for the accurate extraction and quantification of chromophores, presents a longstanding challenge that constrains its successful application in many cases. For the aforementioned reasons, this paper formulated the MSOT unmixing problem as a molecular target detection problem, and investigated alternative methods to the typical inexact linear unmixing and ill-posed nonlinear inversion approaches.

The selection of an appropriate unmixing or sub-pixel detection algorithm can have a major impact on the sensitivity and accuracy of MSOT defining its capabilities in molecular imaging applications. However, since the identification of a globally optimal method cannot be answered based on purely theoretical considerations, comparative studies of different methods should be approached employing extensive datasets in a statistical manner [40]. In the case of MSOT, the production of such datasets constitutes a challenge. Simple phantoms or simulations do not correspond usually to *in vivo* measurements of animals, typically oversimplifying tissue imaging conditions, structure and optical properties. Moreover, a quantitative comparison of algorithmic performance on experimentally collected datasets is practically impossible, as it presupposes exact knowledge of the position and area covered by the molecular component of interest. To overcome this challenge, in this study we proposed a simple target implantation technique that has been adapted to the specificities of the MSOT case. The so created synthetic datasets can enable a comprehensive and quantitative comparison of different detection approaches and a thorough evaluation of their performance under different conditions. To support this evaluation we have also presented detection examples of *in vivo* and *ex vivo* experiments with animals.

Each algorithmic unmixing approach relies on a model to describe the spectral variability of the background tissue and the molecular agent of interest. Under the condition of "low target probability," which can generally be valid for many molecular imaging applications, statistical modeling of tissue background from the available data can significantly outperform standard structured approaches due to the uncertainties associated with the measured spectral responses (Section II-A). AMF and ACE that model the spectral background statistically, employing a whitening transformation for its suppression have showcased an enhanced performance in our evaluations, as compared to OSP which assumes a linear mixture model and a background following the spectra of hemoglobin. Moreover, it has been demonstrated that deterministic nonblind approaches can produce equivalent or better results than blind approaches in terms of sensitivity, without introducing uncertainty in their performance. The AMF demonstrates a more robust performance than semi-blind ICA in our evaluations, indicating, contrary to previous belief, that spectral priors for the optical targets can constitute a much stronger criterion than pure statistical independence. Finally, proof of principle has been provided that the CFAR property of the statistical detection algorithms can be exploited for detection with high specificity, a very important aspect in the application of the technology in biological studies.

The detection sensitivity of multispectral optoacoustic tomography on the one hand depends on the signal amplitude of the target absorbing agent and on the other hand on the ability of extracting the agent from the absorbing tissue background. The first consideration relates mainly to the relative amplitude of the signal as compared to the background absorption. This relative amplitude depends on a multitude of case-specific parameters and system features, such as depth, volume, concentration, and absorbance of the molecular agent, tissue optical properties, the detection sensitivity and frequency bandwidth of the transducer, the spatial impulse response of the system, and the image reconstruction approach.

The performed simulations, demonstrate a significant variance in the sensitivity limits under different conditions like the depth of the implanted agents the background spectral clutter and spectral specifications of the target agent. While the target implantation simulations indeed provide a very realistic platform for comparing the relative detection performance of different algorithmic approaches, a number of assumptions (e.g., regarding optical properties and constant Gruneisen parameter) and additional effects, such as the acoustoelectric and spatial impulse response of the system and the frequency dependent ultrasound attenuation might have a significant effect in the simulated absolute values of μ_α. Specialization of the results for specific incarnations of optoacoustic imaging for defining absolute sensitivity limits is not attempted here, since many of the aforementioned parameters are very implementation and case specific and an argument in this direction would compromise the generality of the presented analysis.

It is instead aimed at creating a general evaluation framework for unmixing algorithms in the context of MSOT that includes all fundamental challenges encountered in experimental tissue imaging (i.e., spectral coloring effects, optoacoustic signal distortions, and effects of tomographic reconstructions). Through this evaluation framework, statistical sub-pixel detection algorithms were identified as the most promising direction for future application and further research, offering characteristics that appear very suitable for the particular challenges of the specific imaging problem. Based on the formulation and the evaluation framework presented in this paper further studies will be ventured in this direction, both in terms of algorithmic research as well as in imaging parameter optimization, for enhancing as well as defining the sensitivity and specificity of MSOT imaging in molecular imaging applications.

REFERENCES

[1] X. Wang, Y. Pang, G. Ku, X. Xie, G. Stoica, and L. V. Wang, "Noninvasive laser-induced photoacoustic tomography for structural and functional imaging of the brain," *Nat. Biotechnol.*, vol. 21, pp. 803–806, Jun. 2003.

[2] R. A. Kruger, W. L. Kiser, D. R. Reinecke, G. A. Kruger, and K. D. Miller, "Thermoacoustic molecular imaging of small animals," *Mol. Imag.*, vol. 2, no. 2, p. 113, 2003.

[3] S. Mallidi, T. Larson, J. Tam, P. P. Joshi, A. Karpiouk, K. Sokolov, and S. Emelianov, "Multiwavelength photoacoustic imaging and plasmon resonance coupling of gold nanoparticles for selective detection of cancer," *Nano Lett.*, vol. 9, no. 8, p. 2825, Aug. 2009.

[4] V. Ntziachristos and D. Razansky, "Molecular imaging by means of multispectral optoacoustic tomography (MSOT)," *Chem. Rev.*, vol. 110, no. 5, pp. 2783–2794, May 2010.

[5] V. Ntziachristos, "Going deeper than microscopy: The optical imaging frontier in biology," *Nature Methods*, vol. 7, no. 8, pp. 603–614, Aug. 2010.

[6] P. Beard, "Biomedical photoacoustic imaging," *Interface Focus*, vol. 1, no. 4, pp. 602–631, Aug. 2011.

[7] N. C. Burton, M. Patel, S. Morscher, W. Driessen, J. Claussen, N. Beziere, T. Jetzfellner, A. Taruttis, D. Razansky, B. Bednar, and V. Ntziachristos, ""Multispectral opto-acoustic tomography (MSOT) of the brain and glioblastoma characterization," *NeuroImage*, vol. 65, pp. 522–528, Jan. 2013.

[8] N. Lozano, W. T. Al-Jamal, A. Taruttis, N. Beziere, N. C. Burton, J. Van den Bossche, M. Mazza, E. Herzog, V. Ntziachristos, and K. Kostarelos, "Liposome-Gold nanorod hybrids for high-resolution visualization deep in tissues," *J. Am. Chem. Soc.*, vol. 134, no. 32, pp. 13256–13258, Aug. 2012.

[9] M. Xu and L. V. Wang, "Universal back-projection algorithm for photoacoustic computed tomography," *Phys. Rev. E*, vol. 71, no. 1, p. 016706, Jan. 2005.

[10] A. Rosenthal, D. Razansky, and V. Ntziachristos, "Fast semi-analytical model-based acoustic inversion for quantitative optoacoustic tomography," *IEEE Trans. Med. Imag.*, vol. 29, no. 6, pp. 1275–1285, Jun. 2010.

[11] X. L. Dean-Ben, V. Ntziachristos, and D. Razansky, "Acceleration of optoacoustic model-based reconstruction using angular image discretization," *IEEE Trans. Med. Imag.*, vol. 31, no. 5, pp. 1154–1162, May 2012.

[12] D. Razansky, M. Distel, C. Vinegoni, R. Ma, N. Perrimon, R. W. Koster, and V. Ntziachristos, "Multispectral opto-acoustic tomography of deep-seated fluorescent proteins in vivo," *Nature Photon.*, vol. 3, no. 7, pp. 412–417, July 2009.

[13] D. Razansky, A. Buehler, and V. Ntziachristos, "Volumetric real-time multispectral optoacoustic tomography of biomarkers," *Nature Protocols*, vol. 6, no. 8, pp. 1121–1129, Jul. 2011.

[14] D. Razansky, N. J. Harlaar, J. L. Hillebrands, A. Taruttis, E. Herzog, C. J. Zeebregts, G. M. van Dam, and V. Ntziachristos, "Multispectral optoacoustic tomography of matrix metalloproteinase activity in vulnerable human carotid plaques," *Mol. Imag. Biol.*, vol. 14, no. 3, pp. 277–285, Jun. 2012.

[15] M. Li, J. Oh, X. Xie, G. Ku, W. Wang, C. Li, G. Lungu, G. Stoica, and L. V. Wang, "Simultaneous molecular and hypoxia imaging of brain tumors in vivo using spectroscopic photoacoustic tomography," *Proc. IEEE*, vol. 96, no. 3, p. 481, Mar. 2008.

[16] C. Kim, E. C. Cho, J. Chen, K. H. Song, L. Au, C. Favazza, Q. Zhang, C. M. Cobley, F. Gao, Y. Xia, and L. V. Wang, "In vivo molecular photoacoustic tomography of melanomas targeted by bioconjugated gold nanocages," *ACS Nano*, vol. 4, no. 8, pp. 4559–4564, Aug. 2010.

[17] E. Herzog, A. Taruttis, N. Beziere, A. A. Lutich, D. Razansky, and V. Ntziachristos, "Optical imaging of cancer heterogeneity with multispectral optoacoustic tomography," *Radiology*, vol. 263, no. 2, pp. 461–468, May 2012.

[18] R. J. Paproski, A. E. Forbrich, K. Wachowicz, T. Harrison, M. M. Hitt, and R. J. Zemp, "Tyrosinase as a dual reporter gene for both photoacoustic and magnetic resonance imaging," *Biomed. Opt. Exp.*, vol. 2, no. 4, pp. 771–780, Mar. 2011.

[19] G. S. Filonov, A. Krumholz, J. Xia, J. Yao, L. V. Wang, and V. V. Verkhusha, "Deep-tissue photoacoustic tomography of a genetically encoded near-infrared fluorescent probe," *Angewandte Chemie Int. Ed.*, vol. 51, no. 6, pp. 1448–1451, Feb. 2012.

[20] J. Stritzker, L. Kirscher, M. Scadeng, N. C. Deliolanis, S. Morscher, P. Symvoulidis, K. Schaefer, Q. Zhang, L. Buckel, M. Hess, U. Donat, W. G. Bradley, V. Ntziachristos, and A. A. Szalay, "Vaccinia virus-mediated melanin production allows MR and optoacoustic deep tissue imaging and laser-induced thermotherapy of cancer," in *Proc. Nat. Acad. Sci.*, Feb. 2013, vol. 110, no. 9, pp. 3316–3320.

[21] B. Wang, E. Yantsen, T. Larson, A. B. Karpiouk, S. Sethuraman, J. L. Su, K. Sokolov, and S. Y. Emelianov, "Plasmonic intravascular photoacoustic imaging for detection of macrophages in atherosclerotic plaques," *Nano Lett.*, vol. 9, no. 6, pp. 2212–2217, Jun. 2009.

[22] J.-W. Kim, E. I. Galanzha, E. V. Shashkov, H.-M. Moon, and V. P. Zharov, "Golden carbon nanotubes as multimodal photoacoustic and photothermal high-contrast molecular agents," *Nature Nanotechnol.*, vol. 4, no. 10, pp. 688–694, Aug. 2009.

[23] A. Taruttis, M. Wildgruber, K. Kosanke, N. Beziere, K. Licha, R. Haag, M. Aichler, A. Walch, E. Rummeny, and V. Ntziachristos, "Multispectral optoacoustic tomography of myocardial infarction," *Photoacoustics*, vol. 1, no. 1, pp. 3–8, Mar. 2013.

[24] A. De La Zerda, C. Zavaleta, S. Keren, S. Vaithilingam, S. Bodapati, Z. Liu, J. Levi, B. R. Smith, T.-J. Ma, O. Oralkan, Z. Cheng, X. Chen, H. Dai, B. T. Khuri-Yakub, and S. S. Gambhir, "Carbon nanotubes as photoacoustic molecular imaging agents in living mice," *Nature Nanotech.*, vol. 3, no. 9, pp. 557–562, Aug. 2008.

[25] A. Taruttis, S. Morscher, N. C. Burton, D. Razansky, and V. Ntziachristos, "Fast multispectral optoacoustic tomography (MSOT) for dynamic imaging of pharmacokinetics and biodistribution in multiple organs," *PLoS One*, vol. 7, no. 1, p. e30491, Jan. 2012.

[26] Z. Yuan and H. Jiang, "Quantitative photoacoustic tomography," *Phil. Trans. R. Soc. A: Math., Phys. Eng. Sci.*, vol. 367, no. 1900, pp. 3043–3054, Aug. 2009.

[27] B. Cox, J. Laufer, and P. Beard, "The challenges for quantitative photoacoustic imaging," in *Proc. SPIE*, 2009, vol. 7177, pp. 717713–717719.

[28] B. Cox, J. G. Laufer, S. R. Arridge, and P. C. Beard, "Quantitative spectroscopic photoacoustic imaging: A review," *J. Biomed. Opt.*, vol. 17, no. 6, p. 061202, Jun. 2012.

[29] B. Cox, S. Arridge, and P. Beard, "Estimating chromophore distributions from multiwavelength photoacoustic images," *J. Opt. Soc. Am. A*, vol. 26, no. 2, pp. 443–455, Feb. 2009.

[30] J. Laufer, B. Cox, E. Zhang, and P. Beard, "Quantitative determination of chromophore concentrations from 2D photoacoustic images using a nonlinear model-based inversion scheme," *Appl. Opt.*, vol. 49, no. 8, pp. 1219–1233, Mar. 2010.

[31] G. Bal and G. Uhlmann, "Inverse diffusion theory of photoacoustics," *Inverse Problems*, vol. 26, no. 8, p. 085010, Aug. 2010.

[32] J. Glatz, N. C. Deliolanis, A. Buehler, D. Razansky, and V. Ntziachristos, "Blind source unmixing in multi-spectral optoacoustic tomography," *Opt. Exp.*, vol. 19, no. 4, pp. 3175–3184, Feb. 2011.

[33] S. Morscher, J. Glatz, N. C. Deliolanis, A. Buehler, D. Razansky, and V. Ntziachristos, "Blind spectral unmixing to identify molecular signatures of absorbers in multispectral optoacoustic tomography," *Proc. SPIE*, vol. 7899, pp. 78993D–78993D-6, 2011.

[34] N. Keshava, "A survey of spectral unmixing algorithms," *Lincoln Lab. J.*, vol. 14, no. 1, pp. 55–78, 2003.

[35] K. Maslov, H. F. Zhang, and L. V. Wang, "Effects of wavelength-dependent fluence attenuation on the noninvasive photoacoustic imaging of hemoglobin oxygen saturation in subcutaneous vasculature in vivo," *Inverse Problems*, vol. 23, no. 6, p. S113, Dec. 2007.

[36] A. Rosenthal, D. Razansky, and V. Ntziachristos, "Quantitative optoacoustic signal extraction using sparse signal representation," *IEEE Trans. Med. Imag.*, vol. 28, no. 12, pp. 1997–2006, Dec. 2009.

[37] T. Jetzfellner, A. Rosenthal, A. Buehler, K. H. Englmeier, D. Razansky, and V. Ntziachristos, "Multispectral optoacoustic tomography by means of normalized spectral ratio," *Opt. Lett.*, vol. 36, no. 21, pp. 4176–4178, Nov. 2011.

[38] J. Laufer, D. Delpy, C. Elwell, and P. Beard, "Quantitative spatially resolved measurement of tissue chromophore concentrations using photoacoustic spectroscopy: Application to the measurement of blood oxygenation and haemoglobin concentration," *Phys. Med. Biol.*, vol. 52, no. 1, p. 141, 2007.

[39] A. Buehler, A. Rosenthal, T. Jetzfellner, A. Dima, D. Razansky, and V. Ntziachristos, "Model-based optoacoustic inversions with incomplete projection data," *Med. Phys.*, vol. 38, no. 3, p. 1694, 2011.

[40] D. Manolakis and G. Shaw, "Detection algorithms for hyperspectral imaging applications," *IEEE Signal Process. Mag.*, vol. 19, no. 1, pp. 29–43, Jan. 2002.

[41] D. Manolakis, D. Marden, and G. A. Shaw, "Hyperspectral image processing for automatic target detection applications," *Lincoln Lab. J.*, vol. 14, no. 1, pp. 79–116, 2003.

[42] H. Ren and I. C. Chein, "A generalized orthogonal subspace projection approach to unsupervised multispectral image classification," *IEEE Trans. Geoscience Remote Sens.*, vol. 38, no. 6, pp. 2515–2528, Nov. 2000.

[43] E. J. Kelly, "An adaptive detection algorithm," *IEEE Trans. Aerosp. Electron. Syst.*, vol. 22, no. 2, pp. 115–127, Mar. 1986.

[44] F. C. Robey, D. R. Fuhrmann, E. J. Kelly, and R. Nitzberg, "A CFAR adaptive matched filter detector," *IEEE Trans. Aerosp. Electron. Syst.*, vol. 28, no. 1, pp. 208–216, Jan. 1992.

[45] S. Kraut, L. L. Scharf, and R. W. Butler, "The adaptive coherence estimator: A uniformly most-powerful-invariant adaptive detection statistic," *IEEE Trans. Signal Process.*, vol. 53, no. 2, pp. 427–438, Feb. 2005.

[46] D. W. J. Stein, S. G. Beaven, L. E. Hoff, E. M. Winter, A. P. Schaum, and A. D. Stocker, "Anomaly detection from hyperspectral imagery," *IEEE Signal Process. Mag.*, vol. 19, no. 1, pp. 58–69, Jan. 2002.

[47] H. Ren, D. Qian, W. Jing, I. C. Chein, J. O. Jensen, and J. L. Jensen, "Automatic target recognition for hyperspectral imagery using high-order statistics," *IEEE Trans. Aerospace Electron. Syst.*, vol. 42, no. 4, pp. 1372–1385, Oct. 2006.

[48] J. Wang and C. I. Chang, "Applications of independent component analysis in endmember extraction and abundance quantification for hyperspectral imagery," *IEEE Trans. Geosci. Remote Sens.*, vol. 44, no. 9, pp. 2601–2616, Sep. 2006.

[49] V. Calhoun and T. Adali, "Semi-blind ICA of FMRI: A method for utilizing hypothesis-derived time courses in a spatial ICA analysis," in *Proc. 2004 14th IEEE Signal Process. Soc. Workshop Mach. Learn. Signal Process.* , 2004, pp. 443–452.

[50] A. Hyvärinen, "Fast and robust fixed-point algorithms for independent component analysis," *IEEE Trans. Neural. Netw.*, vol. 10, no. 3, pp. 626–634, May 1999.

[51] D. Hyde, R. Schulz, D. Brooks, E. Miller, and V. Ntziachristos, "Performance dependence of hybrid x-ray computed tomography/fluorescence molecular tomography on the optical forward problem," *J. Opt. Soc. Am. A*, vol. 26, no. 4, pp. 919–923, Apr. 2009.

[52] S. R. Arridge and J. C. Hebden, "Optical imaging in medicine: II. Modelling and reconstruction," *Phys. Med. Biol.*, vol. 42, no. 5, p. 841, May 1997.

[53] A. Buehler, E. Herzog, D. Razansky, and V. Ntziachristos, "Video rate optoacoustic tomography of mouse kidney perfusion," *Opt. Lett.*, vol. 35, no. 14, pp. 2475–2477, Jul. 2010.

[54] W. F. Basener, E. Nance, and J. Kerekes, "The target implant method for predicting target difficulty and detector performance in hyperspectral imagery," *Proc. SPIE*, vol. 8048, p. 80481H, 2011, "The target implant method for predicting target difficulty and detector performance in hyperspectral imagery," in *SPIE*, 2011, pp. 80481H–80481H-9.

[55] A. Sarantopoulos, G. Themelis, and V. Ntziachristos, "Imaging the bio-distribution of fluorescent probes using multispectral epi-illumination cryoslicing imaging," *Molecular Imag. Biol.*, vol. 13, no. 5, pp. 874–885, Oct. 2011.

Appendix B

Publication: Statistical molecular target detection framework for multispectral optoacoustic tomography

The version herein has been published in the journal "IEEE Tansactions on Medical Imaging" [141].

Statistical Molecular Target Detection Framework for Multispectral Optoacoustic Tomography

Stratis Tzoumas*, Andrii Kravtsiv, Yuan Gao, Andreas Buehler, and Vasilis Ntziachristos*

***Abstract*— Statistical sub-pixel detection via the adaptive matched filter (AMF) has been shown to improve the molecular imaging sensitivity and specificity of optoacoustic (photoacoustic) imaging. Applied to multispectral optoacoustic tomography (MSOT), AMF assumes that the spatially-varying tissue spectra follow a multivariate Gaussian distribution, that the spectrum of the target molecule is precisely known and that the molecular target lies in "low probability" within the data. However, when these assumptions are violated, AMF may result in considerable performance degradation. The objective of this work is to develop a robust statistical detection framework that is appropriately suited to the characteristics of MSOT molecular imaging. Using experimental imaging data, we perform a statistical characterization of MSOT tissue images and conclude to a detector that is based on the t-distribution. More importantly, we introduce a method for estimating the covariance matrix of the background-tissue statistical distribution, which enables robust detection performance independently of the molecular target size or intensity. The performance of the statistical detection framework is assessed through simulations and experimental *in vivo* measurements and compared to previously used methods.**

***Index Terms*— Covariance contamination, molecular imaging, multispectral optoacoustic tomography, photoacoustic tomography, spectral unmixing, statistical sub-pixel detection.**

I. Introduction

MULTISPECTRAL Optoacoustic Tomography (MSOT) offers high-resolution detection of optically absorbing reporter molecules at depths beyond the ones reached by optical microscopy and it is now increasingly considered for visualizing near-infrared fluorescent proteins, fluorescent dyes or absorbing nanoparticles, *in vivo* in small animal or human studies [1]–[3]. MSOT molecular imaging relies on the identification of the spectral signature of a reporter molecule from the absorbing tissue background and it defines a multispectral target detection problem [4].

Multispectral target detection is essentially a binary classification problem where each pixel has to be identified as target or background. Since the spatial extend of the target is typically only a small fraction of the whole image, binary classification algorithms that are based on the minimization of the misclassification rate are not well suited for this problem [5], [6]. Practical multispectral target detection algorithms are commonly based on the Neyman-Pearson criterion (maximize the probability of detection while retaining the probability of false alarm under a constant threshold [7]) and are derived using a generalized likelihood ratio test (GLRT) [5].

Recently, it was shown that the MSOT molecular imaging sensitivity and specificity can be considerably enhanced through the utilization of GLRT statistical detection methods, like the adaptive matched filter (AMF) [8], for extracting weak spectral contributions stemming from molecular agents of biological significance [4], [9]. AMF allows for statistically modeling and suppressing the MSOT tissue background, i.e. it overcomes the challenge of modelling the spectral variability of tissue using exact spectra. Moreover, by offering a constant false alarm rate (CFAR), AMF enables molecular imaging of high specificity, potentially eliminating the need for *ex vivo* validation.

AMF would be optimal for MSOT applications if the spatially-varying background tissue spectra followed a multivariate Gaussian distribution with known parameters and the spectrum of the target molecule within tissue would be known precisely. However, a number of challenges, typically presented in MSOT molecular imaging applications, may compromise the detection performance of AMF. *First*, the MSOT spectral background may not follow a multivariate Gaussian distribution. *Second*, deep seated molecular targets, typically exhibit different spectrum than the one obtained from libraries or individual measurements (*spectral mismatch*) due to the spectral coloring introduced to optical absorbers in deep tissue [4]. *Third*, when the molecular agent is present in high amount within tissue, the presence of the signal of interest (SOI) within the data compromises the accurate computation of the background statistics, i.e. the mean and the covariance matrix, which are typically computed from all available data with maximum likelihood. This effect, commonly referred to as *covariance contamination* in literature, may cause considerable performance degradation [10]–[12]. The two latter effects (i.e. the *spectral mismatch* and the *covariance contamination*) are

Manuscript received May 10, 2016; revised June 9, 2016; accepted June 13, 2016. Date of publication June 22, 2016; date of current version November 29, 2016. The work of S. Tzoumas was supported by the DFG GRK 1371 grant. The work of V. Ntziachristos was supported by an ERC Advanced Investigator Award 233161 and the European Union project FAMOS (FP7 ICT, Contract 317744). *Asterisk indicates corresponding author.*

This paper has supplementary downloadable material available at http://ieeexplore.ieee.org, provided by the authors.

*S. Tzoumas and *V. Ntziachristos are with the Institute of Biological and Medical Imaging (IBMI), and Chair for Biological Imaging, Technische Universität München and Helmholtz Zentrum München, 85764 Munich, Germany (e-mail: strtzoumas@gmail.com; v.ntziachristos@tum.de).

A. Kravtsiv and A. Buehler are with the Institute of Biological and Medical Imaging (IBMI), Helmholtz Zentrum München, 85764 Munich, Germany (e-mail: kravaan@gmail.com; andreas.buehler@helmholtz-muenchen.de).

Y. Gao is with the Karlsruhe School of Optics and Photonics, Karlsruhe Institute of Technology, 76131 Karlsruhe, Germany (e-mail: gyolive@gmail.com).

Color versions of one or more of the figures in this paper are available online at http://ieeexplore.ieee.org.

Digital Object Identifier 10.1109/TMI.2016.2583791

closely linked since the *covariance contamination* does not affect significantly the performance of adaptive processing if the target signal is precisely known [11], [13].

In this work we introduce a novel statistical detection framework for resolving molecular agents within the tissue with multispectral optoacoustic tomography. Using experimental imaging data, we statistically characterize MSOT tissue images and conclude to a GLRT detector that is based on the t-distribution. More importantly, using an archive of agent-free MSOT tissue images we introduce a novel approach for estimating the covariance matrix of the background-tissue statistical distribution. The covariance matrix estimated through this approach is uncontaminated, thus offering robust detection performance independently of the molecular target size or intensity. We validate the performance of the proposed method statistically using simulations of artificial target implantation on experimental MSOT data. We further demonstrate the detection performance in purely experimental MSOT data.

The rest of this manuscript is organized as follows: In Sec. II, we offer background on the characteristics of MSOT molecular imaging and introduce statistical sub-pixel detection in the context of MSOT. In Sec III, we describe the collection of the imaging dataset and the target implantation framework that is used for statistically evaluating the detection performance under different conditions. In Sec. IV we introduce the proposed statistical detection framework. In Sec. V we quantitatively evaluate the performance of the proposed statistical detection framework and compare it with currently utilized methods. Concluding remarks are offered in Sec. VI.

II. Background

A. MSOT Imaging of Molecular Targets

The wavelength (λ) dependent and position ($\mathbf{r}$) dependent multispectral optoacoustic images $P(\mathbf{r}, \lambda)$ can be associated to the concentrations of the absorbing molecules through the following relation:

$$P(\mathbf{r}, \lambda) = C(\mathbf{r})\Phi(\mathbf{r}, \lambda)\sum_i c_i(\mathbf{r})\varepsilon_i(\lambda) + n(\mathbf{r}, \lambda) \qquad (1)$$

In Eq. (1), $\Phi(\mathbf{r}, \lambda)$ is the space and wavelength dependent light fluence, $\varepsilon_i(\lambda)$ are the wavelength dependent molar absorption coefficients of the optical absorbers (i.e. the absorption spectra) and $c_i(\mathbf{r})$ the unknown associated concentrations at a position $\mathbf{r}$. $C(\mathbf{r})$ is a scaling factor associated with system effects (i.e. the system's spatial sensitivity field) and the Grüneisen parameter. Finally, $n(\mathbf{r}, \lambda)$ represents the cumulative effect of various types of superimposed noise, such as electronic noise and image reconstruction artifacts.

Quantitative MSOT imaging aims at estimating the concentrations of all absorbers within tissue. For achieving this goal, the unknown optical fluence $\Phi(\mathbf{r}, \lambda)$ must be estimated and accounted for. Using a light propagation model, the light fluence can be related to tissue absorption $[\mu_\alpha(\mathbf{r}, \lambda) = \sum_i c_i(\mathbf{r})\varepsilon_i(\lambda)]$ and scattering coefficients $[\mu_s'(\mathbf{r}, \lambda)]$, i.e. $\Phi(\mathbf{r}, \lambda) = \Phi(\mathbf{r}, \lambda; c_i(\mathbf{r}), \mu_s'(\mathbf{r}, \lambda))$. Using this model, non-linear inversion schemes have been proposed for quantitatively recovering $c_i(\mathbf{r})$ and $\mu_s'(\mathbf{r}, \lambda)$ [14]. Such non-linear inversion schemes have been investigated in simulations and phantoms [15]. Nevertheless, their *in vivo* application is still limited, possibly due to the increased complexity of *in vivo* tissues. Therefore, the MSOT quantification problem is considered an unmet challenge [16].

In vivo molecular imaging often seeks to accurately detect the position and area occupied by a target molecule within the tissue. In this case, the spectral analysis problem formulates as a detection problem. By reformulating (1) to separate the contribution of the tissue background and the target molecule we obtain:

$$\begin{aligned} P(\mathbf{r}, \lambda) &= B(\mathbf{r}, \lambda) + c_t(\mathbf{r})T(\mathbf{r}, \lambda), \\ B(\mathbf{r}, \lambda) &= C(\mathbf{r})\Phi(\mathbf{r}, \lambda)\sum_i c_b^i(\mathbf{r})\varepsilon_b^i(\lambda) + n(\mathbf{r}, \lambda), \\ T(\mathbf{r}, \lambda) &= C(\mathbf{r})\Phi(\mathbf{r}, \lambda)\varepsilon_t(\lambda). \end{aligned} \qquad (2)$$

In Eq. (2) $c_b^i(\mathbf{r})$ and $\varepsilon_b^i(\lambda)$ are the concentrations and absorption spectra, respectively, of tissue-intrinsic molecules, while $c_t(\mathbf{r})$ and $\varepsilon_t(\lambda)$ are the concentration and absorption spectrum of the extrinsic molecular target. The goal of molecular target detection is to decide between two competing hypotheses for each pixel in the image, namely $c_t(\mathbf{r}) = 0$ (non-existing target), or $c_t(\mathbf{r}) > 0$ (existing target), for extracting the position and area occupied by the molecular agent within tissue. For achieving this, models that capture the background and the target spectral variability ($B(\mathbf{r}, \lambda)$ and $T(\mathbf{r}, \lambda)$) are required. Molecular target detection implies that the amount of the target to be detected is substantially lower than the contribution of background molecules. Therefore, throughout this work it is assumed that the unknown light fluence field is not affected by the molecular target but only by the background tissue molecules (Born-type approximation): $\Phi(\mathbf{r}, \lambda) = \Phi(\mathbf{r}, \lambda; c_b^i(\mathbf{r}), \mu_{s'}(\lambda))$.

$B(\mathbf{r}, \lambda)$ and $T(\mathbf{r}, \lambda)$ are difficult to be modeled due to the effects of the light fluence $\Phi(\mathbf{r}, \lambda)$, which is hereby assumed an unknown function of space and wavelength, and the noise term $n(\mathbf{r}, \lambda)$. Early spectral optoacoustic methods assumed a constant light fluence and solved a system of linear equations for spectrally unmixing all photo-absorbing molecules [17]. Typically, in this linear unmixing approach, the spectra of oxygenated (Hb-O_2 and deoxygenated (Hb) hemoglobin are used for modeling the background tissue absorption $B(\mathbf{r}, \lambda)$.

B. Statistical Sub-Pixel Detection of Molecular Targets

More recently statistical sub-pixel detection methods were shown to outperform previous approaches in molecular imaging cases where the target is sparsely present within the data [4], [9]. Statistical sub-pixel detection methods model the background spectral variability $B(\mathbf{r}, \lambda)$ using a multivariate statistical distribution, while the detector is typically derived through a generalized likelihood ratio test (GLRT) [18]. A well-known algorithm in this category is the AMF [8]:

$$D_{AMF}(\mathbf{x}_i) = \frac{1}{N\mathbf{s}^T\mathbf{G}^{-1}\mathbf{s}}(\mathbf{s}^T\mathbf{G}^{-1}(\mathbf{x}_i - \boldsymbol{\mu}))^2 \qquad (3)$$

In Eq. (3), $\mathbf{x}_i$ is an L-dimensional vector corresponding to the MSOT intensity of the pixel under test (L being the number of wavelengths), $\mathbf{s}$ is an L-dimensional vector representing

the absorption spectrum of the target molecule (i.e. $\varepsilon_t(\lambda)$). $\boldsymbol{\mu}$ and $\mathbf{G}$ are the mean and the covariance matrix (L x L) of the multivariate Gaussian distribution that models the spectral background. Under the assumption that the molecular target lies in "low probability" within the data, the parameters $\boldsymbol{\mu}$ and $\mathbf{G}$ of the background statistical distribution can be computed from the all available pixels with maximum likelihood, i.e. $\boldsymbol{\mu} = \frac{1}{N}\sum_{i=1}^{N} \boldsymbol{x_i}$ and $\mathbf{G} = \frac{1}{N}\sum_{i=1}^{N}(\mathbf{x}_i - \boldsymbol{\mu})(\mathbf{x}_i - \boldsymbol{\mu})^T$, where N is the number of pixels in the MSOT image.

The performance of statistical detection algorithms depends on the accurate computation of its parameters, i.e. the mean $\boldsymbol{\mu}$ and the covariance matrix $\mathbf{G}$ [19]. If the true covariance matrix $\mathbf{G}$ was known, an inaccurate estimate of the mean value only affects the scaling of the detection image. Conversely, inaccurate computation of the covariance matrix can have a major adverse impact on the target detectability [10], [12], [13]. Inaccurate computation of $\mathbf{G}$ may result from the prominent presence of the target spectrum within the pixels that are used for its computation (*covariance contamination)*. A method previously considered for mitigating this effect is *diagonal loading* [20], i.e. the superposition of a diagonal matrix with constant entries to the sample covariance matrix multiplied by a scalar b called *loading factor*, i.e. $\mathbf{G}_{dl} = \mathbf{G} + b\mathbf{I}$. If b is appropriately selected, diagonal loading has been shown to mitigate the effects of covariance contamination in hyperspectral imaging [12]. However, the optimal value of b, depends on the level of contamination, which is generally unknown and may vary substantially depending on the molecular imaging application at hand. For this reason, diagonal loading does not present a robust solution for the MSOT molecular target detection problem.

III. Imaging Data and Target Implantation

A. Synthetic MSOT Data

The quantitative evaluation of detection algorithms in the context of MSOT molecular imaging is performed using artificial target implantation on experimental MSOT data, a concept that was previously described in [4].

1) Experimental MSOT Dataset of Tissue Background: Experimental MSOT images of *in vivo* background tissue were obtained using an In Vision 256-TF MSOT system (iThera Medical GmbH, Munich Germany). A previous version of this system is analytically described elsewhere [21]. The MSOT scanner acquires 2D images at a transverse slice in the focal plane of the ultrasound array. By translating the animal in the imaging chamber, multiple 2D images can be acquired, covering the whole body. Imaging was performed at 21 different excitation wavelengths from 700 nm to 900 nm with a step size of 10 nm. Image reconstruction was performed using a model-based inversion algorithm [22] with Tikhonov regularization. After image reconstruction the tissue area was manually segmented in each image.

The imaging dataset includes three nude mice, imaged *in vivo* at 41-45 different 2D slices covering the entire area of the brain and the area of the liver, kidneys and the lower abdomen area. Each mouse was imaged at two different physiological conditions (breathing 100% O_2 and 20% O_2, i.e. medical air). Two different oxygenation conditions were employed to consider changes in the spectra of hemoglobin in tissue that affect the background spectral variability. The imaging dataset is composed of 292 multispectral images in total.

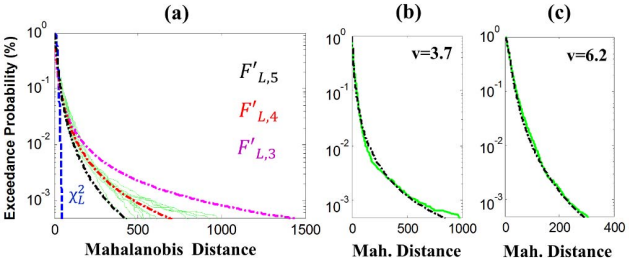

Fig. 1. Statistical characterization of MSOT data through the exceedance probability of their Mahalanobis distance distribution. (a) Probability of exceedance of the Mahalanobis distance of 10 different MSOT images (green solid lines). The theoretical exceedance probability of the χ^2 distribution (blue dashed line) and the F distribution with different degrees of freedom (dash-dotted lines) are also presented for comparison. (b, c) Comparison of the exceedance probability of the Mahalanobis distance of two different MSOT images (b, c solid green lines) with the $F_{L,\upsilon}$ distribution (dash- dotted lines), where υ is selected by minimizing the exceedance metric.

2) Target Implantation 1: Small Targets: Target implantation is achieved through the artificial superposition of targets with the spectra of Indocyanine Green (ICG) or IntegriSense750 (PerkinElmer Inc. Massachusetts, U.S.) at randomly selected positions upon the MSOT background-tissue image. The introduced disk-shaped targets (radius 4 pixels; 37 pixels in total) are implanted at 20 simulated peak absorption coefficients decreasing exponentially from 3 to 0.02 cm^{-1}. The intensity of the implanted target at each pixel is defined by the simulated absorption coefficient and the light fluence at this pixel [$\Phi^{sim}(\mathbf{r}, \lambda)$] which is simulated using a 2D finite element solution of the diffusion approximation and uniform tissue optical properties stemming from literature [4]. The simulated optical fluence is wavelength dependent introducing changes in the spectral signature of the implanted molecular targets, which is computed per pixel as in $s^{imp}(\mathbf{r}, \lambda) = s^{orig}(\mathbf{r}, \lambda)\Phi^{sim}(\mathbf{r}, \lambda)$. We assumed a Born-type approximation where we neglect the effect of the molecular target itself on the simulation of $\Phi^{sim}(\mathbf{r}, \lambda)$. A more analytical description of the target implantation on MSOT images is provided in Ref. [4] and Supp. Fig. 1. We note that, due to a number of simplifying assumptions the simulated absorption coefficient of the implanted targets may not be accurate in absolute value. However, this does not impair the quantitative evaluation since it is only the relative detection performance that is of interest.

A target is considered detectable if there exists a detection threshold T_s that allows for more than 70% of true positives (the true positive set is defined as $TP = \{i \in D_t\colon D(\mathbf{x}_i) > T_s\}$) and less than 0.045% false positives (the false positive set is defined as $FP = \{i \in D_b\colon D(\mathbf{x}_i) > T_s\}$):

$$\exists T_s : |TP| > 0.7\,|D_t| \wedge |FP| < 0.00045\,|D_b|\,, \qquad (4)$$

where i is the pixel index, D_b and D_t are the sets of pixels corresponding to the background and target, respectively, and $|\cdot|$ denotes the cardinality of the set. $D(\mathbf{x}_i)$ is the detection

value attributed to the pixel i. We note that the percentage of 0.045% for false positives was selected because the background area is much larger than the target area. The value $0.00045|D_{\mathrm{b}}|$ is equivalent to $0.5|D_{\mathrm{t}}|$.

In the case of small implanted targets, the detection performance is assessed in terms of minimum detectable agent amount (MDAA; unit cm^{-1}) that is required for successful detection, according to inequality (4). Lower MDAA values indicate higher molecular imaging sensitivity.

3) Target Implantation 2: Large Targets: For quantifying the effects of covariance contamination due to the presence of the molecular target, the target implantation framework was adapted for further considering targets of varying sizes. A large rectangular target occupying a total area of 4096 pixels is initially implanted in tissue background at a randomly selected position. This initial target is iteratively divided into 2, 4, 8 and 16 equally sized rectangular regions corresponding to 2048, 512 and 256 pixels, respectively. In each division stage the target is sequentially implanted at all positions covering the whole initial area of 4096 pixels. In each case the target absorber is implanted at 7 exponentially decreasing simulated absorption coefficient from 3 to 0.03 cm^{-1}. The spectrum of the target at each pixel is computed as in $s^{imp}(\mathbf{r}, \lambda) = s^{orig}(\mathbf{r}, \lambda)\Phi^{sim}(\mathbf{r}, \lambda)$. $\Phi^{sim}(\mathbf{r}, \lambda)$ is computed as described in (III-*A*-2) considering only background tissue absorbers.

For large targets the visibility metric defined in (4) does not offer appropriate intuition on the detection result. Instead, the percentage of the detected pixels, i.e. the percentage of pixels within the target area that are attributed detection values larger than a threshold T_{b}, is computed. This threshold is defined as the average of the 500 larger false-positive detection values (i.e. $T_b = (1/500)\sum_{i=1}^{500} D_b^s(i)$, where D_b^s is a vector containing the detection values attributed to the background sorted in descend order). The average of 500 pixels was selected for avoiding the dominant influence of small outliers in the quantitative analysis. While the region of interest (ROI) corresponding to the target changes according to the target size and position, the same ROI was always used for the computation of false positives. The same false positive ROI was used in order to facilitate a straightforward comparison where any performance differences between large and smaller targets are directly attributed to the effect of covariance contamination (see Suppl. Fig. 2). In each target division stage the total percentage of detected pixels within the whole initial area of 4096 pixels is computed.

B. Experimental Imaging Dataset

For confirming observations stemming from synthetic data, a purely experimental MSOT dataset of mice containing fluorescent molecular targets was compiled:

1) In Vivo Localized Insertion Dataset: A capillary tube (diam. 0.86 mm) containing a fluorescent dye was rectally inserted into an anesthetized CD1 mouse and the animal was imaged in the lower abdominal area. The capillary tube was iteratively filled with the fluorochrome Alexa Fluor 750 (AF750) at an optical density ranging from 6.6 to approx. 0.2 OD for achieving different target intensities.

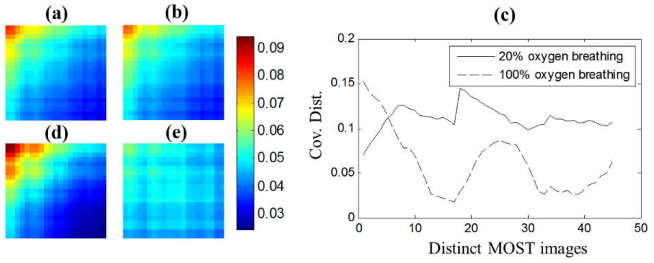

Fig. 2. Comparison of MSOT background-tissue covariance matrices. (a, b) Covariance matrices stemming from two different mice ($\mathbf{G}^1_{\mathrm{GL}}$ and $\mathbf{G}^2_{\mathrm{GL}}$, respectively) using data from the whole body and two different breathing conditions. (c) Graph presenting the distance between $\mathbf{G}^1_{\mathrm{GL}}$ and the covariance matrices $\mathbf{G}^k_{\mathrm{s}}$ corresponding to all anatomical slices of mouse 3. Cov. Dist. $= \|G^1_{\mathrm{GL}}/\|G^1_{\mathrm{GL}}\|_F - \mathbf{G}^k_s/\|G^k_s\|_F\|_F$. (d, e) Covariance matrices produced from single anatomical slices of mouse 3 corresponding to the median (d) and maximum (e) distance as compared to $\mathbf{G}^1_{\mathrm{GL}}$.

The same experiment was performed using the fluorochrome Alexa Fluor 790 (AF790). The dataset is described in Ref. [9]. Imaging was performed at 21 wavelengths from 700 to 900 nm with a step size of 10 nm. The fluorescent target appeared at an imaging depth of ~1 cm in the transverse MSOT image.

2) Brain Tumor Dataset: A nude mouse bearing a brain tumor expressing a near-infrared fluorescent protein (U87-iRFP) was imaged at 12 different wavelengths (690, 695, 700, 705, 710, 715, 720, 730, 750, 770, 800, and 830 nm) in the area of the brain. Fluorescence cryoslicing imaging was employed for validating the location of iRFP post-mortem. The study is described in Ref. [3].

3) Bain Injection Dataset: Different amounts of fluorescently labelled macrophages were injected in the left and the right brain hemisphere of a euthanized nude mouse. Cells were labeled with the near-infrared fluorescent cyanine dye 1,1'-Dioctadecyl-3,3,3',3'-Tetramethylindotricarbocyanine Iodide (DiR). The exact position of the implanted cells was identified post-mortem through cryoslicing fluorescent imaging. Imaging was performed at 21 wavelengths from 700 to 900 nm with a step size of 10 nm. The dataset is analytically described in Ref. [23].

4) Systemic Injection of ICG: 40 nmoles of Indocyanine Green (ICG) diluted in 200 μL saline were injected in the tail-vein of a nude mouse and in the following the animal was imaged in the area of the liver. ICG has been previously documented to accumulate in the liver [24]. Imaging was performed at 21 wavelengths from 700 to 900 nm with a step size of 10 nm.

5) Systemic Injection of AF750: 1.2 nmoles of Alexa Fluor 750 (AF750) diluted in 200 μL saline were injected in the tail-vein of a nude mouse and the animal was imaged in the area of the bladder, where AF750 accumulates [24]. Imaging was performed at 21 wavelengths from 700 to 900 nm.

All animal procedures were approved by the District Government of Upper Bavaria.

IV. Robust Statistical Detection Framework

In this section we describe the statistical detection framework developed. In (IV-*A*), we consider the issue of MSOT background-tissue statistical modeling and in (IV-*B*) we introduce a robust covariance estimation approach for mitigating the effects of covariance contamination. The two concepts are combined in (IV-*C*) for deriving the proposed statistical detection framework.

A. Statistical Characterization of MSOT Data and EC-GLRT Detection

Identifying a statistical distribution that accurately describes the background spectral variability $B(\mathbf{r}, \lambda)$ is an important factor in the design of a target detection algorithm [19]. We hereby compare the multivariate Gaussian assumption, followed by AMF, to the multivariate t-distribution which offers better ability to model multidimensional data with longer tails [25]. Both the Gaussian and the t-distribution belong to the family of the elliptically contoured distributions that were introduced by Manolakis et. al. in hyperspectral imaging for the purpose of synthetic data generation [25]. For statistically characterizing the multidimensional MSOT data we use univariate statistics of their Mahalanobis distance distribution as proposed in [25], [26].

The Mahalanobis distance of L-dimensional data that follow the multivariate Gaussian distribution (m_G see Appendix *A*) is distributed as a χ^2 distribution with L degrees of freedom. By contrast, the Mahalanobis distance of data following the multivariate t distribution with υ degrees of freedom (m_{t}, see Appendix *B*) is distributed as an F distribution with parameters L and υ. By studying the Mahalanobis distance distribution of experimental MSOT data, an appropriate multivariate statistical distribution can be potentially identified for modeling the MSOT tissue background.

The probability of exceedance, which corresponds to the probability that the data will exceed a certain value (Appendix *C*), has been proposed for statistically characterizing the Mahalanobis distance of multidimensional data [26]. The exceedance metric (Eq. (5)), compares the distribution of the Mahalanobis distance $\mathbf{m}$ (Appendix B) to a known probability density function (PDF) f, allowing for the identification of appropriate distributions as well as unknown parameters of such distribution. The exceedance metric is defined through the inverse exceedance probability (Appendix *C*) as in:

$$M_{exc}(\mathbf{m}, f) = \sum_{i=1}^{K} \left| E_{\mathbf{m}}^{-1}(P_i) - E_f^{-1}(P_i) \right|, \tag{5}$$

In Eq. (5), P_i are K logarithmically spaced values of the exceedance probability spanning the range from 1 to 10^{-4}, and E^{-1} is the inverse exceedance probability (Appendix *C*). $E_{\mathbf{m}}$ is the exceedance probability of the Mahalanobis distance distribution of the data, computed numerically, and E_f is the theoretical exceedance probability of the PDF f, which is computed from the analytical expression of f.

Fig. 1(a) presents the probability of exceedance of the Mahalanobis distance for 10 different MSOT background images corresponding to different anatomical areas of a mouse ranging from the brain to the abdominal region (green solid lines). The theoretical exceedance probabilities of the associated χ^2distribution (blue dashed line) and the F distribution for different values of the parameter υ (dash-dotted lines) are also presented for comparison. From the exceedance probability plot it is obvious that the Mahalanobis distance of MSOT data does not follow a χ^2 distribution, while the F distribution provides a far better fit. This indicates that the t-distribution may be more appropriate for modeling the MSOT tissue background. Fig. 1(b), (c) present the distribution of the Mahalanobis distance for two different MSOT images (solid green lines). The dash-dotted black lines correspond to the exceedance probability of the $F_{L,\upsilon}$, where the parameter υ is computed as the value that minimizes the exceedance metric of (5). We observed that different MSOT images may correspond to different degrees of freedom υ. Fig. 1(b), (c) further suggest that the F distribution with optimally selected parameter υ appears capable of modeling well both the main body as well as the tails of the Mahalanobis distance distribution.

Theiler et. al. have derived a generalized likelihood ratio test (GLRT) detector for multivariate data following the t-distribution with υ degrees of freedom ($\upsilon > 2$), termed EC-GLRT detector [27]:

$$D_{EC-GLRT}(\mathbf{x}_i) = \frac{(\upsilon - 1)}{(\upsilon - 2) + (\mathbf{x}_i - \mu)^T \mathbf{G}^{-1} (\mathbf{x}_i - \mu)} \frac{(\mathbf{s}^T \mathbf{G}^{-1} (\mathbf{x}_i - \mu))^2}{s^T \mathbf{G}^{-1} \mathbf{s}} \tag{6}$$

In Eq. (6), $\mathbf{G}$ is the covariance matrix which can be calculated with maximum likelihood and υ are the degrees of freedom of the t-distribution. For $\upsilon = \infty$ the EC-GLRT detector becomes equivalent to AMF. EC-GLRT requires an estimate of the parameter υ, which is hereby estimated for each dataset under test through the minimization of the exceedance metric of (5):

$$\hat{\upsilon} = Arg \min_{\upsilon} M_{exc}(\mathbf{m}, F'_{L,\upsilon}), \tag{7}$$

B. Robust Covariance Matrix Estimation Through Quasi-Local Covariance Shrinkage

A major challenge in achieving simultaneously sensitive and robust detection performance is the estimation of a covariance matrix that is always uncontaminated from the SOI and also close to the true covariance matrix. To achieve this we introduce a covariance estimation scheme where the sample covariance matrix is appropriately merged with an uncontaminated, global covariance matrix derived from an archive of agent-free MSOT images of tissue background. Our covariance estimation approach follows three distinct steps. In a first step, an uncontaminated covariance matrix is estimated by combining the sample covariance matrix of the MSOT image under test and a global covariance matrix that is computed using uncontaminated training data. In a second step, the level of contamination of the image under test is estimated by comparing its sample covariance matrix with a dictionary of uncontaminated ones. Finally, in a third step, the uncontaminated covariance matrix and the sample covariance matrix are appropriately merged based on the estimated level

of covariance contamination. Step one is described in (IV-B-1) and steps two and three are described in (IV-B-2).

1) Estimation of Uncontaminated Covariance Matrix Using Training Data: In MSOT imaging an un-contaminated global covariance matrix can be computed using training data stemming from animals where no molecular agents have been introduced. Fig. 2(a), (b) present two global covariance matrices ($\mathbf{G}^1_{\mathrm{GL}}$ and $\mathbf{G}^2_{\mathrm{GL}}$, respectively) computed from two different mouse datasets (mouse 1 and 2, respectively). Each global covariance matrix was computed as the sample covariance matrix over all pixels of MSOT images spanning the whole body of each mouse and from two different *in vivo* breathing conditions in each case (see Sec. III-A-1). We observe close consistency in the structure of the two covariance matrices. A third mouse dataset was used for investigating differences in the structure of the covariance matrix per anatomical slice and physiological condition. Fig. 2(c) presents the Frobenious norm distance between the normalized global covariance matrix $\mathbf{G}^1_{\mathrm{GL}}/||\mathbf{G}^1_{\mathrm{GL}}||$ and the normalized sample covariance matrices $\mathbf{G}^k_{\mathrm{s}}/||\mathbf{G}^k_{\mathrm{s}}||$ corresponding to different anatomical slices and physiological conditions of mouse 3. Normalization is performed to consider changes in the structure rather than the intensity of the covariance matrix. The covariance matrices of mouse 3 corresponding to the median and the maximum norm distance are presented in Fig. 2(d), (e), respectively. Despite the dramatic differences in anatomy and tissue physiology we observe that the covariance matrix of background-tissue retains a rather consistent structure, indicating the possibility of using training data for covariance estimation.

While $\mathbf{G}_{\mathrm{GL}}$ is uncontaminated, its deviation from the sample covariance matrix of the MSOT image under test may lead to ill background modeling. An alternative quasi-local covariance matrix can be computed through the combination of the global and the sample covariance matrix of the MSOT image under test through the following formula:

$$\mathbf{G}_{\mathrm{QL}} = \mathbf{U}_{\mathrm{GL}}(diag(\mathbf{U}^T_{\mathrm{GL}}\mathbf{G}_s\mathbf{U}_{\mathrm{GL}}))\mathbf{U}^T_{\mathrm{GL}}, \tag{8}$$

In (8) $\mathbf{U}_{\mathrm{GL}}$ is the matrix containing the eigenvectors of $\mathbf{G}_{\mathrm{GL}}$ and $\mathbf{G}_{\mathrm{s}}$ is the sample covariance matrix of the multispectral image under test. *diag* indicates the operator that retains the diagonal elements of the matrix while setting the rest to zero.

$\mathbf{G}_{\mathrm{QL}}$ is uncontaminated by the SOI, as its eigenvectors are not influenced by the target spectrum [13], while it further preserves characteristics of the sample covariance of the data under test. We note that similar covariance estimators have been previously proposed in literature for cases of ill covariance computation due to limited samples [28].

2) Covariance Shrinkage: $\mathbf{G}_{\mathrm{QL}}$ may still deviate from $\mathbf{G}_{\mathrm{s}}$, possibly leading to a reduced detection performance when the data are uncontaminated. Ideally the estimated covariance matrix would vary between $\mathbf{G}_{\mathrm{s}}$ and $\mathbf{G}_{\mathrm{QL}}$ depending on the level of SOI contamination. To achieve this we employ the covariance shrinkage scheme:

$$\mathbf{G}_{\mathrm{est}} = (1-a)\mathbf{G}_s + a\mathbf{G}_{\mathrm{QL}}, \tag{9}$$

where the shrinkage parameter α can vary between 0 (optimal in the case of uncontaminated data) and 1 (optimal in the case of highly contaminated data) adapting to the level of covariance contamination.

The level of contamination could be theoretically estimated through the distance between the sample covariance matrix and the true background covariance matrix, $||\ \mathbf{G}_{\mathrm{s}} - \mathbf{G}_{\mathrm{true}}||_F$. Assuming that the unknown, true covariance matrix lies within a dictionary $\mathbf{D}_{\mathrm{G}}$ of uncontaminated covariance matrices stemming from training MSOT images, the following metric can offer an insight on the level of contamination of the sample covariance matrix:

$$m_c = \underset{\boldsymbol{G}_{\mathbf{true}} \in \boldsymbol{D}_G}{Min} \left\| \frac{\boldsymbol{G}_s}{\|\boldsymbol{G}_s\|_F} - \frac{\boldsymbol{G}_{\mathbf{true}}}{\|\boldsymbol{G}_{\mathbf{true}}\|_F} \right\|_F \tag{10}$$

By means of cross-validation in simulated data, we empirically concluded to the following rule for estimating the shrinkage level using the contamination metric m_c:

$$a = \min\{1, \kappa\sqrt{m_c}\} \tag{11}$$

The empirical rule of Eq. (11) and the selection of the parameter $\kappa = 4$ is explained in (V-B-2). The value of parameter κ was retained constant in all evaluations.

C. Robust Statistical Detection Framework

The hereby proposed statistical detection framework combines the EC-GLRT detector of IV-*A* with the covariance matrix estimation scheme of IV-*B*.

In a first step the sample covariance matrix $\mathbf{G}_{\mathrm{s}}$ of the MSOT image under test is estimated using all available pixels and the level of contamination is assessed through metric m_c of Eq. (10). The covariance matrix dictionary $\mathbf{D}_{\mathrm{G}}$ is computed from the archive of agent-free MSOT images corresponding to the experimental data of Sec. III-*A-1*. We note that in the cross-validation presented in Sec. V, all covariance matrices corresponding to the mouse under test were excluded from the dictionary $\mathbf{D}_{\mathrm{G}}$, which typically includes ~ 200 different covariance matrices. Using the metric m_c, the loading level α is computed according to Eq. (11). The covariance matrix $\mathbf{G}_{\mathrm{est}}$ is estimated through Eq. (9) using the $\mathbf{G}_{\mathrm{QL}}$ covariance matrix of Eq. (8). The $\mathbf{G}_{\mathrm{GL}}$ covariance matrix is estimated from all available agent-free MSOT data of Sec. III-*A*. Similarly to the case of $\mathbf{D}_{\mathrm{G}}$, in the cross-validation presented in Sec. V, all MSOT data corresponding to the mouse under test were excluded from the computation of $\mathbf{G}_{\mathrm{GL}}$.

In a last step, the final detection result is computed. In this step, the MSOT image is initially analysed using the AMF formula of Eq. (3) using $\mathbf{G}_{\mathrm{est}}$ and the detection result $\mathrm{D}_{\mathrm{AMF}}(\mathbf{x}_{\mathrm{i}})$ is compared to a predefined threshold T_{AMF} that is associated with a small false alarm probability (T_{AMF} was selected such that $|\{i \in A : D(\mathbf{x}_i) > T_{AMF}\}| = 0.00002|A|$, where A is the complete set of pixels of the training dataset). If $\mathrm{D}_{\mathrm{AMF}}(\mathbf{x}_i) < T_{\mathrm{AMF}} \forall \mathbf{x}_{\mathrm{i}}$, the AMF has not detected a strong target in the image. In this case, the parameter υ is computed according to Eq. (7) and in the following $\mathrm{D}_{\mathrm{EC-GLRT}}(\mathbf{x}_{\mathrm{i}})$ is computed according to Eq. (6) using $\mathbf{G}_{\mathrm{est}}$ and returned as the output of the detection scheme. If $\mathrm{D}_{\mathrm{AMF}}(\mathbf{x}_i) > \mathrm{T}_{\mathrm{AMF}}$, the AMF has recognized a strong target. In this case, $\mathrm{D}_{\mathrm{AMF}}(\mathbf{x}_{\mathrm{i}})$ is returned as the output of the detection scheme. This latter test is performed for facilitating a better target visualization, as, in the case of

Algorithm 1 Robust Statistical Detection Framework

1. Compute the sample mean $\boldsymbol{\mu}$ and covariance matrix $\mathbf{G_s}$ of the MSOT image $\mathbf{x}$ under test:
$$\boldsymbol{\mu} = \frac{1}{\mathrm{N}} \sum_{i=1}^{N} \boldsymbol{x_i}, \mathbf{G}_s = \frac{1}{N-1} \sum_{i=1}^{N} (\mathbf{x}_i - \boldsymbol{\mu})(\mathbf{x}_i - \boldsymbol{\mu})^T$$
2. Compute $\mathbf{G}_{\mathrm{GL}}$ as the sample covariance matrix over all training data. Compute $\mathbf{G}_{\mathrm{QL}}$ from $\mathbf{G}_{\mathrm{GL}}$ and $\mathbf{G}_{\mathrm{s}}$ according to (8). Compute the covariance matrix dictionary $\mathbf{D}_{\mathrm{G}}$ from each available training MSOT image independently.
3. Estimate the covariance matrix as in:
$$\mathbf{G}_{\mathrm{est}} = (1-a)\mathbf{G}_s + a\mathbf{G}_{\mathrm{QL}}$$
where α is computed from (11) with respect to the metric m_c of (10).
4. If $\mathrm{D}_{\mathrm{AMF}}(\mathbf{x}_i) < T_{\mathrm{AMF}} \forall\ i$, $\hat{\upsilon} = \underset{\upsilon}{Arg\,\min}\, M_{exc}(\mathbf{m}, F'_{L,\upsilon})$, else $\hat{\upsilon} = \infty$.
5. Return: $D(\mathbf{x}_i) = \frac{(\upsilon-1)}{(\upsilon-2)+(\mathbf{x}_i-\mu)^T \mathbf{G}_{\mathrm{est}}^{-1}(\mathbf{x}_i-\mu)} \frac{(\mathbf{s}^T \mathbf{G}_{\mathrm{est}}^{-1}(\mathbf{x}_i-\mu))^2}{\mathbf{s}^T \mathbf{G}_{\mathrm{est}}^{-1} \mathbf{s}}$

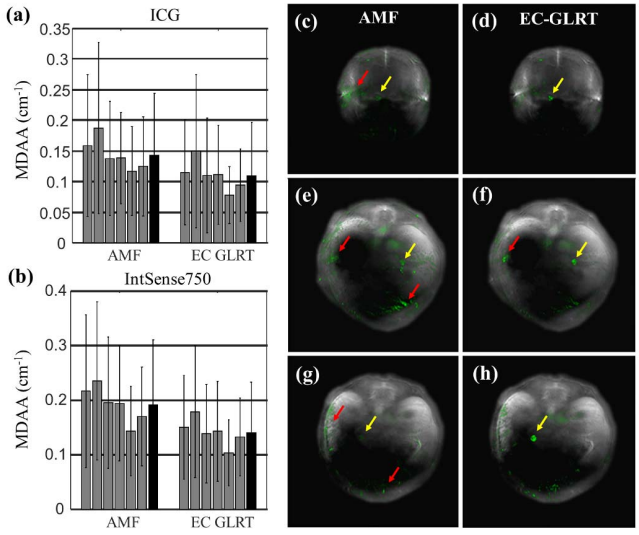

Fig. 3. (a, b) Quantitative comparison of AMF and EC-GLRT in terms of MDAA (see Sec. III-*A-2*) for the cases of ICG (a) and Integrisense750 implanted targets (b). The bar height corresponds to the mean MDAA and the errorbar to the standard deviation over all images employed for evaluation. The six grey errorbars correspond to three different mice imaged at two different physiological conditions each (Sec. III-A-1). The black errorbars correspond to statistics stemming from all data. EC-GLRT with appropriate selection of parameter υ offered consistently a statistically enhanced performance. (c-h) Examples of detection result using AMF (c, e, g) and EC-GLRT (d, f, h) for the same target intensity. The detection result is overlaid onto the anatomical optoacoustic image with green pseudocolor. The yellow arrows point the target positions and the red arrows point the false positives.

strong targets EC-GLRT does not offer optimal visualization due to its intensity normalization property. Algorithm 1 summarizes the hereby proposed detection scheme.

V. Results

A. Performance of EC-GLRT

Figs. 3(a), (b) present a quantitative performance comparison, in terms of MDAA, of AMF vs. EC-GLRT as evaluated using the target implantation framework of Sec. III-*A-2*.

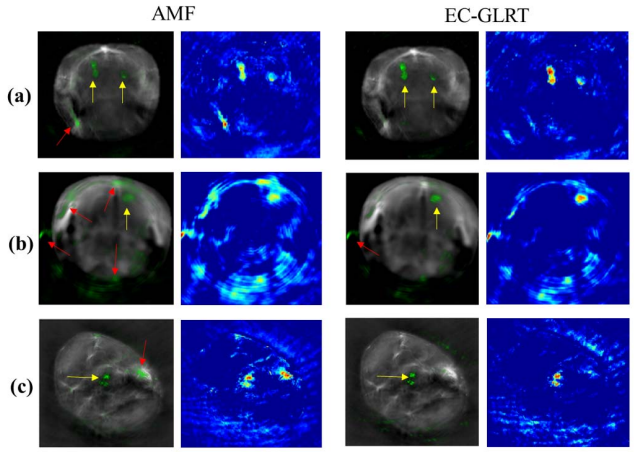

Fig. 4. Comparison of AMF and EC-GLRT in purely experimental data. (a) Mouse brain with two lesions of DiR labelled cells. (b) Mouse brain with a tumor expressing iRFP fluorescent protein. (c) Mouse abdomen with a fluorescent target corresponding to a capillary tube containing AF750. In each case, the detection result is presented standalone on the right side and overlaid onto the anatomical image with green pseudocolor on the left side. Yellow arrows indicate the position of the targets, while red arrows indicate false positives. The standalone detection images corresponding to AMF are presented in square root for facilitating a better visual comparison.

Two different spectral targets are considered, namely ICG (Fig. 3(a)) and IntegriSense750 (Fig. 3(b)). The statistical evaluation was performed using target implantation on all background MSOT images of the imaging dataset (Sec. III-A-1), and 6 different target positions per image. The six grey error-bars correspond to statistics stemming from the three individual mice imaged at two different physiological conditions each. The black error-bars correspond to statistics stemming from all data. The bar height corresponds to the mean MDAA and the error-bar to the standard deviation. According to the quantitative evaluation, EC-GLRT allows for detecting the implanted targets at 20%–30% lower simulated absorbance, therefore offering a statistical performance enhancement that is consistent for all mice and for both implanted targets. Examples of three representative detection cases where the detection result is overlaid onto the anatomical image with green pseudo-color are presented in Fig. 3(c)–(h). The first column (Fig. 3(c), (e), (g)) corresponds to AMF, while the second column (Fig. 3(d), (f), (h)) corresponds to EC-GLRT. For the same target intensity, EC-GLRT resolved the targets (yellow arrows) with less false positives (red arrows) as compared to AMF.

Fig. 4 presents examples of AMF vs EC-GLRT comparison in the case of purely experimental data. Fig. 4(a) corresponds to a case where fluorescently labelled cells have been introduced in the left and right brain hemispheres of a mouse *post mortem* (Sec. III-B-3). Fig. 4(b) corresponds to a mouse brain containing a tumor that is expressing a near infrared fluorescent protein (Sec. III-B-2). Fig. 4(c) corresponds to the dataset described in Sec. III-B-1, where a capillary tube, containing AF750 at an optical density of 0.53 OD has been introduced within tissue. In each case yellow arrows indicate the position of the fluorescent target. In all three cases the detection performance of AMF (first column) is compromised

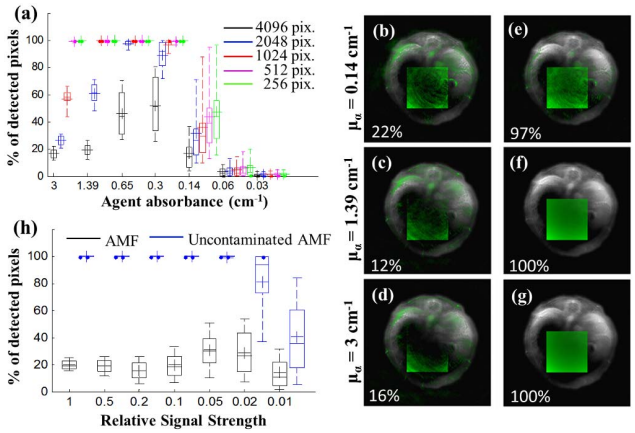

Fig. 5. Effects of covariance contamination on the detection performance of AMF. (a) Statistical evaluation of AMF detection performance in terms of the % of detected pixels (y-axis) for different target sizes (colors) and different target intensities (x-axis), using the target implantation of Sec. III-A-3. Statistics are derived from target implantation on 6 different MSOT images and 6 different target positions per MSOT image. (b-d) Examples of the AMF detection performance in the case of a large target implanted at three different intensities. (e-g) Detection result of uncontaminated AMF for the same targets. (h) Statistical evaluation of the detection performance of standard (black) and uncontaminated AMF (blue) in the case of large targets (4096 pixels) as a function of relative signal strength. Statistics are derived from target implantation on all MSOT images of the experimental dataset (Sec. III-*A-1*).

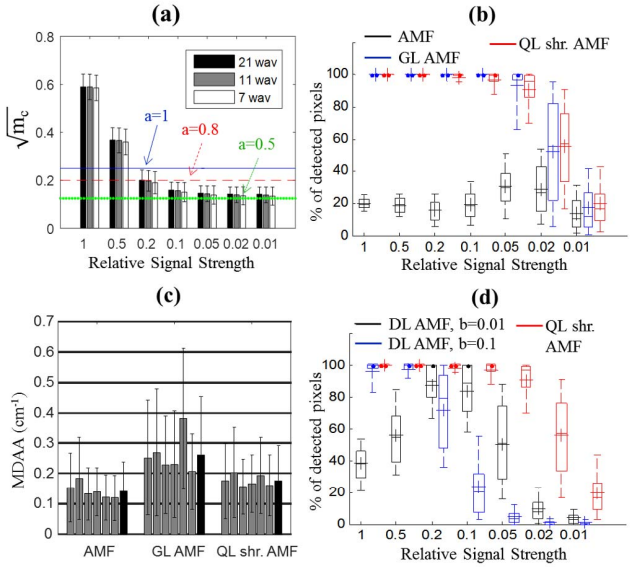

Fig. 6. Evaluation of the QL shrinkage approach.. (a) Values obtained by $\sqrt{m_c}$ (Eq. (10)) under different levels of RSS (x-axis) and under different wavelength sampling approaches (color-bars). The values obtained by α [Eq. (11)] for three different $\sqrt{m_c}$ values are presented with horizontal lines. (b) Performance comparison of AMF, GL AMF, and QL shr. AMF in terms of % of detected pixels in the case of large targets (4098 pixels). Statistics correspond to ICG targets implanted on all background MSOT images. (c) Performance comparison of AMF, GL AMF, and QL shr. AMF in terms of MDAA for the case of small ICG implanted targets. The six grey errorbars correspond to three different mice imaged at two different physiological conditions each. The black errorbars correspond to statistics stemming from all data. (d) Comparison of the detection performance of QL shrinkage (red) and diagonal loading using two different constant loading levels, i.e. $b = 0.1$ (blue) and $b = 0.01$ (black). Statistics in (a)-(d) correspond to target implantation on all experimental data of Sec. III-A-1.

by false positive detection artifacts. Conversely, EC-GLRT (second column) achieves detection of the molecular target with considerably reduced false positives. In each case the detection result is overlaid onto the anatomical image with green pseudocolor (left) and is also presented independently (right) for facilitating a straightforward comparison.

B. Effects of Covariance Contamination and Quasi-Local Covariance Shrinkage

1) Effects of Covariance Contamination: Fig. 5 presents the effects of covariance contamination on the detection performance of AMF. A statistical evaluation of the detection performance of AMF, in terms of percentage of detected pixels, was performed through the implantation of targets of varying sizes, as described in Sec. III-*A-3*. Statistics on the percentage of detected pixels (y axis) for different target sizes (colors) and different target intensities (x axis) are presented in Fig. 5(a). Small targets of 256 pixels (green errorbars) appear fully detectable above a certain simulated agent absorbance. Conversely, in the case of larger targets of 2048 pixels the detection performance is compromised when these targets appear in high intensities, as an effect of covariance contamination. The effects of covariance contamination are more evident in the case of the largest implanted targets (4064 pixels), where the targets are no longer fully detectable at any simulated target intensity. Fig. 5(b)–(d) present the detection result of AMF in the case of a large implanted target for three different simulated intensities. For comparison purposes, Fig. 5(e)–(g) present the ideal detection result of AMF where the uncontaminated background covariance matrix is used instead. Evidently, due to the covariance contamination caused by the large target size, parts of the target are not detectable by AMF at any simulated target intensity. The percentage of detected pixels according to the quantitative evaluation is presented in the lower left part of the individual images.

A more straightforward approach for assessing the performance degradation due to covariance contamination is by investigating the detection performance as a function of the relative signal strength (RSS), i.e. $||T(\mathbf{r}, \lambda)||_2/||\mathrm{B}(\mathbf{r}, \lambda)||_2$, where $T(\mathbf{r}, \lambda)$ represents the implanted target and $\mathrm{B}(\mathbf{r}, \lambda)$ represents the background. Fig. 5(h) presents the detection performance of AMF in the case of large targets (4064 pixels) as a function of RSS (black errorbars). The performance of uncontaminated AMF (blue errorbars) is also presented for comparison. Statistics correspond to targets implanted on all MSOT images of the experimental dataset (Sec. III-*A-1*).

2) Performance of Quasi-Local Covariance Shrinkage: Fig. 6 presents the performance of the proposed quasi-local covariance shrinkage scheme (QL shr. AMF; see Supp. Table I, Appendix). Fig. 6(a) presents the values of $\sqrt{m_c}$ (Eq. (10)) obtained in the case of large ICG implanted targets of 4096 pixels as a function of the RSS. The three different color-bars correspond to wavelength sampling of 21, 10 and 7 equally spaced wavelengths spanning the range of 700-900 nm. The metric m_c appears capable of identifying high levels of covariance contamination (RSS$\geq$ 20%), but there is considerable overlap in its values in low contamination levels (RSS$<$20%). The empirical rule of Eq. (11) and the

value of parameter κ were selected in such a way so that $\alpha = 1$ when the value of m_c indicates a substantial level of contamination (RSS$\geq$ 20%). Due to the overlap of m_c values in the case of low or no contamination, α is typically larger than zero even in uncontaminated cases. The values obtained by m_c under different levels of contamination are relatively unaffected by different wavelength sampling strategies.

Fig. 6(b) presents a quantitative performance comparison of GL AMF (Supp. Table I, Appendix) and QL shr. AMF in the case of large ICG implanted targets of 4096 pixels (high contamination), in terms of % of detected pixels (y-axis) and as a function of RSS (x-axis). The performance degradation of AMF, caused by covariance contamination (black error-bars in Fig. 6(b)), is mitigated by the use of an uncontaminated covariance matrix. In the case of large implanted targets, both GL AMF (blue) and QL shr. AMF (red) offer a comparable performance, successfully mitigating the effects of covariance contamination.

Fig. 6(c) presents a quantitative performance comparison in the case of small ICG targets (uncontaminated case), in terms of MDAA (Sec. III-*A*-2). In the case of small targets GL AMF offers worse detection performance as compared to AMF, increasing the MDAA from 1.5 to 3 times. This performance degradation is expected since in the uncontaminated case, the sample covariance matrix offers better modeling abilities than the global one. QL shr. AMF offers an improved performance with respect to GL AMF, which is only 1.1-1.6 times worse than the one of AMF.

Finally Fig. 6(d) presents a performance comparison of the proposed quasi-local covariance shrinkage approach (QL shr. AMF) and the previously considered diagonal loading scheme (DL AMF; Supp. Table I, Appendix) [12]. A high level of diagonal loading ($b = 0.1$) offers good performance in the case of high target intensities but a considerably reduced performance in the case of low target intensities (blue errorbars). Conversely a lower level of diagonal loading ($b = 0.01$) offers reduced detection performance in the case of high target intensities (black errorbars). Evidently, QL shr. AMF (red errorbars) offers a substantially enhanced performance as compared to DL AMF.

C. Evaluation of Statistical Detection Framework Over Existing Approaches

Fig. 7 compares the performance of the proposed robust statistical detection framework (RSDF) to the one of AMF and to least-squares (LS) spectral fitting [17] which have been previously used in MSOT molecular imaging. In the case of LS fitting the spectra of oxygenated and deoxygenated hemoglobin were used for modeling the tissue background. Fig. 7(a) presents a quantitative comparison in the case of small targets, using the target implantation framework of Sec. III-A-2. According to the simulations, LS fitting offers, on average, 5 times reduced detection performance as compared to AMF and RSDF. AMF and RSDF offer comparable performance. Statistics correspond to all experimental data of Sec. III-A-1. Fig. 7(b) presents the detection results of LS fitting, AMF and RSDF for a representative simulation where

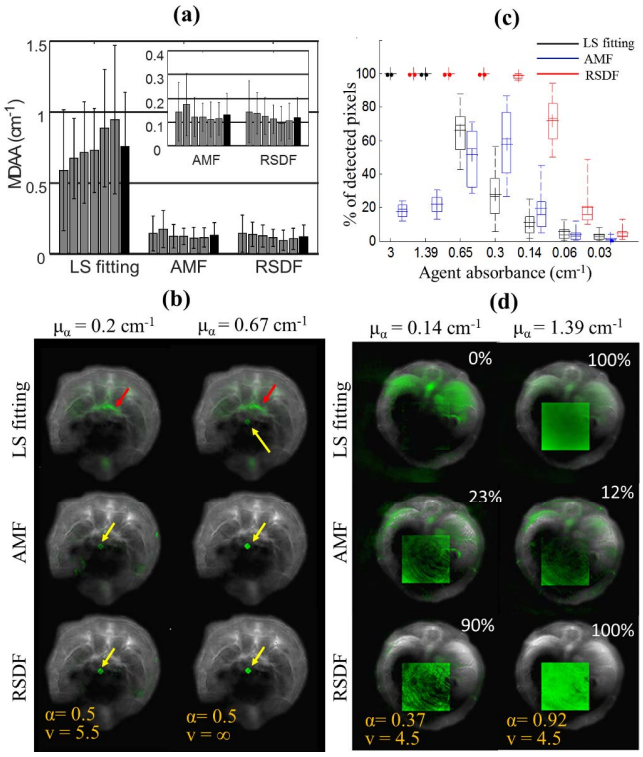

Fig. 7. Quantitative comparison of LS fitting, AMF and RSDF in simulated data. (a) Performance comparison in terms of MDAA for the case of small ICG targets (Sec. III-A-2). The six grey errorbars correspond to three different mice imaged at two different physiological conditions each (Sec. III-A-1). The black errorbars correspond to statistics stemming from all data. (b) Detection examples of LS fitting, AMF and RSDF in two cases where a small ICG target has been implanted in a low (left) and a high (right) intensity. Yellow arrows indicate the position of the target, while red arrows indicate false positives. The parameters α and υ of RSDF are further presented in each case. (c) Performance comparison in terms of % of detected pixels for the case of large (4096 pixel) targets (Sec. III-A-3). Statistics are derived from target implantation on 6 different MSOT images and 6 different target positions per image. (d) Detection examples of LS fitting, AMF and RSDF in two cases where a large ICG target has been implanted at a low (left) and a high (right) intensity. The percentage of detected pixels is presented in each case in the upper right part of the image.

the small ICG target has been implanted onto the experimental MSOT image at two different simulated intensities. The target position is indicated by the yellow arrows while red arrows indicate false positives.

Fig. 7(c) presents a comparison of LS fitting, AMF and RSDF in the case of large targets (4096 pixels), in terms of % of detected pixels. LS fitting offers good detection performance in the case of high target intensities ($\mu_\alpha > 0.65$ cm^{-1}) but a considerably reduced performance in the case of low target intensities. AMF offers reduced detection ability in all simulated target intensities due to the effects of covariance contamination. Conversely, RSDF offers a considerably enhanced performance as compared to AMF and LS fitting. Fig. 7(d) presents the detection results of LS fitting, AMF and RSDF for a representative simulation where the ICG target has been implanted at two different intensities.

Fig. 8 presents detection examples stemming from purely experimental data. The first column corresponds to LS fitting, the second to AMF and the third to RSDF. In the latter

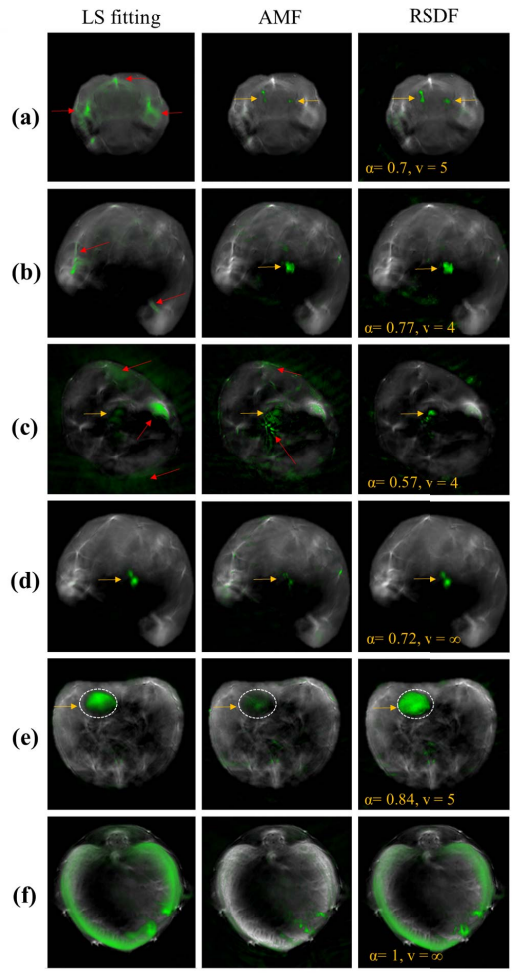

Fig. 8. Comparison of the detection result of LS fitting (left column), AMF (middle column) and RSDF (right column) in the case of purely experimental data. In the latter case the parameters α and υ are presented within the image. (a) DiR labelled macrophages introduced in the left and right brain hemisphere (arrows). (b-d) MSOT images with an insertion of AF790 (b), AF750 at an optical density of approx. 0.25 OD (c) and AF790 at 6.6 OD (d) introduced within tissue (arrows), as described in Sec. III-*B-1*. (e) MSOT images of the abdominal area after systemic injection of 1.2 nmoles of AF750. AF750 accumulates in the area of the bladder (dashed line). (f) MSOT images of the liver after systemic injection 40 nmoles of ICG. In all cases the detection result in overlaid onto the anatomical image with green pseudocolor.

case, the values of α and υ are further presented alongside the images. Fig. 8(a) corresponds to brain images with DiR labelled macrophages (Sec. III-B-3). The position of the cells (yellow arrows) is accurately detected by AMF and RSDF but not by LS fitting which yields substantially stronger false positive detection artifacts. Fig. 8 (b-c) corresponds to the dataset described in Sec. III-B-1 where a capillary tube containing AF790 (b) and AF750 at an optical density of approx. 0.25 OD (c) has been been introduced in deep tissue has been introduced in deep tissue. The location of the fluorochrome (yellow arrows) is detectable only by RSDF (c), or by both AMF and RSDF (b), but not by LS fitting which yields false positives at higher intensities. Fig. 8(d) presents an MSOT image of the same experiment, but in this case the capillary tube has been filled with a high concentration of AF790, corresponding to 6.6 OD. In this case LS fitting and RSDF accurately detect the position of the target, while the performance of AMF is considerably compromised due to the effect of covariance contamination. Fig. 8(e) corresponds to the dataset described in Sec. III-B-5, where the accumulation of AF750 in the bladder is monitored. Again, the detection performance of AMF is compromised due to the large target size, while LS fitting and RSDF accurately detect the fluorochrome bio-distribution in the bladder (dashed line). Finally Fig. 8(f) corresponds to the dataset describe in Sec. III-B-4 where MSOT monitors the accumulation of ICG in the liver. Both RSDF and LS fitting resolve an extensive distribution of ICG in the area of the liver, whereas AMF fails due to the effects of covariance contamination. The detection results of Fig. 8 demonstrate that RSDF combines high molecular imaging sensitivity (Fig. 8(a)–(c)) with a robust performance that is not affected by the target size or intensity (Fig. 8(d)–(f)).

VI. Discussion and Conclusions

Spectral analysis methods play a fundamental role in the ability to extract valuable molecular information from multispectral optoacoustic images. The ultimate goal of spectral unmixing in MSOT imaging is the quantification of the concentrations of all absorbing molecules within tissue. Despite substantial prior work, the quantification of the absorbers' concentrations in experimental *in vivo* images is considered still an open challenge [16].

This work considers the problem of multispectral detection of extrinsic molecular agents in MSOT imaging. As opposed to spectral unmixing, the spectral detection problem seeks to identify the position and area occupied by molecular targets within the tissue [29] and it has a direct application on MSOT molecular imaging. While the multispectral detection problem can be formulated as a binary classification problem, it has some characteristic properties that largely affect the development of appropriate algorithms. *First*, while sufficient data are typically available for accurately training the background class, the sparsity of the targets typically hinders the successful training of the target class. *Second*, the minimization of the misclassification rate is not a good performance metric when the goal is to detect targets that are considerably smaller than the background [5], [6]. For these reasons, practical multispectral detectors typically follow a GLRT approach which seeks to maximize the probability of detection while retaining the probability of false alarm under a predefined threshold (Neyman Pearson criterion) [7]. Moreover, most practical GLRT detectors do not train a target class but assume a linear model of a known target spectrum superimposed on a background that is modeled statistically [5].

GLRT statistical sub-pixel detection has been shown to offer an enhancement in the molecular imaging sensitivity of MSOT [4]. However, common statistical sub-pixel detection algorithms are not optimally suited to the particular characteristics of MSOT molecular imaging. In this work we introduced a robust statistical detection scheme designed according to the characteristics of MSOT molecular imaging. We studied both the aspects of background statistical modeling and covariance

matrix estimation that are key parameters for the design of statistical sub-pixel detectors [19]. This work did not study the effects of spectral mismatch in the detection performance, which will be assessed in future work.

Through a statistical characterization of experimental background-tissue MSOT data we found that the t-distribution appears more accurate in modeling both the main body and the tails of the MSOT data. This observation led to the utilization of a data-adaptive EC-GLRT detector, which in turn offered an enhancement in the detection performance observed both in simulated and experimental data (Fig. 3, 4).

The most significant pitfall of statistical sub-pixel detection in the context of MSOT is the effect of covariance contamination in the cases of extensive presence of the molecular target. Using target implantation simulations of varying target sizes we quantitatively assessed this effect and found that the performance of AMF degrades substantially in the case of large molecular targets (Fig. 5). This effect was also demonstrated in experimental MSOT data (Fig. 8(e), (f)).

For mitigating the effect of covariance contamination we introduced a covariance estimation approach that exploits an archive of training background-tissue MSOT images. Through the comparison of covariance matrices stemming from different anatomical regions and physiological conditions we observed a consistency in the structure, which indicated the possibility of using training data for covariance estimation. However, the simplistic exchange of the sample covariance matrix with a global covariance matrix computed from training data, caused a substantial negative effect on the detection performance in the case of low contamination (Fig. 6), reducing the detection performance up to 3 times. For overcoming this effect we designed a covariance estimation approach, where a quasi-local uncontaminated covariance matrix is appropriately merged with the sample covariance matrix based on the estimated level of the covariance contamination. The proposed covariance estimation scheme offers robust performance that is not affected by covariance contamination, while also retaining good performance in the uncontaminated case. The proposed covariance estimation scheme considerably outperformed diagonal loading, a method previously proposed for mitigating the effects of covariance contamination in hyperspectral remote sensing [12].

The performance of the proposed robust statistical detection framework was evaluated statistically using extensive target implantation simulations and considering targets of different sizes and intensities. The method was found to considerably outperform adaptive matched filter in the case of large targets and the LS fitting approach in the case of weakly absorbing targets. Importantly, RSDF offers an automatic and universal performance independently of the target size or intensity. A number of purely experimental imaging studies further confirmed the direct applicability of the method in experimental molecular imaging data.

ACKNOWLEDGMENT

The authors would like to thank U. Klemm and S. Glasl for assisting in animal handling and image acquisition.

REFERENCES

[1] A. Taruttis and V. Ntziachristos, "Advances in real-time multispectral optoacoustic imaging and its applications," *Nature Photon.*, vol. 9, no. 4, pp. 219–227, 2015.

[2] V. Ntziachristos and D. Razansky, "Molecular imaging by means of multispectral optoacoustic tomography (MSOT)," *Chem. Rev.*, vol. 110, no. 5, pp. 2783–2794, 2010.

[3] N. C. Deliolanis *et al.*, "Deep-tissue reporter-gene imaging with fluorescence and optoacoustic tomography: A performance overview," *Molecular Imag. Biol.*, vol. 16, no. 5, pp. 652–660, 2014.

[4] S. Tzoumas, N. C. Deliolanis, S. Morscher, and V. Ntziachristos, "Unmixing molecular agents from absorbing tissue in multispectral optoacoustic tomography," *IEEE Trans. Med. Imag.*, vol. 33, no. 1, pp. 48–60, Jan. 2014.

[5] D. Manolakis and G. S. Shaw, "Detection algorithms for hyperspectral imaging applications," *IEEE Signal Process. Mag.*, vol. 19, no. 1, pp. 29–43, Jan. 2002.

[6] N. M. Nasrabadi, "Hyperspectral target detection: An overview of current and future challenges," *IEEE Signal Process. Mag.*, vol. 31, no. 1, pp. 34–44, Jan. 2014.

[7] S. M. Kay, *Fundamentals of statistical signal processing: Detection Theory*, vol. 2. Upper Saddle River, NJ, USA: Prentice-Hall, 1998.

[8] F. C. Robey, D. R. Fuhrmann, E. J. Kelly, and R. Nitzberg, "A CFAR adaptive matched filter detector," *IEEE Trans. Aerosp. Electron. Syst.*, vol. 28, no. 1, pp. 208–216, Jan. 1992.

[9] S. Tzoumas, A. Nunes, N. C. Deliolanis, and V. Ntziachristos, "Effects of multispectral excitation on the sensitivity of molecular optoacoustic imaging," *J. Biophoton.*, vol. 8, no. 8, pp. 629–637, 2014.

[10] B. D. Carlson, "Covariance matrix estimation errors and diagonal loading in adaptive arrays," *IEEE Trans. Aerosp. Electron. Syst.*, vol. 24, no. 4, pp. 397–401, Jul. 1988.

[11] J. Theiler and B. R. Foy, "Effect of signal contamination in matched-filter detection of the signal on a cluttered background," *IEEE Geosci. Remote Sens. Lett.*, vol. 3, no. 1, pp. 98–102, Jan. 2006.

[12] S. Niu, S. E. Golowich, V. K. Ingle, and D. G. Manolakis, "Implications and mitigation of model mismatch and covariance contamination for hyperspectral chemical agent detection," *Opt. Eng.*, vol. 52, no. 2, p. 026202, 2013.

[13] D. G. Manolakis, V. K. Ingle, and S. M. Kogon, *Statistical and Adaptive Signal Processing: Spectral Estimation, Signal Modeling, Adaptive Filtering and Array Processing*. Norwood, MA, USA: Artech House, 2005.

[14] B. T. Cox, S. R. Arridge, and P. C. Beard, "Estimating chromophore distributions from multiwavelength photoacoustic images," *J. Opt. Soc. Am. A*, vol. 26, no. 2, pp. 443–455, 2009.

[15] J. Laufer, B. Cox, E. Zhang, and P. Beard, "Quantitative determination of chromophore concentrations from 2D photoacoustic images using a nonlinear model-based inversion scheme," *Appl. Opt.*, vol. 49, no. 8, pp. 1219–1233, 2010.

[16] B. Cox, J. G. Laufer, S. R. Arridge, and P. C. Beard, "Quantitative spectroscopic photoacoustic imaging: A review," *J. Biomed. Opt.*, vol. 17, no. 6, pp. 061202-1–061202-22, 2012.

[17] M.-L. Li *et al.*, "Simultaneous molecular and hypoxia imaging of brain tumors in vivo using spectroscopic photoacoustic tomography," *Proc. IEEE*, vol. 96, no. 3, pp. 481–489, Mar. 2008.

[18] E. J. Kelly, "An adaptive detection algorithm," *IEEE Trans. Aerosp. Electron. Syst.*, vol. 22, no. 2, pp. 115–127, Mar. 1986.

[19] S. Matteoli, M. Diani, and J. Theiler, "An overview of background modeling for detection of targets and anomalies in hyperspectral remotely sensed imagery," *IEEE J. Sel. Topics Appl. Earth Observ. Remote Sens.*, vol. 7, no. 6, pp. 2317–2336, Jun. 2014.

[20] H. Cox, R. Zeskind, and M. Owen, "Robust adaptive beamforming," *IEEE Trans. Acoust., Speech, Signal Process.*, vol. 35, no. 10, pp. 1365–1376, Oct. 1987.

[21] A. Buehler, E. Herzog, D. Razansky, and V. Ntziachristos, "Video rate optoacoustic tomography of mouse kidney perfusion," *Opt. Lett.*, vol. 35, no. 14, pp. 2475–2477, 2010.

[22] A. Rosenthal, D. Razansky, and V. Ntziachristos, "Fast semi-analytical model-based acoustic inversion for quantitative optoacoustic tomography," *IEEE Trans. Med. Imag.*, vol. 29, no. 6, pp. 1275–1285, Jun. 2010.

[23] S. Tzoumas *et al.*, "Immune cell imaging using multi-spectral optoacoustic tomography," *Opt. Lett.*, vol. 39, no. 12, pp. 3523–3526, 2014.

[24] A. Taruttis, S. Morscher, N. C. Burton, D. Razansky, and V. Ntziachristos, "Fast multispectral optoacoustic tomography (MSOT) for dynamic imaging of pharmacokinetics and biodistribution in multiple organs," *PLoS ONE*, vol. 7, no. 1, p. e30491, 2012.

[25] D. G. Manolakis, D. Marden, J. P. Kerekes, and G. A. Shaw, "Statistics of hyperspectral imaging data," *Proc. SPIE*, vol. 4381, pp. 308–316, Aug. 2001.

[26] D. B. Marden and D. G. Manolakis, "Using elliptically contoured distributions to model hyperspectral imaging data and generate statistically similar synthetic data," *Proc. SPIE*, vol. 5425, pp. 558–572, Aug. 2004.

[27] J. Theiler and B. R. Foy, "EC-GLRT: Detecting weak plumes in non-Gaussian hyperspectral clutter using an elliptically-contoured generalized likelihood ratio test," in *Proc. IEEE Int. Geosci. Remote Sens. Symp. (IGARSS)*, Jul. 2008, pp. I-221–I-224.

[28] N. Gorelik, D. Blumberg, S. R. Rotman, and D. Borghys, "Nonsingular approximations for a singular covariance matrix," *Proc. SPIE*, vol. 8390, pp. 839021-1–839021-8, May 2012.

[29] P. Mohajerani, S. Tzoumas, A. Rosenthal, and V. Ntziachristos, "Optical and optoacoustic model-based tomography: Theory and current challenges for deep tissue imaging of optical contrast," *IEEE Signal Process. Mag.*, vol. 32, no. 1, pp. 88–100, Jan. 2015.

Appendix C

Publication: Effects of multispectral excitation on the sensitivity of molecular optoacoustic imaging

The version herein has been published in the "Journal of Biophotonics" [138].

S. Tzoumas, A. Nunes, N.C. Deliolanis, V. Ntziachristos: Effects of multispectral excitation on the sensitivity of molecular optoacoustic imaging. Journal of Biophotonics. 2015. vol. 8. pp. 629-637.

J. Biophotonics **8**, No. 8, 629–637 (2015) / **DOI** 10.1002/jbio.201400056

Journal of BIOPHOTONICS

FULL ARTICLE

Effects of multispectral excitation on the sensitivity of molecular optoacoustic imaging

Stratis Tzoumas[1], *Antonio Nunes*[1], *Nikolaos C. Deliolanis*[2], *and Vasilis Ntziachristos**, [1]

[1] Institute for Biological and Medical Imaging, Helmholtz Zentrum München, German Research Center for Environment and Health, Ingolstädter Landstraße 1, 85764 Neuherberg, Germany, and Chair for Biological Imaging, Technische Universität München, Arcisstraße 21, 80333 Munich, Germany
[2] Fraunhofer Project Group for Automation in Medicine and Biotechnology, 1–2 Theodor-Kutzer-Ufer, 68167 Mannheim, Germany

Received 11 May 2014, revised 27 July 2014, accepted 11 August 2014
Published online 3 October 2014

Key words: Multispectral optoacoustic imaging, molecular imaging, sensitivity

Molecular optoacoustic (photoacoustic) imaging typically relies on the spectral identification of absorption signatures from molecules of interest. To achieve this, two or more excitation wavelengths are employed to sequentially illuminate tissue. Due to depth-related spectral dependencies and detection related effects, the multispectral optoacoustic tomography (MSOT) spectral unmixing problem presents a complex non-linear inversion operation. So far, different studies have showcased the spectral capacity of optoacoustic imaging, without however relating the performance achieved to the number of wavelengths employed. Overall, the dependence of the sensitivity and accuracy of optoacoustic imaging as a function of the number of illumination wavelengths has not been so far comprehensively studied. In this paper we study the impact of the number of excitation wavelengths employed on the sensitivity and accuracy achieved by molecular optoacoustic tomography. We present a quantitative analysis, based on synthetic MSOT datasets and observe a trend of sensitivity increase for up to 20 wavelengths. Importantly we quantify this relation and demonstrate an up to an order of magnitude sensitivity increase of multi-wavelength illumination vs. single or dual wavelength optoacoustic imaging. Examples from experimental animal studies are finally utilized to support the findings.

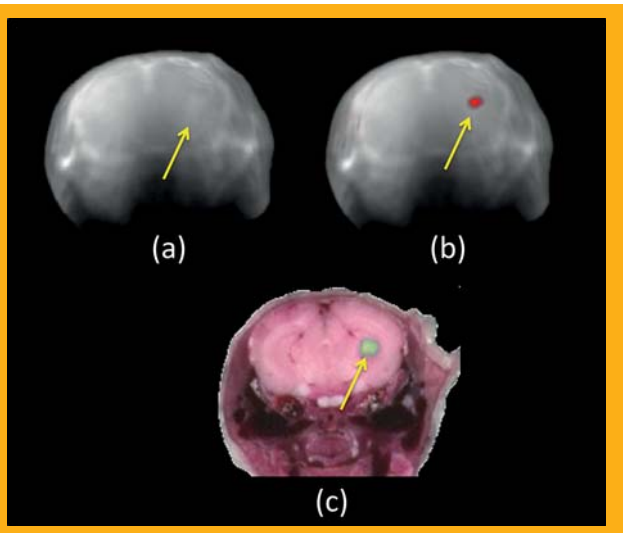

In vivo MSOT imaging of a mouse brain bearing a tumor that is expressing a near-infrared fluorescent protein. (**a**) Monochromatic optoacoustic imaging at the peak excitation wavelength of the fluorescent protein. (**b**) Overlay of the detected bio-distribution of the protein (red pseudocolor) on the monochromatic optoacoustic image. (**c**) *Ex vivo* validation by means of cryoslicing fluorescence imaging.

* Corresponding author: e-mail: v.ntziachristos@tum.de, Phone: +49 89 3187 3852, Fax: +49 89 3187 3017

Journal of BIOPHOTONICS

1. Introduction

Optoacoustic imaging comes with remarkable molecular imaging capabilities, enabling the visualization of optical absorbing agents at high resolution and accurate spatial localization within deep tissue [1]. The ability to image fluorescent dyes [2–4], near-infrared fluorescent proteins [5, 6] or photo-absorbing nanoparticles [7, 8] has been demonstrated in a number of applications. The combination of high resolution imaging with sensing of optical contrast within several mm to cm deep inside tissues leads to new diagnostic or theranostic abilities and provides a novel tool for biological discovery.

The molecular imaging capabilities of optoacoustic imaging relate to the overall ability to reliably resolve the presence of molecules of interest from the absorbing tissue background [9]. For this reason, two or more excitation wavelengths are utilized in many applications in order to enhance the contrast of a specific molecule and enable the accurate visualization of its bio-distribution. Specifically, a number of studies operate using dual wavelength excitation and simple subtraction techniques [10, 11], linear approximations of the spectral unmixing problem [3, 6, 12], correlation based approaches [8], or blind source separation algorithms [13, 14] and adaptive detection approaches [9]. Today, there are no systematic studies offering a thorough relation of these approaches to the performance achieved as a function of the excitation wavelengths, although comparisons of a small set of methods can be found in the literature.

In this work we studied the effect of the number of excitation wavelengths employed on the underlying molecular imaging sensitivity and accuracy. Such relationship has not been yet established. Correspondingly different optoacoustic studies report on the ability to perform molecular imaging without relating the performance achieved to the excitation wavelengths employed. Intuitively, information from additional excitation wavelengths can be effectively used to improve performance in the sense of sensitivity or quantification accuracy. However, a particular complication for studying the relation of wavelength number and MSOT performance is that the MSOT unmixing problem is a complex non-linear and ill-posed open problem [15]. We hereby formulate the unmixing problem of MSOT as a molecular target detection problem and investigate the relative sensitivity achieved using monochromatic, dual wavelength and multispectral optoacoustic tomography as a function of the excitation wavelengths employed. We base our conclusions on a statistical quantitative analysis performed using synthetic MSOT datasets that were created using target implantation on experimental measurements [9]. This analysis is supported by examples from purely experimental *in vivo* data obtained from animals.

2. Background

The wavelength (λ) dependent and position ($\boldsymbol{r}$) dependent multispectral optoacoustic images $P(\boldsymbol{r}, \lambda)$ can be associated to the concentrations of the absorbing molecules through a non-linear relation i.e,

$$P(\boldsymbol{r},\lambda) = C(\boldsymbol{r})\, \Phi(\boldsymbol{r},\lambda) \cdot \sum_i c_i(\boldsymbol{r})\, \varepsilon_i(\lambda) \qquad (1)$$

where $\Phi(\boldsymbol{r}, \lambda)$ is the wavelength dependent unknown optical fluence, $\varepsilon_i(\lambda)$ are the wavelength dependent molar extinction coefficients of the optical absorbers in the sample and $c_i(\boldsymbol{r})$ the unknown associated concentrations at a position $\boldsymbol{r}$. Finally $C(\boldsymbol{r})$ is a scaling factor associated with system effects and the photoacoustic efficiency (Grüneisen parameter $\Gamma(\boldsymbol{r})$).

Many studies have linearly approximated Eq. (1) by assuming constant $\Phi(\boldsymbol{r}, \lambda)$ throughout tissue and invert Eq. (1) for unmixing several photoabsorbing agents using least squares methods [3, 6, 12]. In many cases, spectra of oxygenated ($Hb–O_2$) and deoxygenated (Hb) hemoglobin are typically used for modeling the tissue absorption. This approach may be fairly accurate for superficial tissues, where the optical fluence does not change over the field imaged. But even in such simple cases where some linearity can be efficiently approximated, there is no direct relationship established between the number of wavelengths required as a function of absorbers resolved and the underlying signal to noise ratio available. Moreover, the linear approximation is increasingly non accurate as the imaging depth increases. In deep tissue, the unknown $\Phi(\boldsymbol{r}, \lambda)$ may have a non-straightforward effect on the performance of the inexact linear fitting under different wavelength sampling cases.

Another relatively straightforward approach considered for spectral optoacoustic imaging of an extrinsically administered agent is the use of only two wavelengths [10, 11]. This method is generally considered for opto-acoustic agents with a relatively sharp feature in their spectrum. Typically, the two wavelengths are selected around the sharp spectral feature, i.e. in close spectral proximity. Then the images obtained in the two wavelengths are subtracted and the contrast resolved is attributed to the administered agent under the assumption that the background tissue absorption does not change significantly between these two wavelengths.

Iterative model based inversion approaches have also been suggested to solve Eq. (1) [15–17]. Typically, such approaches attempt to relate the optical fluence dependence $\Phi(\boldsymbol{r}, \lambda; \mu_a(\boldsymbol{r}, \lambda), \mu_s(\boldsymbol{r}, \lambda))$ on tissue optical absorption $\mu_a(\boldsymbol{r}, \lambda)$ and scattering $\mu_s(\boldsymbol{r}, \lambda)$ coefficients, using a light propagation model. In this manner they define a non-linear inversion problem for simultaneously estimating $\Phi(\boldsymbol{r}, \lambda)$ and the concentrations $c_i(\boldsymbol{r})$ of the absorbers. It has been shown in the

simple case of a partially homogeneous phantom [17] that 8 wavelengths can result in accurate inversion. However, no *in vivo* demonstrations have become available with this approach, possibly due to the increased complexity of tissues *in vivo* leading to an ill-posed problem that may be hard to be inverted.

More recently statistical sub-pixel detection techniques [9] were tested in the context of MSOT and were shown to improve upon previous approaches in molecular imaging cases where the molecular target is present in "low probability" within the data (such as cases of tumor targeting or expression of fluorescent proteins). Such methods model the combined effect of tissue absorption and optical fluence as well as any other background spectral perturbation induced due to noise and negative values using a multivariate statistical distribution (typically Gaussian) derived from the available data.

A complication of studying the effect of wavelengths on the detection sensitivity of a spectral target is therefore the strong relation of sensitivity with the unmixing method assumed. An additional complication relates to the particular selection of wavelengths and chromophore employed. Herein, five different implementations of target detection approaches were investigated as described in the methods, to impart a more general understanding of the influence of wavelength number on the MSOT sensitivity in the context of different spectral algorithms.

3. Methods

3.1 Multispectral optoacoustic measurements

Synthetic data and experimental measurements from mice were employed to study the effect of excitation wavelengths on the MSOT detection sensitivity. Both the experimental and synthetic data supporting this study were acquired using two small animal tomographic optoacoustic imaging systems. Specifically, a prototype 64-element MSOT system and a state of the art 256-channel real-time imaging MSOT scanner (iThera Medical GmbH, Kreiling Germany) were employed. The general characteristics of the prototype system are described in [18]. Briefly, the system employs an OPO tunable laser (wavelength range 680–950 nm) for illumination, with 10 Hz pulse repetition rate, and parallel 64-channel ultrasound detection employing a curved ultrasound array. Image acquisition speed is 10 frames per second. The elements of the ultrasound array (5 MHz central frequency with –6 dB of >50%) are deployed in a circular 2-D geometry around the sample (radius 4 cm) covering an angle of 172 degrees. The 256-channel system shares common characteristics with the 64-channel system but utilizes an array of 256 ultrasound elements covering an angle of 270 degrees instead of 64 channels covering 172 degrees. Data from two different systems were used to investigate the generality of the conclusions under different instrumentation conditions. All optoacoustic images were reconstructed using a model-based inversion algorithm described in [19, 20] and Tikhonov regularization in the inversion process.

3.1.1 Synthetic data

The synthetic MSOT data employed in this study were previously described in [9]. The data are formed by applying a target implantation technique on experimental MSOT images of animals acquired *in vivo*. Briefly, experimental multispectral optoacoustic images of a nude mouse (in the areas of brain and kidneys) were acquired *in vivo* using the prototype 64-channel MSOT system, and a spectral target was artificially introduced on the reconstructed images at different positions and in gradually decreasing simulated concentrations. Herein, two different spectral targets were considered. One spectral target assumed the spectrum of Indocyanine Green (ICG) with peak absorption at 780 nm. The second spectral target assumed the spectrum of IntegriSense750 (Perkin-Elmer Inc. Massachusetts, U.S.) with an absorption peak at 750 nm. Therefore four dataset cases were generated, i.e. Brain-ICG, Brain-IntegriSense750, Kidneys-ICG, and Kidneys-IntegriSense750. The spectral target was placed either near the tissue surface (Brain-ICG, Kidneys – IntegriSense750), or deep within tissue (Brain-IntegriSense750, Kidneys – ICG) at 6 distinct and randomly selected positions for each distinct dataset case. The target was always implanted at 25 logarithmically decreasing intensities simulating gradually decreasing agent concentrations corresponding to a peak absorbance from 5 cm^{-1} to 0.01 cm^{-1}. The intensity at each position is defined by the simulated concentration of the spectral target and light intensity in the specific position as computed using a light propagation model and assumptions on tissue optical properties [9].

3.1.2 In-vivo data

To confirm the observations from synthetic data we performed MSOT of animals *in vivo*. A polyester capillary tube (with inner and outer diameters of 0.86 mm and 1.26 mm, respectively) was rectally inserted into an anesthetized CD1 mouse, instead of a rectal thermometer, and the animal was imaged using the 256 channel MSOT system in the lower abdominal area. The capillary tube was iteratively filled with the fluorochrome Alexa Fluor 790 at decreasing concen-

trations corresponding to optical absorption of 15.2 cm^{-1}, 5.06 cm^{-1} and 1,265 cm^{-1}. For this experiment 22 wavelengths were utilized in the range 690 nm to 900 nm with a step size of 10 nm. Additionally, a nude mouse with a brain tumor expressing a near-infrared fluorescent protein (iRFP) was imaged in the head area using the prototype 64-element MSOT system at 12 different wavelengths (690, 695, 700, 705, 710, 715, 720, 730, 750, 770, 800, and 830 nm) [5]. Fluorescence cryoslicing imaging was employed in this case as the gold standard for validating the MSOT studies [21].

3.2 Target detection methods

Five spectral target detection approaches were considered in this study to better understand the effects of different algorithms, wavelength selection approaches, and number of excitation wavelengths employed on the sensitivity achieved.

Method 1 (M1) assumed monochromatic optoacoustic imaging at the peak absorption wavelength of target molecule.

Method 2 (M2) assumed imaging at two wavelengths and subsequent subtraction of the resulting images. Method 2 employed one measurement at a wavelength at the peak of the absorption spectrum and a second measurement intuitively at a wavelength where the spectral target exhibited low absorption but close to the wavelength of the maximum absorption. For ICG the low absorption wavelength was selected at 850 nm. For IntegriSense750 the low absorption wavelength was chosen at 800 nm. For Alexa Fluor 790 the low absorption wavelength was chosen at 890 nm. For iRFP the low absorption wavelength was selected at 730 nm.

Method 3 (M3) was also a subtraction method which performed imaging at 2 wavelengths. Method 3 employed one measurement at a wavelength at the peak of target absorption (as in Method 2) but then iteratively tested all different possibilities for the second wavelength in order to optimize the detection result. This method was only applied in the synthetic dataset, where prior knowledge of the known target was available, in order to identify the best possible result achievable using only two wavelengths. We note that this method is not applicable in practice, where the target location is unknown.

Method 4 (M4) was based on the assumption that the absorbing tissue background can be modeled as a linear mixture of the spectra of hemoglobin:

$$\boldsymbol{x} = \boldsymbol{S}\boldsymbol{A} \tag{2}$$

In Eq. (2), $\boldsymbol{x}$ is the matrix of the multispectral optoacoustic images (with dimensionality $M \times N$, where M is the number of wavelengths and N the number of pixels), $\boldsymbol{S}$ is the $M \times K$ spectrum matrix, with K being the number of components (here $K = 3$, namely oxy- and deoxy- hemoglobin and the agent), and $\boldsymbol{A}$ is the $K \times N$ unknown matrix proportional to the concentrations of the three unmixed components. In this case, the unmixed agent component can be obtained by the third row of matrix $\boldsymbol{A}$. The matrix $\boldsymbol{A}$ is estimated under a least squares approach as in $\boldsymbol{A} = \boldsymbol{S}^{+}\boldsymbol{x}$, where $\boldsymbol{S}^{+}$ is the Moore-Penrose pseudoinverse of matrix $\boldsymbol{S}$. Under the assumption of the linear mixture model (Eq. (2)), three wavelengths are theoretically adequate for unmixing a molecular target from oxy- and deoxy-hemoglobin. In this case the three wavelengths were optimally selected for minimizing the condition number of the spectrum matrix $\boldsymbol{S}$. Specifically the 3×3 matrix $\boldsymbol{S}$ was computed for all possible 3-wavelength combinations, and its condition number was calculated. The matrix $\boldsymbol{S}$ (and the associated wavelength sampling) that is associated with the minimum condition number was selected for spectral unmixing. Similar approaches have been proposed for wavelength selection in optoacoustic imaging [22, 23].

Method 5 (M5) was statistical sub-pixel detection, (assuming multispectral imaging of more than 3 wavelengths) by means of the Adaptive Matched Filter (AMF) [24]. The application of this method in the context of MSOT data is explained in [9]. Briefly,

Table 1 Molecular target detection methodologies.

Name	Method	Wavelength selection
M1	Contrast of single wavelength optoacoustic image	Peak excitation wavelength of fluorochome
M2	Dual wavelength subtraction	First wavelength at peak excitation and intuitively selected second wavelength.
M3	Dual wavelength subtraction	First wavelength at peak excitation and optimally selected second wavelength
M4	Linear unmixing with hemoglobin spectra and agent spectrum.	3 wavelengths selected for minimizing the condition number of spectrum matrix $\boldsymbol{S}$.
M5	Adaptive Matched Filter	Uniformly sampled

* Selected methodologies for molecular opotacoustic imaging.

the unmixed agent component at a specific position $\boldsymbol{r}$ is given by the following equation:

$$D(\boldsymbol{x}_r) = \frac{1}{\boldsymbol{s}^T\boldsymbol{\Sigma}^{-1}\boldsymbol{s}} \cdot \boldsymbol{s}^T\boldsymbol{\Sigma}^{-1}(\boldsymbol{x}_r - \boldsymbol{\mu}) \quad (3)$$

where $\boldsymbol{x}_r$ is the $M \times 1$ data vector corresponding to position $\boldsymbol{r}$, $\boldsymbol{s}$ is the $M \times 1$ spectrum of the target agent, and $\boldsymbol{\Sigma}$ and $\boldsymbol{\mu}$ are the assumed covariance and mean of the background, respectively. To understand the performance of this method in relation to the number of wavelengths employed we applied the AMF algorithm for a different number of uniformly sampled wavelengths, i.e. for 20, 16, 13, 10, 8, 7, 5, 4 wavelengths

As evident from the selection of methods herein, only Method 5 can examine the effect of an increasing number of wavelengths on the MSOT accuracy. Therefore the selection of methods 1–4 is done for comparison purposes, in order to better understand the importance of illumination wavelengths against established optoacoustic methods utilizing 1 or 2 wavelengths or methods that seek to minimize wavelengths by following an optimal wavelength selection strategy. Methods 2, 4 are often employed in the literature since many optoacoustic studies today generate measurements at a small number of wavelengths. We note that wavelength selection prior to measurements presupposes exact knowledge of the optoacoustic spectra of tissue, and thus it becomes possible only under the assumption of the linear mixture model with hemoglobin. In the last category (M5) we selected the AMF since it has been shown to outperform linear unmixing approaches for such confined spectral targets [9]. In the context of AMF it is not possible to select the excitation wavelengths in an optimal sense prior to imaging. For this reason, in the case of AMF we selected an equidistant distribution of wavelengths.

3.3 Sensitivity analysis

Each of Methods 1–5 used with a certain synthetic dataset was applied sequentially to data obtained from all the spectral target titrations corresponding to a simulated peak absorption coefficient from $\mu_a^{sim} = 5$ cm^{-1} to $\mu_a^{sim} = 0.01$ cm^{-1}. This was performed in order to determine the value of agent absorbance for which the spectral target was no longer visible using a specific detection method. Visibility was defined as a relation between true positive and false positive detected pixels using a metric defined in [9]. Specifically, a target is considered invisible if the mean value of the true positive detected pixels is smaller than the mean value of false positives (i.e. non-target pixels with detection values higher than the mean detection values of the target). Examples

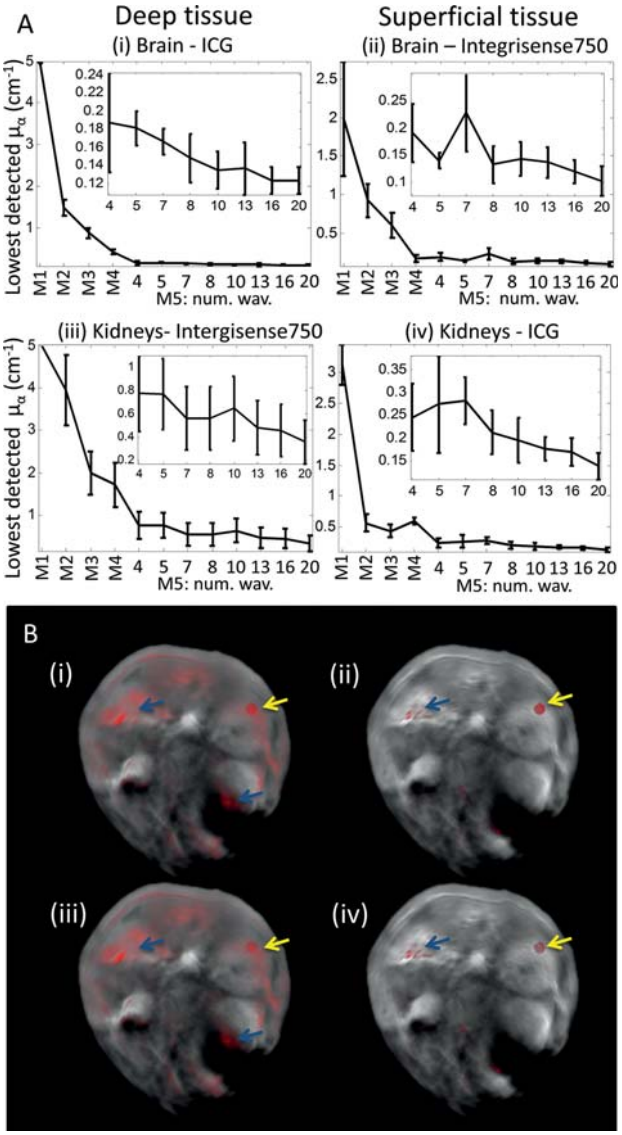

Figure 1 (**A**). Quantitative analysis of MSOT sensitivity (*y*-axis) as a function of wavelengths. The graphs correspond to the synthetic datasets of (**i**) Brain – ICG, (**ii**) Brain – IntegriSense750, (**iii**) Kidneys – IntegriSense750, (**iv**) Kidneys – ICG. (**B**). Detection examples from the Kidneys – ICG dataset. (**i**), (**ii**) Detection examples for marginally detected targets using M3 and M5 respectively. (**iii**), (**iv**) Detection examples for targets considered undetected using M3 and M5 respectively.

of marginally visible targets and targets that are considered invisible, according to this metric, are presented in Figure 1. Correspondingly, sensitivity is defined herein as the minimum simulated absorbance of a spectral target that is necessary for the accurate extraction of its bio-distribution from the absorbing tissue background. A sensitivity matrix is computed for each distinct dataset (e.g. Brain – ICG) after applying each method to all 6 image instances corresponding to the different target locations. In the fol-

Journal of BIOPHOTONICS

lowing statistics corresponding to the mean and the standard deviation of the sensitivity matrix are computed and presented for comparison of the different approaches.

4. Results

4.1 Synthetic data

Figure 1A presents a quantitative analysis of the four synthetic data cases employed herein and depicts the MSOT sensitivity as a function of wavelengths and spectral method selected. Lower μ_a values in the y-axis indicate better sensitivity. The values in each graph correspond to the mean sensitivity values calculated for 6 different randomly selected positions of the implanted target, and the error bars correspond to the standard deviation from all 6 target positions. Figure 1B presents two detection examples from the Kidneys – ICG dataset with the detection result superimposed on the anatomical image using red color. Figure 1B (i) and (iii) correspond to the detection result obtained using M3 when the target was implanted at a simulated absorbance of 0.38 cm^{-1} and 0.29 cm^{-1}, respectively. Figure 1B (ii) and (iv) correspond to the detection result obtained using M5 with 20 wavelengths when the target was implanted at a simulated absorbance of 0.17 cm^{-1} and 0.13 cm^{-1}, respectively. The molecular target is considered marginally visible in Figure 1B (i) and Figure 1B (ii), and invisible in Figure 1B (iii) and Figure 1B (iv), according to the visibility metric employed. The yellow arrows on the figures indicate the position of the implanted target while the blue arrows indicate false positive detected areas.

Table 2 summarizes ratios that quantitatively demonstrate the sensitivity enhancement achieved using (i) M5 with 20 excitation wavelengths as compared to monochromatic optoacoustic imaging (M1), (ii) M5 with 20 excitation wavelengths as compared to M2, (iii) M5 with 20 excitation wavelengths as compared to M3, (iv) M5 with 20 excitation wavelengths as compared to M4 and (iv) M5 with 20 excitation wavelengths as compared to M5 with 4 excitation wavelengths.

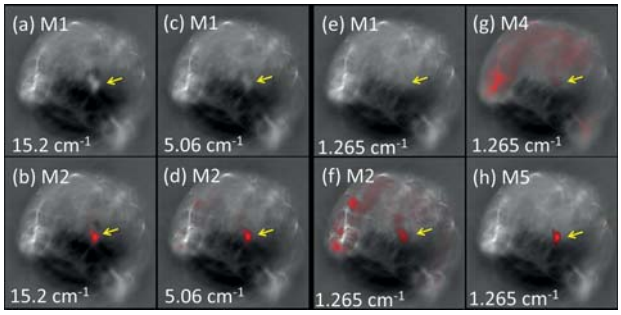

Figure 2 Visual comparison of the detection results of monochromatic optoacoustic imaging using M1 (**a**, **c**, **e**), dual wavelength imaging using M2 (**b**, **d**, **f**), 3 wavelength imaging (specifically 690 nm, 790 nm and 900 nm) using M4 (**g**) and multispectral optoacoustic imaging using M5 and 22 wavelengths (**h**), in the case of a fluorochrome present in deep tissue in varying concentrations. The yellow arrows point at the expected position of the fluorochome.

4.2 In vivo data

Figure 2 depicts the images from the *in vivo* mouse study obtained from the lower abdominal area for different methods and fluorochrome concentrations. Figure 2(a), (c), (e) show the detection result obtained by Method 1 for 15.2 cm^{-1}, 5.06 cm^{-1} and 1.265 cm^{-1} respectively. Without spectral differentiation it is difficult to understand where the spectral target is located only by observing the image. However since we know by means of the controlled experiment that the fluorochrome is located at the area pointed to by the yellow arrow, it is clear that the fluorochrome can be seen at 15.2 cm^{-1} and 5.06 cm^{-1} but virtually disappears at 1.265 cm^{-1}.

Figure 2(b), (d), (f) shows the corresponding results when using M2. Image subtraction allows for the generation of a "spectral target" image which can be superimposed on the "anatomical" image using red color in this case. This improves the ability

Table 2 Quantitative ratios, demonstrating the sensitivity enhancement achieved under different spectral methods and as a function of wavelengths.

Dataset	Sensitivity comparison				
	(i)*	(ii)	(iii)	(iv)	(v)
(a) Brain – ICG	40.6	12.2	7.3	3.7	1.5
(b) Brain –Integr. 750	19.5	9	5.9	1.7	1.9
(c) Kidneys – ICG	21.1	3.9	3	4.1	1.8
(d) Kidneys – Integr. 750	14	11.1	5.6	4.8	2.2

* Sensitivity enhancement of M5 (20 wav.) vs. (i) M1, (ii) M2, (iii) M3, (iv) M4, (v) M5 (4 wav.).

to understand the presence of a spectral target on the image, as demonstrated by comparing for example Figure 2(c) to (d). Method 2 also shows that in contrast to Method 1, it can also resolve the spectral target at the 1,265 cm^{-1} absorbance (Figure 2(f)). However, Figure 2(f) also reveals that several false signals appear on the image which compromise the overall accuracy of the method. The false signals can be attributed to spectral differences in other areas of the tissue, due to the wavelength dependent tissue absorption.

Finally, Figure 2(g), (h) show the corresponding results of Method 4, and Method 5 utilizing 22 wavelengths, respectively, applied in the case of the 1.265 cm^{-1} absorbance. In the case of M4 (Figure 2 (g)) false positives in irrelevant parts of the image compromise the ability of the method to detect the target. In the case of M5 (Figure 2(h)) the target appears accurately detected with minimal false positives.

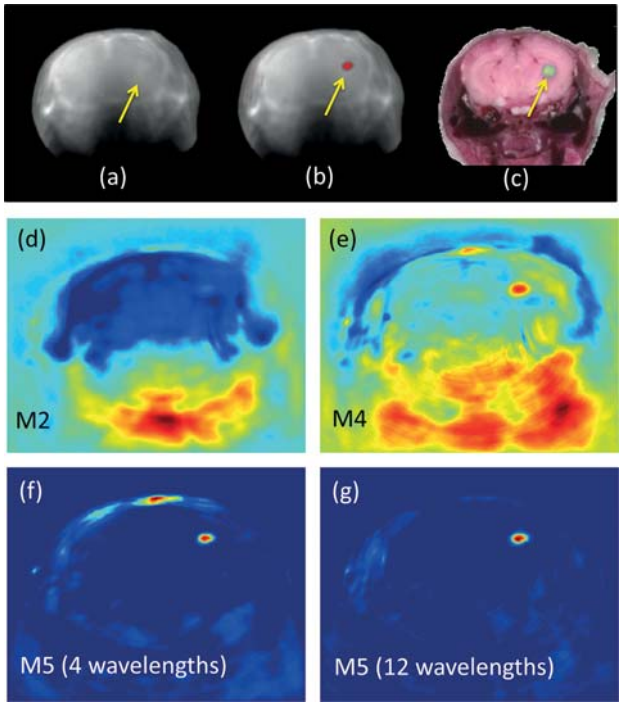

Figure 3 Visual comparison of the detection results of different molecular optoacoustic methods in the case of *in vivo* MSOT imaging of a mouse brain bearing a tumor that is expressing a fluorescent protein. (**a**) Monochromatic optoacoustic imaging at the peak excitation wavelength of the fluorescent protein (M1). (**b**) Overlay of the detection result using M5 with 12 excitation wavelengths, and the anatomical optoacoustic image. (**c**) Validation of the position of the fluorescent protein by means of cryoslicing fluorescence imaging. (**d**–**g**) Detection result using: (**d**) M2 (selected wavelengths 680 nm and 730 nm), (**e**) M4 (selected wavelengths 700 nm, 750 nm and 830 nm), (**f**) M5 with four excitation wavelengths (700 nm, 715 nm, 750 nm and 830 nm) and (**g**) M5 using 12 excitation wavelengths.

Figure 3 presents results from the *in vivo* study imaging a brain tumor expressing iRFP. Figure 3(a) presents the monochromatic optoacoustic image at the peak absorption wavelength of the fluorescent protein, whereby it is not possible to identify the tumor cells. Figure 3(b) presents the detection result when using Method 5 with 12 wavelengths, overlaid to the anatomical image. Figure 3(c) presents the validation using cryoslicing fluorescent imaging. Figure 3(d) depicts the detection result from the *in-vivo* brain tumor study when using M2. Figure 3(e) presents the corresponding detection result when using M4, Figure 3(f) shows the detection result when using M5 with 4 wavelengths, and Figure 3(g) shows the detection result when using M5 with 12 wavelengths.

The results visually represent in the *in vivo* case a performance similar to the one observed on Figure 1 for synthetic data, i.e. that an increase in the number of wavelengths and use of the AMF algorithm can improve the *in vivo* detection sensitivity and accuracy by suppressing false positive detection artifacts.

5. Discussion

Sensitivity is an important parameter in MSOT and overall optoacoustic imaging, which is not yet thoroughly studied in literature, mainly due to the dependence on several parameters including depth, tissue optical properties and imaging methodology employed. By identifying optimal strategies for sensitive MSOT imaging one can ultimately also approach the issue of accurately quantifying the sensitivity of each strategy based on a validated methodology. In this study we opted to establish a relation between the number of illumination wavelengths employed and the sensitivity achieved. We showed quantitatively what can be also intuitively understood, that the sensitivity of molecular optoacoustic imaging depends on the number of excitation wavelengths employed and cannot be defined independently of their number.

The fundamental question of the effect of multiple excitation wavelengths on the performance of optoacoustic imaging is however not only of theoretical significance in determining the sensitivity of the optoacoustic method but also required in the design of appropriate optoacoustic systems and experimental protocols. However, a complication in addressing this question relates to the spectral unmixing approach assumed. Different spectral unmixing algorithms have been considered and more may be proposed in the future. The overall performance depends on a number of parameters such as the properties of the tissue and the spectral target, the particular system and geometry employed and the

mathematical method considered for image reconstruction. In this study we selected to employ the AMF algorithm that has been recently shown to be superior to linear unmixing methods as it allows accurate spectral detection independently of assumptions of the background tissue properties or optical fluence present. In that respect the AMF approach is robust for *in vivo* measurements under the assumption of sparse spectral agent distribution, as the case of fluorochromes targeting spatially localized lesions. To understand this method and the effect of wavelengths in the context of simpler optoacoustic studies considered so far we also utilized a single wavelength (Method 1), two dual-wavelength subtraction methods (Method 2, Method 3), as well as a method that seeks to minimize the excitation wavelengths employed through an optimal wavelength selection approach (Method 4).

The particular strategy followed for wavelength selection presents an additional complication for studying the sensitivity as a function of the excitation wavelengths employed. Optimal wavelength selection prior to imaging can only be considered under the assumption of an a priori structured model that describes the background spectral variability. Currently, wavelength selection approaches have only been considered under the assumption that tissue background follows a linear mixture model with the spectra of hemoglobin, which does not consider depth related nonlinearities, noise and reconstruction related effects. One such approach has been included herein for reasons of consistency. In the case of statistical sub-pixel detection algorithms, such as AMF, a similar wavelength selection approach cannot be followed, due to the fact that the spectral tissue background is not considered known, but is modelled from the available data. For this reason, in the case of the AMF we followed a uniform wavelength sampling approach.

Studies were performed on both simulated (synthetic) and *in vivo* data. Synthetic data help better understand the effect of different parameters on the result, as they offer full control of the experimental parameters. *In vivo* studies then helped confirm the observations on synthetic data under realistic *in vivo* experimental conditions. The findings clearly demonstrate that MSOT can effectively enhance the sensitivity over monochromatic optoacoustic imaging in the order of 14–40 times (Figure 1). This indicates that the sensitivity of MSOT is more than an order of magnitude better than single wavelength optoacoustic imaging when detecting spectral moieties, a result that was previously undocumented. Compared to dual-wavelength subtraction methods, MSOT studies at >10 wavelength further reveal a significant sensitivity enhancement that can also reach up to an order of magnitude, even in cases whereby the target absorption spectrum is sharp; a requirement for subtraction methods. The experimental results in Figures 2 and 3 confirm the results of the synthetic data quantitative evaluation, showing the ability of MSOT to accurately extract a fluorochrome deep within tissue *in vivo*, at the optical density which cannot be accurately retrieved by monochromatic or subtraction methods. This is optimally demonstrated in the tumor imaging example shown in Figure 3 whereby only Method 5 at 12 wavelengths accurately resolves the genetically modified cells.

The quantitative evaluations on synthetic data indicate a rather consistent trend of sensitivity enhancement with wavelengths when using an adaptive detection algorithm (namely AMF). When using 20 wavelength, the sensitivity can be enhanced up to more than 4 times as compared to 3 optimally selected wavelengths and linear unmixing, showing that a frequently followed assumption that that three wavelengths are adequate for unmixing blood and a single fluorochrome can be an oversimplification. Since the spectral unmixing problem is non-linear, and the background tissue spectral perturbations are additionally affected by a multitude of noise and reconstruction related factors, more wavelengths can indeed offer better tissue modeling capabilities. Specifically, we observed a rather consistent performance enhancement of doubling the sensitivity in the cases between 4 and 20 wavelengths.

Finally we observed that in certain cases (e.g. Figure 1A (ii)) using less wavelengths can result in equivalent or better performance than more. Indeed it is theoretically possible that less wavelength may result in better class separability between the target agent and the absorbing background [25]. In this respect, class separability metrics have been proposed for identifying optimal wavelength subsets in order to optimize the detection performance [25]. However when statistical detection methods are concerned, wavelength selection is a post-processing step, since such wavelength rejection methods presuppose that all wavelengths have been previously acquired.

6. Conclusion

In conclusion, multiple excitation wavelengths and appropriate unmixing algorithms have a major impact on sensitivity as compared to single or dual wavelength optoacoustic imaging. Moreover, sensitivity exhibits a statistical trend of increase with the number of wavelengths employed. Wavelength selection may have an additional impact on the sensitivity achievable. However, wavelength selection is generally based on approximate and rather inaccurate models for background absorption spectral variability. In this respect, the employment of more excita-

tion wavelengths provides higher probability to accurately capture and account for the absorption spectral variability, and thus better probability for sensitive molecular imaging. The statistical evaluation of Figure 1 can be considered for general guidance in selecting the number of wavelengths desired.

This study investigated the effect of the excitation wavelengths on the sensitivity of molecular optoacoustic imaging. This study did not establish the exact sensitivity limits under different scenarios. This latter case is the object of follow up studies which would have to take into consideration the reported results and define then sensitivity for a particular system and experimental scenario under assumptions specific to the problem studied.

Conflict of interest Vasilis Ntziachristos declares financial interests with the company iThera Medical, GmbH.

Author biographies Please see Supporting Information online.

Acknowledgements All animal experiment were approved by the District Government of Upper Bavaria. The work of S. Tzoumas was supported by the DFG GRK 1371 grant and the Alexander S. Onassis Public Benefit Foundation. The work of V. Ntziachristos was supported by the European Union project FAMOS (FP7 ICT, Contract 317744).

References

[1] V. Ntziachristos and D. Razansky, Chemical Reviews **110**, 2783 (2010).
[2] E. Herzog, A. Taruttis, N. Beziere, A. A. Lutich, D. Razansky, and V. Ntziachristos, Radiology **263**, 461 (2012).
[3] M. Li, J. Oh, X. Xie, G. Ku, W. Wang, C. Li, G. Lungu, G. Stoica, and L. V. Wang, PROCEEDINGS-IEEE **96**, 481 (2008).
[4] A. Taruttis, M. Wildgruber, K. Kosanke, N. Beziere, K. Licha, R. Haag, M. Aichler, A. Walch, E. Rummeny, and V. Ntziachristos, Photoacoustics **1**, 3 (2013).
[5] N. C. Deliolanis, A. Ale, S. Morscher, N. C. Burton, K. Schaefer, K. Radrich, D. Razansky, and V. Ntziachristos, Molecular Imaging and Biology **1** (2014).
[6] G. S. Filonov, A. Krumholz, J. Xia, J. Yao, L. V. Wang, and V. V. Verkhusha, Angewandte Chemie International Edition **51**, 1448 (2012).
[7] J.-W. Kim, E. I. Galanzha, E. V. Shashkov, H.-M. Moon, and V. P. Zharov, Nature Nanotechnology **4**, 688, (2009).
[8] S. Mallidi, T. Larson, J. Tam, P. P. Joshi, A. Karpiouk, K. Sokolov, and S. Emelianov, Nano Letters **9**, 2825 (2009).
[9] S. Tzoumas, N. Deliolanis, S. Morscher, and V. Ntziachristos, IEEE Transactions on Medical Imaging **33**, 48 (2014).
[10] R. A. Kruger, W. L. Kiser, D. R. Reinecke, G. A. Kruger, and K. D. Miller, Molecular Imaging **2**, 113 (2003).
[11] L. Li, H. F. Zhang, R. J. Zemp, K. Maslov, and L. V. Wang, Journal of Innovative Optical Health Sciences **1**, 207 (2008).
[12] D. Razansky, M. Distel, C. Vinegoni, R. Ma, N. Perrimon, R. W. Koster, and V. Ntziachristos, Nature Photonics **3**, 412 (2009).
[13] J. Stritzker, L. Kirscher, M. Scadeng, N.C. Deliolanis, S. Morscher, P. Symvoulidis, K. Schaefer, Q. Zhang, L. Buckel, and M. Hess, Proceedings of the National Academy of Sciences **110**, 3316 (2013).
[14] J. Glatz, N. C. Deliolanis, A. Buehler, D. Razansky, and V. Ntziachristos, Optics Express **19**, 3175 (2011).
[15] B. Cox, J. G. Laufer, S. R. Arridge, and P. C. Beard, Journal of Biomedical Optics **17**, 61202 (2012).
[16] B. Cox, S. Arridge, and P. Beard, JOSA A **26**, 443 (2009).
[17] J. Laufer, B. Cox, E. Zhang, and P. Beard, Applied Optics **49**, 1219 (2010).
[18] D. Razansky, A. Buehler, and V. Ntziachristos, Nature Protocols **6**, 1121 (2011).
[19] A. Rosenthal, D. Razansky, and V. Ntziachristos, IEEE Transaction on Medical Imaging **29**, 1275 (2010).
[20] X. L. Dean-Ben, V. Ntziachristos, and D. Razansky, IEEE Transactions on Medical Imaging **31**, 1154 (2012).
[21] A. Sarantopoulos, G. Themelis, V. Ntziachristos, Molecular Imaging and Biology **13**, 874–885 (2011).
[22] G. P. Luke, S. Y. Nam, and S. Y. Emelianov, Photoacoustics **1**, 36 (2013).
[23] Z. Yuan and H. Jiang, Optics Letters **34**, 1714 (2009).
[24] F. C. Robey, D. R. Fuhrmann, E. J. Kelly, and R. Nitzberg, IEEE Transactions on Aerospace and Electronic Systems **28**(1), 208–216, 1992.
[25] N. Keshava, in: 2001 IEEE International Conference on Acoustics, Speech, and Signal Processing, Proceedings (ICASSP'01), 3149–3152.

Appendix D

Publication: Immune cell imaging using multi-spectral optoacoustic tomography

The version herein has been published in the journal "Optics Letters" [139]. It is hereby reprinted with permission.

Immune cell imaging using multi-spectral optoacoustic tomography

Stratis Tzoumas,† Angelika Zaremba,† Uwe Klemm, Antonio Nunes, Karin Schaefer, and Vasilis Ntziachristos*

Institute for Biological and Medical Imaging (IBMI), Technische Universität München and Helmholtz Zentrum München, German Research Center for Environment and Health, Ingolstädter Landstrasse 1, 85764 Neuherberg, Germany

**Corresponding author: v.ntziachristos@tum.de*

Received March 24, 2014; accepted April 26, 2014;
posted May 6, 2014 (Doc. ID 208229); published June 9, 2014

Multispectral optoacoustic tomography (MSOT) offers the potential to image in high-resolution cells tagged with optical labels. In contrast to single wavelength imaging, multispectral excitation and spectral unmixing can differentiate labeled moieties over tissue absorption in the absence of background measurements. This feature can enable longitudinal cellular biology studies well beyond the depths reached by optical microscopy. However, the relation between spectrally resolved fluorescently labeled cells and optoacoustic detection has not been systematically investigated. Herein, we measured titrations of fluorescently labeled cells and establish the optoacoustic signal generated by these cells as a function of cell number and across different cell types. We then assess the MSOT sensitivity to resolve cells implanted in animals. © 2014 Optical Society of America

OCIS codes: (170.5120) Photoacoustic imaging; (170.3880) Medical and biological imaging; (170.1530) Cell analysis.
http://dx.doi.org/10.1364/OL.39.003523

Microscopy plays a critical role in cell biology, enabling observations of cell–cell and cell–host interactions *in vivo* [1]. However, the limited penetration of microscopy methods only allows superficial observations. Many applications, however, require cell imaging at different scales. Recent cell-based therapy studies, including cell-based cancer immunotherapy and stem cell treatments, have shown the potential of cell therapy to develop into a novel therapeutic platform. Various therapeutic cell types, such as T cells, dendritic cells and natural killer cells are administered to cancer patients after *ex vivo* manipulation to target and inhibit tumor growth, with significantly fewer side effects on normal cells [2]. Likewise, macrophages have been considered for treating cancer, fibrosis, and inflammation [3–5]. However, the assessment of therapeutic cell bio-distribution largely relies on *ex vivo* examinations. As a result, the migration and targeting of cells and underlying dynamic processes have not yet been fully elucidated, even though critical for understanding the mechanisms leading to successful treatment.

Imaging methods that allow the macroscopic visualization of cell bio-distribution through entire living organisms have been considered, but come with their own limitations. The most popular modality, bioluminescence imaging (BLI), is fundamentally limited by a lack of quantification. The signal recorded in BLI is a surface-weighted low resolution photon intensity signal, with limited ability to accurately resolve its spatial origin in three dimensions or relate this signal to the number of cells generating it. Fluorescence epi-illumination imaging (FEI) comes with similar limitations. Diffuse optical tomography approaches and nuclear imaging methods, such as fluorescence molecular tomography (FMT) or Positron Emission Tomography, respectively, have also been considered. They typically offer three-dimensional imaging ability and better quantification capacity over BLI or FEI, but are similarly limited by resolution that is no better than 1 mm in small animals and worse in larger animals. Overall, nuclear imaging techniques are further limited by the need to employ radioisotopes, which decay and do not enable long-term observations. Conversely, optical methods, such as FMT, allow for longitudinal studies but are less sensitive to nuclear methods, particularly as the depth of the activity increases. High-resolution radiologic methods, such MRI and x-ray CT are less frequently regarded for imaging cells due to their low sensitivity.

With the advent of multispectral optoacoustic tomography (MSOT), there are novel possibilities for macroscopic cell imaging. MSOT can offer optical contrast in high-resolution, beyond the penetration depth of conventional microscopy. The ability to image un-labeled, highly absorbing cells [6], or cells labeled with fluorescent proteins and nanoparticles, has been already demonstrated [7–9]. However, no systematic study has been so far performed to assess MSOT sensitivity in immune cell imaging.

In this Letter, we take a first step toward relating MSOT signals to the spectrally resolved absorption properties of labeled immune cells. A particular MSOT feature is the use of multiwavelength illumination and the application of spectral unmixing techniques to capture the spectra of different absorbing moieties. Recently, we have reported on the use of statistical sub-pixel detection techniques [10] yielding sensitive and accurate MSOT sensing, beyond the capacity of linear unmixing methods. Of particular importance was to identify the sensitivity of MSOT combined with appropriate spectral processing methods for the application of cell imaging. We employ these methods herein, for understanding the detection ability for cells labeled with fluorescent dyes. From an optoacoustic detection standpoint, fluorescent labels present perhaps a worst case scenario for cell imaging with MSOT over other labeling methods, such as gold nanoparticles [11]. From a biology point of view, however, fluorescent labels are better established and characterized. Importantly, fluorescent labels come with the advantage that the cells can be also visualized by traditional optical methods, for example fluorescence

microscopy, to better understand the loading and other biological parameters.

For MSOT measurements, we employed a state-of-the art 256-channel real-time imaging MSOT scanner (iThera Medical GmbH, Kreiling, Germany). The general characteristics of a similar 64-channel system have been described elsewhere [12]. The system employs an OPO tunable laser for illumination in the NIR and parallel detection of 256 channels to achieve fast, real-time imaging. Two types of cells were employed in the studies to examine the effects of cell variability. Jurkat T cells were grown in RPMI 1640 media (Invitrogen No. 31870074) containing 10% FBS, 2 mM l-glutamine, 1 mM sodium pyruvate, nonessential amino acids, and penicillin–streptomycin. In addition, J774A.1 mouse macrophages were cultured in RPMI 1640 media, including 10% FBS and penicillin–streptomycin. Cells were labeled with the near-infrared fluorescent cyanine dye 1,1'-dioctadecyl-3,3,3',3'-tetramethylindotricarbocyanine iodide (DiR) for optoacoustic detection. DiR is a lipophilic, near-infrared fluorescent cyanine dye that can be incorporated into the cell membrane. For labeling, 1×10^6 cells were incubated with DiR for 15 min at room temperature while mixing every 5 min. Optimal labeling results were determined by testing different DiR concentrations and monitoring cell viability using MTT assay (Roche Applied Science, Penzberg, Upper Bavaria, Germany), according to the manufacturer's instruction. Optimal labeling of the J774A.1 macrophage cell line was achieved using 10 μM DiR, leading to an overall labeling of about 99.6% of cells (SD ± 0.58%) and a cell viability of 97%. Optimal labeling of Jurkat cells was found when using 5 μM DiR, which led to an overall labeling of 97.6% (SD ± 1.23%) and a cell viability of about 91%. The degree of cell labeling was determined by counting fluorescence-positive cells in the overlay with the DIC image ($n = 4$).

MSOT cell imaging *in vitro*. Cells were first imaged *in vitro* by utilizing 2 cm–diameter cylindrical phantoms made of 1.3% agar (Sigma-Aldrich) and 1.2% by volume Intralipid emulsion (Sigma-Aldrich), leading to an optically diffusive medium with acoustic properties similar to those of tissue. The use of an absorption-less phantom was selected herein to explicitly study the signal contribution of only the labeled cells. Measurements in animals then provided a reference medium with tissue absorption for comparison purposes. The labeled cells were enclosed within a 3 mm diameter plastic tube implanted into the agar cylinder, as shown in Fig. 1(a). Both Jurkat cells [Fig. 1(b)] and J774A.1 cells [Fig. 1(c)] were imaged using exactly the same imaging parameters. The labeled cells were enclosed within a 3 mm diameter plastic tube implanted into the agar cylinder, as shown in Fig. 1(a). Three different labeled cell concentrations were inserted into the 3 mm tubes, corresponding to 1250, 2500, and 5000 cells in the volume imaged. Unlabeled cells were also imaged as controls (Fig. 1). MSOT imaging was performed in one imaging plane (~200 μm in plane resolution, ~800 μm cross section). The phantom images were reconstructed at a wavelength of 720 nm, where the DiR signal is prominent [Figs. 1b(i)–1b(iii) and Figs. 1c(i)–1c(iii)]. Overall, a linear increase in signal

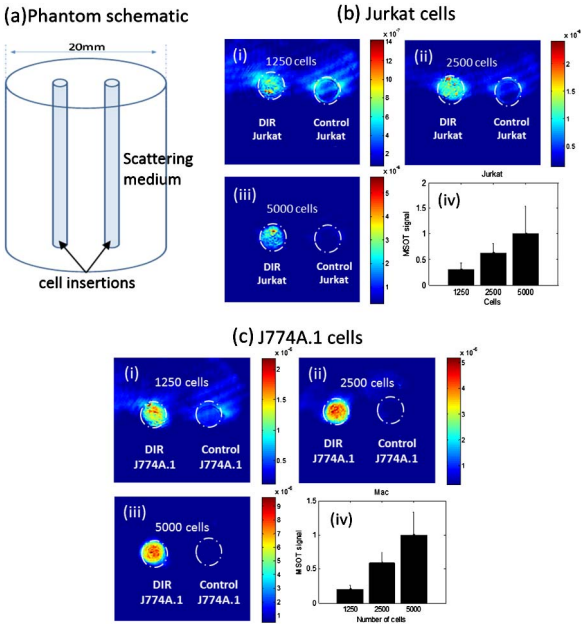

Fig. 1. *In vitro* optoacoustic imaging (720 nm) of DiR-labeled cells. (a) Schematic of the phantoms used in the *in vitro* tests. Labeled and unlabeled cells are inserted in 3 mm diameter tubes that are placed within a 20 mm diameter scattering phantom. (b) Imaging of Jurkat cells: (i)–(iii) optoacoustic signal generated by 1250, 2500, and 5000 DiR-labeled cells, respectively; and (iv) optoacoustic signal intensity comparison for different amounts of labeled cells. The bar heights indicate the mean intensity within the region of interest and the error bars indicate the standard deviation. (c) Imaging of J774A.1 cells: (i)–(iii) optoacoustic signal generated by 1250, 2500, and 5000 DiR-labeled J774A.1 cells, respectively; and (iv) optoacoustic signal intensity comparison for different amounts of labeled cells. The bar heights indicate the mean intensity within the region of interest and the error bars indicate the standard deviation.

intensity with increasing cell number is observable [Figs. 1b(iv) and 1c(iv)], as it is theoretically expected.

The relative absorbance of labeled cells was characterized using the same scattering phantom as the one described in Fig. 1(a). For contrasting the signal obtained from labeled cells with a well-characterized absorption signal, we employed India Ink for reference measurements. In particular, labeled Jurkat [Fig. 2(a)] and J774A.1 cells [Fig. 2(b)] were sequentially imaged next to an insertion of black India Ink with an absorbance of $\mu_a = 0.5\ \mathrm{cm}^{-1}$, the latter determined by a photospectrometer. Imaging was performed at 720 nm using MSOT. The optoacoustic signal intensity produced by 5000 Jurkat [Fig. 2(a)] and J774A.1 cells [Fig. 2(b)] was imaged together with an identical amount of ink. We observed that the optoacoustic signal produced by J774A.1 cells was almost twice as high as the one produced by Jurkat cells [Fig. 2(c)]. To explain this difference, we measured the cell sizes and found that macrophages had larger diameters compared with the T cell line [Fig. 2(d)]: J774A.1 = 17.94 μm, SD ± 1.99; Jurkat = 13.44 μm, SD ± 2.1; (statistics stemming after counting $n = 47$ cells per cell line using the "Leica Application Suite" software). The larger cell diameters of the J774A.1 cells represents a near doubling of cell surface, which indicates double DiR concentration per cell and can explain the optoacoustic signal measured [Fig. 2(c)].

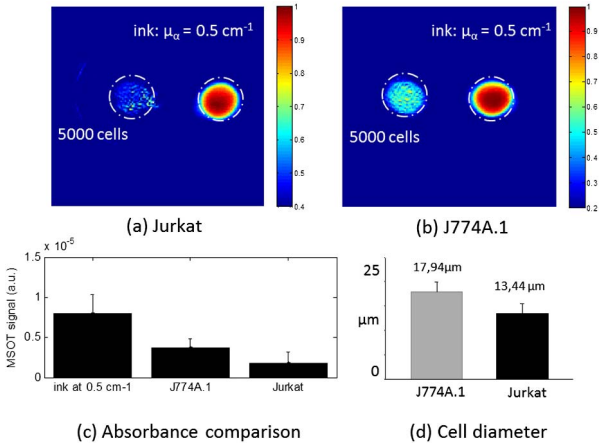

Fig. 2. Comparison and quantification of the absorbance of DiR-labeled cells. Single-wavelength (720 nm) optoacoustic phantom images of (a) 5000 DiR-labeled Jurkat cells and (b) J774A.1 cells, next to black India Ink of absorption coefficient 0.5 cm^{-1}. (c) Comparison in terms of optoacoustic signal intensity between the ink reference and the 5000 Jurkat and J774A.1 cells. (d) Comparison of the cell diameters of Jurkat and J774A.1 cells.

Labeled cells are highly scattering, making photospectrometry a nonideal method for estimating their absorbance in absolute values. Optoacoustic imaging can serve as a better alternative in this respect. Assuming that the differences in Grüneissen coefficient are insignificant, we can quantify the absolute absorbance of the labeled cells through comparison with the black India Ink. Specifically, based on Fig. 2(c), we found that 5000 Jurkat cells produce an optoacoustic signal that corresponds to μ_a of ~0.12 cm^{-1}, and 5000 J774A.1 cells to μ_a of ~0.25 cm^{-1}. Using this information, and the linear signal response as a function of cell number (Fig. 1), we can approximate the absorbance as a function of the number of cells. Knowing that tissue absorption in the NIR ranges is in the area of 0.1 to 0.4 cm^{-1} [13], we hypothesize that, to produce enough contrast for accurate MSOT sensing, cell clusters in the range of 1000–10,000 would be required.

Animal imaging. To confirm the theoretical prediction and the overall ability to detect labeled immune cells in tissues, we selected the cell line with the stronger labeling ability to provide first insights into the MSOT sensitivity for fluorescently labeled cells. We performed two experiments. In each experiment we injected two different amounts of cells in the left (injection 1) and the right brain hemispheres (injection 2) of a euthanized mouse. In experiment A, we injected locally 25,000 J774A.1 cells in the left and 10,000 J774A.1 cells in the right brain hemisphere. In experiment B, we injected locally 5000 J774A.1 cells in the left and 2500 J774A.1 cells in the right brain hemisphere. Mice were euthanized before cell injection and then imaged using MSOT. After MSOT imaging, the mice were imaged using cryoslicing fluorescence imaging [14] to verify the position of the cell insertions. Euthanasia was performed according to procedures approved by a local subcommittee on animal research.

For MSOT imaging, the mice were placed horizontally on a thin polyethylene membrane and placed within the MSOT scanner. Sound coupling and animal temperature maintenance was achieved by surrounding the membrane with water actively controlled at 34°C. Excitation wavelengths from 700 to 900 nm, in steps of 10 nm, were collected. MSOT images were reconstructed for each wavelength using a model-based reconstruction algorithm [15]. Afterward, the cell bio-distribution was spectrally resolved from the absorbing tissue background using the measured spectrum of the labeled cells and an adaptive matched filter (AMF), as in [10]. After the completion of each MSOT measurement, the mice were frozen and tissue slices were photographed and imaged with a fluorescence camera. The fluorescence measurements were superimposed in green pseudocolor on the color images. The fluorescence cryoslice images are shown next to the MSOT images for validation purposes.

Figure 3 depicts the results from experiments A and B. In each case, the cell insertions are explicitly pointed with white arrows. Figures 3(a) and 3(b) correspond to experiment A and Figs. 3(c) and 3(d) to experiment B. Figure 3(a) presents an overlay of the J774A.1 cell bio-distribution as detected using MSOT/AMF unmixing (red) on the anatomical optoacoustic image at 900 nm. Figure 3(b) shows a corresponding fluorescence cryoslice image, which confirms the results of the noninvasive MSOT image. We note that the signals captured by fluorescence imaging are generally of lower resolution (due to photon diffusion) compared with the MSOT images, and some minor disagreement is expected. Figure 3(c) demonstrates imaging of macrophages at amounts of 5000 and 2500. In all cases, the signals are reliably detected.

Our data show that the J774A.1 macrophages were detectable in *ex vivo* mice via MSOT in all four titrations, from 25,000 to 2500 cells. Retrospective analysis, based

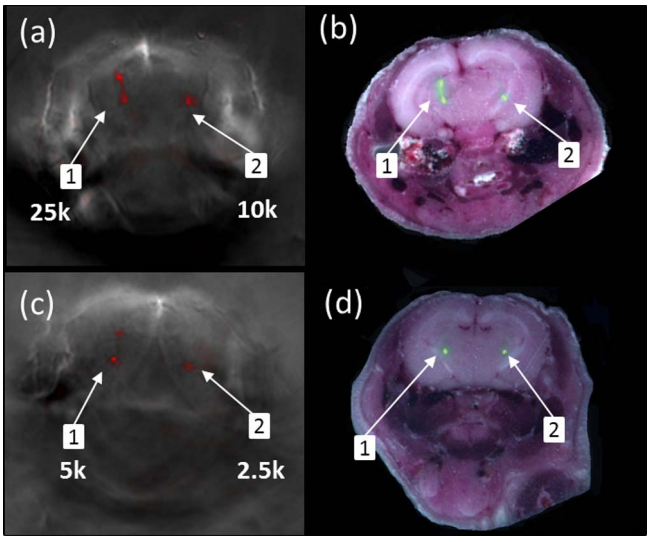

Fig. 3. *Ex vivo* animal study. (a) and (c) Overlay of the spectrally resolved signal stemming from the DiR-labeled J774A.1 cells (red color) onto the anatomical optoacoustic image (at 900 nm) for experiments A and B, respectively. The white arrows indicate the positions of the cell insertions. (b) and (d) Overlay of the fluorescent signal stemming from the DiR-labeled cells (green color) onto the anatomical cryoslice image for experiments A and B, respectively.

on the signal-to-noise characteristics of these four measurement points, indicates that sensitivities of the order of 1000 cells or less may be possible. However, an exact determination of sensitivity is best performed on a per case basis. MSOT sensitivity depends on multiple parameters, including system parameters, in particular the light intensity deposited on the tissue, the ultrasound detector sensitivity, the excitation wavelengths employed, and the spectral unmixing method utilized. It further depends on the depth of the cell activity and the optical properties of tissue. A third dependence of the sensitivity is on the lesion size. Cells distributing over a larger volume will generally generate lower ultrasound frequencies than cells accumulating in smaller lesions. Since higher ultrasound frequencies attenuate more strongly than lower frequencies, the detection of cells over very small volumes will be more challenging. Finally, a fourth dependence is on the particular label employed.

We should note that it is common to determine optoacoustic sensitivity by multiplying the total number of cells imaged with the ratio of the volume of the optoacoustic voxel over the total volume that the cells are distributed in. This gives some very favorable sensitivity numbers, which may be rather inaccurate. This is because, as mentioned, a very small volume emits an optoacoustic signal of much higher frequency content, which is attenuated more strongly than the lower frequency signals emitted from a larger volume. This nonlinear relationship of sensitivity with volume has been shown before [16]. Instead, sensitivity should be demonstrated on a per case basis for the actual distribution volume, or by using models that account for this nonlinear behavior.

The demonstration of experimentally detecting at least ~2500 cells from a small volume inside tissue gives a first indication of MSOT as a cell imaging method. An important additional parameter that will affect sensitivity is the labeling approach employed. Herein, we selected a fluorescent label that is commonly employed for cell imaging applications and binds to the surface of the cells. We observe that the size of the cell surface plays an important role on the optoacoustic signal generated and that smaller cells may be more challenging to detect. Alternative labels, such as gold nanoparticles, could potentially improve detection sensitivity. However, the ability to offer better detection characteristics with nanoparticles should be explicitly demonstrated, as it relies also on labeling efficiency, i.e., how many particles can be taken up by the target cells.

In summary, we have demonstrated, for the first time to our knowledge, the ability of MSOT to image, within tissue, leukocytes labeled with a fluorescent dye. Of particular importance was the identification of sensitivity metrics as they relate to biological exploration. For this reason, signals obtained from labeled cells were first contrasted to signals obtained from characterized amounts of India Ink. Then, measurements from animals were obtained to interrogate the ability and sensitivity to resolve cells in tissues.

All animal experiments were approved by the District Government of Upper Bavaria. We thank the groups of Prof. Angela Krackhardt, Technische Universität München, Germany, for providing the Jurkat cells. We further acknowledge support from EU project FAMOS (FP7 ICT, Contract 317744) (Spectral algorithms), the Federal Ministry of Education and Research, Photonic Science Germany (Tech2See-13N12624) (Cell labeling) the ERC Advanced Grant (233161) (MSOT development).

†These authors contributed equally to this work.

References

1. J. Condeelis and J. E. Segall, Nat. Rev. Cancer **3**, 921 (2003).
2. N. P. Restifo, M. E. Dudley, and S. A. Rosenberg, Nat. Rev. Immunol. **12**, 269 (2012).
3. H. Liu, X. Wu, S. Wang, W. Deng, L. Zan, and S. Yu, Oncol.Res. **20**, 275 (2013).
4. J. A. Thomas, C. Pope, D. Wojtacha, A. J. Robson, T. T. Gordon-Walker, S. Hartland, P. Ramachandran, M. Van Deemter, D. A. Hume, J. P. Iredale, and S. J. Forbes, Hepatology **53**, 2003 (2011).
5. D. Ferenbach and D. Kluth, Semin. nephrol. **30**, 345 (2010).
6. E. M. Strohm, E. S. Berndl, and M. C. Kolios, J. Photoacoustics **1**, 49 (2013).
7. D. Razansky, M. Distel, C. Vinegoni, R. Ma, N. Perrimon, R. W. Koster, and V. Ntziachristos, Nat. Photonics **3**, 412 (2009).
8. A. Taruttis, M. Wildgruber, K. Kosanke, N. Beziere, K. Licha, R. Haag, M. Aichler, A. Walch, E. Rummeny, and V. Ntziachristos, J. Photoacoustics **1**, 3 (2013).
9. S. Y. Nam, L. M. Ricles, L. J. Suggs, and S. Y. Emelianov, PLoS One **7**, e37267 (2012).
10. S. Tzoumas, N. Deliolanis, S. Morscher, and V. Ntziachristos, IEEE Trans. Med. Imaging, **33**, 48 (2014).
11. P. P. Joshi, S. J. Yoon, Y.-S. Chen, S. Emelianov, and K. V. Sokolov, Biomed. Opt. Express **4**, 2609 (2013).
12. A. Buehler, E. Herzog, D. Razansky, and V. Ntziachristos, Opt. Lett. **35**, 2475 (2010).
13. S. L. Jacques, Phys. Med. Biol. **58**, 37 (2013).
14. A. Sarantopoulos, G. Themelis, and V. Ntziachristos, Molecular Imaging Biol. **13**, 874 (2011).
15. A. Rosenthal, D. Razansky, and V. Ntziachristos, IEEE Trans. Med. Imaging **29**, 1275 (2010).
16. D. Razansky, J. Baeten, and V. Ntziachristos, Med. Phys. **36**, 939 (2009).

Appendix E

Publication: Eigenspectra optoacoustic tomography achieves quantitative blood oxygenation imaging deep in tissues

The version herein has been published in the journal "NatureCommunications"[142]. The author's version is hereby reprinted with permission.

Eigenspectra optoacoustic tomography achieves quantitative blood oxygenation imaging deep in tissues

Stratis Tzoumas[1,2†], Antonio Nunes[1,†] , Ivan Olefir[1], Stefan Stangl[3], Panagiotis Symvoulidis[1,2], Sarah Glasl[1,2], Christine Bayer[3], Gabriele Multhoff[3,4], Vasilis Ntziachristos[1,2*]

[1] *Institute for Biological and Medical Imaging (IBMI), Helmholtz Zentrum München, Ingolstädter Landstrasse 1, Neuherberg, Germany*
[2] *Chair for Biological Imaging, Technische Universität München, Trogerstr. 9, München, Germany*
[3] *Department of Radiation Oncology, Klinikum rechts der Isar, Technische Universität München, Ismaninger Str. 22, München, Germany*
[4] *CCG – Innate immunity in Tumor Biology, Helmholtz Zentrum München, Ingolstädter Landstrasse 1, Neuherberg, Germany*

Light propagating in tissue attains a spectrum that varies with location due to wavelength-dependent fluence attenuation, an effect that causes spectral corruption. Spectral corruption has limited the quantification accuracy of optical and optoacoustic spectroscopic methods and impeded the goal of imaging blood oxygen saturation (sO_2) deep in tissues; a critical goal for the assessment of oxygenation in physiological processes and disease. Here, we describe light fluence in the spectral domain and introduce eigenspectra Multispectral Optoacoustic Tomography (eMSOT) to account for wavelength dependent light attenuation and estimate blood sO_2 within deep tissue. We validate eMSOT in simulations, phantoms and animal measurements and spatially resolve sO_2 in muscle and tumors, validating our measurements with histology data. eMSOT shows substantial sO_2 accuracy enhancement over previous optoacoustic methods, potentially serving as a valuable tool for imaging tissue pathophysiology.

The assessment of tissue oxygenation is crucial for understanding tissue physiology and characterizing a multitude of conditions including cardiovascular disease, diabetes, cancer hypoxia[1] or metabolism. Today, tissue oxygenation (pO_2) and hypoxia measurements remain challenging and often rely on invasive methods that may change the tissue physiology, such as single point needle polarography or immunohistochemistry[2]**.** Non-invasive imaging methods have been also considered, underscoring the importance of assessing pO_2, but come with limitations. Positron emission tomography (PET) or single-photon emission computed tomography (SPECT) assess cell hypoxia through the administration of radioactive tracers[2], but are often not well suited for quantifying tissue oxygenation, suffer from low spatial resolution and are unable to provide longitudinal or dynamic imaging capabilities. Electron paramagnetic resonance imaging[3] can measure tissue pO_2 but is not widely used and offers limited spatial and temporal resolution. Imaging methods using tracers may be further limited by restricted tracer bio-distribution, in particular to hypoxic areas. Tracer-free modalities have also been researched, in particular BOLD MRI[4], which however primarily assesses only deoxygenated hemoglobin and therefore presents challenges in quantifying oxygenation and blood volume[5].

Measurement of blood oxygen saturation levels (sO_2) is a vital tissue physiology measurement and can provide an alternative way to infer tissue oxygenation and hypoxia. Arterial sO_2 is widely assessed by the pulse oximeter, but this technology cannot be applied to measurements other than arterial blood. Optical microscopy methods like phosphorescence quenching microscopy[6] or optoacoustic (photoacoustic) microscopy[7] can visualize oxygenation in blood vessels and capillaries but are restricted to superficial (<1mm depth) measurements. Diffuse optical methods received significant attention in the last two decades for sensing and imaging oxy- and deoxygenated hemoglobin deeper in tissue[8]. Despite recent progress[9], diffuse optical methods are inherently limited in spatial resolution and accuracy, due to photon scattering. Owing to the high heterogeneity of blood sO_2 in tissue, the values reported by diffuse optical methods are often hard to interpret.

Multispectral optoacoustic tomography (MSOT) detects the spectra of oxygenated and deoxygenated hemoglobin in high resolution deep within tissues, since signal detection and image reconstruction are not significantly affected by photon scattering[10,11]. Despite the principal MSOT suitability for non-invasive imaging of blood oxygenation, accuracy remains limited by the dependence of light fluence on depth and light color. Unless explicitly accounted for, the wavelength dependent light fluence attenuation with depth alters the spectral features detected and results in inaccurate estimates of blood sO_2[12,13]. Despite at least two decades of research in optical imaging, the problem of light fluence correction has not been conclusively solved. To date this problem has been primarily studied from an optical property quantification point of view[14,13]. However, it is not possible today to accurately image tissue optical properties *in-vivo*, in high-resolution, and compute light fluence[13]. Therefore, quantitative sO_2 measurement deep in tissue *in-vivo* remains an unmet challenge. Conventional spectral optoacoustic methods[15,16] typically ignore the effects of light fluence and employ linear spectral fitting with the spectra of oxy- and deoxy-hemoglobin for estimating sO_2 (linear unmixing), a common simplification that can introduce substantial errors in deep tissue.

In this work we found that the spectral patterns of light fluence expected within the tissue can be modeled as an affine function of a few reference base spectra, independently of the specific distribution of tissue optical properties or the depth of the observation. We show how this principle can be employed to solve the spectral corruption problem without knowledge of the tissue optical properties, and significantly increase the accuracy of spectral optoacoustic methods. The proposed method, termed eigenspectra-MSOT (eMSOT), can provide quantitative estimation of blood sO_2 in deep tissue. We

† Equal author contribution
* Correspondence to V.N. (v.ntziachristos@tum.de)

demonstrate the superior performance of the method with more than 2000 simulations, phantom measurements and *in-vivo* controlled experiments. Then, using eMSOT, we image oxygen gradients in the skeletal muscle *in-vivo*, previously only accessible through invasive methods. Furthermore, we show the application of eMSOT in quantifying blood oxygenation gradients in tumors during tumor growth or O_2 challenge and relate label-free non-invasive eMSOT readings to tumor hypoxia; demonstrating the ability to measure quantitatively the perfusion hypoxia level in tumors, as confirmed with invasive histological gold standards.

RESULTS

eMSOT concept and application

A new concept of treating light fluence in diffusive media/tissues is introduced, based on the observation that the light fluence spectrum at different locations in tissue is the result of a cumulative light absorption operation by tissue chromophores, such as hemoglobin. We therefore hypothesized that there exists a small number of base spectra that can be combined to predict any fluence spectrum present in tissue; therefore avoiding the unattainable task of knowing the distribution of tissue optical properties at high resolution. To prove this hypothesis, we first applied Principal Component Analysis (PCA) on 1470 light fluence spectral patterns, which were computed by simulating light propagation in tissues at 21 different (uniform) oxygenation states of hemoglobin and 70 different discrete depths (**Methods**). PCA analysis yielded four significant base spectra, i.e. a mean light fluence spectrum (**Figure 1a**) and three fluence *Eigenspectra* (**Figure 1b-d**). PCA was used due to its optimality in modeling the spectral variability of light fluence in a linear manner (see **Methods**). We found that the selection of three *Eigenspectra* offers a simple model with relatively high modeling accuracy (**Figure 1e**).

We then postulated that light fluence spectra in arbitrary and non-uniform tissues can be modeled as a superposition of the mean fluence spectrum (Φ_M) and the three *Eigenspectra* ($\Phi_i(\lambda)$, i=1..3) multiplied by appropriate scalars m_1, m_2 and m_3, termed *Eigenfluence* parameters. To validate this hypothesis we computed the light fluence in >500 simulated tissue structures of different and non-uniform optical properties and hemoglobin oxygenation values (**Supplementary Note 1**). For each pixel, we fitted the simulated light fluence spectrum to the *Eigenspectra* model and derived the *Eigenfluence* parameters (m_1, m_2, m_3) and a fitting residual value. The residual value represents the error of the *Eigenspectra* model in matching the simulated data and typically assumed values below 1% (see **Supplementary Note 1, Supplementary Fig. 1**) indicating that three *Eigenspectra* can accurately model all simulated fluence spectra generated in tissues of arbitrary structure. We further observed that the values of m_2 vary primarily with tissue depth while the values of m_1, m_3 also depend on the average levels of background tissue oxygenation (see **Figure 1f-h**). Intuitively this indicates that the second *Eigenspectrum* $\Phi_2(\lambda)$ is mainly associated with the modifications of light fluence spectrum due to depth and the average optical properties of the surrounding tissue, while the first *Eigenspectrum* $\Phi_1(\lambda)$ is also associated with the "spectral shape" of light fluence that relates to the average oxygenation of the surrounding tissue. Localized measurements of light fluence spectra obtained *in vivo* and *post mortem* corroborated these observations (**Supplementary Fig. 2**).

Following these observations, we propose eigenspectra MSOT (eMSOT), based on three eigenspectra $\Phi_1(\lambda)$, $\Phi_2(\lambda)$, $\Phi_3(\lambda)$, as a method that formulates the blood sO_2 estimation problem as a non-linear spectral unmixing problem (see **Methods**), i.e.:

$$P(\mathbf{r},\lambda) = \Phi'(\mathbf{r},\lambda)\cdot(c'_{HbO2}(\mathbf{r})\cdot\varepsilon_{HbO2}(\lambda) + c'_{Hb}(\mathbf{r})\cdot\varepsilon_{Hb}(\lambda)), \qquad (1)$$

where $P(\mathbf{r},\lambda)$ is the multispectral optoacoustic image intensity obtained at a position $\mathbf{r}$ and wavelength λ, $\varepsilon_{HbO2}(\lambda)$ and $\varepsilon_{Hb}(\lambda)$ are the wavelength dependent molar extinction coefficients of oxygenated and deoxygenated hemoglobin, $c'_{HbO2}(\mathbf{r})$ and $c'_{Hb}(\mathbf{r})$ are the relative concentrations of oxygenated and deoxygenated hemoglobin (proportional to the actual ones with regard to a common scaling factor, see **Methods**), and $\Phi'(\mathbf{r},\lambda) = \Phi_M(\lambda) + m_1(\mathbf{r})\Phi_1(\lambda) + m_2(\mathbf{r})\Phi_2(\lambda) + m_3(\mathbf{r})\Phi_3(\lambda)$. Eq. (1) defines a non-linear inversion problem, requiring measurements at 5 wavelengths or more for recovering the 5 unknowns, i.e. $c'_{HbO2}(\mathbf{r})$, $c'_{Hb}(\mathbf{r})$, $m_1(\mathbf{r})$, $m_2(\mathbf{r})$, $m_3(\mathbf{r})$ and is solved as a constrained optimization problem (see **Methods, Supplementary Note 2, Supplementary Fig. 3**). Since the light fluence varies smoothly in tissue, we only compute the *Eigenfluence* parameters on a coarse grid subsampling the region of interest (**Figure 1i**), for computational efficiency. Then, cubic interpolation is employed to compute the *Eigenfluence* parameters in each pixel within the convex hull of the grid (**Figure 1j**) and calculate a fluence spectrum $\Phi'(\mathbf{r},\lambda)$ for each pixel using these parameters. Eq. (1) is then solved for $c'_{HbO2}(\mathbf{r})$ and $c'_{Hb}(\mathbf{r})$ and sO_2 is computed (see **Methods**).

The performance of eMSOT was validated using simulated data obtained from a light propagation model (finite element solution of the diffusion equation) applied on >2000 randomly created maps of different optical properties, simulating different tissue physiological states (**Supplementary Note 3**). **Figure 1k** depicts a representative example of a simulated blood sO_2 map and visually showcases the differences between the eMSOT sO_2 image (middle), the sO_2 image obtained using linear unmixing (left) and the original sO_2 simulated image (right). eMSOT offered significantly lower sO_2 estimation error with depth, compared to the linear fitting method (**Figure 1l**). A substantially improved sO_2 estimation accuracy was observed using eMSOT over linear unmixing when we analyzed the complete simulation data-set (**Figure 1m).** In particular, for imaging tissue depths of >5mm eMSOT offered a 3-8 fold sO_2 estimation improvement over linear unmixing (**Supplementary Fig. 4n**). A thorough validation of eMSOT performance across different data-sets, optical properties and grid densities is presented in **Supplementary Note 3, Supplementary Tables 1** and **2,** and **Supplementary Fig. 4.**

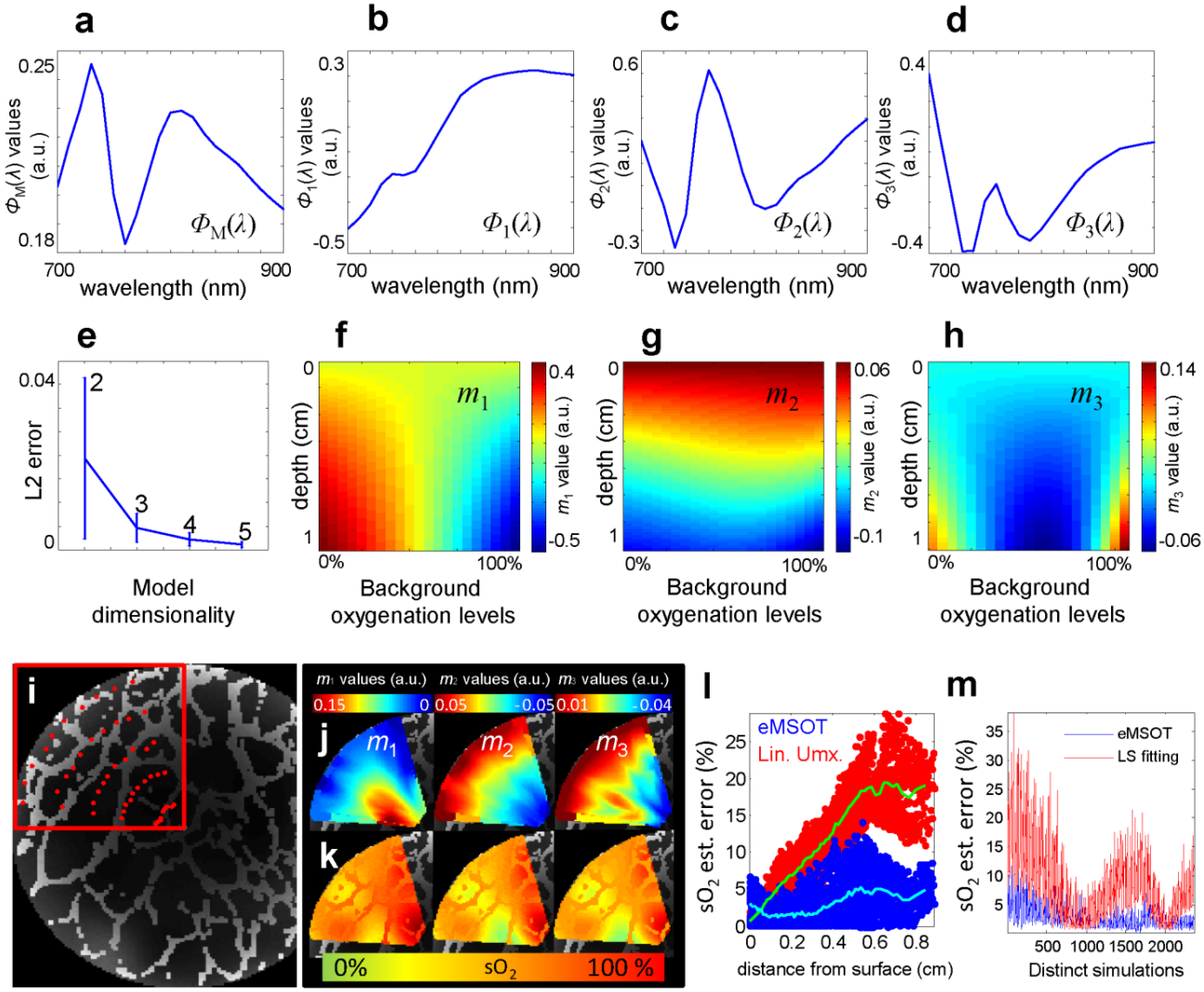

Figure 1. eMSOT concept and application. (a-d) The *Eigenspectra* model composed of a mean fluence spectrum $\Phi_M(\lambda)$ **(a)** and the three fluence *Eigenspectra* $\Phi_1(\lambda)$, $\Phi_2(\lambda)$ and $\Phi_3(\lambda)$, **(b), (c), (d),** respectively, as derived by applying PCA on a selected training data-set of light fluence spectra (**Methods**). (**e**) Statistics of the L2 norm error of the *Eigenspectra* model on the training dataset for different model dimensionalities. Error-bar denotes s.d.. (**f-h**) Values of the parameters m_1, m_2 and m_3 as a function of tissue depth (y axis) and tissue oxygenation (x axis). The values have been obtained after fitting the light fluence spectra of the training data-set (see **Methods**) to the *Eigenspectra* model. **(i)** Application of a circular grid (red points) for eMSOT inversion on an area of a simulated MSOT image. (**j**) After eMSOT inversion the model parameters m_1, m_2 and m_3 are estimated for all grid points and maps of m_1, m_2 and m_3 are produced for the convex hull of the grid by means of cubic interpolation. These maps are used to spectrally correct the original MSOT image. (**k**) Blood sO_2 estimation using linear unmixing (left), eMSOT (middle) and Gold standard sO_2 (right) of the selected region. (**l**) sO_2 estimation error of the analyzed area sorted per depth in the case of linear unmixing (red points) and eMSOT (blue points). (**m**) Mean sO_2 error of linear unmixing (red) and eMSOT (blue) corresponding to >2000 simulations of random structures and optical properties (see **Supplementary Note 3**).

For experimentally assessing the accuracy of eMSOT, we performed a series of blood phantom experiments that suggest an up to 10-fold more reliable sO_2 estimation derived by eMSOT, as compared to conventional linear unmixing (**Supplementary Note 4, Supplementary Fig. 5**). In addition, controlled mouse measurements (n=4) were performed *in-vivo*, under gas anesthesia, by rectally inserting capillary tubes containing blood at 100% and 0% sO_2 levels (**Methods**). The mice were imaged in the lower abdominal area under 100% O_2 and 20% O_2 breathing conditions (**Figure 2a). Figure 2a** presents the eMSOT grid applied on the images processed (left column), the sO_2 maps obtained with linear unmixing (middle column) and with eMSOT (right column). The spectral fitting of linear unmixing (left) and eMSOT (right) corresponding to a pixel in the area of the capillary tube (yellow arrows in **a**) are presented in **Figure 2b** along with the estimated sO_2 values. In the controlled *in-vivo* experiments, the mean linear unmixing error ranged from 16 to 35% while eMSOT offered a mean sO_2 error ranging from 1 to 4% indicating an order of magnitude improved accuracy (**Figure 2c**).

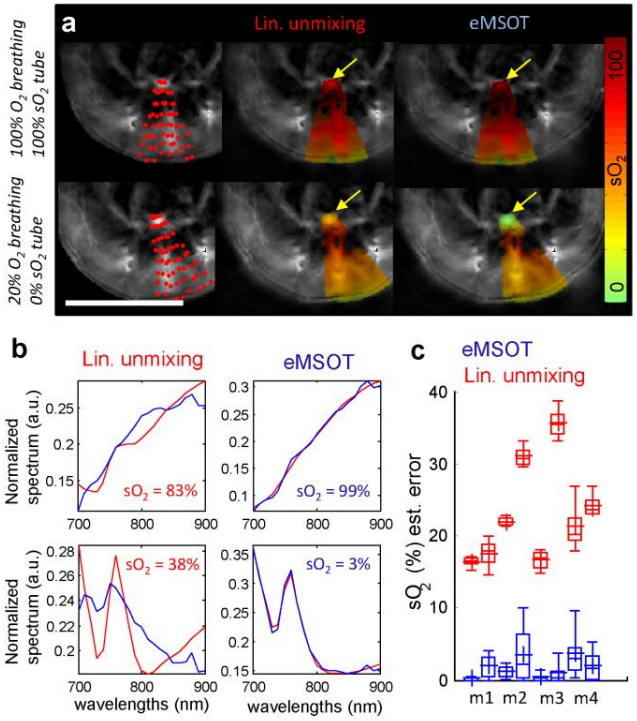

Figure 2. Comparison of eMSOT sO_2 estimation accuracy over conventional spectral optoacoustic method. (**a**) eMSOT application in the case of *in-vivo* controlled experiments under 100% O_2 (**a** upper row) and 20% O_2 (**a** lower row) breathing. Capillary tubes containing blood of 100% sO_2 (upper row) and 0% sO_2 (lower row) were inserted within tissue (arrows). Scale bar 1cm. (**b**) Spectral fitting and sO_2 estimation in the insertion area (yellow arrows in **a**) using linear unmixing (left column) and eMSOT (right column). The blue curves correspond to $P(\mathbf{r},\lambda)$ (left column) and $P^{eMSOT}(\mathbf{r},\lambda)$ (right column) while the red curves correspond to $c_{HbO2}{}^{lu}(\mathbf{r})\varepsilon_{HbO2}(\lambda)+c_{Hb}{}^{lu}(\mathbf{r})\varepsilon_{Hb}(\lambda)$ (left column; the term lu refers to linear unmixing) and $c'_{HbO2}{}^{eMSOT}(\mathbf{r})\varepsilon_{HbO2}(\lambda)+c'_{Hb}{}^{eMSOT}(\mathbf{r})\varepsilon_{Hb}(\lambda)$ (right column)**.** (**c**) sO_2 estimation error using eMSOT (blue) and linear unmixing (red) in all four animal experiment repetitions m1-m4. Two values are reported for each experiment corresponding to a 100% sO_2 insertion (left) and 0% sO_2 insertion (right). Statistics are derived from all pixels in a region of interest (ROI) corresponding to the insertion area for each dataset. The boxes include 25%-75% and the error-bars 9%-91% of the data. The mean value is denoted with the plus symbol.

Imaging blood oxygenation gradients in muscle and tumor

Blood oxygenation and oxygen exchange in the microcirculation have been traditionally studied through invasive, single-point polarography or microscopy measurements in vessels and capillaries of the skeletal muscle[17]. Research for macroscopic methods that could non-invasively resolve muscle oxygenation was broadly pursued in the past two decades by considering Near-Infrared Spectroscopy (NIRS) and Diffuse Optical Tomography (DOT), which, however can only report bulk tissue sO_2 values[18,19]. In a next set of experiments we, therefore, studied whether eMSOT could non-invasively quantify the oxygenation gradient in the skeletal muscle and we compared this performance to conventional spectral optoacoustic methods. eMSOT was applied in the area of the hindlimb muscle of mice undergoing an O_2 challenge as described in **Supplementary Note 5** (n=6 animal experiments); three of the mice were then sacrificed with an overdose of CO_2, the latter binding to hemoglobin and deoxygenating blood.

eMSOT applied in the hindlimb muscle area (grid shown in **Figure 3a**) resolved oxygenation gradients as a function of breathing conditions *in-vivo* (**Figure 3 b-c**) and *post-mortem* after CO_2 breathing (**Figure 3d**). The *post-mortem* deoxygenated muscle served herein as a control experiment and was also analyzed with linear unmixing for comparison (**Figure 3e**). In the *post-mortem* case, linear unmixing overestimated the sO_2 as a function of tissue depth (**Figure 3e**) and yielded large errors in matching the tissue spectra (**Figure 3f** – upper row). Conversely, eMSOT offered sO_2 measurements in agreement with the expected physiological states (**Figure 3b-d**) and consistently low fitting residuals (**Figure 3f –** lower row, **Supplementary Fig. 6**). **Figure 3d-e** and **Figure 3f** demonstrate the prominent effects of spectral corruption with depth that impair the accuracy of conventional spectral optoacoustic methods but are tackled by eMSOT. The estimated blood sO_2 values corresponding to a deep tissue area (yellow rectangle in **Figure 3b**) are tabulated in **Figure 3g** for eMSOT and linear unmixing and depict that the latter demonstrated unrealistically small sO_2 changes between the normoxic *in-vivo* and anoxic *post-mortem* (after CO_2 breathing) states.

In addition to physiological tissue features, MSOT also reveals tissue morphology. MSOT images at a single wavelength (900 nm) captured prominent vascular structures likely corresponding to femoral vessels or their branches (**Figure 3h**) with implicitly co-registered eMSOT blood-oxygenation images (**Figure 3i**). This hybrid mode enables the study of physiology at specific tissue areas. We selected to study blood oxygenation measurements at a region of interest around large vessels (ROI-1; **Figure 3h**) and a region of interest within the muscle presenting no prominent vascular structures (ROI-2; **Figure 3h**) for the 100% O_2, 20% O_2 and CO_2 breathing conditions. Average tissue sO_2 was typically measured at 60%-70% saturation under medical air breathing and at 70%-80% saturation under 100% O_2 breathing near large vessels (**Figure 3j**). Average tissue blood oxygenation away from large vessels (ROI-2) was estimated consistently lower, at 35 -50% saturation under normal breathing conditions and 45-60% saturation under 100% O_2 breathing (**Figure 3k**).

The low blood saturation values in tissue (35 -50%) cannot be explained by considering arterial and venous blood saturation. However, previous studies based on direct microscopy measurements in vessels and capillaries through polarography, hemoglobin spectrophotometry and phosphorescence quenching microscopy have revealed similar oxygenation gradient in the skeletal muscle[17] with hemoglobin saturation in the femoral artery found to range between 87-99% sO_2[17,20], while rapidly dropping down to 50-60% sO_2 in smaller arterioles[20,21]. The average oxygen saturation in venules and veins has been found to range between 45%-60% sO_2 under normal breathing conditions, reaching up to 70% at 100% O_2 breathing[21,22]. Average capillary blood oxygenation has been estimated at 40% sO_2 with a large standard deviation[22], often reported lower, at an average, than venular oxygenation[17]. Therefore, the eMSOT

values measured at ROI-1 possibly relate to a weighted average of arterial/arteriolar and venous/venular sO_2 in the skeletal muscle, while the values measured at ROI-2, which anatomically presents no prominent vasculature, relate more to capillary sO_2 measurements.

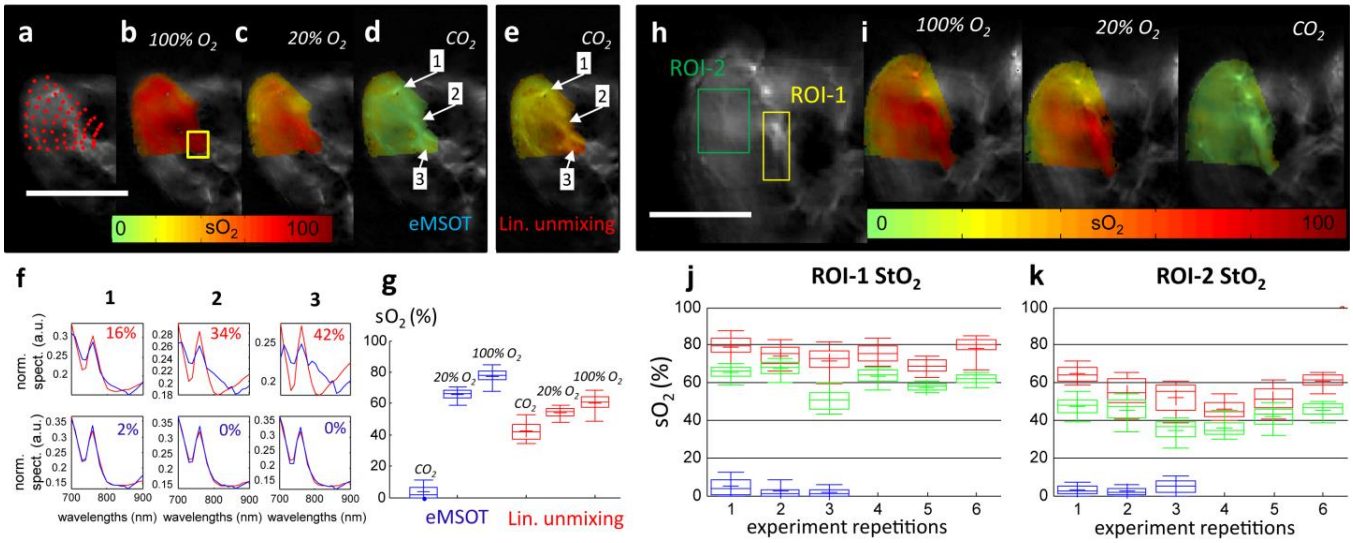

Figure 3. eMSOT measurements of tissue blood oxygenation in the muscle. (**a-d**) eMSOT grid applied on the area of the hindlimb muscle (**a**) and eMSOT tissue blood sO_2 estimation in the case of 100% O_2 breathing (**b**), 20% O_2 breathing (**c**) and *post-mortem* after CO_2 breathing (**d**). (**e**) sO_2 estimation using linear unmixing in the *post mortem* case after CO_2 breathing. Scale bar 1cm. (**f**) Normalized spectra, spectral fitting and sO_2 values of linear unmixing (upper row) and eMSOT (lower row) for the three points indicated in (**d**) and (**e**). The blue curves correspond to $P(\mathbf{r},\lambda)$ (upper row) and $P^{eMSOT}(\mathbf{r},\lambda)$ (lower row) while the red curves correspond to $c_{HbO2}{}^{lu}(\mathbf{r})\varepsilon_{HbO2}(\lambda)+c_{Hb}{}^{lu}(\mathbf{r})\varepsilon_{Hb}(\lambda)$ (upper row) and $c'_{HbO2}{}^{eMSOT}(\mathbf{r})\varepsilon_{HbO2}(\lambda)+c'_{Hb}{}^{eMSOT}(\mathbf{r})\varepsilon_{Hb}(\lambda)$ (lower row)**.** (**g**) Estimated blood sO_2 of a deep tissue area (yellow box in **b**) using eMSOT (blue) and linear unmixing (red) under different breathing conditions of CO_2, 20% O_2 and 100% O_2. **(h)** Anatomical MSOT image of the hindlimb area at an excitation wavelength of 900 nm. Two regions were selected for presenting the sO_2 values, one close to prominent vasculature (ROI-1) and one corresponding to soft tissue (ROI-2). Scale bar 0.5cm. **(i)** eMSOT sO_2 estimation *in-vivo* under 100% (left) and 20% O_2 breathing (middle) and *post-mortem* after CO_2 breathing (right). Scale bar 0.5cm. **(j, k)** Estimated tissue sO_2 of ROI-1 **(j)** and ROI-2 **(k)** under 100% (red) and 20% O_2 breathing (green) and *post-mortem* after CO_2 breathing (blue). The x-axis positions correspond to 6 different animal experiment repetitions. Statistics in **g**, **j** and **k** are derived from all pixels in the corresponding ROIs. The boxes include 25%-75% and the errorbars 9%-91% of the data. The mean value is denoted with the plus symbol.

The improved accuracy observed in eMSOT over previous approaches and general agreement with invasive tissue measurements prompted the further study of perfusion hypoxia emerging from the incomplete delivery of oxygenated hemoglobin in tissue areas. We hypothesized that measurements of blood saturation could be employed as a measure of tissue hypoxia, assuming natural hemoglobin presence in hypoxic areas. To examine this hypothesis we applied eMSOT to measure blood oxygenation in 4T1 solid tumors orthotopically implanted in the mammary pad of 8 mice (**Methods, Supplementary Note 6**). MSOT revealed the tumor anatomy and eMSOT exposed tumor heterogeneity, which was found consistent to anatomical features identified through cryoslice color photography and H&E staining (**Supplementary Note 6, Supplementary Fig. 7c-g**). Furthermore, imaging tumors at different time-points revealed the progression of hypoxia during tumor growth (**Figure 4a-b**). The spread of hypoxia, i.e. the percentage of the hypoxic area (area presenting sO_2 values below a threshold which varied from 50% to 25% sO_2) over the total tumor area, also increased during tumor progression (**Figure 4c**). Following the *in-vivo* measurements we harvested the tumor tissue and related the non-invasive eMSOT findings to the histological assessment of tumor hypoxia (see **Supplementary Note 6 & Supplementary Fig. 7**). Tumor tissue was stained by Hoechst 33342[23] (indicating perfusion) and Pimonidazole[24] (indicating cell hypoxia). The results indicated close correspondence between the hypoxic areas detected by eMSOT using hemoglobin as a hypoxia sensor (**Figure 4b**) and the histology slices (**Figure 4d**)**.** We found that eMSOT could not only quantitatively distinguish between high and low hypoxia levels in the tumors, but the spatial sO_2 maps further presented congruence with the spatial appearance of hypoxia spread and reduced perfusion seen in the histology slices **(Figure 4e-g)**. A quantitative congruence analysis is shown in **Supplementary Figure 7**. Finally, clear differences were also observed between the hypoxic tumor and healthy tissue response to an O_2 breathing challenge (**Figure 4h; Supplementary Fig. 8**), with areas in the core of the tumor presenting a limited response to such external stimuli, likely due to the presence of non-functional vasculature.

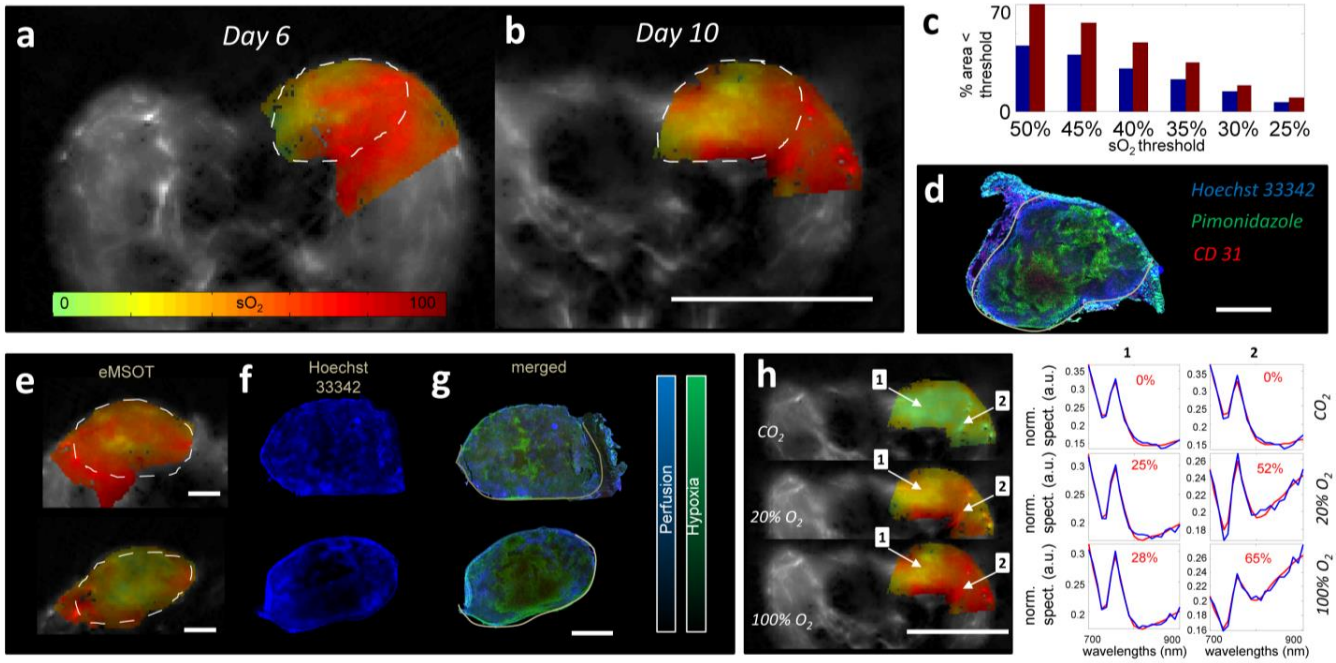

Figure 4. eMSOT measurements of tissue blood oxygenation in tumor. (a-b) sO_2 maps of a 4T1 tumor implanted in the mammary pad at day 6 (**a**) and day 10 (**b**) after cell inoculation. Dashed lines represent a segmentation of the tumor area. Scale bar 1cm. (**c**) Bar-plot presenting the percentage of the total tumor area containing sO_2 values lower than a specific sO_2 threshold (x-axis). Blue bars correspond to the tumor imaged at day 6 and red bars correspond to the tumor imaged at day 10, presented in (**a, b**). (**d**) Merged Hoechst 33342, CD 31 and Pimonidazole staining of the tumor presented in (**b**). Scale bar, 2mm. (**e-g**) Examples of a highly perfused (upper row) and a low perfused (lower row) tumor analysed with eMSOT for sO_2 estimation (**e**), Hoechst 33342 staining (**f**), and merged with Pimonidazole staining (**g**). Tumor areas presenting lower sO_2 values in eMSOT measurements also showed lower Hoechst 33342 signal intensity, representing reduced perfusion in these areas. Scale bar, 2mm. (**h,** left) sO_2 maps of a tumor under an O_2–CO_2 challenge. Scale bar 1cm. The computed sO_2 values and the eMSOT spectral fit of points 1 and 2 (arrows) are presented in (**h** right) for the three breathing conditions. The blue curves correspond to $P^{\mathrm{eMSOT}}(\mathbf{r},\lambda)$ while the red curves correspond to $c'_{\mathrm{HbO2}}{}^{\mathrm{eMSOT}}(\mathbf{r})\varepsilon_{\mathrm{HbO2}}(\lambda)+c'_{\mathrm{Hb}}{}^{\mathrm{eMSOT}}(\mathbf{r})\varepsilon_{\mathrm{Hb}}(\lambda)$

DISCUSSION

Spectral corruption has so far limited the potential of optical and optoacoustic methods to offer accurate, quantitative assessment of blood oxygen saturation deep inside tissues. Conventional computational methods in optical imaging propose to invert a light transport operator to recover tissue optical properties (absorption and scattering)[13]; then use these properties for calculating tissue physiological parameters. However, the very high numerical complexity and ill-posed nature of the inversion problem has not allowed so far accurate, high-resolution sO_2 imaging. We hereby followed an alternative approach that describes the spectral features of light fluence as a combination of spectral base functions. Using this principle, we formulated the sO_2 quantification problem as a non-linear spectral unmixing problem that does not require knowledge of tissue optical properties or the inversion of a light transport operator. Effectively, eMSOT converts sO_2 imaging from a problem that is spatially dependent on light propagation and optical properties, as common in traditional optical methods, to a problem solved in the spectral domain. Therefore, sO_2 can be directly quantified without estimating tissue optical properties.

eMSOT requires theoretically at least 5 excitation wavelengths for resolving spectral domain parameters and the relative oxygenated and deoxygenated hemoglobin concentrations. We hereby utilized 21 wavelengths for ensuring high accuracy. The recent evolution of video-rate MSOT imaging systems, based on fast tuning optical parametric oscillator lasers[25] allows the practical implementation of the method. Modern MSOT systems offer 5 wavelength scans at 20Hz or better. Therefore eMSOT is a technology that optimally interfaces to a new generation of fast and handheld spectral optoacoustic systems[26].

The method developed demonstrated quantitative, non-invasive blood oxygenation images in phantoms and tissues *in-vivo* (muscle and tumor) in high-resolution, showing good correlation with the expected physiological state or the histologically observed spatial distribution of perfusion and hypoxia. eMSOT measures blood oxygenation. We hypothesized that a correlation exists to tissue oxygenation measurements by assuming a wide presence of hemoglobin in tissues. We demonstrated congruence (**Supplementary Note 6**) between traditional invasive histological assays resolving tissue hypoxia and eMSOT analysis. Importantly, not only average values are resolved, but there is a close spatial correspondence between hypoxia patterns resolved by eMSOT non-invasively and histological analysis (**Figure 4, Supplementary Fig. 7**).

High-resolution non-invasive imaging of blood oxygenation across entire tissues and tumors offers novel abilities in studying physiological and pathological conditions. This goal has been pursued for decades with near-infrared methods, but the strong effects of photon scattering and

photon diffusion on the signals detected limited the imaging resolution and often impeded accurate quantification[27]. Optoacoustic imaging improves the resolution achieved, over diffuse optical imaging methods but its sO_2 estimation accuracy has been limited so far by depth-dependent fluence attenuation and spectral corruption effects. We showed that conventional spectral optoacoustic methods employing linear unmixing can significantly misestimate blood saturation values in several controlled measurements, including simulations and animal measurements. eMSOT was tested on a vast data-set consisting of >2000 tissue simulations and was consistently found to provide from a comparable to substantially better sO_2 estimation accuracy over linear unmixing. (**Supplementary Note 3**). The large number of simulations was necessary to validate eMSOT, which presents a non-convex optimization problem. eMSOT was further tested on tissue mimicking blood phantoms (**Supplementary Note 4**) and controlled *in-vivo* experiments (**Figure 2, Supplementary Note 5**). In all cases tested, eMSOT offered from comparable to significantly more accurate performance over conventional spectral optoacoustic methods.

A particular challenge in this study was the confirmation of the eMSOT values obtained *in-vivo*. Polarography measurements are invasive, disrupt the local microenvironment and do not allow to recover spatial information. Nuclear methods using tracers are not well suited for longitudinal studies and utilize tracers which need to distribute in hypoxia areas i.e. areas with problematic supply. Therefore the results may not directly compare to eMSOT, even though such study is planned as a next step. BOLD MRI only resolves the effects of deoxygenated hemoglobin but cannot observe oxygenated hemoglobin. For this reason, we selected to utilize traditional histology methods, using cryoslicing, which allows to maintain spatial orientation so that eMSOT and histological results could be compared not only in terms of quantity but also in regard to the spatial appearance.

eMSOT proposes a solution to a fundamental challenge in optical and optoacoustic imaging. In the absence of established and reliable methods that can image blood oxygenation, it may be that eMSOT becomes the gold standard method in blood and tissue oxygenation studies. Its congruence with tissue hypoxia may also allow a broad application in tissue and cancer hypoxia studies. Nevertheless eMSOT performs optimally when applied on well-reconstructed parts of optoacoustic images (**Supplementary Note 5**). For this reason, it was selectively applied herein to the part of the image that is within the optimal sensitivity field of the detector employed. An eMSOT advantage is that it is insensitive to scaling factors such as the Grüneisen coefficient or the spatial sensitivity field of the imaging system (**Methods**). However, due to its scale invariance eMSOT only allows for quantifying blood sO_2 and not absolute blood volume, a goal that will be interrogated in future studies. Next steps further include the eMSOT validation with a larger pool of tissue physiology interrogations spanning from cancer, cardiovascular and diabetes research, relation of physiological phenotypes to metabolic and "-omic" outputs and in clinical application.

METHODS

Animal preparation and handling

All procedures involving animal experiments were approved by the Government of Upper Bavaria. For the preparation of orthotopic 4T1 tumor models, 8 week old, adult female, athymic, Nude-Foxn1 mice (Harlan, Germany) were orthotopically inoculated in the mammary pad with cell suspensions (0.5 million 4T1 cells (CRL-2539). Animals (n=8) were imaged *in-vivo* using MSOT after the tumors reached a suitable size. All imaging procedures were performed under anesthesia using 1.8% Isoflurane. In the O_2 challenge experiment, the mouse was initially breathing 100% O_2 and in the following medical air (20% O_2). During the O_2 Challenge, the mice were stabilized for a period of 10 minutes under each breathing condition before MSOT acquisition. For controlled mouse measurements (n=4), MSOT acquisition was performed on mice under gas anesthesia and breathing 100% O_2 or 20% O_2 by rectally inserting a capillary tube containing pig blood at 100% or 0% sO_2 oxygenation levels. Mice were sacrificed during MSOT imaging with an overdose of CO_2 or after MSOT acquisition by a Ketamine/Xylazine overdose. In the following the mice were stored at -80°C for further analysis.

4T1 cell line was acquired from ATCC (ATCC-CRL-2539, #5068892). The cells were authenticated by the ACTT by several analysis tests: Post-Freeze viability, Morphology, Mycoplasma contamination, post freeze cell growth, interspecies Determination; bacteria & fungal contamination. Additional mycoplasma contamination tests were also performed. For the animal studies no randomization, blinding or statistical methods were performed.

MSOT imaging

Optoacoustic imaging was performed using a real-time whole body mouse imaging scanner, MSOT In Vision 256-TF (iThera-Medical GmbH, Munich, Germany). The system utilizes a cylindrically focused 256-element transducer array at 5MHz central frequency covering an angle of 270 degrees. The system acquires cross-sectional (transverse) images through the animal. The animals are placed onto a thin clear polyethylene membrane. The membrane separates the animals from a water bath, which is maintained at 34°C and is used for acoustic coupling and maintaining animal temperature while imaging. Image acquisition speed is at 10Hz[28]. Imaging was performed at 21 wavelengths from 700 nm to 900 nm with a step size of 10 nm and at 20 consecutive slices with a step size of 0.5 mm. Image reconstruction was performed using a model-based inversion algorithm[29,30] with a non-negativity constraint imposed during inversion and with Tikhonov regularization.

eMSOT method and sO_2 maps

All optoacoustic images $P(\mathbf{r},\lambda)$ obtained over excitation wavelength λ were calibrated to correct for the intensity of laser power per pulse, and for the absorption of water surrounding the tissue. With HbO_2 and Hb being the main tissue absorbers in the near-infrared, multispectral

optoacoustic images can be related to the concentrations of oxy- and deoxy-hemoglobin through Eq. (2).

$$P(\mathbf{r},\lambda) = C(\mathbf{r}) \| \mathbf{\Phi}(\mathbf{r}) \|_2 \frac{\Phi(\mathbf{r},\lambda)}{\| \mathbf{\Phi}(\mathbf{r}) \|_2} (c_{\mathrm{HbO2}}(\mathbf{r}) \varepsilon_{\mathrm{HbO2}}(\lambda) + c_{\mathrm{Hb}}(\mathbf{r}) \varepsilon_{\mathrm{Hb}}(\lambda)). \quad (2)$$

In Eq. (2), $\Phi(\mathbf{r},\lambda)$ is the space and wavelength dependent optical fluence, $C(\mathbf{r})$ is a spatially varying scaling factor corresponding to the effects of the system's spatial sensitivity field and the Grüneisen coefficient, $\varepsilon_{\mathrm{HbO2}}(\lambda)$ and $\varepsilon_{\mathrm{Hb}}(\lambda)$ are the wavelength dependent molar extinction coefficients of oxygenated and deoxygenated hemoglobin, while $c_{\mathrm{HbO2}}(\mathbf{r})$ and $c_{\mathrm{Hb}}(\mathbf{r})$ the associated concentrations at a position $\mathbf{r}$. $\mathbf{\Phi(r)}$ is a vector corresponding to the light fluence spectrum at position $\mathbf{r}$, and $\|\mathbf{\Phi}(\mathbf{r})\|_2$ is its norm across all excitation wavelengths at a position $\mathbf{r}$. We define $\Phi'(\mathbf{r},\lambda) = \Phi(\mathbf{r},\lambda)/\|\mathbf{\Phi}(\mathbf{r})\|_2$ which corresponds to the normalized wavelength dependence of light fluence at a specific position (i.e. normalized spectrum of light fluence).

The space-only dependent factors $C(\mathbf{r})$ and $\|\mathbf{\Phi}(\mathbf{r})\|_2$ do not affect the estimation of blood sO_2 which is calculated as a ratio once the relative concentrations of HbO_2 and Hb are known. We define $c'_{\mathrm{HbO2}}(\mathbf{r}) = C'(\mathbf{r}) c_{\mathrm{HbO2}}(\mathbf{r})$ and $c'_{\mathrm{Hb}}(\mathbf{r}) = C'(\mathbf{r}) c_{\mathrm{Hb}}(\mathbf{r})$, respectively, where $C'(\mathbf{r}) = C(\mathbf{r})\|\mathbf{\Phi}(\mathbf{r})\|_2$ is a common, space-only dependent scaling factor. Using this notation, Eq. (2) can be transformed into Eq. (1). Given $c'_{\mathrm{HbO2}}(\mathbf{r})$ and $c'_{\mathrm{Hb}}(\mathbf{r})$, blood oxygen saturation can be computed as in:

$$sO_2(\mathbf{r}) = \frac{c'_{\mathrm{HbO2}}(\mathbf{r})}{c'_{\mathrm{HbO2}}(\mathbf{r}) + c'_{\mathrm{Hb}}(\mathbf{r})}. \quad (3)$$

For the accurate quantitative extraction of the relative concentrations $c'_{\mathrm{HbO2}}(\mathbf{r})$ and $c'_{\mathrm{Hb}}(\mathbf{r})$, accounting for, or estimating the wavelength dependence of the light fluence $\Phi'(\mathbf{r},\lambda)$ is further required.

The *Eigenspectra* model. eMSOT is based on the observation that the spectral patterns of light fluence present in tissue can be modeled as an affine function of only a few base spectra, independently of tissue depth and the specific distribution of optical properties of the tissue imaged. This hypothesis stems from the notion that the spectrum of light fluence is the result of the cumulative light absorption by hemoglobin; thus the spectrum of light fluence will always be related to the spectra of hemoglobin in a complex non-linear manner. This complex relation can be linearized using a data-driven approach, i.e. through the application of Principal Component Analysis (PCA) on a selected set of light fluence spectra.

The wavelength dependence of the light fluence was herein modeled as a superposition of a mean fluence spectrum $\Phi_{\mathrm{M}}(\lambda)$ and a linear combination of a number of light fluence *Eigenspectra* $\Phi_{\mathrm{i}}(\lambda)$. This model was derived by applying PCA on a training dataset comprised of a set of light fluence spectral patterns. Briefly, a training dataset was formed through the creation of multispectral light fluence simulations using the 1-D analytical solution of the diffusion equation for infinite media. A set of light fluence spectral patterns $\Phi_{z,ox}(\lambda)$ were computed for high physiological tissue optical properties (μ_a=0.3 cm^{-1}, μ_s'=10 cm^{-1}), tissue depths ranging from z=0 to z=1 cm with a step size of 0.143 mm (70 discrete depths in total) and for 21 different uniform background tissue oxygenations ($ox \in \{0\%, 5\%, 10\%, \ldots, 100\%\}$). The so computed set of light fluence spectra $\Phi_{z,ox}(\lambda)$ was normalized ($\Phi'_{z,ox}(\lambda) = \Phi_{z,ox}(\lambda)/\|\mathbf{\Phi_{z,ox}}\|_2$) and used in the following as training data in the context of PCA in order to create an affine, 3-dimensional model consisting of a mean fluence spectrum $\Phi_{\mathrm{M}}(\lambda)$ and three *Eigenspectra* $\Phi_{\mathrm{i}}(\lambda)$. PCA was used for offering a minimum square error property in capturing the spectral variability of the simulated light fluence spectra, in a linear manner. Three components were selected for providing a relatively simple model while also offering a small model error with respect to the training data-set (**Figure 1e**). The wavelength dependence of the light fluence $\Phi'(\mathbf{r},\lambda)$ at any arbitrary tissue position $\mathbf{r}$ can thus be modeled as a superposition of the mean fluence spectrum and three fluence *Eigenspectra* multiplied by appropriate scalar parameters $m_1(\mathbf{r})$, $m_2(\mathbf{r})$, and $m_3(\mathbf{r})$, (hereby referred to as *Eigenfluence* parameters) as per Eq. (4):

$$\Phi'(\mathbf{r},\lambda) = \Phi_{\mathrm{M}}(\lambda) + m_1(\mathbf{r})\Phi_1(\lambda) + m_2(\mathbf{r})\Phi_2(\lambda) + m_3(\mathbf{r})\Phi_3(\lambda) \quad (4)$$

The so created 3-dimensional affine forward model of the wavelength dependence of light fluence was tested with regard to light fluence spectral patterns produced in completely heterogeneous media with varying and randomly distributed optical properties and oxygenation values and demonstrated high accuracy (**Supplementary Fig. 1**). The forward model was further tested through *in-vivo* and *ex-vivo* light fluence measurements, obtained from controlled experiments (**Supplementary Fig. 2**).

Through simulations, it was observed that the values of the m_2 *Eigenfluence* parameter relate primarily to tissue depth and the average tissue optical properties. This trend was observed both in the case of tissue simulations with uniform optical properties (**Figure 1g**) as well as in complex and randomly created tissue simulations described in **Supplementary Note 1, 3**. Conversely, the values of the *Eigenfluence* parameters m_1 and m_3 relate both to tissue depth as well as to tissue background oxygenation. Specifically both m_1 and m_3 present a trend of increasing absolute values with depth and a sign that relates to background tissue oxygenation. These observations were confirmed with *in-vivo* and *ex-vivo* light fluence measurement experiments (**Supplementary Note 1**).

Model Inversion. Using the *Eigenspectra* model of light fluence, the blood sO_2 quantification problem at a position $\mathbf{r}$ formulates as the problem of estimating $c'_{\mathrm{HbO2}}(\mathbf{r})$ and $c'_{\mathrm{Hb}}(\mathbf{r})$ by minimizing $f(\mathbf{r};\ m_1(\mathbf{r}),\ m_2(\mathbf{r}),\ m_3(\mathbf{r}),\ c'_{\mathrm{HbO2}}(\mathbf{r}),\ c'_{\mathrm{Hb}}(\mathbf{r}))$, for brevity noted $f(\mathbf{r})$, defined according to Eq, (5):

$$f(\mathbf{r}) = \sqrt{\sum_{\lambda} \left(P(\mathbf{r},\lambda) - (\Phi_{\mathrm{M}}(\lambda) + \sum_{i=1}^{3} m_i(\mathbf{r})\Phi_i(\lambda)) \cdot (c'_{\mathrm{HbO2}}(\mathbf{r}) \cdot \varepsilon_{\mathrm{HbO2}}(\lambda) + c'_{\mathrm{Hb}}(\mathbf{r}) \cdot \varepsilon_{\mathrm{Hb}}(\lambda)) \right)^2} \quad (5)$$

A solution for the 5 unknowns (namely the 3 light fluence

model parameters, $m_{1...3}(\mathbf{r})$ and the relative blood concentrations $c'_{HbO2}(\mathbf{r})$ and $c'_{Hb}(\mathbf{r})$) can be obtained using a non-linear optimization algorithm and at least 5 excitation wavelengths. The relative blood concentrations $c'_{HbO2}(\mathbf{r})$ and $c'_{Hb}(\mathbf{r})$ are proportional to the actual ones ($c_{HbO2}(\mathbf{r})$ and $c_{Hb}(\mathbf{r})$) with regard to a common scaling factor. However, as stated before, this fact does not affect the computation of sO_2.

The minimization problem defined by Eq. (5) is ill-posed and may converge to a wrong solution unless properly constrained. For achieving inversion stability and accurate sO_2 estimation results, the cost function f of Eq. (5) is simultaneously minimized in a set of grid points placed in the image domain (**Figure 1i**), where three independent constraints are further imposed to the *Eigenfluence* parameters. These constraints correspond to the relation of the *Eigenfluence* parameters between neighbor grid points and to the allowed search space for the *Eigenfluence* parameters:

(i) Since the values of the second *Eigenfluence* parameter m_2 present a consistent trend of reduction with tissue depth observed both in the case of uniform tissue simulations (see **Fig. 1g**) as well as in simulations with random structures, m_2 is constrained to obtain smaller values in the case of grid points placed deeper into tissue.

(ii) As the light fluence spectrum is bound to vary smoothly in space due to the nature of diffuse light propagation, large variations of the *Eigenfluence* parameters m_1, and m_3 between neighbor pixels are penalized. This spatial smoothness constraint is achieved through the incorporation of appropriate regularization parameters α_i to the cost function for constraining the variation of the model parameters (see Eq. (6)). The values of the regularization parameters were selected using cross-validation on simulated data-sets (**Supplementary Note 2**).

(iii) Since the values of m_1 and m_3 are strongly dependent on background tissue oxygenation, an initial less accurate estimation of tissue sO_2 can be effectively used to reduce the total search-space to a constrained relevant sub-space. The limits of search space for the *Eigenfluence* parameters m_1 and m_3 corresponding to each grid point are identified in a preprocessing step as analytically described in **Supplementary Note 2**.

Assuming a polar grid of P arcs (arcs are enumerated with the enumeration initiating from tissue surface) and L radial lines (see **Supplementary Fig. 3b**) with a total of PL points at positions $\mathbf{r}_{p,l}$, and let the vector $\mathbf{m}_i = [m_i(\mathbf{r}_{1,1}), m_i(\mathbf{r}_{1,2}), \ldots, m_i(\mathbf{r}_{1,L}), m_i(\mathbf{r}_{2,1}), \ldots, m_i(\mathbf{r}_{p,l}), \ldots, m_i(\mathbf{r}_{P,L})]^T$ correspond to the values of the *Eigenfluence* parameter i (i=1, 3) over all such points, the new inverse problem is defined as the minimization of cost function f_{grid} defined in Eq. (6) under the constraints defined in Eq. (7).

$$f_{grid} = \sum_{p,l} f(\mathbf{r}_{p,l}) + a_1 \| \mathbf{W}\mathbf{m}_1 \|_2 + a_3 \| \mathbf{W}\mathbf{m}_3 \|_2 \quad (6)$$

$$\begin{aligned}
&T_2^{\min} < m_2(\mathbf{r}_{p,l}) < T_2^{\max}, \forall p,l, \\
&m_2(\mathbf{r}_{p+1,l}) < m_2(\mathbf{r}_{p,l}), m_2(\mathbf{r}_{p+1,l+1}) < m_2(\mathbf{r}_{p,l}), m_2(\mathbf{r}_{p+1,l-1}) < m_2(\mathbf{r}_{p,l}), \forall p,l, \\
&T_i^{\min}(\mathbf{r}_{p,l}) < m_i(\mathbf{r}_{p,l}) < T_i^{\max}(\mathbf{r}_{p,l}), \forall p,l, i = 1,3, \\
&c'_{HbO_2}(\mathbf{r}_{p,l}) \geq 0, \forall p,l, \\
&c'_{Hb}(\mathbf{r}_{p,l}) \geq 0, \forall p,l,
\end{aligned} \quad (7)$$

In Eq. (6), the term $a_1 \| \mathbf{W}\mathbf{m}_1 \|_2 + a_3 \| \mathbf{W}\mathbf{m}_3 \|_2$ implements the spatial smoothness constraints imposed on $m_1(\mathbf{r}_{p,l})$ and $m_3(\mathbf{r}_{p,l})$. The matrix $\mathbf{W}$ describes a connectivity graph defined on the grid of points assumed (**Supplementary Fig. 3b**) and its structure and function are analytically described in **Supplementary Note 2**. In Eq. (7) $T_2^{\min}$ and $T_2^{\max}$ are the search-space limits for $m_2(\mathbf{r}_{p,l})$ which are constant for all grid points and correspond to the maximum and minimum values of m_2 on the training data-set (**Figure 1g**). $T_i^{\min}(\mathbf{r}_{p,l})$ and $T_i^{\max}(\mathbf{r}_{p,l})$, with i=1,3 are the search-space limits for $m_1(\mathbf{r}_{p,l})$ and $m_3(\mathbf{r}_{p,l})$, which are computed per grid point in a preprocessing step as described in **Supplementary Note 2**. The inverse problem defined by Eq. (6), (7) was hereby solved through the utilization of the sequential quadratic programming algorithm of MATLAB toolbox.

Fluence correction and sO_2 quantification. The minimization of cost function f_{grid} (Eq. (6)) under the constraints of Eq. (7) yields an estimate of $m_i(\mathbf{r}_{p,l})$ for each *Eigenfluence* parameter i and each grid point $\mathbf{r}_{p,l}$. The *Eigenfluence* parameters in the convex hull of the grid are in the following estimated by means of cubic interpolation. We note that due to the nature of diffuse light propagation the *Eigenfluence* parameters are expected to vary smoothly in tissue and thus their interpolation is not expected to introduce large errors in the result (see **Supplementary Note 3 and Supplementary Table 2**). The wavelength dependence of light fluence is computed for each pixel within the convex hull of the grid as in $\Phi'(\mathbf{r},\lambda) = \Phi_M(\lambda) + m_1(\mathbf{r})\Phi_1(\lambda) + m_2(\mathbf{r})\Phi_2(\lambda) + m_3(\mathbf{r})\Phi_3(\lambda)$, where $\Phi_i(\lambda)$ is the ith fluence *Eigenspectrum*. Finally, a spectrally-corrected eMSOT image is obtained after dividing the original image $P(\mathbf{r},\lambda)$ with the normalized wavelength dependent light fluence $\Phi'(\mathbf{r},\lambda)$ at each position $\mathbf{r}$ and wavelength λ, i.e. $P^{eMSOT}(\mathbf{r},\lambda) = P(\mathbf{r},\lambda)/\Phi'(\mathbf{r},\lambda)$. The relative concentrations of HbO_2 and Hb ($c'^{\mathbf{eMSOT}}_{\mathbf{HbO2}}(\mathbf{r})$, $c'^{\mathbf{eMSOT}}_{\mathbf{Hb}}(\mathbf{r})$) are computed for each pixel of $P^{eMSOT}(\mathbf{r},\lambda)$ image independently through nonnegative constrained least squares fitting with the spectra of oxygenated and deoxygenated hemoglobin. Thus the eMSOT blood sO_2 maps retain the original resolution of the MSOT imaging system.

We note that both the *Eigenspectra* model and the inversion scheme were hereby optimized for the application of small animal imaging. The *Eigenspectra* model was trained for a maximum depth of 1 cm and the inversion scheme was designed with respect to the same tissue depth and optical properties within the physiological range (**Supplementary Note 2, 3**).

Linear unmixing. Under the simplifying assumption that the light fluence attains a flat spectrum irrespective of the tissue position $\Phi(\mathbf{r},\lambda) = \Phi(\mathbf{r})$ and by assuming hemoglobin as

the major absorber in tissue, optoacoustic spectra can be modeled as a linear combination of the spectra of oxy- and deoxy-hemoglobin. The term linear unmixing refers hereby to the computation of the relative concentrations of HbO_2 and Hb (c_{HbO2}^{lu}**(r),** c_{Hb}^{lu}**(r)**) and subsequently blood sO_2, through nonnegative constrained least squares fitting of the original image $P(\mathbf{r},\lambda)$ with the spectra of Hb and HbO_2.

Blood phantom preparation

For validating the accuracy of eMSOT in quantifying blood oxygenation in deep tissue, we prepared tissue mimicking phantoms, containing blood at known oxygenations levels. Specifically, for simulating tissue background, 2cm –diameter cylindrical solid phantoms were created by using 1.5% Agarose Type I, Sigma-Aldrich (solidifying in $<37^{o}$), 2% intralipid and 3-5% freshly extracted pig blood diluted in NaCl. Different blood oxygenation levels were achieved by diluting oxygen in whole blood (oxygenation process) or by mixing the blood with different amounts of Sodium Dithionite ($Na_2O_4S_2$) (deoxygenation process)[31]. The blood oxygenation levels were monitored using a Bloodgas Analyzer (Eschweiler Gmbh & Co. KG, Kiel Germany).

Cryoslicing color imaging and H&E staining of tumors

After MSOT acquisition, a subset of the mice bearing 4T1 mammarian tumors (n=4) were sacrificed and examined for tumor and tissue anatomy**.** Mice were embedded in an optimal cutting temperature compound (Sakura Finetek Europe BV, Zoeterwonde, NL) and frozen at -80°C. In the following the mice were sliced at an orientation similar to the one of MSOT imaging and color photographs were recorded. The cryoslicing imaging system is based on a cryotome (CM 1950, Leica Microsystems, Wetzlar, Germany), fitted with CCD-based detection camera. During this process, 10 µm slices throughout the whole tumor volume were collected for further histological analysis.

Several slides per tumor were subjected to H&E staining and imaging. The slides containing 10µm cryo-sections were first pre-fixed in 4% PFA (Santa Cruz Biotechnology Inc., Dallas, Texas, USA). Then, they were rinsed with distilled water and incubated 30 seconds with Haemotoxylin acide by Meyer (Carl Roth, Karlsruhe, Germany) to stain the cell nuclei. The slides were then rinsed in tap water again before incubation for 1 second in Eosin G (Carl Roth, Karlsruhe, Germany) to stain cellular cytoplasm. After rinsing in distilled water, the slides were dehydrated in 70%, 94% and 100% ethanol and incubated for 5 minutes in Xylene (Carl Roth, Karlsruhe, Germany) before being cover slipped with Rotimount (Carl Roth, Karlsruhe, Germany) cover media. Representative slides were observed using Zeiss Axio Imager M2 microscope with AxioCam 105 Color, and pictures were then processed using a motorized stitching Zen Imaging Software (Carl Zeiss Microscopes GmbH, Jena, Germany).

Pimonidazole staining of tumor tissues.

A subset of the tumor-bearing mice (n=4) was examined for functional characteristics of the tumors by Pimonidazole histological staining. The hypoxia marker Pimonidazole (Hypoxyprobe, catalog #HP6-100 kit, Burlington, MA, USA) was injected i.p. at 100 mg/kg body weight in a volume of 0.1 ml saline ≈1.5h before tumor excision, and the perfusion marker Hoechst 33342 (Sigma, Deisenhofen, Germany) was administered i.v. at 15 mg/kg body weight in a volume of 0.1 ml saline 1min before the tumor-bearing mice were sacrificed. The tumors were excised immediately after the animals were sacrificed. The orientation of the tumors with respect to the mouse body was retained. 8 µm cryosections were sliced throughout the tumor. The cryosections were fixed in cold (4°C) acetone, air dried and rehydrated in PBS before staining. Pimonidazole was stained with the FITC-labelled anti-Pimonidazole antibody (Hypoxyprobe, Burlington, MA, USA) diluted 1:50 in primary antibody diluent (PAD, Serotec, Oxford, U.K.) by incubating for 1h at 37°C in the dark.

Code and data availability

The code and all relevant data of this work will be made available upon request.

REFERENCES

1. Vaupel, P. & Harrison, L. Tumor hypoxia: causative factors, compensatory mechanisms, and cellular response. *The oncologist*, **9**, 4-9 (2004).
2. Serganova, I., Humm, J., Ling, C. & Blasberg, R. Tumor hypoxia imaging. *Clinical Cancer Research*, **12**, 5260-5264 (2006).
3. Elas, M., *et al.* Quantitative tumor oxymetric images from 4D electron paramagnetic resonance imaging (EPRI): Methodology and comparison with blood oxygen level-dependent (BOLD) MRI. *Magnetic resonance in medicine*, **49**, 682-691 (2003).
4. Ogawa, S., Lee, T.-M., Kay, A.R. & Tank, D.W. Brain magnetic resonance imaging with contrast dependent on blood oxygenation. *Proceedings of the National Academy of Sciences*, **87**, 9868-9872 (1990).
5. Klassen, L.M. & Menon, R.S. NMR simulation analysis of statistical effects on quantifying cerebrovascular parameters. *Biophysical journal*, **92**, 1014-1021 (2007).
6. Rumsey, W.L., Vanderkooi, J.M. & Wilson, D.F. Imaging of phosphorescence: a novel method for measuring oxygen distribution in perfused tissue. *Science*, **241**, 1649-1651 (1988).
7. Zhang, H.F., Maslov, K., Stoica, G. & Wang, L.V. Functional photoacoustic microscopy for high-resolution and noninvasive in vivo imaging. *Nature biotechnology*, **24**, 848-851 (2006).
8. Durduran, T., Choe, R., Baker, W. & Yodh, A. Diffuse optics for tissue monitoring and tomography. *Reports on Progress in Physics*, **73**, 076701 (2010).
9. Eggebrecht, A.T., *et al.* Mapping distributed brain function and networks with diffuse optical tomography. *Nature Photonics*, **8**, 448-454 (2014).
10. Ntziachristos, V. Going deeper than microscopy: the optical imaging frontier in biology. *Nature methods*, **7**, 603-614 (2010).
11. Mohajerani, P., Tzoumas, S., Rosenthal, A. & Ntziachristos, V. Optical and Optoacoustic Model-Based Tomography: Theory and current challenges for deep tissue imaging of optical contrast. *Signal Processing Magazine, IEEE*, **32**, 88-100 (2015).
12. Maslov, K., Zhang, H.F. & Wang, L.V. Effects of wavelength-dependent fluence attenuation on the noninvasive photoacoustic imaging of hemoglobin oxygen saturation in subcutaneous vasculature in vivo. *Inverse Problems*, **23**, S113 (2007).
13. Cox, B., Laufer, J.G., Arridge, S.R. & Beard, P.C. Quantitative spectroscopic photoacoustic imaging: a review. *Journal of Biomedical Optics*, **17**, 61202 (2012).
14. Arridge, S.R. & Hebden, J.C. Optical imaging in medicine: II. Modelling and reconstruction. *Physics in medicine and biology*, **42**, 841 (1997).

15. Li, M.-L., *et al.* Simultaneous molecular and hypoxia imaging of brain tumors in vivo using spectroscopic photoacoustic tomography. *Proceedings of the IEEE*, **96**, 481-489 (2008).
16. Gerling, M., *et al.* Real-Time Assessment of Tissue Hypoxia In Vivo with Combined Photoacoustics and High-Frequency Ultrasound. *Theranostics*, **4**, 604 (2014).
17. Tsai, A.G., Johnson, P.C. & Intaglietta, M. Oxygen gradients in the microcirculation. *Physiological reviews*, **83**, 933-963 (2003).
18. Mesquita, R.C., *et al.* Hemodynamic and metabolic diffuse optical monitoring in a mouse model of hindlimb ischemia. *Biomedical optics express*, **1**, 1173-1187 (2010).
19. Rajaram, N., Reesor, A.F., Mulvey, C.S., Frees, A.E. & Ramanujam, N. Non-Invasive, Simultaneous Quantification of Vascular Oxygenation and Glucose Uptake in Tissue. *PloS one*, **10**, e0117132 (2015).
20. Swain, D.P. & Pittman, R.N. Oxygen exchange in the microcirculation of hamster retractor muscle. *American Journal of Physiology-Heart and Circulatory Physiology*, **256**, H247-H255 (1989).
21. Tsai, A.G., Cabrales, P., Winslow, R.M. & Intaglietta, M. Microvascular oxygen distribution in awake hamster window chamber model during hyperoxia. *American Journal of Physiology-Heart and Circulatory Physiology*, **285**, H1537-H1545 (2003).
22. Stein, J., Ellis, C. & Ellsworth, M. Relationship between capillary and systemic venous PO2 during nonhypoxic and hypoxic ventilation. *American Journal of Physiology-Heart and Circulatory Physiology*, **265**, H537-H542 (1993).
23. Smith, K., Hill, S., Begg, A. & Denekamp, J. Validation of the fluorescent dye Hoechst 33342 as a vascular space marker in tumours. *British journal of cancer*, **57**, 247 (1988).
24. Varia, M.A., *et al.* Pimonidazole: a novel hypoxia marker for complementary study of tumor hypoxia and cell proliferation in cervical carcinoma. *Gynecologic oncology*, **71**, 270-277 (1998).
25. Buehler, A., Kacprowicz, M., Taruttis, A. & Ntziachristos, V. Real-time handheld multispectral optoacoustic imaging. *Optics letters*, **38**, 1404-1406 (2013).
26. Taruttis, A. & Ntziachristos, V. Advances in real-time multispectral optoacoustic imaging and its applications. *Nature Photonics*, **9**, 219-227 (2015).
27. Boas, D.A., *et al.* The accuracy of near infrared spectroscopy and imaging during focal changes in cerebral hemodynamics. *Neuroimage*, **13**, 76-90 (2001).
28. Razansky, D., Buehler, A. & Ntziachristos, V. Volumetric real-time multispectral optoacoustic tomography of biomarkers. *Nature Protocols*, **6**, 1121-1129 (2011).
29. Rosenthal, A., Razansky, D. & Ntziachristos, V. Fast semi-analytical model-based acoustic inversion for quantitative optoacoustic tomography. *IEEE transactions on medical imaging*, **29**, 1275-1285 (2010).
30. Dean-Ben, X.L., Ntziachristos, V. & Razansky, D. Acceleration of Optoacoustic Model-Based Reconstruction Using Angular Image Discretization. *IEEE transactions on medical imaging*, **31**, 1154-1162 (2012).
31. Briely-Sabo, K. & Bjornerud, A. Accurate de-oxygenation of ex vivo whole blood using sodium Dithionite. in *Proc. Intl. Sot. Mag. Reson. Med*, **8,** 2025 (2000).

ACKLOWLEDGEMENTS

Vasilis Ntziachristos acknowledges support from an ERC Advanced Investigator Award 233161 and the Deutsche Forschungsgemeinschaft (DFG), Sonderforschungsbereich-824 (SFB-824), subproject A1.. The work of Stratis Tzoumas was supported by the DFG GRK 1371 grant. The authors would like to thank Elena Nasonova and Karin Radrich for assisting in the blood phantom preparation and Amir Rosenthal and Juan Aguirre for the valuable discussions.

AUTHOR CONTRIBUTION

S.T. conceived the concept of eigenspectra. S.T. and I.O. implemented and optimized eMSOT and performed the simulations and the numerical validations. S.T. and P.S. performed the blood phantom experiments. A.N., S.T., G.M. S.S. and V.N. designed the experimental animal study. A.N. performed all *in vivo* imaging experiments with the help of S.G.. A.N., S.G., S.S. and C.B. performed the histological analysis. S.T. analyzed all experimental MSOT data. All authors contributed in interpreting the data and writing the paper. V.N. supervised the project.

Eigenspectra optoacoustic tomography achieves quantitative blood oxygenation imaging deep in tissues

Stratis Tzoumas[1,2], Antonio Nunes[1] , Ivan Olefir[1], Stefan Stangl[3], Panagiotis Symvoulidis[1,2], Sarah Glasl[1,2], Christine Bayer[3], Gabriele Multhoff[3,4], Vasilis Ntziachristos[1,2*]

[1] *Institute for Biological and Medical Imaging (IBMI), Helmholtz Zentrum München, Ingolstädter Landstrasse 1, Neuherberg, Germany*
[2] *Chair for Biological Imaging, Technische Universität München, Trogerstr. 9, München, Germany*
[3] *Department of Radiation Oncology, Klinikum rechts der Isar, Technische Universität München, Ismaninger Str. 22, München, Germany*
[4] *CCG – Innate immunity in Tumor Biology, Helmholtz Zentrum München, Ingolstädter Landstrasse 1, Neuherberg, Germany*

SUPPLEMENTARY MATERIAL

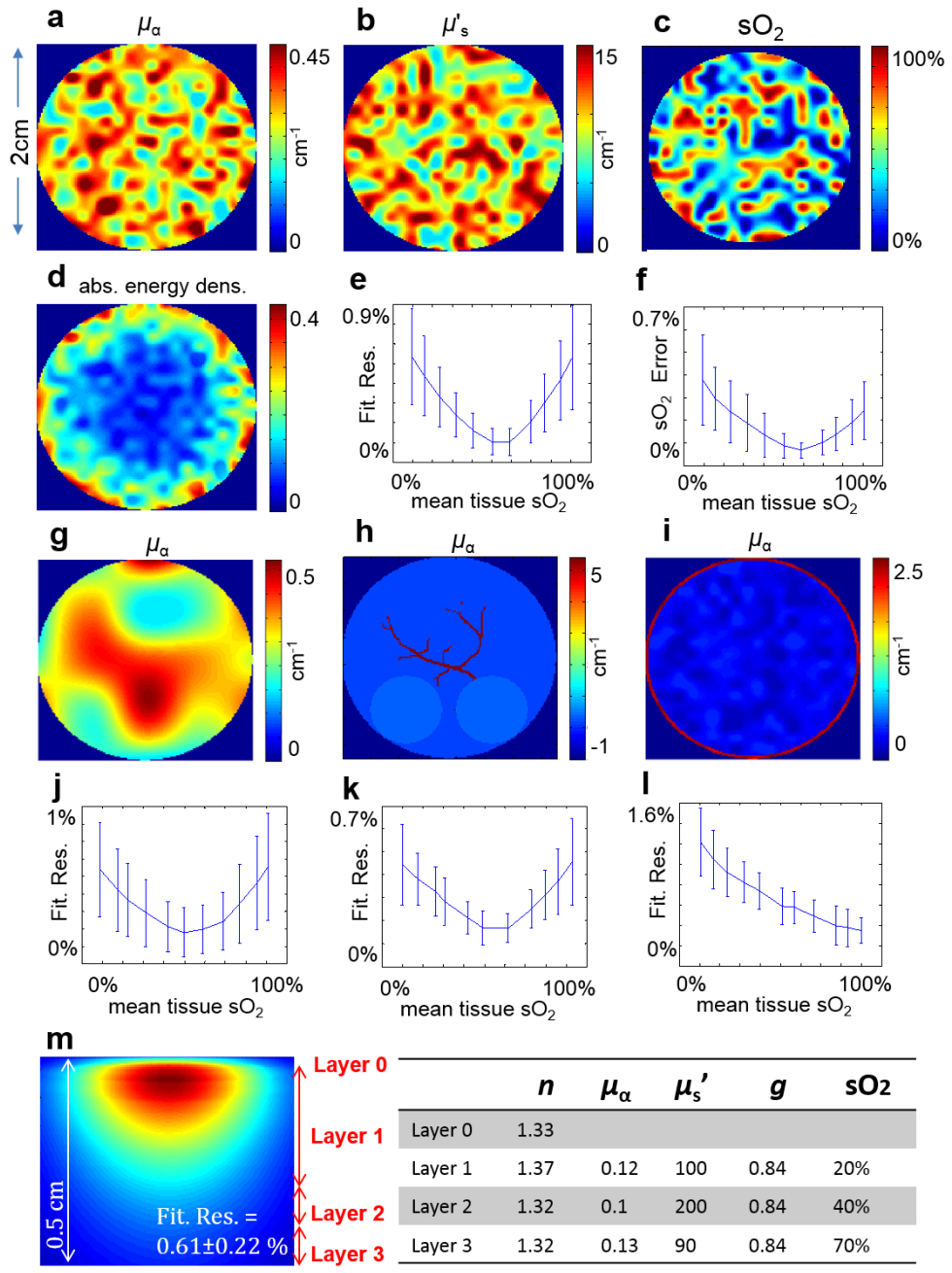

	n	μ_α	μ_s'	g	sO_2
Layer 0	1.33				
Layer 1	1.37	0.12	100	0.84	20%
Layer 2	1.32	0.1	200	0.84	40%
Layer 3	1.32	0.13	90	0.84	70%

Supplementary Figure 1. Numerical validation of the *Eigenspectra* model of light fluence in tissue simulations of arbitrary structures. **(a,b)** Examples of the assumed random spatial maps of **(a)** $\mu_\alpha(\mathbf{r})$ at 800 nm and **(b)** $\mu_s'(\mathbf{r})$, with random, normally distributed values. **(c)** Example of a random spatial map of sO_2. **(d)** Example of multi-wavelength absorbed energy density simulation (wavelength 800 nm presented), created using the FEM DE light propagation model. **(e)** Statistics (–error-bars indicate standard deviation) of the fitting residual of the *Eigenspectra* model computed from all pixels of each simulated multispectral dataset. **(f)** Error propagated to sO_2 estimation due to the fluence approximation using the *Eigenspectra* model (forward model error). **(g-i)** Examples of tissue simulations of low spatial variation of optical properties **(g)**, partially uniform optical properties with highly absorbing vessel like structures **(h)** and cases of high melanin absorption at the tissue surface as well as wavelength dependent scattering **(i)**. **(j-l)** Statistics of the fitting residual of the forward model corresponding to the simulations presented in (**g-i**), respectively. **(m)** Monte Carlo simulations of the wavelength dependent light fluence (fluence of one wavelength is presented) in the ballistic and semi-ballistic regime, assuming semi-uniform multi-layered tissue; Layers are highlighted with red arrows and their optical properties are summarized in the enclosed table. Statistics of the fitting residual of the *Eigenspectra* model (mean and standard deviation) are also presented.

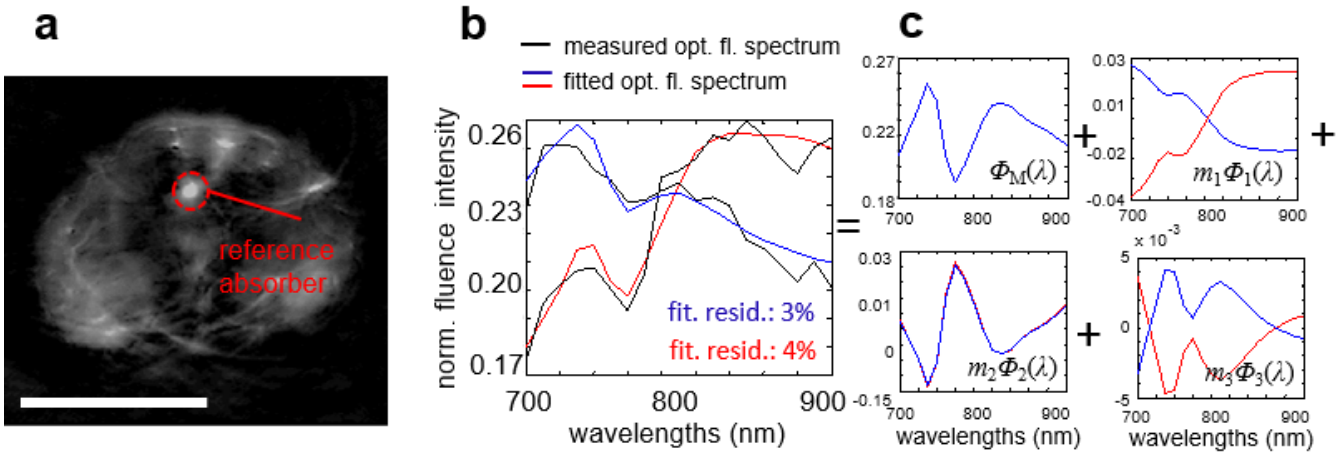

Supplementary Figure 2. Validation of the *Eigenspectra* model using light fluence measurements obtained *in vivo* and *post mortem*. (a) MSOT image (one wavelength presented) of a CD1mouse imaged in the abdominal region with a capillary tube containing a reference absorber inserted in the lower abdominal area (red circle). Scale bar, 1 cm. **(b)** Comparison of the measured spectrum of light fluence in the area of absorber insertion (black curves) with the fitted spectrum using the 3-dimensional *Eigenspectra* model in the case of *in-vivo* imaging (blue curve) and *post-mortem* imaging (red curve). **(c)** The two light fluence spectra corresponding to the *in vivo* (blue) and *post mortem* case (red) are decomposed into a linear combination of spectra $\Phi_M(\lambda)$, $m_1\Phi_1(\lambda)$, $m_2\Phi_2(\lambda)$ and $m_3\Phi_3(\lambda)$.

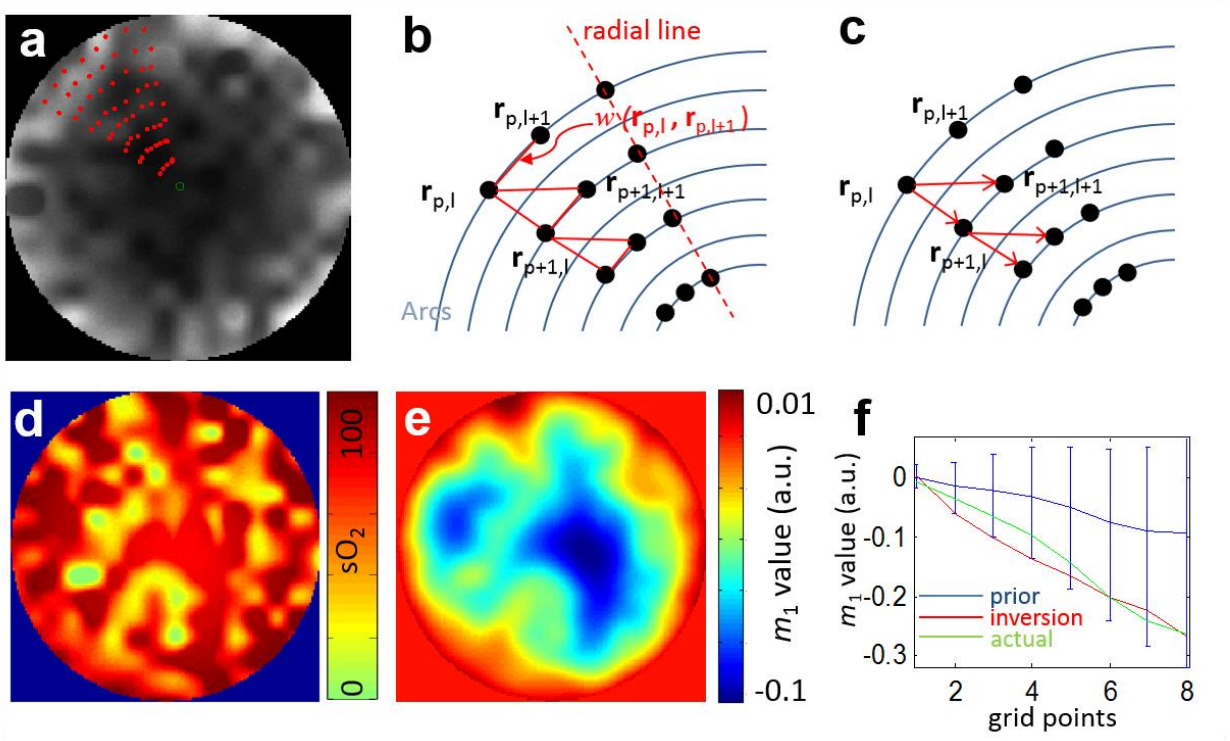

Supplementary Figure 3. Explanation of eMSOT constrained inversion. (**a**) eMSOT inversion is performed simultaneously on a grid of points in the image domain (red points). (**b**) A non-directed weighted connectivity graph defined on the grid of points penalizes large variations of the *Eigenfluence* parameters m_1 and m_3 between neighbor points. The penalization is inversely proportional to the distance w between the grid points. (**c**) A directed graph on the grid of points enforces a decrease on the values of m_2 with depth. (**d-f**) An initial approximation of tissue blood oxygenation is obtained using nonnegative constrained least squares fitting (**d**) and used for obtaining a prior estimate of $\acute{m}_1(\mathbf{r})$ (**e**) and $\acute{m}_3(\mathbf{r})$ model parameters. These prior estimates are used for constraining the total search space for m_1 and m_3 during optimization. (**f**) Prior $\acute{m}_1$ estimate (blue line), limits of the search space (blue vertical lines), actual m_1 values (green line) and m_1 values estimated after optimization (red line) for a radial line of the grid presented in (**a**).

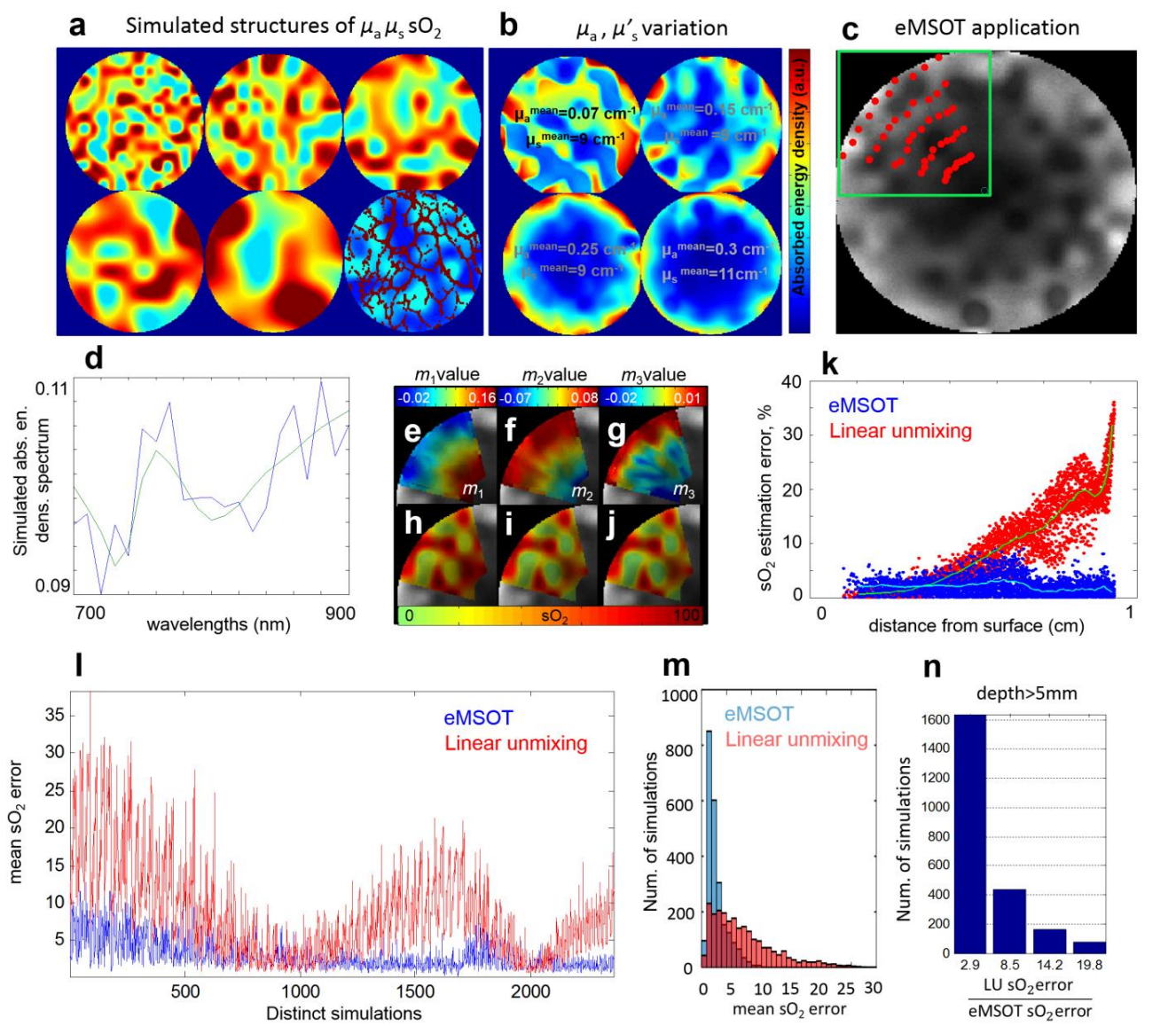

Supplementary Figure 4. Numerical validation of eMSOT in simulations of arbitrarily structured tissues. (a) Examples of the assumed random maps of optical absorption, optical scattering and sO_2 varying from finely granulated to smoothly varying structures and vessel-like patters. The combination of these maps was used to simulate the absorbed energy density of complex tissue using a light propagation model. (**b**) The simulations of multispectral absorbed energy density were formed using varying mean optical properties simulating weakly to strongly absorbing/scattering tissue. **(c)** Simulated multispectral optoacoustic image (one wavelength presented). A polar grid is placed on the upper left part of the image for analysis using eMSOT. **(d)** Original (green) and noisy (blue) simulated absorbed energy density spectrum stemming from one pixel of **(c)**. **(e-g)** Maps of *Eigenfluence* parameters m_1, m_2 and m_3, respectively, obtained after inversion and interpolation. **(h-i)** sO_2 estimation using linear unmixing (**h**) and eMSOT (**i**). (**j**) Actual simulated sO_2 map. (**k**) sO_2 estimation error corresponding to all pixels of the analyzed area using conventional linear unmixing (red points) and eMSOT (blue points), sorted per depth. (**l**) Mean sO_2 error of linear unmixing (red) and eMSOT (blue) corresponding to each simulated data-set tested (2358 data-sets in total). (**m**) Histogram of the mean sO_2 estimation error corresponding to eMSOT (blue) and linear unmixing (red) for all simulated data-sets tested. (**n**) Histogram of the relative sO_2 estimation error of linear unmixing as compared to eMSOT for all simulated data-sets tested and simulated tissue depths > 5mm.

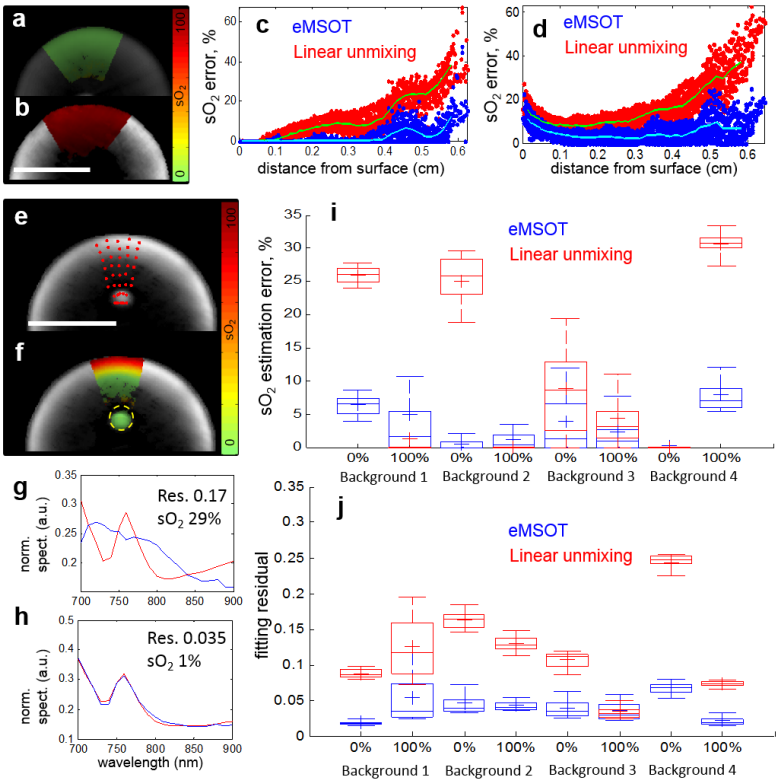

Supplementary Figure 5. Validation of eMSOT using blood phantoms. **(a, b)** eMSOT sO_2 estimation in the case of a uniformly deoxygenated blood phantom (**a**) and a uniformly oxygenated phantom (**b**). Scale bar, 1 cm. (**c, d**) sO_2 estimation error of eMSOT (blue dots) and linear unmxing (red dots) sorted per depth for the case of the deoxygenated phantom (**c**) and oxygenated phantom (**d**). (**e, f**) eMSOT grid application (**e**) and sO_2 estimation (**f**) in the case of a blood phantom with non-uniform background oxygenation containing an insertion of 0% sO_2. The insertion area is marked with a yellow dashed circle. Scale bar, 1 cm. (**g, h**) Spectral fitting and sO_2 estimation corresponding to a pixel in the insertion area in (**f**) using linear unmixing (**g**) and eMSOT (**h**). The blue curves correspond to $P(\mathbf{r},\lambda)$ (**g**) and $P^{\mathrm{eMSOT}}(\mathbf{r},\lambda)$ (**h**) while the red curves correspond to $c_{\mathrm{HbO2}}{}^{\mathrm{lu}}(\mathbf{r})\varepsilon_{\mathrm{HbO2}}(\lambda)+c_{\mathrm{Hb}}{}^{\mathrm{lu}}(\mathbf{r})\varepsilon_{\mathrm{Hb}}(\lambda)$ (**g**) and $c'_{\mathrm{HbO2}}{}^{\mathrm{eMSOT}}(\mathbf{r})\varepsilon_{\mathrm{HbO2}}(\lambda)+c'_{\mathrm{Hb}}{}^{\mathrm{eMSOT}}(\mathbf{r})\varepsilon_{\mathrm{Hb}}(\lambda)$ (**h**). (**i**) Statistics on the sO_2 estimation error of eMSOT (blue) and linear unmixing (red) corresponding to the insertion region of eight different phantoms of four different backgrounds each containing an insertion of 0% and 100% sO_2. (**j**) Statistics on the fitting residual of eMSOT (blue) and linear unmixing (red) corresponding to the insertion region. Statistics in (**i, j**) are derived from all pixels the ROIs corresponding to the insertion area of each phantom. The boxes include 25%-75% and the error-bars 9%-91% of the data. The mean value is denoted with the plus symbol.

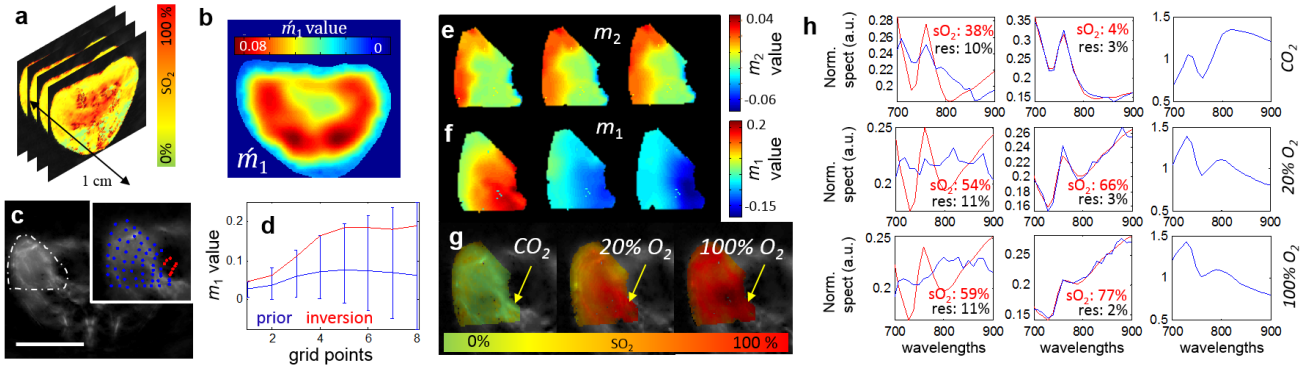

Supplementary Figure 6. Explanation of eMSOT application on experimental tissue images. (**a**) Initial sO_2 maps (computed using linear unmixing) corresponding to multiple MSOT slices surrounding the central slice to be analyzed. (**b**) Prior $\acute{m}_1(\mathbf{r})$ map computed using a 3D FEM DE light propagation model and the initial sO_2 maps as described in **Supplementary Note 2**. (**c**) Selection of a high intensity area in a well-reconstructed part of the image for the automatic application of a grid for eMSOT application. Scale bar, 1 cm. (**d**) Prior $\acute{m}_1$ (blue line), limits of search space (blue vertical lines) and estimated m_1 after eMSOT inversion, corresponding to a radial line of the grid in (**c**). (**e-g**) m_2 (**e**), m_1 (**f**) and sO_2 maps (**g**) computed after eMSOT inversion for the same tissue area under three different breathing conditions. (**h**) Original optoacoustic spectra ($P(\mathbf{r},\lambda)$; left, blue), eMSOT spectra ($P^{\mathrm{eMSOT}}(\mathbf{r},\lambda)$; middle, blue) and estimated spectrum of light fluence (right) corresponding to a deep tissue point (yellow arrow in **g**). Red curves correspond to $c_{\mathrm{HbO2}}{}^{\mathrm{lu}}(\mathbf{r})\varepsilon_{\mathrm{HbO2}}(\lambda)+c_{\mathrm{Hb}}{}^{\mathrm{lu}}(\mathbf{r})\varepsilon_{\mathrm{Hb}}(\lambda)$ (left) and $c'_{\mathrm{HbO2}}{}^{\mathrm{eMSOT}}(\mathbf{r})\varepsilon_{\mathrm{HbO2}}(\lambda)+c'_{\mathrm{Hb}}{}^{\mathrm{eMSOT}}(\mathbf{r})\varepsilon_{\mathrm{Hb}}(\lambda)$ (middle). The fitting residual and the estimated sO_2 value are also presented in each case.

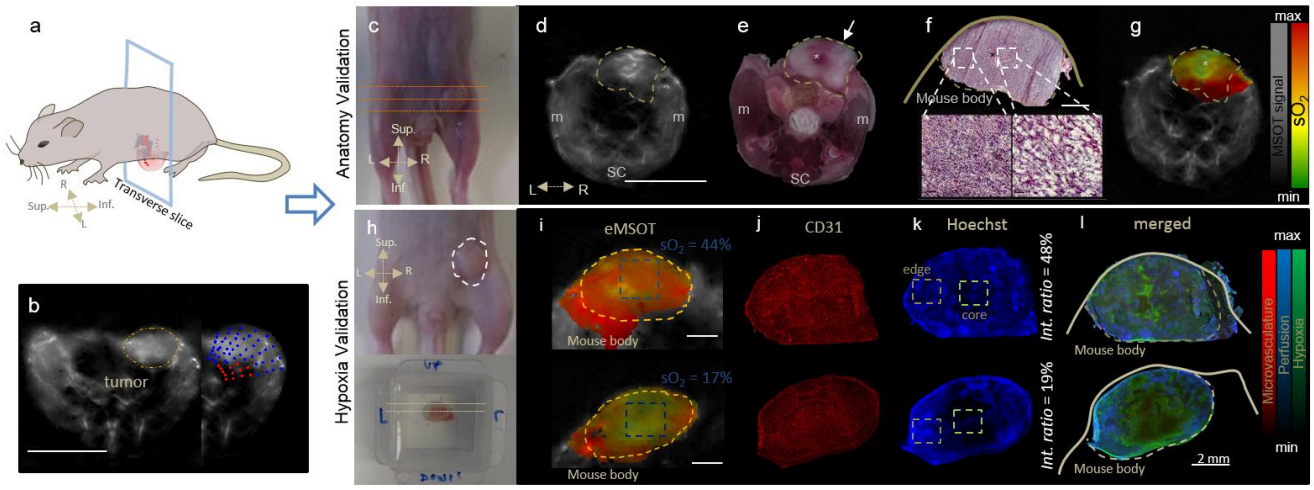

Supplementary Figure 7. eMSOT tumor imaging and histological validation. (**a**) Schematic representation of MSOT imaging at a transverse slice within the tumor area (**b**) Cross-sectional optoacoustic image at a central tumor transverse slice. The tumor region is segmented with a dashed line. The eMSOT grid is further presented (blue and red dots). (**c**) Image of the lower abdominal area displaying the orthotopic mammary tumor. Dashed lines present the orientation of cryoslicing and MSOT imaging. (**d-g**) Anatomical optoacoustic image (**d;** Scale bar, 1cm, m: muscle, sc: spinal cord) and the corresponding cryosliced color photography (**e**), H&E staining of the tumor region (**f;** Scale bar, 2mm) and eMSOT sO_2 analysis of the tumor area (**g**). (**h,** lower) Excised tumor used for functional staining. Yellow dashed lines indicate the slicing orientation. (**i-l**) Examples of a highly perfused (upper row) and low perfused (lower row) tumor analysed with eMSOT for sO_2 estimation (**i**), CD31 staining (**j**), Hoeachst33342 staining (**k**), and merged with Pimonidazole staining (**l**). Scale bar, 2mm. The tumor margins are presented in (**i**) indicated by yellow dashed lines. Blue dashed rectangles indicate a region in the tumor core, the average sO_2 values of which is displayed on the upper right. The intensity ratio of Hoechst33342 staining was calculated by dividing the mean intensity value in the tumor core (green dashed rectangle in (**k**)) over the one in the tumor boundary (grey rectangle in (**k**)).

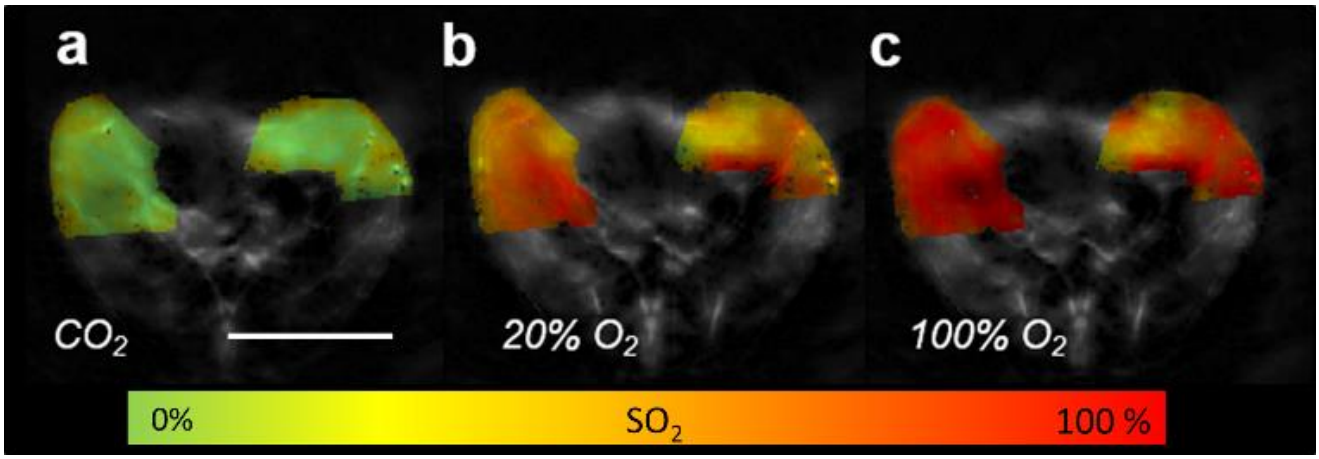

Supplementary Figure 8. Comparison of healthy tissue and tumor sO_2 measurements under a breathing challenge. (a-c) Healthy tissue (left) and tumor (right) sO_2 estimation post-mortem after CO_2 breathing (**a**) and *in-vivo* under 20% O_2 (**b**) and 100% O_2 breathing (**c**).

	Physiological range (30%-80% mean sO_2)				0%-30% mean sO_2	80%-100% mean sO_2	Vessel network (30%-80% sO_2)	
μ_α^{mean} (cm^{-1})	[0.07-0.15]		[0.2-0.3]		[0.07-0.3]	[0.07-0.3]	[0.1, 0.2, 0.3]	
μ_s^{mean}(cm^{-1})	[7-11]		[7-11]		[7-11]	[7-11]	[7, 9, 11]	
Noise lvl.	2.5%	4.5%	2.5%	4.5%	2.5%	2.5%	2.5%	2.5%
Scale							1-3	3-6
Mean sO_2 error	2.36% (4.54%)	2.67% (4.65%)	2.82% (7.9%)	3.38% (7.9%)	5.1% (15.6%)	1.85% (11%)	2.45% (5.83%)	2.0% (4.4%)
% of pixels <10% error	98.6% (89.4%)	98.1% (89.1%)	97.1% (70.8%)	95.0% (70.4%)	85.8% (38%)	99.5% (56%)	98.3% (81.7%)	99.1% (87.5%)
% of pixels <15% error	99.8% (97.2%)	99.7% (97%)	99.3% (85%)	98.7% (84.8%)	97% (57%)	99.9% (74.9%)	99.8% (93%)	99.8% (96%)

Supplementary Table 1. Statistics of the eMSOT performance as evaluated on a large simulated data-set composed of 2358 distinct simulations (red corresponds to conventional linear unmixing).

Grid points	12	30	56	108
Av. computational speed (sec)	1.8 sec	10 sec	52 sec	487 sec
Mean sO_2 error	3.16%	2.74%	2.5%	2.36%
% of pixels <10% error	95.9%	97.7%	98.1%	98.5%

Supplementary Table 2. Statistics of the eMSOT performance as a function of grid density. Statistics correspond to 108 simulated data-sets of $\mu_\alpha^{mean} \in$ [0.1-0.3] cm^{-1}, μ_s^{mean}=10cm^{-1} and mean sO_2 varying between 30%-80%.

Supplementary Note 1: Numerical and experimental validation of the *Eigenspectra* model of light fluence (forward model validation).

For validating the accuracy of the *Eigenspectra* model for light fluence ($\Phi_M(\lambda)$, $\Phi_1(\lambda)$, $\Phi_2(\lambda)$, $\Phi_3(\lambda)$) over light fluence spectra created in arbitrary tissues, we created simulations of the absorbed energy density of arbitrary tissues at different wavelengths (700 nm to 900 nm with a step of 10 nm), using light propagation models. Assuming a circular structure of 1 cm radius, random maps of optical absorption [$\mu_a(\mathbf{r})$] and reduced scattering coefficient [$\mu_s'(\mathbf{r})$] were formed (**Supplementary Fig. 1a** and **b**, respectively), the values of which follow a Gaussian distribution ($\mu_a(\mathbf{r}) \sim N(\mu_a^{mean}, \mu_a^{std})$ where $\mu_a^{mean} \in \{0.07, 0.1, 0.15, 0.2, 0.25, 0.3, 0.35\}$ cm^{-1} and μ_a^{std}=0.1 cm^{-1}, $\mu_s'(\mathbf{r}) \sim N(\mu_s^{mean}, \mu_s^{std})$ where $\mu_s^{mean} \in \{7, 9, 11\}$ cm^{-1} and μ_s^{std}=3 cm^{-1}. The so created absorption maps ($\mu_a(\mathbf{r})$) correspond to tissue absorption at an excitation wavelength of 800 nm (isosbestic point of hemoglobin). The absorption maps for different excitation wavelengths are computed based on the one at 800 nm and the absorption spectra of oxy- and deoxy-hemoglobin. The relative amount of oxy- versus deoxy-hemoglobin at each position **r** is defined by a random map of tissue blood oxygenation (**Supplementary Fig. 1c**). Different blood sO_2 maps were simulated (one example presented in **Supplementary Fig. 1c**) with spatially varying random oxygenation values, and with an average tissue oxygenation varying from ~10% to 90% and a standard deviation of 30%.

The multispectral absorption and scattering maps were employed in a 2D finite-element-method (FEM) solution of the diffusion equation (DE)[1] to simulate multispectral optoacoustic data-sets (i.e. multi-wavelength absorbed energy density) of tissue with arbitrary structure, optical properties and oxygenation. One such example is shown in **Supplementary Fig. 1d** for a single wavelength. From these datasets, the normalized wavelength dependent light fluence $\Phi'(\mathbf{r},\lambda)=\Phi(\mathbf{r},\lambda)/\|\mathbf{\Phi(r)}\|_2$ was calculated for each position **r** in the image. The residual value obtained after comparing the simulated fluence spectra $\mathbf{\Phi'(r)}$ to their approximation using the basis functions of the *Eigenspectra* model ($\mathbf{\Phi'_{Model}(r)}$) was computed (res $=\|\mathbf{\Phi'(r)}-\mathbf{\Phi'_{Model}(r)}\|_2/\|\mathbf{\Phi'(r)}\|_2$) for each pixel in the image **r** and statistics of this residual value are presented in **Supplementary Fig. 1e.** Statistics correspond to all pixels of 21 simulations per mean oxygenation level, corresponding to different mean optical absorption and scattering (231 simulations in total). **Supplementary Fig. 1f** further plots the error of the forward model in the sO_2 estimation (i.e. the error propagated in sO_2 estimation due to the approximation of $\Phi'(\mathbf{r},\lambda)$ with $\Phi'_{Model}(\mathbf{r},\lambda)$).

The *Eigenspectra* forward model was tested with 231 simulations of high (**Supplementary Fig. 1a-c**) and 231 simulations of low spatial variation of optical properties (example shown in **Supplementary Fig. 1g**) and blood oxygenation maps. Moreover the forward model was tested in simulations of blob-like features (representing organs) and vessel-like structures (**Supplementary Fig. 1h**). In this case, the blob-like structures correspond to μ_a = 0.3 cm^{-1}, the background to μ_a = 0.1 cm^{-1} and the vessel like structures to μ_a = 5.4 cm^{-1} and μ_s' = 16 cm^{-1}. The μ_s' and sO_2 maps corresponding to the background followed a random distribution as previously described and the sO_2 of the vessel-like structure was retained uniform and 25% higher than the mean oxygenation of the background. Statistics on the fitting residual of the forward model on the simulations of **Supplementary Fig. 1a, g, h** are presented in **Supplementary Fig. 1e, j, k**, respectively. We observed a small error in the forward model independently of tissue structure and the variations of optical properties and tissue oxygenation.

To assess the potential influence of parameters not included in the model such as the absorption of melanin and the wavelength dependence of scattering we further created simulations containing a strongly absorbing melanin component at the tissue surface (μ_a = 2.5 cm^{-1}) and an exponentially decaying scattering coefficient ($\mu_s'= 18.9(\lambda/500)^{-0.6}$ cm^{-1}) that corresponds to whole blood measurements[2]; an example presented in **Supplementary Fig. 1i**. The assumed optical properties were again following a normal distribution with $\mu_a(\mathbf{r}) \sim N(\mu_a^{mean}, \mu_a^{std})$ where $\mu_a^{mean} \in \{0.07, 0.1, 0.15, 0.2, 0.25, 0.3, 0.35\}$cm^{-1} and μ_a^{std}=0.1 cm^{-1}, $\mu_s'(\mathbf{r}) \sim N(\mu_s^{mean}, \mu_s^{std})$) where $\mu_s^{mean} \in \{7, 9, 11\}$ and μ_s^{std} =3 cm^{-1} (21 simulations per mean oxygenation, 231 simulations in total). Similar to the absorption maps, the so created scattering maps $\mu_s'(\mathbf{r})$ correspond to tissue scattering at an excitation wavelength of 800 nm. The scattering maps for different excitation wavelengths are computed based on the one at 800 nm and the exponentially decaying curve of the scattering coefficient. In this case the fitting residual of the forward model is increased (**Supplementary Fig. 1 l**) but is still preserved in relatively low levels indicating that the model retains accuracy despite the simplifying assumptions in its creation.

The accuracy of the forward model in the ballistic regime was tested using Monte Carlo simulations[3] of multi-layered tissue (**Supplementary Fig. 1 m**). Four different tissue layers were assumed with different oxygenation levels and optical properties. In this case the fitting residual of the forward model is similar to the one when using the diffusion equation: 0.61±0.22%.

The graphs indicate a small model error, supporting the hypothesis that a simple affine model with only three *Eigenspectra* can capture the spectral variability of $\Phi'(\mathbf{r},\lambda)$ in complex tissue structures, independently of the distribution of the optical properties. We hereby note that the error in sO_2 estimation depicted in **Supplementary Fig. 1f** is just indicative of the model accuracy (error of the forward model) and does not relate to the actual blood sO_2 estimates that can be obtained through this procedure by solving the inverse problem (estimation error of the inverse problem).

To experimentally investigate the validity of the *Eigenspectra* model of light fluence we obtained measurements from small animals *in-vivo* and *post-mortem*. We measured the light fluence in tissue by inserting a reference chromophore with well characterized spectrum within tissue. Specifically, a capillary tube was rectally inserted into an anesthetized CD1 mouse and the animal was imaged in the lower abdominal area *in-vivo* using the MSOT system. The capillary tube was filled with black India ink, the spectrum of which was previously measured in the photospectrometer. The animal was imaged *in-vivo* under 100% O_2 breathing and *ex-vivo*. These two different physiological conditions were employed in order to investigate the influence of the average background tissue oxygenation on the spectrum of the light fluence.

The per-wavelength image intensity at the region of the ink insertion (i.e. the optoacoustic measured spectrum which corresponds to the multiplication of the local absorption with the local light fluence) was elementwise divided by the actual absorption spectrum of ink. The resulting spectrum after division corresponds to the wavelength dependence of the local light fluence. The measured light fluence spectrum computed in this way was fitted to the *Eigenspectra* model and the two curves and the fitting residual are presented in **Supplementary Fig. 2.**

Supplementary Fig. 2a presents a single wavelength optoacoustic image of the mouse in the abdominal area. The area where the light fluence is measured is indicated with a red circle. **Supplementary Fig. 2b** presents the spectrum of the experimentally measured light fluence (black curves) and the fitting result using the *Eigenspectra* model in the case of *in-vivo* (blue curve) and *post-mortem* imaging (red curve). The low fitting residuals indicate good agreement of the model with experimental reality. **Supplementary Fig. 2c** presents the decomposition of the two fitted light fluence spectra as a linear combination of the mean fluence spectrum and the three *Eigenspectra*. While the first and the third *Eigenspectra* components change dramatically with respect to the two different tissue oxygenation states, the second component that corresponds to tissue depth remains relatively unchanged. Moreover the values of the m_1 parameter obtained after fitting were positive in the *post-mortem* case and negative in the *in vivo* case, an observation that is in accordance with the dependence of m_1 on background tissue oxygenation, presented in **Figure 1f**. This observation was confirmed by performing the same experiment in 2 more animals. Overall, the low fitting residual even in the case of experimental data obtained *in-vivo* indicates good agreement between theory and experimental reality.

Supplementary Note 2: Constrained inversion

Spatial smoothness constraint. The spatial characteristics of light fluence were exploited for overcoming the ill-posed nature of the optimization problem defined by Eq. (5). In contrary to tissue absorption which can vary arbitrarily, the light fluence is bound to vary smoothly in space due to the nature of diffuse light propagation. In the context of the *Eigenspectra* model inversion, such *a priori* information can be incorporated by attempting simultaneous inversion on a grid of points defined in the image domain (an example of such a grid is shown in **Supplementary Fig. 3a**).

In our implementation, this *ad hoc* spatial smoothness constraint is enforced by assuming a weighted non-directed graph (**Supplementary Fig. 3b**) that connects the neighbor grid points with edges that carry weights *w*, which are inverse proportional to the distance between the neighbor grid points. As described in **Methods**, a circular grid of *P* arcs and *L* radial lines (**Supplementary Fig. 3b**) is assumed containing *PL* points at positions $\mathbf{r}_{p,l}$. The arcs are enumerated from 1 to *P*, with higher indexes indicating larger tissue depths. We define the vector $\mathbf{m_i} = [m_i(\mathbf{r}_{1,1}), m_i(\mathbf{r}_{1,2}), \ldots, m_i(\mathbf{r}_{1,L}), m_i(\mathbf{r}_{2,1}), \ldots, m_i(\mathbf{r}_{p,l}), \ldots, m_i(\mathbf{r}_{P,L})]^T$ (dimensions $PL\times1$) which contains all values of the *Eigenfluence* parameter *i* (i=1…3) over all grid points. Using this notation the objective function of the eMSOT inverse problem is defined in Eq. (6), where the term $a_1 \| \mathbf{W}\mathbf{m}_1 \|_2 + a_3 \| \mathbf{W}\mathbf{m}_3 \|_2$ enforces the *ad hoc* spatial smoothness constraints imposed on m_1 and m_3.

The matrix **W** implements the weighted non-directed connectivity graph (**Supplementary Fig. 3b**) and it has dimensions of $K\times PL$, where *K* is the total number of edges of the connectivity graph: $K=|E|$ where *E* is the set of all edges of the connectivity graph**.** We re-enumerate grid points as follows: $\mathbf{r}_{p,l} \rightarrow \mathbf{r}_{(p-1)P+l}$, so that every grid point has a corresponding index in the range of 1… *PL*. Let *u* and *v* be the indices specifying two of the grid points: $\mathbf{r}_u$ and $\mathbf{r}_v$. If these points are connected, the pair $e_{u,v} = (\mathbf{r}_u, \mathbf{r}_v)$ is an edge, i.e. $e_{u,v} \in E$. Let us now enumerate the edges of the graph and let $k_{u,v} \in \{1...K\}$ be the index of an edge $e_{u,v}$. Each row of matrix **W** corresponds to a single edge of the connectivity graph shown in **Supplementary Fig. 3b**, and it contains only two non-zero elements corresponding to the points it connects. For instance, for an edge $e_{u,v}$ there is a corresponding row in **W** with an index $k_{u,v}$ that has non-zero elements at the columns *u* and *v* corresponding to the connected points $\mathbf{r}_u$ and $\mathbf{r}_v$. The values of the two non-zero elements per row are: $\mathbf{W}_{k_{u,v},u} = d(e_{u,v})$ and $\mathbf{W}_{k_{u,v},v} = -d(e_{u,v})$, where $d(e_{u,v}) = 1/\|\mathbf{r}_u - \mathbf{r}_v\|_2$. The multiplication $\mathbf{W}\mathbf{m}_i$ results into a vector of *K* elements (corresponding to the *K* edges), which are equal to $d(e_{u,v})(m_i(\mathbf{r}_u) - m_i(\mathbf{r}_v))$. When the regularization terms $\|\mathbf{W}\mathbf{m}_i\|_2 = \sqrt{\sum_{e_{u,v}\in E} d^2(e_{u,v})(m_i(\mathbf{r}_u) - m_i(\mathbf{r}_v))^2}$, i=1,3, are added to the minimization function f_{grid}, they enforce a simultaneous minimization of the spatial variation of m_1 and m_3 *Eigenfluence* parameters.

The values of the regularization parameters α_1 and α_3 were selected using cross-validation on simulated data-sets with finely granulated structures (**Supplementary Fig. 1a-c**). We did not observe high sensitivity of the result obtained to small changes of the regularization parameters. The same values for the regularization parameters were used for all simulated and experimental data presented in the work.

Constraint of m_2 with tissue depth. An additional spatial fluence constraint is applied in the case of the second *Eigenfluence* parameter m_2. Through simulations of uniform optical properties as well as simulations with randomly varying optical properties it was observed that the values of m_2 are strongly and consistently associated with tissue depth, obtaining lower values in deeper tissue areas. Through the definition of an additional directed graph based on the assumed gird (**Supplementary Fig. 3c**) the value of m_2 at a certain grid point was enforced to obtain larger values than the ones of its direct neighbors placed deeper in tissue. Since the grid arcs are enumerated from 1 to *P*, with higher indexes indicating larger tissue depths this constraint is expressed through the following set of inequalities:

$$m_2(\mathbf{r}_{p+1,l}) < m_2(\mathbf{r}_{p,l}), m_2(\mathbf{r}_{p+1,l+1}) < m_2(\mathbf{r}_{p,l}), m_2(\mathbf{r}_{p+1,l-1}) < m_2(\mathbf{r}_{p,l}), \forall p, l,$$

Search-space constraints through an initial sO_2 approximation. For further enhancing the inversion stability, additional constraints were imposed to the *Eigenfluence* parameters that relate to both depth and background tissue oxygenation (i.e. m_1 and m_3) based on a first approximate estimate of tissue blood oxygenation. By performing linear spectral unmixing on the raw multispectral optoacoustic images $P(\mathbf{r},\lambda)$ a first estimation map of blood sO_2 levels can be obtained. It is noted that this sO_2 map is incrementally erroneous with tissue depth, however it can serve as a first approximation for constraining the total search-space for m_1 and m_3 to a more relevant sub-space. Using the so created sO_2 map (**Supplementary Fig. 3d**) and by assuming uniform tissue optical properties (i.e. μ_α= 0.3 cm^{-1} at 800 nm and μ_s'=10 cm^{-1}) a light fluence map is simulated using a FEM of the DE. By fitting the simulated light fluence spectra $\Phi'(\mathbf{r},\lambda)$ to the *Eigenspectra* model, prior estimates of all model parameters $\acute{m}_1(\mathbf{r})$, $\acute{m}_2(\mathbf{r})$ and $\acute{m}_3(\mathbf{r})$ can be obtained for each pixel $\mathbf{r}$. A map of $\acute{m}_1(\mathbf{r})$ corresponding to the sO_2 map of **Supplementary Fig. 3d** is presented in **Supplementary Fig. 3e** while the values of $\acute{m}_1(\mathbf{r}_{p,l})$ for all grid positions $\mathbf{r}_{p,l}$ corresponding to one radial line of the gird in **Supplementary Fig. 3a** are presented in **Supplementary Fig. 3f** (blue line).

The optimization problem of Eq. (6) is solved, with the values of $m_1(\mathbf{r}_{p,l})$ and $m_3(\mathbf{r}_{p,l})$ constrained to lie within a region surrounding the initial prior estimate $\acute{m}_i(\mathbf{r}_{p,l})$ (blue vertical lines in **Supplementary Fig. 3f**):

$$T_i^{\min}(\mathbf{r}_{p,l}) < m_i(\mathbf{r}_{p,l}) < T_i^{\max}(\mathbf{r}_{p,l}), \forall p, l, i = 1,3.$$

The limits of the allowed search space ($T_i^{\min}(\mathbf{r}_{p,l})$, $T_i^{\max}(\mathbf{r}_{p,l})$) were selected *ad hoc* as a function of the prior *Eigenfluence* values $\acute{m}_i(\mathbf{r}_{p,l})$ and tissue depth, through the comparison of the prior and the real *Eigenfluence* parameters computed in tissue simulations of varying (uniform) optical properties ($\mu_\alpha \in$ [0.1-0.3]cm^{-1} at 800 nm, μ_s'=10 cm^{-1}) and all uniform oxygenation levels. It is noted that the allowed search space is incrementally larger with tissue depth since in deep tissue the original sO_2 estimates (and thus the *Eigenfluence* priors) usually deviate significantly from the true values. **Supplementary Fig. 3f** presents an example of constrained inversion corresponding to a radial grid line of the simulation of **Supplementary Fig. 3a**: The blue line indicates the prior $\acute{m}_1(\mathbf{r}_{p,l})$ across a radial line of the grid, the blue vertical lines indicate the limits of search space, the green line indicates the actual $m_1(\mathbf{r}_{p,l})$ values of the grid points and the red line the estimated ones after nonlinear optimization. The same function for computing the limits ($T_i^{\min}(\mathbf{r}_{p,l})$, $T_i^{\max}(\mathbf{r}_{p,l})$) as a function of the prior $\acute{m}_i(\mathbf{r}_{p,l})$ estimate and tissue depth was used for all simulated and experimental data presented in the work. We note that this constraint (identified through trends in uniform tissue data) may not always be exact in data of complex structures of optical properties and oxygenation; thus excluding in certain cases the optimal solution from the allowed search space. Despite this, the evaluation of **Supplementary Note 4** indicated that the enforcement of this constraint typically leads to a solution close to the optimal one even in such cases, while it minimizes the possibility or an irrelevant convergence in all cases; sacrificing thus accuracy for robustness.

Supplementary Note 3: Numerical validation of eMSOT.

For investigating the ability of eMSOT to obtain accurate quantitative estimates of tissue blood oxygenation we validated its performance using numerical simulations of multi-wavelength absorbed energy density. The absorbed energy density simulations were formed as described in **Supplementary Note 1** using random or semi-random maps of absorption, scattering coefficient and blood oxygenation. A large validation data-set of 2358 different simulations was employed. The optical properties and sO_2 maps followed a random spatial variation with different structural characteristics ranging from finely granulated to smoothly varying structures (**Supplementary Fig. 4a**) as well as highly absorbing vascular structures with an absorption coefficient ranging from 1 to 6 times larger than the mean tissue background (**Supplementary Fig. 4a right low**). In each case the mean tissue optical properties varied from low to high tissue absorption and scattering (**Supplementary Fig. 4b**) in the physiological range ($\mu_\alpha^{\text{mean}} \in$ {0.07, 0.1, 0.15, 0.2, 0.25, 0.3} cm^{-1} at 800 nm and $\mu_s^{\text{mean}} \in$ {7, 9, 11} cm^{-1}). For each combination of μ_α^{mean}, μ_s^{mean}, different random blood sO_2 maps were assumed ranging from a mean tissue oxygenation of 10% to 90%. Random Gaussian noise with energy varying from 2.5% to 4.5% of the original energy of the spectra in each pixel was further superimposed.

Supplementary Fig. 4c presents a simulated multispectral optoacoustic image (one wavelength presented) after incorporating the optical property maps in a FEM solution of the diffusion equation. A polar grid of 50 points is applied in the upper-left part of the simulation for the application of the eMSOT method. The parameters of inversion and the constraints employed were the same with the ones used for analyzing the *in-vivo* datasets and are analytically described in **Methods** and **Supplementary Note 2**. An example of the original (green) and the noisy spectrum (blue) corresponding to a pixel of **Supplementary Fig. 4c** with 4.5% superimposed random noise is visualized in **Supplementary Fig. 4d**. **Supplementary Fig. 4e-g** present the recovered maps of the *Eigenfluence* parameters $m_1(\mathbf{r})$, $m_2(\mathbf{r})$ and $m_3(\mathbf{r})$ after inversion and interpolation in the convex hull of the grid. **Supplementary Fig. 4h-j** present the sO_2 estimation using linear unmixing (**h**), eMSOT sO_2 estimation (**i**), as well as the actual simulated sO_2 map (**j**). **Supplementary Fig. 4k** presents the corresponding errors in sO_2 estimation of

eMSOT (blue points) and linear unmixing (red points) in all pixels of the analyzed area, sorted per depth. The sO_2 estimation error maps in the whole analyzed area were used for statistically evaluating the eMSOT performance.

Upon evaluation of the method on a set of 2358 created simulations, we observe that in the physiological range of mean tissue oxygenation between 30% and 80% the mean sO_2 estimation error ranges from 2.4% to 3.4% depending on the levels of random noise, while in ~97% of the cases the sO_2 error did not exceed 10% (**Supplementary Table 1**). We did not observe dramatic performance differences between different mean optical properties or different structures of the optical properties. We further did not observe significant performance degradation with high levels of superimposed noise indicating that the inversion scheme is rather robust to noise. The largest errors were observed in the case of less than 30% mean tissue oxygenation. In this case the mean sO_2 error was 5% and in ~97% of the cases the error was less than 15%. The results of the statistical evaluation of the method over all simulations tested are analytically presented in **Supplementary Table 1**.

Supplementary Fig. 4l presents the mean sO_2 error of linear unmixing and eMSOT corresponding to each simulated data-set tested, while **Supplementary Fig. 4m** present the histogram of the mean sO_2 error corresponding to all simulations. In 88% of all cases tested, eMSOT offered a lower mean estimation error than conventional linear unmixing. In the rest 12% of the cases linear unmixing offered a better estimation, but the mean sO_2 errors were comparable and both were lower than 8%. Finally, **Supplementary Fig. 4n** presents a histogram of the relative sO_2 error yielded by linear unmixing over eMSOT for all simulated data-sets tested and for simulated tissue depths>5 mm; indicating that eMSOT typically offered 3 to 8-fold enhanced sO_2 estimation accuracy in deep tissue.

The statistical evaluation of **Supplementary Table 1** corresponds to the application of a polar grid of an angle step of $\pi/20$ rads and a radial step of 0.14 cm (40 grid points). The effect of the grid density on the sO_2 estimation accuracy was further tested through the application of different grid densities containing 12, 30, 49 and 108 grid points deployed in a $\pi/4$ disk area; the results are summarized in **Supplementary Table 2**. We observed that the sO_2 estimation accuracy does not increase dramatically with an increased grid density due to the smooth spatial variations of light fluence in tissue.

Supplementary Note 4: Validation of eMSOT with tissue mimicking blood phantoms

Blood phantoms with controlled oxygenation levels were created for validating the eMSOT accuracy under experimental conditions where gold standard is available. Different blood sO_2 levels were created by adding different amounts of Sodium Dithionite ($Na_2O_4S_2$)[4], a chemical that allows for efficient deoxygenation of blood. Control experiments indicated that blood solutions in NaCl and intralipid could be stably retained at 100% sO_2 under no $Na_2O_4S_2$ addition and at 0% under 100 mg/g $Na_2O_4S_2$ addition. When $Na_2O_4S_2$ was added at a concentration of 2-4 mg/g, blood solutions were initially deoxygenated but would gradually change to higher oxygenation levels.

A number of cylindrical (diameter 2cm) tissue mimicking solid blood phantoms were created consisting of 3%-5% blood in a solution of NaCl, intralipid (2%) and low temperature melting Agarose. Four different states of background blood oxygenation were formed though the administration of 100 mg/g $Na_2O_4S_2$ (corresponding to 0% sO_2 background), 3 mg/g $Na_2O_4S_2$, 4 mg/g $Na_2O_4S_2$ (corresponding to an unknown and spatially varying sO_2 in background) and 0 mg/g $Na_2O_4S_2$ (corresponding to 100% sO_2 background). A 3mm diameter insertion containing a sealed capillary tube filled with 20% blood at 0% sO_2 and 100% sO_2 was introduced at a depth of 5-8mm within each solid blood phantom. The phantoms were imaged using MSOT and the images were analyzed using the eMSOT method and conventional linear unmixing.

Supplementary Fig. 5a-b present the application of the eMSOT method in the case of a uniform phantom of 0% sO_2 and a phantom of 100% sO_2, respectively. **Supplementary Fig. 5c-d** present the sO_2 estimation error of the eMSOT method (blue dots) and linear unmixing (red dots) for all analyzed pixels sorted per imaging depth.

Supplementary Fig. 5e-f present the application of the eMSOT method in the case of a phantom with an unknown, non-uniform sO_2 background and an insertion of 0% sO_2 blood. The eMSOT grid is placed appropriately to cover the insertion area. **Supplementary Fig. 5g-h** present the initial spectrum in the insertion area [$P(\mathbf{r},\lambda)$] and the sO_2 estimation using linear unmixing (**g**) as well as the corrected spectrum [$P^{\mathrm{eMSOT}}(\mathbf{r},\lambda)$] and sO_2 estimation using eMSOT method (**h**). **Supplementary Fig. 5i** summarizes the sO_2 estimation error of linear unmixing (red) and eMSOT method (blue) corresponding to the insertion area in the case of 8 different blood phantoms (4 different backgrounds and 2 different insertions per background). eMSOT offers higher accuracy with an sO_2 estimation error that is typically less than 10%, as opposed to linear unmixing that can be associated with errors as high as 30%. Finally, **Supplementary Fig. 5i** presents the fitting residual of linear unmixing (red) and eMSOT (blue) in each case.

Supplementary Note 5: Application of eMSOT on experimental tissue images

In experimental tissue data (muscle and tumor analysis) the prior $\acute{m}_1(\mathbf{r})$ and $\acute{m}_3(\mathbf{r})$ maps were computed as described in **Supplementary Note 2** by using a 3D FEM DE light propagation model and 20 sO_2 maps corresponding to 20 consecutive MSOT slices (with a step size 0.5 mm) surrounding the central slice to be analyzed (**Supplementary Fig. 6a**). This was performed in order to provide robust *Eigenfluence* prior estimates even in cases of substantial sO_2 variations in the 3D illuminated volume (MSOT illumination width ~ 1 cm). **Supplementary Fig. 6b** presents the prior $\acute{m}_1(\mathbf{r})$ map corresponding to an animal imaged *post-mortem* after CO_2 breathing.

eMSOT accuracy depends on the quality of the measured optoacoustic spectra in the grid area. For ensuring successful application, an image area of high intensity (high SNR) and fidelity (visually presenting no reconstruction artefacts e.g. due to ill

acoustic coupling) and typically corresponding to the central-upper part of the image (corresponding to the focal area of the ultrasound sensors and eliminating the possibility of reconstruction artefacts due to the limited angle of coverage) was selected for applying the eMSOT method. Upon manual segmentation of an area, a polar grid is automatically applied in the image domain (**Supplementary Fig. 6c**). The grid point location is automatically updated so that the points occupy the highest intensity pixels in their local vicinity. Grid points that correspond to image values under a predefined threshold (i.e. red points in **Supplementary Fig. 6c**) are excluded from the inversion process. The measured optoacoustic spectra corresponding to the grid points are in the following used in the context of the constrained inversion algorithm described in **Methods** and **Supplementary Note 2** to obtain estimates of $m_1(\mathbf{r}_{p,l})$, $m_2(\mathbf{r}_{p,l})$ and $m_3(\mathbf{r}_{p,l})$ for each grid point $\mathbf{r}_{p,l}$. **Supplementary Fig. 2d** presents the prior $\acute{m}_1(\mathbf{r}_{p,l})$ (blue line), the limits of search space (blue vertical lines) and the $m_1(\mathbf{r}_{p,l})$ estimated by the constrained inversion (red line) for a radial line of the grid in **Supplementary Fig. 6c**.

Upon the estimation of $m_1(\mathbf{r}_{p,l})$, $m_2(\mathbf{r}_{p,l})$ and $m_3(\mathbf{r}_{p,l})$ in all grid points, the *Eigenfluence* maps for the intermediate grid points are computed by means of cubic interpolation (see **Methods**). **Supplementary Fig. 6e, f** presents the $m_2(\mathbf{r})$ (**e**) and $m_1(\mathbf{r})$ (**f**) *Eigenfluence* maps corresponding to the same tissue area imaged under different physiological conditions, namely *post-mortem* after CO_2 breathing (left), *in-vivo* under 20% O_2 breathing (middle) and *in-vivo* under 100% O_2 breathing (right). While the $m_2(\mathbf{r})$ spatial map that corresponds mainly to tissue depth remains relatively unchanged under all three physiological conditions, $m_1(\mathbf{r})$ that corresponds more to background tissue oxygenation presents substantial differences between the three different states. The *Eigenfluence* maps are used to correct for the wavelength dependence of light fluence in the selected tissue area (**Methods**) and in the following blood oxygen saturation maps are computed using non-negative constrained least squares fitting of the corrected eMSOT image with the spectra of oxy- and deoxy-hemoglobin (**Supplementary Fig. 6g)**. Pixels that are associated with a fitting residual above a certain threshold are excluded from the sO_2 maps.

After eMSOT application, the raw optoacoustic spectra (blue lines in **Supplementary Fig. 6h** left) are decomposed into the element-wise product of the corrected normalized absorption spectra (blue lines in **Supplementary Fig. 6h** middle) and the estimated light fluence spectra (**Supplementary Fig. 6h** right). While linear fitting with the spectra of oxy- and deoxy-hemoglobin results in a high fitting residual and an inaccurate sO_2 estimation when applied on the raw optoacoustic spectra (red lines in **Supplementary Fig. 6h** left), it results in a low fitting residual after eMSOT correction (red lines **Supplementary Fig. 6h** middle) independently of tissue depth.

Supplementary Note 6: Imaging tumor hypoxia with eMSOT and histological validation

Mice (n=8), bearing orthotopically implanted 4T1 mammary tumors were imaged with MSOT at transverse slices in the lower abdominal area (schematic representation in **Supplementary Fig. 7a**). **Supplementary Fig. 7b** presents an anatomical optoacoustic image showing a slice which corresponds approximately to the central section of the tumor. The tumor region (upper right part of the image) can be recognized as it displays an enhanced contrast and different anatomic characteristics as compared to the symmetric normal tissue region. The tumor region is manually segmented (dashed segmentation line, **Supplementary Fig. 7b**). The eMSOT grid is set to cover the tumor area as well as adjacent healthy tissue (**Supplementary Fig. 7b right**).

After MSOT imaging, the mice were sacrificed and prepared for histological analysis. A subset of the mice (n=4) were examined for tumor and tissue anatomy. Following MSOT acquisition, the mice were frozen and the lower abdominal region containing the tumor mass (dashed lines in **Supplementary Fig. 7c**) was cryosliced in transverse orientation, similar to the one of MSOT imaging (see **Supplementary Fig. 7a**). True color images of the whole body, including the tumor mass, were obtained and histological slices derived thereof were isolated for H&E staining. **Supplementary Fig. 7d-g** presents an anatomical optoacoustic image at the central tumor cross-section (**d**), the corresponding cryoslice true color photography (**e**), H&E tumor staining (**f**) and eMSOT sO_2 analysis (**g**). The cryoslice true color photography displays the tumor heterogeneity, presenting sub-regions with prominent red color (marked in **Supplementary Fig. 7e** with an asterisk). These central necrotic areas, appearing to be suffused with blood, spatially correlate to the central hypoxic region in the core of the tumor as identified in the eMSOT image (**Supplementary Fig. 7g;** marked with an asterisk). Central necrotic areas could be confirmed by H&E staining (**Supplementary Fig. 7f**).

Another subset of the mice (n=4) was examined for functional characterization of the tumors through CD31/Hoeachst33342/Pimodinazole histological staining. Throughout this process, the tumors were excised and the 3D orientation of the tumor with regard to the MSOT image was retained (**Supplementary Fig. 7h,** lower picture). In the following, the excised tumors were sectioned and ~8 µm thick slices were immunohistochemically stained for studying micro-vascularization (CD31 staining) and cellular hypoxia (Pimonidazole staining). Vascular perfusion was determined following Hoechst33342 detection.

Supplementary Fig. 7i presents the eMSOT sO_2 estimation of two tumors presenting different levels of oxygenation. The tumor areas, as identified by the anatomical images, are segmented with a yellow dashed line. The average sO_2 levels of the central tumor areas (blue dashed rectangle) are further displayed in the image. The corresponding CD31 staining, as shown in **Supplementary Fig. 7j** reveals a dense tumor microvasculature in both tumors. This might explain the high tumor contrast in optoacoustic imaging. Hoechst 33342 staining (**Supplementary Fig. 7k**) reveals substantial differences in the perfusion patterns of the two tumors, with the first tumor appearing to be perfused both in the boundary (grey dashed box) and the core (green dashed box). In an effort to quantify the perfusion patterns, the ratio of the Hoechst image intensity in the core vs the boundary

was computed (intensity ratio 48%). The second tumor displays less perfusion in the core, as compared to the boundary (intensity ratio 19%). This finding indicates less functionality of the microvasculature in the core, which might explain the lower eMSOT sO_2 values as compared to the first tumor. The less perfused tumor areas (dark areas in **k**) appear spatial congruence with the areas of reduced blood oxygenation revealed by eMSOT (**i**). The non-perfused tumor areas further appear spatially correlated to cell hypoxia as identified by Pimonidazole staining (**l**, green). Cell hypoxia, as determined by Pimonidazole staining, may be a consequence of both, perfusion hypoxia (revealed by Hoechst33342 and eMSOT) and also diffusion hypoxia, which does not display eMSOT signal. Although, due to technical reasons, it may be challenging to achieve exact co-registration between *in-vivo* eMSOT tumor images and *ex-vivo* histology, the given histological analyses present strong evidence on the ability of eMSOT to detect perfusion related hypoxia within solid tumors. Furthermore, clear discrimination of different levels of hypoxia within single tumors, as well as intra-tumoral hypoxia-related heterogeneity could be demonstrated.

Supplementary References

1 Mohajerani, P. *Robust Methods for Fluorescence Imaging and Tomography* Doctoral Dissertation thesis, TU München, (2014).

2 Jacques, S. L. Optical properties of biological tissues: a review. *Physics in medicine and biology* **58**, R37 (2013).

3 Wang, L., Jacques, S. L. & Zheng, L. MCML—Monte Carlo modeling of light transport in multi-layered tissues. *Computer methods and programs in biomedicine* **47**, 131-146 (1995).

4 Briely-Sabo, K. & Bjornerud, A. in *Proc. Intl. Sot. Mag. Reson. Med.* 2025.

Appendix F

Publication: Spatiospectral denoising framework for multispectral optoacoustic imaging based on sparse signal representation

The version herein has been published in the journal "Medical Physics" [78]. It is hereby reprinted with permission.

Spatiospectral denoising framework for multispectral optoacoustic imaging based on sparse signal representation

Stratis Tzoumas,[a] Amir Rosenthal, and Christian Lutzweiler
Institute for Biological and Medical Imaging, Helmholtz Zentrum München, German Research Center for Environment and Health, Ingolstädter Landstrasse 1, Neuherberg 85764, Germany and Chair for Biological Imaging, Technische Universität München, Arcisstrasse. 21 D-80333, Munich, Germany

Daniel Razansky
Institute for Biological and Medical Imaging, Helmholtz Zentrum München, German Research Center for Environment and Health, Ingolstädter Landstrasse 1, Neuherberg 85764, Germany and Faculty of Medicine, Technische Universität München, Ismaninger Strasse 22, 81675, Munich, Germany

Vasilis Ntziachristos
Institute for Biological and Medical Imaging, Helmholtz Zentrum München, German Research Center for Environment and Health, Ingolstädter Landstrasse 1, Neuherberg 85764, Germany and Chair for Biological Imaging, Technische Universität München, Arcisstrasse. 21 D-80333, Munich, Germany

(Received 17 March 2014; revised 1 August 2014; accepted for publication 8 August 2014; published 8 October 2014)

Purpose: One of the major challenges in dynamic multispectral optoacoustic imaging is its relatively low signal-to-noise ratio which often requires repetitive signal acquisition and averaging, thus limiting imaging rate. The development of denoising methods which prevent the need for signal averaging in time presents an important goal for advancing the dynamic capabilities of the technology.
Methods: In this paper, a denoising method is developed for multispectral optoacoustic imaging which exploits the implicit sparsity of multispectral optoacoustic signals both in space and in spectrum. Noise suppression is achieved by applying thresholding on a combined wavelet-Karhunen–Loève representation in which multispectral optoacoustic signals appear particularly sparse. The method is based on inherent characteristics of multispectral optoacoustic signals of tissues, offering promise for general application in different incarnations of multispectral optoacoustic systems.
Results: The performance of the proposed method is demonstrated on mouse images acquired *in vivo* for two common additive noise sources: time-varying parasitic signals and white noise. In both cases, the proposed method shows considerable improvement in image quality in comparison to previously published denoising strategies that do not consider multispectral information.
Conclusions: The suggested denoising methodology can achieve noise suppression with minimal signal loss and considerably outperforms previously proposed denoising strategies, holding promise for advancing the dynamic capabilities of multispectral optoacoustic imaging while retaining image quality. [http://dx.doi.org/10.1118/1.4893530]

Key words: optoacoustic imaging, photoacoustic imaging, multispectral imaging, denoising, wavelets, sparse signal representation

1. INTRODUCTION

Optoacoustic tomography, also termed photoacoustic tomography, measures acoustic waves generated by the absorption of pulsed or modulated light in tissue and forms 2D or 3D optical absorption images within several millimeters to centimeters deep inside tissues.[1–4] A number of optoacoustic imaging systems have been suggested spanning from microscopy[5] and tomographic systems for preclinical small animal imaging,[1,2,6] to systems developed for intravascular imaging,[7] endoscopy[8,9] or breast imaging.[10,11] Optoacoustic imaging performed with monochromatic illumination can produce high resolution images of soft tissue anatomy and vasculature. By illuminating tissue at multiple wavelengths and utilizing spectral unmixing techniques, tissue physiological and molecular features can also be resolved.[12] Multispectral optoacoustic tomography (MSOT) has been shown to resolve the biodistribution of fluorescent proteins[13,14] or molecular probes of biological importance such as fluorescent or other absorbing dyes,[15–17] or visualize blood oxygenation.[5]

Advances in data acquisition systems, the possibility of wavelength tuning between individual pulses without additional overhead, and fast laser pulsing have enabled MSOT to be performed at video-rates,[18] facilitating its use for dynamic imaging and enabling handheld imaging while minimizing motion artifacts. Video-rate MSOT may facilitate its clinical translation in applications where rapid acquisition and immediate feedback is required.[7,8] Additionally, imaging at high frame rates opens new possibilities for preclinical studies,

e.g., monitoring of rapid biological processes such as real-time studies of pharmacokinetics,[19] physiological responses to drugs, or blood oxygenation changes for neuroimaging applications.[20,21]

Signal-to-noise ratio (SNR) in optoacoustic imaging is limited by the amount of excitation energy that can be safely deposited in tissue, as regulated by ANSI limits. To further improve the sensitivity achievable, it becomes therefore important to develop methods that maximize the SNR achieved and reduce the noise present in the detected signals and the reconstructed images. A common approach for increasing the SNR relies on repetitive signal acquisition and averaging (also termed temporal averaging or signal averaging). However, signal averaging slows down the acquisition of individual frames and hinders fast imaging of dynamic phenomena. In this respect, alternative approaches based on hardware solutions or signal-processing methods are of interest for enhancing the SNR and thus the quality of optoacoustic images without affecting temporal resolution.

In this work, we present the problem of noise reduction in optoacoustic imaging and review signal characteristics and previously proposed approaches. We subsequently present a combined spatial and spectral transformation for sparsely representing multispectral optoacoustic signals, namely, the wavelet-Karhunen–Loève transformation, that have been previously applied for denoising color images.[22] By adapting this methodology to the optoacoustic case, we formulate a spatiospectral denoising method that utilizes a translation-invariant wavelet-Karhunen–Loève transform (w-KLT) and information from all available optoacoustic signals corresponding to all wavelengths and projections. The presented method is validated on simulations based on experimentally derived datasets and compared qualitatively and quantitatively with previously proposed noise reduction strategies. We demonstrate that the combination of structural and spectral processing improves considerably the denoising performance over previously considered approaches.

2. BACKGROUND

Optoacoustic signals are typically corrupted by additive electronic noise caused by common system thermal noise or electromagnetic interference. While the use of advanced hardware solutions may suppress noise levels, the SNR achieved in the measurements is typically limited. Therefore, signal-processing-based denoising methods are of interest for further improving image quality.

2.A. Signal averaging approaches

A common procedure reported in numerous applications of optoacoustic imaging is signal denoising via temporal averaging. Assuming white Gaussian noise, the signal SNR [most commonly defined in decibels as $\mathrm{SNR} = 20\log_{10}(S/\sigma_{\mathrm{noise}})$, where S may indicate the peak, the mean, or the root-mean-square of the effective signal, while σ_{noise} is typically the standard deviation of the noise] increases with the $10\log_{10}(N_T)$ rule, where N_T is the number of averaged repetitions of the same signal. Signal averaging involves no information loss when temporal changes such as motion or physiological changes of tissue can be disregarded. However, such changes cannot be always ignored in practice, which compromises the applicability of temporal averaging in *in vivo* applications. In addition, averaging reduces the effective frame rate which limits the imaging speed achievable. The overhead of signal averaging becomes more problematic in multispectral image acquisition in which case $N_T \times M$ pulses are required instead of M, where M is the number of wavelengths sampled.

A form of spatial averaging is additionally performed on the surface of finite-size ultrasound detectors. Ultrasound sensors with large numerical aperture are typically utilized in optoacoustic imaging for providing increased SNR, which is proportional to their surface. Conversely, signal integration over large surfaces introduces a broadening in the impulse response of the system and may distort the reconstructed images.[23,24] When the imaging system is tomographic, the image reconstruction algorithm effectively offers noise suppression through the superposition of projection signals in the image domain. However, such noise suppression in the process of image formation has less impact in the case of nontomographic systems such as microscopes, endoscopes, or intravascular catheters.

2.B. Denoising via thresholding in sparse representations

Filtering in the frequency domain is a common approach for suppressing random noise and it is more effective for cases where the spectrum of the signal collected has little overlap with the spectrum of noise. However, since optoacoustic signals are broadband, it is in principle difficult to separate them from white random noise without introducing considerable signal loss or signal distortions. Optoacoustic signals are well-localized in time and may be modeled as a superposition of N-shaped pulses that correspond to signals generated by elementary spherelike structures.[25] This characteristic indicates that wavelet representations, and especially translation-invariant wavelet frames, could offer an effective sparse representation which could offer robust denoising methods. Various wavelet-thresholding approaches have been implemented for the restoration of optoacoustic signals without affecting temporal resolution.[26] Such approaches typically implement different thresholding operators in orthogonal wavelet bases[11,27,28] or translation-invariant wavelet frames,[29] while the selection of the mother wavelet is usually performed in an *ad hoc* manner in order to resemble the theoretical N-shape of optoacoustic pressure signals. Moreover, sparse representations of optoacoustic signals and images in wavelet bases have been recently used to enhance the image reconstruction quality using compressed sensing approaches[30]

or the reconstruction speed[31] in model-based inversion approaches.

All aforementioned variations of the general wavelet-thresholding framework[32] have demonstrated denoising capabilities by exploiting the sparsity offered in wavelet representations of optoacoustic signals. However, when multispectral optoacoustic imaging is utilized, such approaches perform suboptimally since they ignore the available multispectral information, which can be effectively used for further decorrelating the true signal from noise. The optoacoustic spectral responses of tissue consist of a linear combination of a small number of spectral signatures associated with tissue-intrinsic absorbers such as hemoglobin and melanin. Light attenuation with depth additionally affects the measured spectra (spectral coloring) in a nonlinear manner;[33] however, in general, since the different spectral signatures are few, it can be expected that the multispectral information of tissue can be effectively captured in a sparse manner. This hypothesis has directed herein the consideration of a combined representation that takes advantage of signal characteristics both in the space and in the spectral dimension using the combined wavelet-Karhunen–Loève transform.[22]

3. THEORY

In this section, we provide a concise overview of the Karhunen–Loève transform and its integration with the wavelet transform. We seek herein to identify a sparse dictionary for the optoacoustic signals that would represent their temporal (or spatial) features and integrate additional spectral information. In MSOT, or other multichannel acquisitions, signals commonly exhibit correlation within the different wavelengths (channels) employed; however, in this case white noise is completely uncorrelated. Taking advantage of this information, multichannel denoising techniques may better decorrelate the true signal from noise, enabling more efficient noise suppression. While Bayesian approaches can also be of relevance when stochastic signal modeling is available, simple thresholding operators can also be applied in sparse representations of the multispectral information. An ideal denoising approach would exploit both structural and spectral priors for defining a maximally sparse representation of the signals. In the case of multispectral images or signals, such a representation can be offered by the wavelet-Karhunen–Loève transform that has been previously explored for denoising RGB images.[22]

3.A. The Karhunen–Loève transform

The KLT, also referred to as principal component analysis, is a linear transformation that offers the possibility of representing a set of observations in a new orthogonal basis with the property of minimizing the mean square error (MSE) (from all possible orthonormal transformations) when truncating coefficients. In this respect, the KLT can offer a representation, where a set of highly correlated observations, such as multispectral optoacoustic signals and images, can be represented in a compressed manner by concentrating their energy in only a few coefficients (first principal components). Given a set of L observations $\mathbf{X}(t)=(x_1(t),x_2(t),\ldots,x_L(t))^T$ (i.e., a set of multisensory signals or multispectral images) with $t=1\ldots N$ (N being the dimension of each signal) and their mean values $\mathbf{M}=(m_1,\ldots,m_L)^T$, and let the mean-free vector $\mathbf{X}'(t)=(x'_1(t),x'_2(t),\ldots,x'_L(t))^T=\mathbf{X}(t)-\mathbf{M}$, the KLT $\mathbf{Y}(t)$ of vector $\mathbf{X}(t)$ is defined by the following linear relation:

$$\mathbf{Y}(t)=\mathbf{V}\,\mathbf{X}'(t). \tag{1}$$

In Eq. (1), $\mathbf{Y}(t)=(y_1(t),y_2(t),\ldots,y_L(t))^T$ and the orthonormal matrix $\mathbf{V}$ is a $L\times L$ matrix, the rows of which are formed by the eigenvectors of the covariance or the correlation matrix $\mathbf{G}$ of $\mathbf{X}'$. The eigenvector matrix $\mathbf{V}$ defines thus an orthonormal basis that is specific to the set of observations $\mathbf{X}$ and provides a compressed representation with most signal energy accumulated in the first coefficients when these observations are highly correlated. The correlation matrix $\mathbf{G}$ is calculated from the mean-free data $x'_l(t)$ according to the following equation:

$$\mathbf{G}_{m,n}=\frac{\sum_{t=1}^{N}x'_m(t)x'_n(t)}{\sqrt{\sum_{t=1}^{N}x'_m(t)^2}\sqrt{\sum_{t=1}^{N}x'_n(t)^2}}. \tag{2}$$

The original signals can be recovered by projecting them to the initial space after applying the inverse KLT

$$\mathbf{X}(t)=\mathbf{V}^T\mathbf{Y}(t)+\mathbf{M}. \tag{3}$$

3.B. Wavelet-Karhunen–Loève transform

The combined w-KLT of a set of observations is derived through the sequential computation of the wavelet transform of each observation in space followed by the KLT of the resulting set of mean-free detail and approximation wavelet coefficients. In accordance with the notation of Sec. 3.A, let $c'_l(j,k)$ denote the mean-free detail wavelet coefficients of the observation signal $x_l(t)$ that correspond to the scale index j ($1\le j\le J$) (index of wavelet decomposition level) and the position index k ($1\le k\le N_j$, with N_j depending on the scale j for orthonormal while being constant for translation-invariant wavelet transforms) and $c'_l(J+1,k)$, the associated mean-free approximation coefficients, and let the vector of the observations $\mathbf{C}'(j,k)=(c'_1(j,k),c'_2(j,k),\ldots,c'_L(j,k))^T$, and the subtracted mean values $\mathbf{M}(j)=(m_1(j),m_2(j),\ldots,m_L(j))^T$ (we note that the means of the detail coefficients are zero). Then, the w-KLT can be defined by the following relation:

$$\mathbf{Y}(j,k)=\mathbf{U}\mathbf{C}'(j,k). \tag{4}$$

Here, $\mathbf{Y}(j,k)=(y_1(j,k),y_2(j,k),\ldots,y_L(j,k))^T$ is the vector of the transformed coefficients, while the $L\times L$ eigenvector matrix $\mathbf{U}$ is computed from the correlation matrix $\mathbf{G}$ of the demeaned wavelet coefficients either per wavelet scale[22] or

uniformly for all scales. Since in general the wavelet coefficients will correspond to both signal and noise, only the high valued coefficients (that more probably correspond to signal rather than noise) can be used for a better estimation of the correlation matrix **G**, an approach that has been proposed in Ref. 22. In this respect, the correlation matrix is computed in accordance with Eq. (2), where instead of the signal values $x'_l(t)$, the high valued wavelet coefficients are used

$$\mathbf{G}_{m,n} = \frac{\sum_{j=1}^{J+1}\sum_{k=1}^{N_j} {\rho_T}^{\text{corr}}[c'_m(j,k)]\,{\rho_T}^{\text{corr}}[c'_n(j,k)]}{\sqrt{\sum_{j=1}^{J+1}\sum_{k=1}^{N_j} {\rho_T}^{\text{corr}}[c'_m(j,k)]^2}\sqrt{\sum_{j=1}^{J+1}\sum_{k=1}^{N_j} {\rho_T}^{\text{corr}}[c'_n(j,k)]^2}}. \tag{5}$$

In Eq. (5), ${\rho_T}^{\text{corr}}(c)$ is a preliminary threshold operator applied only for the calculation of **G**. It is important to note that the threshold operator ${\rho_T}^{\text{corr}}(c)$ is not associated with signal rejection but with a selection of wavelet coefficients that will contribute to the calculation of the correlation matrix. We note that for reasons of consistency with previous implementations of the same transform,[22] we used the correlation matrix to compute KLT. However, the covariance matrix (that is more commonly selected) offers similar performance while also enhancing computation speed.

The original signals $x_l(t)$ can be recovered by projecting the Karhunen–Loève transformed wavelet coefficients $\mathbf{Y}(j,k)$ to the initial wavelet space using $\mathbf{C}(j,k) = \mathbf{U}^{\mathbf{T}}\mathbf{Y}(j,k) + \mathbf{M}(j)$ and a subsequent signal reconstruction from the wavelet coefficients $c_l(j,k)$. This process will be referred to as the inverse w-KLT.

4. METHODS

In this section, the w-KLT-based denoising scheme for multispectral optoacoustic signals and images is described. MSOT images are typically formed by a large set of measured optoacoustic pressure signals $x_l(p,t)$ of spatial (or temporal) dimension $t = 1\ldots N$ that correspond to a number of the different projections (i.e., time resolved signals corresponding to specific ultrasound transducer positions, $p = 1\ldots N_p$) and excitation wavelengths ($l = 1\ldots N_w$). The measured signals typically correspond to the true optoacoustic signals $s_l(p,t)$ with some level of superimposed random noise $n_l(p,t)$

$$x_l(p,t) = s_l(p,t) + n_l(p,t). \tag{6}$$

Noise for different spectral bands and projections is typically assumed to be independent white Gaussian with a variance $\sigma^2_{p,l}$ that can be accurately estimated from experimental measurements possibly from the first signal samples, where no true optoacoustic signal is expected to be present.

A three-step procedure is hereby presented for signal denoising. In the first step, noisy signals $x_l(p,t)$ are subject to the w-KLT transformation thus giving rise to the w-KLT coefficients $y_l(p,j,k)$ according to the formulation in Sec. 3.B. In the second step, a nonlinear thresholding operator ρ_T is applied to these coefficients to reject noise while retaining the relevant signal. Finally, in the third step, the estimated denoised signals $\tilde{x}_l(p,t)$ are recovered after transforming the thresholded w-KLT coefficients $\tilde{y}_l(p,j,k)$ to the original space with the inverse w-KLT transform. The details of the denoising algorithm and its application are described in Subsections 4.A–4.D.

4.A. Decomposition stage

Spatial and spectral decorrelation of the optoacoustic signals from the associated random noise is achieved using the w-KLT. A translation-invariant wavelet transform was utilized for decomposing the signals in space. Translation-invariant wavelet transforms are redundant frame representations that typically offer enhanced denoising capabilities.[34] Daubechie's mother wavelet 2 (db2) (Ref. 35) has been selected in an *ad hoc* manner for wavelet decomposition, since its bipolar shape is expected to capture the inherent N-shape of optoacoustic signals. Wavelet decomposition is performed along dimension t in the signal domain leading to $c_l(p,j,k)$ wavelet coefficients according to the formulation of Sec. 3.B, where p corresponds here to the different projections and $k = 1\ldots N$ for all scales of the detail as well as for the approximation coefficients.

Computation of the correlation matrix is a key step for decorrelating the signal from noise. Following the paradigm of Ref. 22 only high valued wavelet coefficients were selected to contribute in estimation of matrix **G**. This is performed using a preliminary hard thresholding operator ${\rho_T}^{\text{corr}}$, associated with threshold ${T_{p,j,l}}^{\text{corr}}$, which is applied on the mean-free wavelet coefficients

$$\begin{aligned} &{\rho_T}^{\text{corr}}[c'_l(p,j,k)] \\ &\quad = \begin{cases} c'_l(p,j,k) & \text{if } |c'_l(p,j,k)| \geq {T_{p,j,l}}^{\text{corr}} \\ 0 & \text{if } |c'_l(p,j,k)| < {T_{p,j,l}}^{\text{corr}} \end{cases}. \end{aligned} \tag{7}$$

Since the same tissue absorbers (and thus spectral responses) are expected to be captured in all projections and scales of the wavelet transform, all available high valued wavelet coefficients are combined for the calculation of a global correlation matrix **G**, that is computed in accordance with Eq. (5), including the wavelet coefficients from all available projections

$$\mathbf{G}_{m,n} = \frac{\sum_{p=1}^{N_p}\sum_{j=1}^{J+1}\sum_{k=1}^{N}\rho_T{}^{\mathrm{corr}}[c'_m(p,j,k)]\rho_T{}^{\mathrm{corr}}[c'_n(p,j,k)]}{\sqrt{\sum_{p=1}^{N_p}\sum_{j=1}^{J+1}\sum_{k=1}^{N}\rho_T{}^{\mathrm{corr}}[c'_m(p,j,k)]^2}\sqrt{\sum_{p=1}^{N_p}\sum_{j=1}^{J+1}\sum_{k=1}^{N}\rho_T{}^{\mathrm{corr}}[c'_n(p,j,k)]^2}} \quad (8)$$

The correlation matrix results in the creation of a base of eigenvectors $\mathbf{U}$ after eigendecomposition. Projecting the wavelet coefficients on base $\mathbf{U}$ results in the w-KLT coefficients $y_l(p,j,k)$ of the original signals $x_l(p,t)$.

4.B. Thresholding stage

The w-KLT coefficients $y_l(p,j,k)$ of the original signals $x_l(p,t)$ are in the following subject to a thresholding operator ρ_T that aims to reject noise while preserving most of the energy of the actual signal. The denoised coefficients are obtained as $\tilde{y}_l(p,j,k) = \rho_T(y_l(p,j,k))$. A hard thresholding operator has been hereby selected that is associated with a threshold value $T_{p,j,l}$

$$\rho_T[y_l(p,j,k)] = \begin{cases} y_l(p,j,k) & \text{if } |y_l(p,j,k)| \geq T_{p,j,l} \\ 0 & \text{if } |y_l(p,j,k)| < T_{p,j,l} \end{cases}. \quad (9)$$

Threshold values are typically selected to be proportional to the standard deviation of the noise, meaning that the value of the threshold $T_{p,j,l}$ may vary with spectral dimension l, projection p, or the wavelet scale j if the standard deviation of the noise is not uniform across such dimensions (e.g., colored noise). Colored noise with a varying standard deviation across such dimensions can be typical in multispectral optoacoustic measurements as the laser power varies with wavelength and the sensitivity of ultrasound sensors typically varies with frequency.

Since the thresholding operator is applied in the w-KLT of the signals, it is important to calculate the noise variance in this representation. Let $\sigma^2_{p,j,l}$ be a noise variance estimate in the original wavelet transform and let the vector $\mathbf{S}_{p,j} = (\sigma^2_{p,j,1},\sigma^2_{p,j,2},\ldots,\sigma^2_{p,j,N_w})^T$, then in the w-KLT representation, the noise variance in each spectral channel, projection, and frequency band can be easily computed analytically as $\mathbf{S}'_{p,j} = \mathbf{U}^2\mathbf{S}_{p,j}$, with $\mathbf{S}'_{p,j} = (\sigma'^2_{p,j,1},\sigma'^2_{p,j,2},\ldots,\sigma'^2_{p,j,N_w})^T$, where $\mathbf{U}^2$ is the elementwise (Hadamard) product of the eigenvector matrix with itself, $\mathbf{U}^2 = \mathbf{U}\mathrm{o}\mathbf{U}$.

Two thresholding operators have been defined up to now, one being $\rho_T{}^{\mathrm{corr}}$ applied for the calculation of the correlation matrix and one being ρ_T applied in the final denoising step. The associated thresholds are defined as $T_{p,j,l}{}^{\mathrm{corr}} = \lambda^{\mathrm{corr}}\sigma_{p,j,l}$ and $T_{p,j,l} = \lambda\sigma'_{p,j,l}$.

4.C. Validation platform based on experimental measurements

The performance of the presented spatiospectral denoising technique was directly evaluated on MSOT images and signals. A dataset obtained from *in vivo* small animal imaging was selected to offer a suitable validation platform whereby signals demonstrate realistic properties both structurally and spectrally.

Multispectral optoacoustic cross-sectional images of the mouse head and the kidney area were acquired at 22 uniformly sampled wavelengths ($N_w = 22$) from 690 to 900 nm with a step size of 10 nm (Fig. 1). The data were acquired using an experimental MSOT setup described in Ref. 6. A picture of the system is presented in Scheme 1, where the illumination, the ultrasound array, the animal positioning, the animal holder, and the imaging plane are pointed with dashed arrows. The system employs an OPO tunable laser for illumination with pulse repetition rate of 10 Hz. Illumination is guided through fiber bundles in order to create a ring-shaped illumination pattern (~7 mm width) on the surface of the animal. Parallel ultrasound detection of 64 channels (acquiring simultaneously 64 "projection" signals, $N_p = 64$) is achieved using a curved ultrasound array. The elements of the ultrasound array (5 MHz central frequency with −6 dB of >50%) are deployed in a circular 2D geometry around the sample (radius 4 cm) covering an angle of 172°. The system acquires 2D images in a transverse slice through the animal in the x–y plane. The effective field of view of the imaging system is 2.5 × 2.5 cm and is depicted in Scheme 1 using a transparent rectangle.

The original signals [Fig. 2(a)] were averaged 100 times and band-pass filtered within the bandwidth of the ultrasound sensors, to diminish system electronic noise. The averaged and filtered signals [Fig. 2(b)] were assumed to be noise-free serving as the gold standard $s_l(p,t)$ for calculating the estimation error and evaluating the current method against previously proposed approaches. From the acquired signals, 2D optoacoustic images were reconstructed using a 2D model-based inversion algorithm.[36,37]

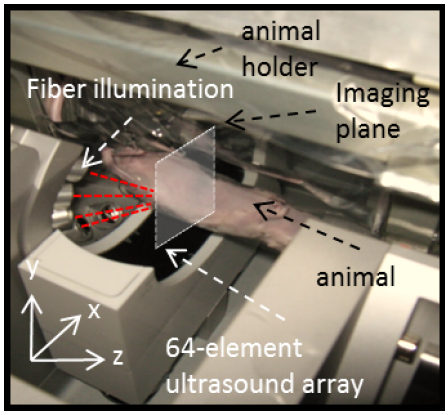

Scheme 1. Annotated color photograph of the experimental MSOT imaging setup. The animal holder, the fiber illumination, the imaging plane, the animal, and the ultrasound transducer are annotated with dashed arrows.

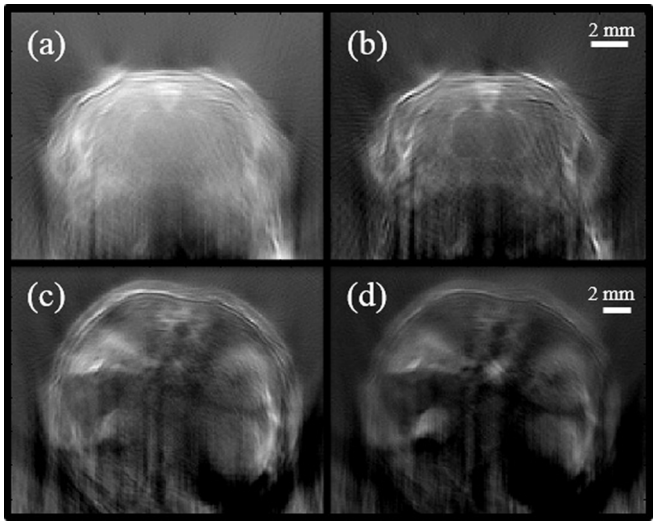

FIG. 1. *In vivo* multispectral optoacoustic measurements used for the creation of noise simulations. (a) and (b) Anatomical image of a mouse brain at an excitation wavelength of 690 nm (a) and 900 nm (b). (c) and (d) Anatomical image of the kidney area of a mouse at an excitation wavelength of 690 nm (c) and 900 nm (d).

Random white Gaussian noise $n_l(p,t)$ independent across the spectral channels was artificially superimposed to the original signals $s_l(p,t)$ at equal standard deviations for each projection and wavelength, $\sigma_{l,p} = \sigma$. The superimposed noise was selected to be either independent across projections and wavelengths [Fig. 2(g)], or "parasitic" [Fig. 2(f)]. In the case of parasitic noise, the noise is also random Gaussian and independent across the wavelengths, but the same noise pattern is superimposed on each one of the projections p. Such parasitic noise may be present in optoacoustic systems that utilize ultrasound arrays (simultaneous acquisition of all signal projections), in the presence of electromagnetic interference. Parasitic noise causes the production of ring artifacts after image reconstruction [Fig. 2(f)] making the noise influence obvious and distinguishable from the actual image structures at visual inspection. Using this technique for producing noise simulations does not bias the performance of the denoising methods when these are applied in the signal domain. Each signal in the dataset of N_p projections and N_w wavelengths will correspond to a different peak signal-to-noise ratio (PSNR) according to the signal amplitude and the noise levels. The average PSNR of all signals of a specific dataset is used as an indicator of the level of the superimposed noise.

4.D. Evaluation of denoising performance

Evaluation of the denoising performance was performed both qualitatively, by visual inspection of the denoised signals and the reconstructed images, and quantitatively through the calculation of the estimation error e_{sig}. For each set of measured optoacoustic signals, consisting of $N_p \times N_w$ pressure signals, the average normalized error across all projections and wavelengths is calculated from the denoised ($\tilde{x}_l(p,t)$) and gold standard ($s_l(p,t)$) signals

$$e_{\text{sig}} = \frac{1}{(N_p N_w)} \sum_{l=1}^{N_w} \sum_{p=1}^{N_p} \frac{\sqrt{\sum_{t=1}^{N} (\tilde{x}_l(p,t) - s_l(p,t))^2}}{\sqrt{\sum_{t=1}^{N} s_l(p,t)^2}}. \tag{10}$$

The quantitative evaluation of the estimation error is computed in the signal (and not image) domain in order to avoid introducing bias from the reconstruction algorithm employed. However, visual inspection is performed in the image domain to better identify the effect of signal loss on the associated tissue structures, while the MSE between the images

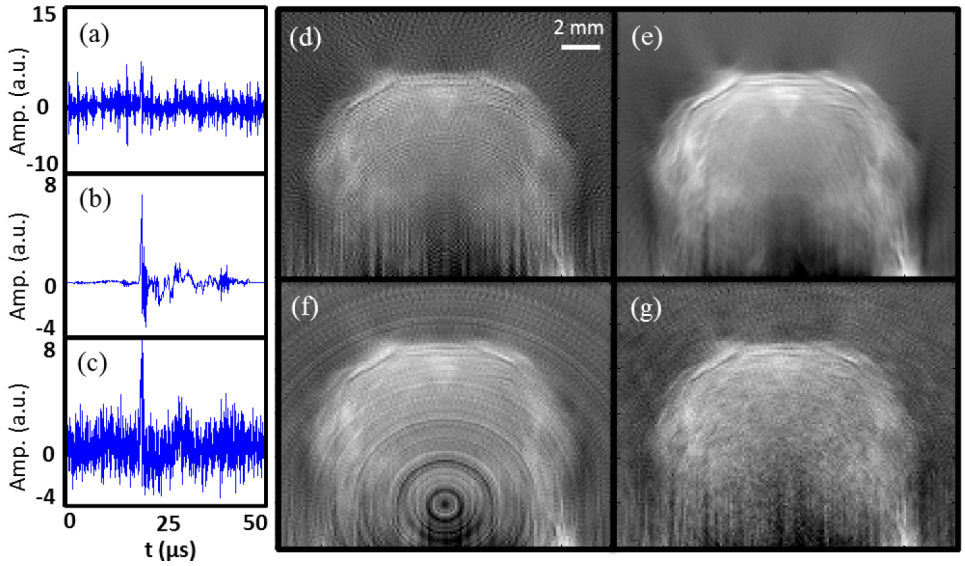

FIG. 2. Noise simulations based on small animal imaging data. (a) A typical optoacoustic signal before any processing. (b) Optoacoustic signal after 100 averages and band-pass filtering, assumed as the gold standard $s_l(p,t)$. (c) Noisy signal $\tilde{x}_l(p,t) = s_l(p,t) + n_l(p,t)$ produced after superimposing noise of $\sigma = 1$ to the original signal $s_l(p,t)$. (d) Optoacoustic image of a mouse brain, reconstructed from the unprocessed signals. (e) Optoacoustic image reconstructed from gold standard signals $s_l(p,t)$. (f) and (g) Optoacoustic image reconstructed from noisy signals $\tilde{x}_l(p,t)$ with superimposed parasitic (f) and independent noise (g).

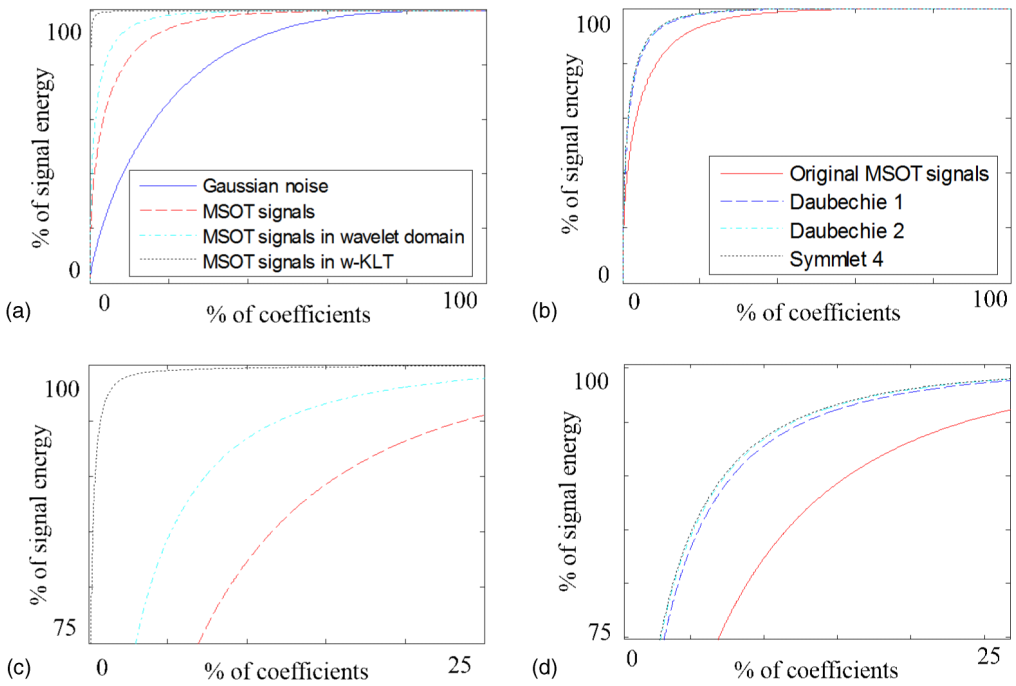

FIG. 3. Sparsity comparison of multispectral optoacoustic signals of the brain dataset in different signal representations. (a) Lorenz curves for Gaussian noise (blue solid curve), MSOT signals (red dashed curve), translation-invariant wavelet transform of MSOT signals (cyan dash-dot curve), and translation-invariant w-KLT of MSOT signals (black dot curve). (b) Lorenz curves for MSOT signals in the translation-invariant wavelet domain using different mother wavelets. (c) and (d) Magnification of the upper-left part of (a) and (b), respectively.

reconstructed from the denoised signals with respect to the images reconstructed from the noise-free signals are also provided.

5. RESULTS

This section summarizes the results of the spatiospectral denoising method on experimental and artificially generated noisy datasets of multispectral optoacoustic signals and images. Section 5.A compares signal sparsity of multispectral optoacoustic signals under different representations. Section 5.B presents a qualitative and quantitative evaluation of the spatiospectral denoising method and a comparison with previously proposed denoising strategies. Section 5.C discusses the application of the method in the signal and the image domain. Finally, Sec. 5.D demonstrates the application of the presented method in purely experimental noisy datasets.

5.A. Sparsity of multispectral optoacoustic signals in different representations

The efficiency of denoising approaches that are based on thresholding operators highly relies on the sparsity offered in the selected signal representation. Figure 3(a) shows the Lorenz curves[38] of the signal energy for the cases of white Gaussian noise (blue solid curve) and of the multispectral optoacoustic dataset of the brain used in this study in the original (red dashed curve), the translation-invariant wavelet (cyan dash-dot curve), and the w-KLT (black dot curve) representation. We note that the Lorenz curve for white Gaussian data is independent of the base used. Figure 3(b) shows the Lorenz curves of the signal energy for the same dataset in the original (red solid curve) and in the translation-invariant wavelet transform using three different mother wavelets with compact support but different spatial patterns, namely, Daubechie 1 (db1, also referred to as Haar), Daubechie 2 (db2), and Symmlet 4.[35] Figures 3(c) and 3(d) present a magnification of the upper-left part of Figs. 3(a) and 3(b), respectively, for a better visualization of the curve differences.

Clearly, the w-KLT transform offers greatly enhanced sparsity as compared to the wavelet transform, compressing most signal energy in only a few coefficients. Moreover, the differences in sparsity under different wavelet bases are minimal indicating that the selection of an optimal wavelet basis is of much less significance as compared to the utilization of the available spectral information.

5.B. Evaluation of denoising performance and comparison with previously proposed approaches

In this section, the performance of the presented spatiospectral denoising method is validated and compared against pure spatial denoising. Spatial denoising refers, here, to the use of hard thresholding on the translation-invariant wavelet transformation of the signals with a threshold that is proportional to the standard deviation of the noise ($T_{p,j,l}{}^{\text{spatial}} = \lambda\sigma_{p,j,l}$). This purely spatial denoising method is similar to previously published denoising strategies for optoacoustic imaging.[11,27–29] Spatiospectral denoising refers to our proposed use of hard thresholding in the w-KLT domain as described in Sec. 4. Both methods use the same mother wavelet (db2) and the same decomposition level to facilitate a straightforward

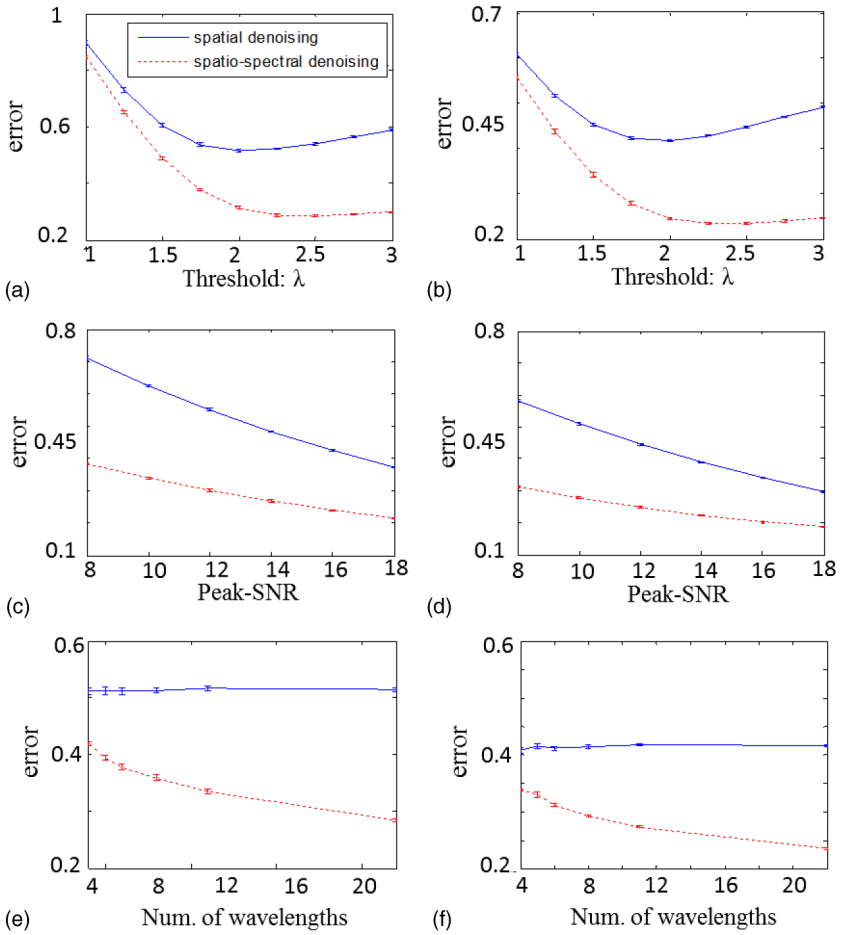

FIG. 4. Quantitative comparison of the estimation errors as computed by Eq. (10), between spatial (blue solid curves) and spatiospectral denoising (red dot curves). The errorbars indicate the standard deviation of the normalized average estimation error among ten different noise instantiations. (a) and (b) Quantitative comparison of the estimation errors for different selection of the threshold $T = \lambda\sigma$, with λ varying from 1 to 3. (c) and (d) Quantitative comparison of the estimation errors for different noise levels from a mean PSNR of 8–18 dB. (e) and (f) Quantitative comparison of the estimation errors (mean PSNR = 13 dB) with a varying number of sampled wavelengths from 4 to 22 wavelengths in total. For all cases, the first column [(a), (c), and (e)] corresponds to the brain dataset, while the second column [(b), (d), and (f)] corresponds to the kidney dataset.

comparison. Thus, any performance differences are associated with the utilization of the additional spectral information. The results obtained by these two methods were compared quantitatively (Fig. 4) by means of the average normalized estimation error as computed by Eq. (10). The quantitative evaluation is performed under ten different instantiations of random Gaussian noise and the mean and standard deviation (errorbars) of the normalized average estimation error are presented. Qualitative comparisons were also performed based on visual inspection of the denoised signals and the associated reconstructed images (Figs. 5 and 6). Finally, Fig. 7 presents a visual comparison between signal averaging and the proposed spatiospectral denoising method.

Figure 4 presents a direct quantitative comparison between the spatial and the spatiospectral denoising methods with respect to the estimation error of Eq. (10). Figures 4(a) and 4(b) present the estimation error for the brain and kidney MSOT datasets, respectively, as a function of the threshold value $T = \lambda\sigma$, with $\lambda \in [1,3]$. The average PSNR of the noisy signals was 13 dB. The graphs indicate that the estimation error produced by spatiospectral denoising (red dot curve) is considerably lower than the one of spatial denoising (blue solid curve) independently of the threshold value, indicating better noise rejection with less signal loss. Moreover, the graphs indicate optimal threshold values for the two methods. Specifically λ was selected to be 2 for spatial denoising and 2.5 for spatiospectral denoising for the rest of the evaluation (we note that λ^{corr} was selected to be 2 under a similar evaluation). Figures 4(c) and 4(d) present a comparison of the estimation error as a function of the superimposed noise (average PSNR $\in$ [8,18] dB). Spatiospectral denoising consistently outperforms spatial denoising and appears more efficient in cases of high noise. Finally, Figs. 4(e) and 4(f) show a direct comparison of the two methods with a varying spectral dimension from 4 to 22 wavelengths (average PSNR of 13 dB and λ being 2 for spatial and 2.5 for spatiospectral denoising). When more wavelengths are used, the spatiospectral denoising method results in a lower estimation error; however, it considerably outperforms standard spatial denoising even in the case of only four wavelengths.

Figure 5 offers a visual comparison between spatial and spatiospectral denoising in the case of parasitic noise of

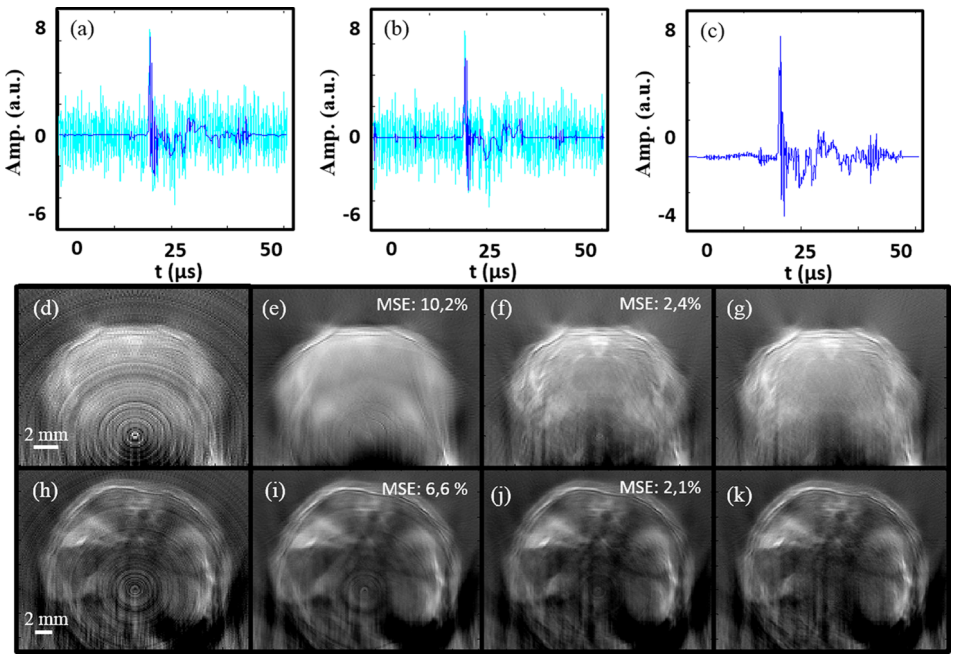

FIG. 5. Comparison between signals and images obtained using spatial and spatiospectral denoising in the case of superimposed parasitic noise of PSNR = 13 dB. (a) Overlay of w-KLT thresholded signal on noisy. (b) Overlay of wavelet thresholded signal on noisy. (c) Gold standard signal. (d)–(g) Reconstructed image of the brain at 690 nm from (d) noisy signals, (e) spatial signal denoising, (f) spatiospectral signal denoising, and (g) gold standard signals. (h)–(k) Corresponding reconstructed images of the kidneys' area at 690 nm.

PSNR = 13 dB. Figure 5(a) presents an overlay of a noisy signal of an arbitrarily selected projection and wavelength with the denoised signal after using the spatiospectral denoising method. Figure 5(b) shows an overlay of the same noisy signal with the signal after spatial denoising. Figure 4(c) displays the noise-free signal for comparison. Figures 5(d)–5(g) show the images of the brain at 690 nm reconstructed from the noisy signals [Fig. 5(d)], from the signals after spatial denoising [Fig. 5(e)], from the signals after spatiospectral denoising [Fig. 5(f)] and from the noise-free signals [Fig. 5(g)]. Finally, Figs. 5(h)–5(k) present the reconstructed images of the kidneys at 690 nm corresponding to the noisy (h), spatially denoised (i), spatiospectrally denoised (j), and noise-free (k) associated signals.

Inspection of the denoised signals [Figs. 5(a) and 5(b)] demonstrates that both methods effectively remove most of the Gaussian noise. However, fine signal details that are retained in the case of spatiospectral denoising [Fig. 5(a)] were rejected in the case of spatial denoising [Fig. 5(b)], where only the coarse signal structure is preserved. Inspection of the associated reconstructed images [Figs. 4(e) and 4(i) for spatial and Figs. 5(f) and 5(j) for spatiospectral denoising] indicates that such loss of information may result in a major degradation of the structural information. Both in the case of the brain [Fig. 5(f)] and

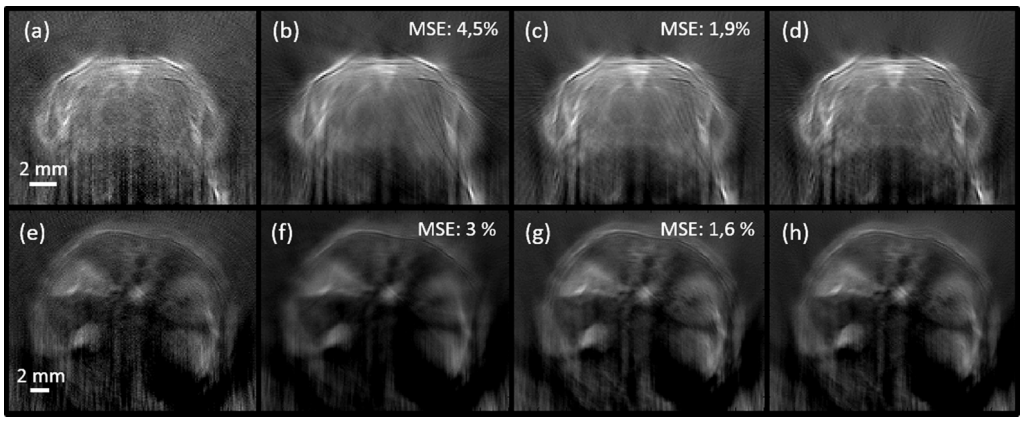

FIG. 6. Comparison between images obtained using spatial and spatiospectral denoising in the case of independent noise of PSNR = 13 dB. (a)–(d) Reconstructed image of the brain at 900 nm from (a) noisy signals, (b) spatially denoised, (c) spatiospectrally denoised signals, and (d) gold standard signals. (e)–(h) Corresponding reconstructed images of the kidneys' area at 900 nm.

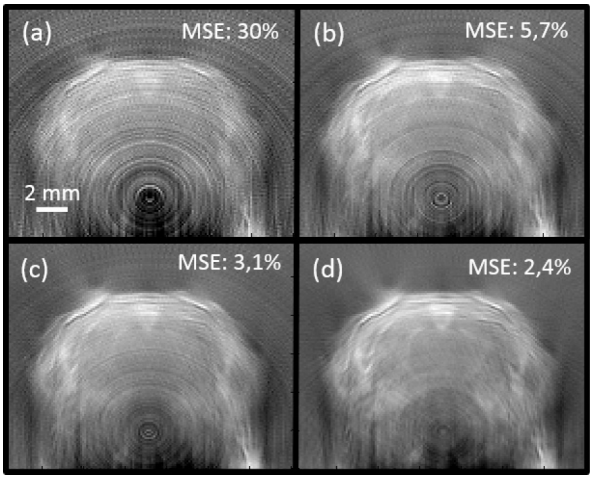

FIG. 7. Visual comparison between signal averaging and denoising using the spatiospectral denoising method. (a) Initial image reconstructed from signals with parasitic noise (PSNR 13 dB). (b) Image corresponding to five averaged signal repetitions (20 dB). (c) Image corresponding to ten averaged signal repetitions (23 dB). (d) Image reconstructed after spatiospectral denoising the original noisy signals of average PSNR 13 dB.

the kidney dataset [Fig. 5(j)], the proposed method appears to effectively remove the parasitic noise, while preserving most image structure, indicating minimal signal loss.

Figure 6 offers a visual comparison between spatial and spatiospectral denoising in the case of uncorrelated noise resulting in a signal PSNR of 13 dB. The images of the brain [Figs. 6(a)–6(d)] and kidney datasets [Figs. 6(e)–6(h)] at 900 nm are presented, as reconstructed from the noisy [Figs. 6(a) and 6(d)], spatially denoised [Figs. 6(b) and 6(f)], spatiospectrally denoised [Figs. 6(c) and 6(g)], and noise-free signals [Figs. 6(d) and 6(h)]. Once again spatiospectral denoising [Figs. 6(c) and 6(g)] demonstrates efficient noise rejection while preserving fine image structures, which are lost in the case of pure spatial denoising [Figs. 6(b) and 6(f)].

Finally, Fig. 7 shows a visual comparison between signal averaging and the spatiospectral denoising method. Figure 7(a) shows an image of the brain dataset at 690 nm, with superimposed parasitic noise of average PSNR = 13 dB. Figures 7(b) and 7(c) show the denoised images, obtained by temporal averaging as a function of averaged signal repetitions. The initial PSNR of 13 dB [Fig. 7(a)] is increased to 20 [Fig. 7(b)] and 23 dB [Fig. 7(c)] after five and ten averaged signal repetitions, respectively. The image quality after ten averaged signal repetitions closely resembles the denoised image obtained by spatiospectral denoising shown in Fig. 7(d), indicating the potential of faster image acquisition with the same image quality, in the case of noisy systems.

5.C. Denoising in the image domain

Denoising can be equivalently applied in the signal or the image domain. If the system is tomographic and the noise is independent across projections, the SNR level in the image domain is expected to be higher, offering an advantage in the case of nonlinear thresholding approaches (we note that this applies less in the case of nontomographic modalities or in the case of parasitic noise). Moreover, the wavelet representation in the image domain may offer enhanced sparsity making a thresholding denoising method more efficient. However, the denoising performance will also depend on the performance of the tomographic reconstruction algorithm employed. Reconstruction artifacts further contribute to noise in the image domain, while the estimation of the noise levels in the image domain can be more challenging. Figure 8 presents a comparison between denoising in the signal and the image domain. Figure 8(a) presents an image from the brain dataset at 900 nm reconstructed from noisy signals with PSNR = 13 dB; Fig. 8(b) shows the reconstructed image that corresponds to the denoised signals using spatiospectral denoising in the signal domain and Fig. 8(c) presents the resulting image after using spatiospectral denoising in the image domain. In the latter

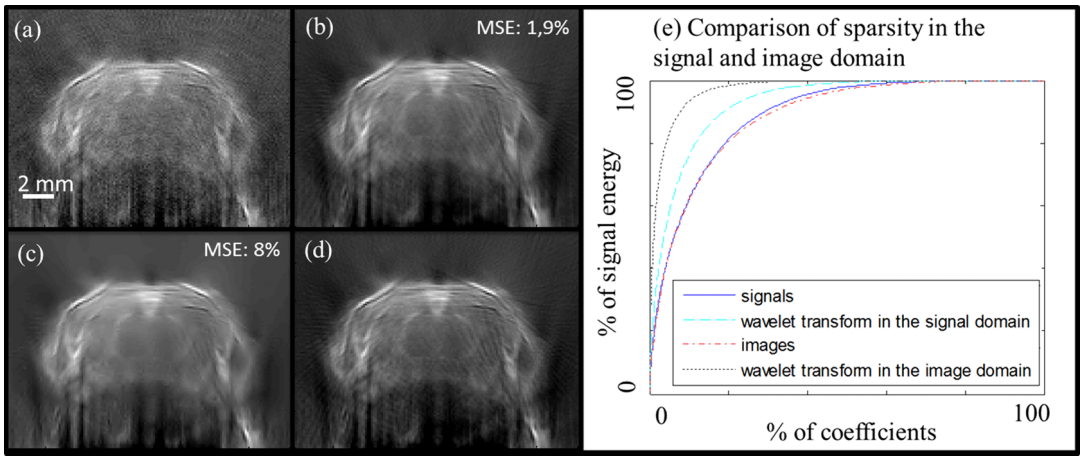

FIG. 8. Comparison between denoising in the signal and the image domain. (a) Noisy image. (b) Denoising in the signal domain followed by image reconstruction. (c) Denoising in the image domain. (d) Reconstruction from the noise-free signals. (e) Comparison of sparsity between the wavelet transform in the image and the signal domain.

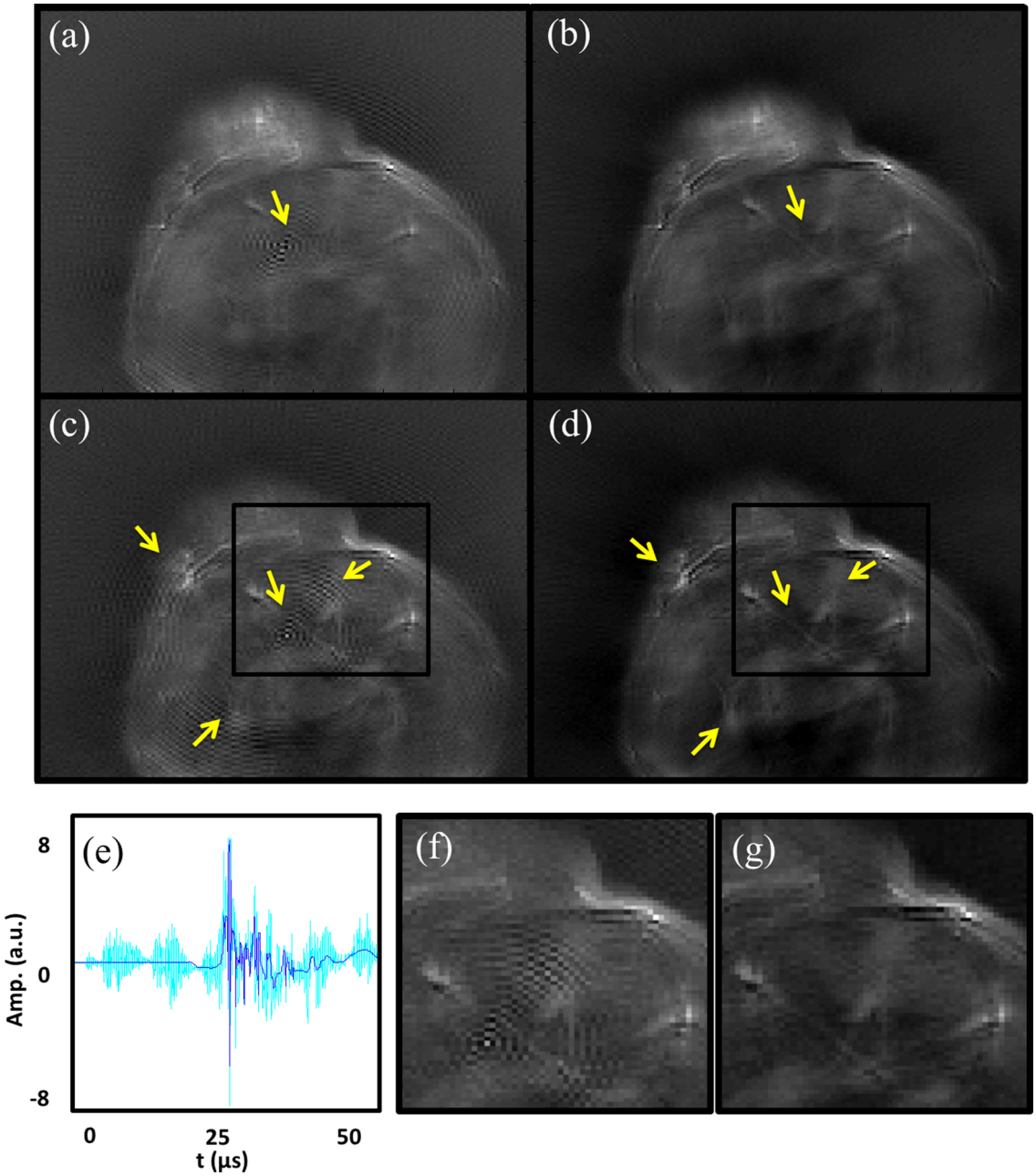

FIG. 9. Denoising of a purely experimental dataset in the case of very strong parasitic noise due to electromagnetic interference. (a) and (c) Original multispectral images of a nude mouse in the abdominal area with a subcutaneous tumor, at wavelengths of 700 and 900 nm, respectively. (b) and (d) Corresponding reconstructed images after spatiospectral signal denoising. (e) Overlay of original noisy and denoised signal. (f) and (g) Magnification of central tissue area of (c) and (d), respectively.

case, a 2D wavelet transform with the same mother wavelet (db2) was applied in the reconstructed image. Figure 8(d) presents the image reconstructed from the noise-free signals. Finally, Fig. 8(e) presents a comparison on the sparsity offered by wavelet transforms in the signal and image domain with no noise present. While the wavelet transform in the image domain offers higher sparsity, when denoising is applied in the image domain, the MSE with respect to the image reconstructed from the noise-free signals appears higher. This may be due to the fact that some reconstruction artifacts are also rejected. However, this effect is hard to quantify.

5.D. Application in experimentally derived noisy datasets

In the following, the performance of the denoising method is demonstrated in a purely experimental dataset acquired from the abdominal area of a nude mouse bearing a subcutaneous tumor. Imaging was performed at eight uniformly sampled wavelengths ($N_w = 8$) from 700 to 900 nm. A similar MSOT setup to the one described in Sec. 4.C was hereby used that employs an ultrasound array of 256 elements ($N_p = 256$) covering an angle view of 270°. Strong parasitic noise was present in the experimental data at certain

projections due to electromagnetic interference, which led to the formation of ring artifacts in the image domain after tomographic reconstruction. Figure 9 shows the application of the spatiospectral denoising method on the experimental data. Figures 9(a) and 9(c) correspond to the images reconstructed from the noisy signals at 700 and 900 nm, respectively. Figures 9(b) and 9(d) correspond to the images reconstructed from the associated denoised signals. Figure 9(e) shows the superposition of a noisy and the associated denoised signal, correspond to an arbitrary projection and wavelength. Finally, Figs. 9(f) and 9(g) present a magnification of the central tissue for better visual inspection. The presented spatiospectral denoising method successfully restores the data by rejecting the superimposed noise while preserving fine image details.

6. DISCUSSION

One of the major challenges in MSOT is the relatively low SNR of the detected ultrasound signals. To overcome this challenge, repetitive signal averaging or a hardware approach is usually adopted (e.g., the employment of low-noise electronics, electric insulation, and large ultrasound detectors). However, hardware solutions often come with disadvantages such as high cost, bulky setup, and image distortions, while signal averaging largely compromises the temporal resolution. In contrast, algorithmic solutions have the advantage of improving image quality based on available data without any additional cost other than computation time and some potential signal loss.

In this paper, we sought to identify a highly sparse representation for multispectral optoacoustic signals for formulating a general denoising methodology for this imaging technology. Optoacoustic signals are well-localized in space and can be modeled as a superposition of N-shaped pulses, indicating that wavelet bases with compact support can offer an appropriate sparse representation. Additionally, the optoacoustic spectral responses of tissue consist of a nonlinear combination of a small number of spectral signatures associated with tissue-intrinsic absorbers, indicating that spectral profiles can further be sparsely represented using an appropriate transformation. By reviewing such fundamental signal characteristics both in space and in spectrum, we identified the w-KLT as a highly suitable representation for MSOT signals. When applied in experimental tissue data obtained *in vivo*, this transformation showcased substantially increased sparsity as compared to common alternative representations (Fig. 3). A number of denoising studies in optoacoustic imaging were mainly seeking to identify an appropriate mother wavelet.[27–29] The presented Lorenz curves (Fig. 3) indicate that the mother wavelet has a much lower impact as compared to the further utilization of the multispectral information that is often available.

The proposed denoising method was applied mainly in the signal domain where an accurate estimation of the noise levels is typically available. An application in the image domain can be more challenging due to the influence of the reconstruction algorithm employed and the lack of gold standard. In the signal domain, the method combines information from all available signals stemming from different projections for the calculation of a single correlation matrix $\mathbf{G}$. In contrast to common multispectral images, MSOT signals are expected to contain similar spectral characteristics across different frequencies and projections. In this respect, one global correlation matrix $\mathbf{G}$ may result in more robust performance, especially in cases where certain frequencies or projections are more prone to noise than others.

Evaluated on biological samples imaged *in vivo*, the presented denoising framework demonstrated great noise suppression capabilities with minimal signal loss while considerably outperforming previously proposed strategies that are based solely on spatial signal characteristics (Figs. 5 and 6). Computationally, the methodology does not introduce significant overhead over the simple wavelet-thresholding approach. Specifically, the required computational time for denoising a dataset composed of 22 wavelengths, 64 projections, and 1024 samples per projection using an Intel i5-4200U CPU is 20 s for spatiospectral denoising versus 17.5 s for spatial denoising, indicating an overhead of ~15%. A potential drawback of the presented approach is the possible misclassification of true optoacoustic signals as noise when such signals correspond to spectral outliers, like molecular agents with a distinct spectrum that appear in very low amounts within tissue.[33] For such applications of the technology, an alternative denoising approach that is not associated with signal loss should ideally be developed.

Our current work demonstrated the denoising capabilities in the case of a tomographic multispectral optoacoustic system, but the proposed approach could similarly be applied to multispectral optoacoustic microscopy, as well as clinical translations of the technology, that demand rapid image acquisition and immediate feedback. In addition, the w-KLT that was hereby identified to offer very suitable properties in terms of sparsity for multispectral optoacoustic signals and images could be potentially further exploited for data compression or in the context of advanced tomographic reconstruction approaches[31] for enhancing the reconstruction speed of multispectral optoacoustic images.

ACKNOWLEDGMENTS

The authors would like to thank Uwe Klemm, Sarah Glasl, and Dr. Antonio Nunes for assisting in animal handling and image acquisition. All animal experiments were approved by the District Government of Upper Bavaria. The work of S. Tzoumas was supported by the DFG GRK 1371 grant and the Alexander S. Onassis Public Benefit Foundation. The work of V. Ntziachristos was supported by the European Union project FAMOS (FP7 ICT, Contract No. 317744) and the FP7-PEOPLE-2013-IAPP BRAINPATH—Molecular Imaging of Brain Pathophysiology, Project No. 612360. The work of D. Razansky was supported by the European Research Council under grant agreement ERC-2010-StG-260991.

[a]Author to whom correspondence should be addressed. Electronic mail: strtzoumas@gmail.com

[1]X. Wang, Y. Pang, G. Ku, X. Xie, G. Stoica, and L. V. Wang, "Noninvasive laser-induced photoacoustic tomography for structural and functionalin vivo imaging of the brain," Nat. Biotechnol. **21**, 803–806 (2003).
[2]R. A. Kruger, W. L. Kiser, D. R. Reinecke, G. A. Kruger, and K. D. Miller, "Thermoacoustic molecular imaging of small animals," Mol. Imaging **2**, 113–123 (2003).
[3]V. Ntziachristos, "Going deeper than microscopy: The optical imaging frontier in biology," Nat. Methods **7**, 603–614 (2010).
[4]P. Beard, "Biomedical photoacoustic imaging," Interface Focus **1**, 602–631 (2011).
[5]H. F. Zhang, K. Maslov, G. Stoica, and L. V. Wang, "Functional photoacoustic microscopy for high-resolution and noninvasive in vivo imaging," Nat. Biotechnol. **24**, 848–851 (2006).
[6]D. Razansky, A. Buehler, and V. Ntziachristos, "Volumetric real-time multispectral optoacoustic tomography of biomarkers," Nat. Protoc. **6**, 1121–1129 (2011).
[7]S. Sethuraman, S. R. Aglyamov, J. H. Amirian, R. W. Smalling, and S. Y. Emelianov, "Intravascular photoacoustic imaging using an IVUS imaging catheter," IEEE Trans. Ultrason. Ferroelectr. Freq. Control **54**, 978–986 (2007).
[8]J. M. Yang, K. Maslov, H. C. Yang, Q. Zhou, K. K. Shung, and L. V. Wang, "Photoacoustic endoscopy," Opt. Lett. **34**, 1591–1593 (2009).
[9]J.-M. Yang, C. Favazza, R. Chen, J. Yao, X. Cai, K. Maslov, Q. Zhou, K. K. Shung, and L. V. Wang, "Simultaneous functional photoacoustic and ultrasonic endoscopy of internal organs in vivo," Nat. Med. **18**, 1297–1302 (2012).
[10]R. A. Kruger, R. B. Lam, D. R. Reinecke, S. P. Del Rio, and R. P. Doyle, "Photoacoustic angiography of the breast," Med. Phys. **37**, 6096–6100 (2010).
[11]S. A. Ermilov, T. Khamapirad, A. Conjusteau, M. H. Leonard, R. Lacewell, K. Mehta, T. Miller, and A. A. Oraevsky, "Laser optoacoustic imaging system for detection of breast cancer," J. Biomed. Opt. **14**, 024007 (2009).
[12]V. Ntziachristos and D. Razansky, "Molecular imaging by means of multispectral optoacoustic tomography (MSOT)," Chem. Rev. **110**, 2783–2794 (2010).
[13]D. Razansky, M. Distel, C. Vinegoni, R. Ma, N. Perrimon, R. W. Koster, and V. Ntziachristos, "Multispectral opto-acoustic tomography of deep-seated fluorescent proteins in vivo," Nat. Photonics **3**, 412–417 (2009).
[14]G. S. Filonov, A. Krumholz, J. Xia, J. Yao, L. V. Wang, and V. V. Verkhusha, "Deep-tissue photoacoustic tomography of a genetically encoded near-infrared fluorescent probe," Angew. Chem., Int. Ed. **51**, 1448–1451 (2012).
[15]M. Li, J. Oh, X. Xie, G. Ku, W. Wang, C. Li, G. Lungu, G. Stoica, and L. V. Wang, "Simultaneous molecular and hypoxia imaging of brain tumors in vivo using spectroscopic photoacoustic tomography," Proc. IEEE **96**, 481–489 (2008).
[16]S. Mallidi, T. Larson, J. Tam, P. P. Joshi, A. Karpiouk, K. Sokolov, and S. Emelianov, "Multiwavelength photoacoustic imaging and plasmon resonance coupling of gold nanoparticles for selective detection of cancer," Nano Lett. **9**, 2825–2831 (2009).
[17]A. Taruttis, M. Wildgruber, K. Kosanke, N. Beziere, K. Licha, R. Haag, M. Aichler, A. Walch, E. Rummeny, and V. Ntziachristos, "Multispectral optoacoustic tomography of myocardial infarction," Photoacoustics **1**, 3–8 (2013).
[18]A. Buehler, M. Kacprowicz, A. Taruttis, and V. Ntziachristos, "Real-time handheld multispectral optoacoustic imaging," Opt. Lett. **38**, 1404–1406 (2013).
[19]A. Taruttis, S. Morscher, N. C. Burton, D. Razansky, and V. Ntziachristos, "Fast multispectral optoacoustic tomography (MSOT) for dynamic imaging of pharmacokinetics and biodistribution in multiple organs," PLoS One **7**, e30491 (2012).
[20]N. C. Burton, M. Patel, S. Morscher, W. H. Driessen, J. Claussen, N. Beziere, T. Jetzfellner, A. Taruttis, D. Razansky, B. Bednar, and V. Ntziachristos, "Multispectral opto-acoustic tomography (MSOT) of the brain and glioblastoma characterization," NeuroImage **65**, 522–528 (2013).
[21]L. D. Liao, M. L. Li, H. Y. Lai, Y. Y. I. Shih, Y. C. Lo, S. Tsang, P. C. P. Chao, C. T. Lin, F. S. Jaw, and Y. Y. Chen, "Imaging brain hemodynamic changes during rat forepaw electrical stimulation using functional photoacoustic microscopy," NeuroImage **52**, 562–570 (2010).
[22]J. L. Starck and P. Querre, "Multispectral data restoration by the wavelet Karhunen–Loève transform," Signal Processing **81**, 2449–2459 (2001).
[23]A. Rosenthal, V. Ntziachristos, and D. Razansky, "Model-based optoacoustic inversion with arbitrary-shape detectors," Med. Phys. **38**, 4285–4295 (2011).
[24]M. A. A. Caballero, A. Rosenthal, A. Buehler, D. Razansky, and V. Ntziachristos, "Optoacoustic determination of spatio-temporal responses of ultrasound sensors," IEEE Trans. Ultrason. Ferroelectr. Freq. Control **60**, 1234–1244 (2013).
[25]G. Diebold, T. Sun, and M. Khan, "Photoacoustic monopole radiation in one, two, and three dimensions," Phys. Rev. Lett. **67**, 3384–3387 (1991).
[26]C. Li and L. V. Wang, "Photoacoustic tomography and sensing in biomedicine," Phys. Med. Biol. **54**, R59–R97 (2009).
[27]J. A. Viator, B. Choi, M. Ambrose, J. Spanier, and J. S. Nelson, "In vivo port-wine stain depth determination with a photoacoustic probe," Appl. Opt. **42**, 3215–3224 (2003).
[28]L. Zeng, D. Xing, H. Gu, D. Yang, S. Yang, and L. Xiang, "High antinoise photoacoustic tomography based on a modified filtered backprojection algorithm with combination wavelet," Med. Phys. **34**, 556–563 (2007).
[29]S. H. Holan and J. A. Viator, "Automated wavelet denoising of photoacoustic signals for circulating melanoma cell detection and burn image reconstruction," Phys. Med. Biol. **53**, N227–N236 (2008).
[30]J. Provost and F. Lesage, "The application of compressed sensing for photoacoustic tomography," IEEE Trans. Med. Imaging **28**, 585–594 (2009).
[31]A. Rosenthal, T. Jetzfellner, D. Razansky, and V. Ntziachristos, "Efficient framework for model-based tomographic image reconstruction using wavelet packets," IEEE Trans. Med. Imaging **31**, 1346–1357 (2012).
[32]D. L. Donoho and J. M. Johnstone, "Ideal spatial adaptation by wavelet shrinkage," Biometrika **81**, 425–455 (1994).
[33]S. Tzoumas, N. Deliolanis, S. Morscher, and V. Ntziachristos, "Unmixing molecular agents from absorbing tissue in multispectral optoacoustic tomography," IEEE Trans. Med. Imaging **33**, 48–60 (2014).
[34]R. R. Coifman and D. L. Donoho, "Translation-invariant de-noising," in *Lecture Notes In Statistics* (Springer-Verlag, New York, NY, 1995), pp. 125–150.
[35]S. Mallat, *A Wavelet Tour of Signal Processing* (Academic, New York, NY, 1999).
[36]A. Rosenthal, D. Razansky, and V. Ntziachristos, "Fast semi-analytical model-based acoustic inversion for quantitative optoacoustic tomography," IEEE Trans. Med. Imaging **29**, 1275–1285 (2010).
[37]X. L. Dean-Ben, V. Ntziachristos, and D. Razansky, "Acceleration of optoacoustic model-based reconstruction using angular image discretization," IEEE Trans. Med. Imaging **31**, 1154–1162 (2012).
[38]N. Hurley and S. Rickard, "Comparing measures of sparsity," IEEE Trans. Inf. Theory **55**, 4723–4741 (2009).